Multifrequency Studies of S-shaped Radio Galaxies

A thesis submitted in fulfilment of the requirements

for the degree of Doctor of Philosophy in Astronomy

by

Arpita Misra

JAGIELLONIAN UNIVERSITY
IN KRAKÓW

Doctoral School of Exact and Natural Sciences

Astronomical Observatory of the Jagiellonian University

Supervisor: Marek Jamrozy

June 2025

Abstract

Radio galaxies produce the largest and the most powerful outflows in the universe through bipolar jets of relativistic plasma, launched from the vicinity of supermassive black holes (SMBHs) at their centers. These jets are fuelled by the accretion of infalling gas and matter, making them vital tracers of SMBH activity. Radio analysis of these galaxies remains one of the most effective methods for probing the past of SMBHs at galactic centers wherein the radio morphology plays a critical role in studying the inner workings of the host galaxy. Many interesting morphologies have been discovered and have been extensively studied such as C- and U-shaped tailed radio galaxies and X-shaped winged radio galaxies. However, the morphological class of the rarer S-shaped radio galaxies, that are often interpreted as a signature of jet precession, have remained observationally sparse. Despite their potential to shed light on the dynamics of active galactic nuclei (AGN) and the central SMBH, they remain dominantly underexplored. Radio observations provide one of the most effective means of probing the past behavior of SMBHs, as the extended structures captured in multifrequency radio maps preserve the evolutionary history of these systems over timescales ranging from decades to hundreds of millions of years.

In this thesis, I present a detailed radio study of a previously unexplored sample of S-shaped radio galaxies using high-sensitivity and multifrequency data from the uGMRT, as well as LOFAR and the VLA. The spatial coverage obtained from the multifrequency radio maps helps unravel the entire course of evolution of a radio galaxy, from a scale of tens of years to hundreds of millions of years. High-resolution images at both low and high radio frequencies help track peculiar behavior of SMBHs, such as restarting, double-double, and twisted jet radio galaxies among many others. Thorough investigation is presented for two such sources (one S-shaped and an X-shaped) that exhibit compelling signatures of jet precession and reorientation, resulting in highly peculiar radio morphologies.

Chapter 1 provides a concise introduction to radio galaxies, with a particular focus on their morphological classification. It also outlines key aspects of AGN physics and includes a

discussion on current and upcoming radio telescopes that enable such studies.

In Chapter 2, a detailed morphological analysis is presented for a sample of S-shaped radio galaxies, based on dedicated multifrequency radio observations. This sample, selected based on their characteristic large-scale S-shaped morphology, has not been previously studied in detail. The analysis includes study of the lobe curvature, jet symmetry, hotspot structures, and diffuse emission trails. Several sources exhibit signs of jet bending, multiple hotspots, and misalignments suggestive of jet precession and reorientation events.

In Chapter 3, a unique X-shaped radio galaxy is investigated using multifrequency radio data. The source exhibits two pairs of inner and outer lobes indicative of restarting activity, and its host galaxy, CGCG 292–057, shows optical features characteristic of a post-merger system. Various particle injection models were applied to the radio spectra of the lobes, while the radio core spectrum was analyzed using absorption models. Notably, the core displays a double-peaked spectrum with distinct spectral turnovers at both low and high frequencies. The two spectral turnovers observed in the core are best explained by synchrotron radiation undergoing absorption in two zones within the central nuclear region, suggesting a complex structure of the AGN core environment. Spectral ageing analysis of the lobes and wings supports a scenario involving rapid jet realignment, with an estimated reorientation timescale of a few million years.

In Chapter 4, a multiwavelength study of an inversion-symmetric S-shaped radio galaxy, PKS 2300-18, is presented using dedicated uGMRT and JVLA radio observations. The source displays large scale diffuse emission surrounding S-shaped jets with its quasar host interacting with a nearby companion galaxy. Spectral ageing analysis, based on particle injection model, reveals a maximum plasma age of $\sim$40 Myr, while a kinematic jet precession model suggests a precession period of $\sim$12 Myr. Optical spectra of the central region of the host galaxy shows double-peaked broad emission lines, indicating complex broad-line region kinematics. X-ray data from Chandra modeled with thermal and power-law components provide additional insight into the AGN's central engine.

S-shaped jets in radio galaxies suggest a complex and dynamic central engine, raising important questions about the mechanisms driving deviations from classical radio morphologies. This thesis presents the most extensive sample-based investigation of S-shaped radio galaxies to date, utilizing multifrequency radio observations to explore their morphological evolution. It includes the first comprehensive multiwavelength analysis of a giant S-shaped radio galaxy, tracing its history from sub-parsec to megaparsec scales. Such studies offer valuable insight into the otherwise elusive dynamical behavior of SMBHs and AGN-galaxy co-evolution, particularly in distant galaxies where direct observations are challenging.

Streszczenie

Radiogalaktyki związane są z największymi i najbardziej energetycznymi ukierunkowanymi wypływami we Wszechświecie. Współosiowe, przeciwnie skierowane dżety naładowanych relatywistycznych cząstek emanują z okolic supermasywnych czarnych dziur (ang. supermassive black holes, SMBHs) znajdujących się w centrach ich galaktyk macierzystych. Dżety te są napędzane przez akrecję materii na zwarty centralny obiekt, co czyni je istotnymi wyznacznikami aktywności SMBHs. Analiza wielkoskalowych radiowych struktur galaktyk aktywnych (ang. active galactic nuclei, AGNs) pozostaje jedną z najskuteczniejszych metod badania przeszłości SMBHs znajdujących się w centrach galaktyk macierzystych. Istnieje wiele interesujących typów radiogalaktyk, które zostały już dogłębnie zbadane. Są nimi m. im. radiogalaktyki wygięte w kształcie liter "C" i "U" oraz radioźródła z podwójnymi parami płatów w kształcie litery "X". Jednym ze słabo poznanych typów pozostają radiogalaktyki, których morfologia przypomina kształt litery "S". Ich dziwnie wygięte struktury są często przypisywane precesji obiektów centralnych i związanych z nimi dżetów. Grupa tych obiektów jest niezbyt liczna. Pomimo ich potencjalnie dużego znaczenia w poznaniu AGNów i centralnych SMBHs, pozostają one w dużej mierze niezbadane. Wieloczęstotliwościowe obserwacje radiowe tych obiektów stanowią jeden z najskuteczniejszych sposobów badania ewolucji aktywnych SMBHs. Analiza map radiowych pozwala na odtworzenie historii tych systemów w skali czasowej od dziesięcioleci do setek milionów lat.

W niniejszej rozprawie przedstawiono szczegółowe badania radiowe kilku niezbadanych dotąd radiogalaktyk S-kształtnych. Wykorzystano w tym celu bardzo czułe, wieloczęstotliwościowe dane pochodzące z radioteleskopów uGMRT, LOFAR i VLA. Duża kątowa zdolność rozdzielcza i dobre przestrzenne pokrycie rozciągłych struktur analizowanych tutaj Wieloczęstotliwościowych obserwacji radiowych są kluczowe w analizie przebiegu ewolucji struktur radiogalaktyk, w skalach od dziesiątek lat do setek milionów lat. Obrazy o wysokiej rozdzielczości, zarówno na niskich, jak i wysokich częstotliwościach radiowych, pomagają śledzić aktywność SMBHs i generowanych przez nie typowych oraz osobliwych struktur

posiadających, np. oznaki wznawianej aktywności oraz wygiętych dżetów. Ponadto, w rozprawie przedstawiono szczegółowe badania dwóch nietypowych radiogalaktyk – jednej w kształcie litery "S", drugiej w kształcie litery "X". Oba obiekty posiadają silne symptomy precesji i reorientacji osi dżetów, co można stwierdzić w oparciu o analizę ich osobliwych struktur radiowych.

Rozdział pierwszy rozprawy zawiera zwięzłe wprowadzenie do tematyki radiogalaktyk, ze szczególnym uwzględnieniem ich klasyfikacji morfologicznej. Przedstawiono tutaj również kluczowe aspekty fizyki AGNów. Ponadto, podano charakterystyki współczesnych i planowanych radioteleskopów, które umożliwiają prowadzenie prezentowanych tutaj badań.

W rozdziale drugim przedstawiono szczegółową analizę morfologiczną próbki galaktyk w kształcie litery "S", opartą o dedykowane wieloczęstotliwościowe obserwacje radiowe. Próbka ta, została skonstruowana na podstawie charakterystycznej S-kształtnej wielkoskalowej morfologii tych obiektów. Obiekty z tej próbki nie były wcześniej szczegółowo badane. Przeprowadzona tutaj analiza obejmuje badanie krzywizny płatów, symetrii dżetów, struktur gorących plam oraz wielko-skalowej emisji dyfuzyjnej. Wiele analizowanych w niniejszej rozprawie obiektów wykazuje oznaki wygięcia dżetów, obecności wielokrotnych gorących plam i występowania niewspółosiowo-symetrycznych struktur sugerujących precesję i/lub reorientację dżetów.

W rozdziale trzecim zaprezentowano badania, oparte o wieloczęstotliwościowe dane radiowe, unikatowej radiogalaktyki o strukturze w kształcie litery "X". Analizowany obiekt posiada dwie pary płatów – wewnętrzne i zewnętrzne, co jest oznaką wznawiania aktywności dżetowej. Jego galaktyka macierzysta CGCG 292-057 posiada zaburzoną strukturę związaną z kolizją z innym obiektem. W analizie widma radiowego płatów uwzględniano kilka modeli wstrzyknięcia i ewolucji relatywistycznych naładowanych cząstek oraz różne konfiguracje pola magnetycznego. W analizie widma radiowego jądra uwzględniono absorpcję promieniowania. Bimodalny charakter rozkładu strumienia jądra, z maksimami na niskich i wysokich częstotliwościach, można wyjaśnić absorpcją promieniowania synchrotronowego w dwóch obszarach w pobliżu centralnego AGNu, które różnią się

znacznie własnościami fizycznymi. Analiza "starzenia" się widma płatów i ich przedłużeń (tzw. skrzydeł) doprowadziła do stworzenia scenariusza, który proponuje szybkie przeorientowanie osi dżetów w skali czasowej wynoszącej kilka milionów lat.

W rozdziale czwartym przedstawiono wieloczęstotliwościowe badania obrotowo-symetrycznej, S-kształtnej radiogalaktyki PKS 2300-18. Są one oparte na dedykowanych obserwacjach radiowych pochodzących z interferometrów uGMRT i VLA. Badany obiekt posiada wielkoskalową emisję dyfuzyjną otaczającą dżety przypominające kształtem literę "S". Emanują one z kwazara oddziaływującego z towarzyszącą galaktyką. Analiza widma struktury radiowej oparta o modelowanie strat synchrotronowych ujawniła maksymalny wiek plazmy rowny ok. 40 mln lat. Modelowanie kinematycznego przeorientowywania dżetów sugeruje okres precesji rowny ok. 12 mln lat. Spektroskopowe badania optyczne tego obiektu pokazały obecność w jego widmie szerokich linii emisyjnych o podwójnej strukturze, co wskazuje na złożoną kinematykę gazu w obszarze bliskim centralnej czarnej dziury. Ponadto, modelowanie widma rentgenowskiego uzyskanego za pomocą teleskopu Chandra ujawniło w pobliżu SMBH obecność dwuskładnikowego ośrodka opisanego składową termiczną i wykładniczą.

Radiogalaktyki posiadające S-kształtne dżety związane są ze złożoną i dynamicznie zmieniającą się konfiguracją centralnego źródła. Prowadzenie badań tego typu obiektów pozwala na poznanie mechanizmów prowadzących do powstawania unikatowych struktur radiowych odbiegających od klasycznych struktur o symetrii osiowej. Niniejsza rozprawa przedstawia najbardziej obszerne jak dotąd badania radiogalaktyk w kształcie litery "S". Oparte są one na wieloczęstotliwościowych obserwacjach radiowych rozciągłych dyfuzyjnych struktur i kompleksowej ich analizie. W szczególności, rozprawa przedstawia pierwszą wszechstronną wieloczęstotliwościową analizę gigantycznej radiogalaktyki, która umożliwia badanie ewolucji jej struktury w skali od sub-parsekowej do megaparseków. Przedstawione w niniejszej rozprawie wyniki dają możliwość obserwacyjnego poznania, nieuchwytnej w inny sposób, dynamiki SMBH oraz długoczasowej koewolucji AGNu i macierzystej galaktyki. Ma to duże znaczenie szczególnie w przypadku obiektów odległych, dla których bezpośrednie obserwacje zachowania ich SMBHs są praktycznie niemożliwe.

Acknowledgements

Here, I would like to express my heartfelt gratitude towards the people who have played an important role in my journey and in my life so far.

First and foremost, I am deeply grateful to my parents and my sister, whose unwavering support has guided and empowered me in the pursuit of my dreams. I am grateful to my father, whose genuine excitement for my research and constant willingness to support me in every possible way is extremely encouraging. I would like to thank my mother, who is also my first teacher, without her selfless support I would not be where I am today. She embraced my dreams as her own and stood by me through every challenge along the way. I will remain forever indebted to them. I would like to thank my younger sister, who has been the pillar of support throughout my PhD journey. Despite the distance, she has always been available to me at times of need. She is my best friend and also my constant source of joy and happiness, and also the illustrator of Figure 1.8!

During my school years, if there was one teacher who left a lasting impact on my life, it was my English teacher, Mrs. Y.V. Rao. If I am able to articulate myself clearly in English today, the credit goes to her. She cared deeply for her students, not only teaching us language but also instilling in us good manners and values. Most importantly, she was the first teacher who truly believed in me and supported me unconditionally. My love for English poetry and literature began in her classroom. I hope that one day she will feel satisfied with the progress I have made in my vocabulary and language skills. My knowledge of physics and mathematics during my school years was shaped and strengthened by my physics teacher, Mr. Prabhakar Behera. I remain deeply grateful to him for nurturing my interest in the sciences during those formative years. I would also like to thank Mathur Sir, who, during my college days, was the first teacher to truly listen to my dream of becoming an astronomer. His support and guidance played a crucial role in helping me pursue that path.

I would like to express my heartfelt gratitude to Dr. Ananda Hota, because of whom my journey in astronomy began during my undergraduate days, through the Rad@home Collaboratory. His mentorship and guidance played a pivotal role in shaping my path and leading me successfully towards my PhD journey. I owe much of my foundational understanding of astronomy to him, and I remain immensely grateful for his support and inspiration. I would also like to thank Mr. Santosh K. Agarwalla, who taught me quantum mechanics, nuclear physics, and mathematical physics during my master's degree. I still vividly remember the excitement I felt attending his classes, his enthusiasm and clarity

made complex topics feel effortless to grasp and a joy to learn. I am equally grateful to Mr. Nrusingh Biswal, my master's thesis supervisor. Despite being based in the U.S. while I was in India, he remained fully committed to guiding me with dedication and care. His support was instrumental in helping me learn and complete my research work. I will always be grateful to him for his encouragement and mentorship.

During my PhD journey, I was grateful to be guided by my supervisor, Prof. Marek Jamrozy, whose mentorship helped me take professional steps into the field of astronomy and helped me establish myself as an independent researcher. I would also like to express my sincere thanks to my auxiliary supervisor, Dr. Urszula Pajdosz-Śmierciak, for her guidance during my PhD and for her crucial support, especially during the process of observation proposal writing. I would like to thank Dorota Kozieł and Marek Weżgowiec for being incredibly kind and supportive collaborators. It has been a truly rewarding experience working with both of you. I would like to thank Tomasz and Greg for always helping me with IT-related issues, and my officemate, Oleh Kobzar, for being so kind and genuinely wonderful company. I would like to extend my heartfelt gratitude to our faculty members, Łukasz Stawarz, Jerzy Krzesiński, Stanisław Zoła, Marian Soida, Krzysztof Chyży and Arti Goyal, for their invaluable guidance throughout my PhD journey and their kindness and support from the very first day. I feel truly fortunate to have been part of such a positive and welcoming environment during my time at the observatory.

I would like to thank the OAUJ Indian PhD student community, who welcomed me warmly from the very beginning of my studies. Thanks to Unnikrishnan, Angel, Syed, Aditya, Subhrata for making my journey in Krakow truly memorable, and especially Goutham for helping me alot during my final few months leading to the submission of this thesis. I would also like to thank Ania, Patryk, Sebastian, and Basia for always being such wonderful company at the observatory. I truly cherished all our conversations and the time we spent together. I would also like to thank Nikita, Tamasa, Pragyan, and Sourav, my oldest and dearest friends since school and college, for always being there for me. Despite the distance, their unfailing care and support during my times of need have meant the world to me, and I am deeply grateful for their friendship.

My journey in astronomy began because of Stephen Hawking. He will forever remain my inspiration and a symbol of hope, someone who overcame extraordinary challenges and persevered in his passion and became one of the greatest theoretical physicists and cosmologists of our time. I am also deeply grateful to Brian Greene, whose remarkable work through the World Science Festival has helped me fuel my own passion for sharing knowledge. His intellectually rich conversations with leading experts, made freely accessible to

the world, have been truly inspiring. I am equally thankful to have encountered Tom Kibble, who was a British cosmologist, whose intellect, character, and leadership will forever inspire me.

I would like to wholeheartedly thank Jagiellonian University for generously supporting me throughout my studies, through multiple grants awarded for conference travel and in recognition of my scientific publications. I am incredibly grateful to have had the opportunity to work at the Observatory. I have cherished every season spent here. The calm and serene atmosphere created a truly peaceful working environment, making the Observatory feel like a second home to me.

Finally, I would like to express my sincere gratitude to Poland, especially to Kraków, for the warmth and hospitality. Though I wasn't born here, I have always felt genuinely welcomed. The kindness and generosity of the people around me have left a lasting impression and for that, I will always be grateful. Kraków will forever hold a special place in my heart as my second home. Thank you for having me here. *Dziękuję Bardzo*!

Contents

List of Figures

List of Tables

Abbreviations

ADAF	Advection Dominated Accretion Flow
AGN	Active Galactic Nucleus
ASKAP	Australian Square Kilometre Array Pathfinder
BBH	Binary Black Hole
BLR	Broad Line Region
BZ	Blandford-Znajek
DDRG	Double-double Radio Galaxy
EHT	Event Horizon Telescope
EMU	Evolutionary Map of the Universe
FIRST	Faint Images of the Radio Sky at Twenty centimeter
FR	Fanaroff and Riley
HT	Head Tail
ICM	Intracluster Medium
IGM	Intergalactic Medium
JVLA	Karl G. Jansky Very Large Array
KH	Kelvin–Helmholtz

LINER	Low Ionization Nuclear Emission Line Region
LOFAR	Low Frequency Array
LoLSS	LOFAR LBA Sky Survey
LoTSS	LOFAR Two-metre Sky Survey
MAD	Magnetically Arrested Disk
MRI	Magnetohydrodynamic Instability
NAT	Narrow Angle Tail
NLR	Narrow Line Region
NVSS	NRAO VLA Sky Survey
ORCs	Odd Radio Circles
RIAF	Radiatively Inefficient Accretion Flow
SANE	Standard and Normal Evolution
SKA	Square Kilometre Array
SMBH	Supermassive Black Hole
TGSS	TIFR GMRT Sky Survey
uGMRT	upgraded Giant Metrewave Radio Telescope
UV	Ultraviolet
VLBI	Very Long Baseline Interferometry
VLASS	VLA Sky Survey
WAT	Wide Angle Tail

List of Publications

Publications

1. Paper 1. *Multiwavelength investigations of PKS 2300–18: S-shaped radio quasar with precessing jets and double-peaked broad emission-line spectrum, Misra, A., Jamrozy, M., Wezgowiec, M., Kozieł-Wierzbowska, D., 2025, MNRAS, 536, 2025*.

2. Paper 2. *Multifrequency analysis of the radio emission from a post-merger galaxy CGCG 292-057, Misra, A., Jamrozy, M., Wezgowiec, M., 2023, MNRAS, 523, 1648*.

3. Paper 3. *Low Frequency Observations of Peculiar Radio Galaxies, Misra A., Jamrozy M., Pajdosz-Smierciak U., 2022, Proceedings of the Polish Astronomical Society Conference, P66*.

Dedicated to my Mother

Chapter 1

Introduction

1.1 Historical Perspective

On 26 April 1920, two astronomers, Harlow Shapley and Heber Curtis found themselves locked in the middle of the Great Debate at the Smithsonian Museum of Natural History. The debate centered on a profound question that had perplexed astronomers for centuries: the true nature of spiral nebulae and their implications for the scale of the Universe. In the year 1750, Thomas Wright speculated that some of the nebulae observed in the sky were not actually part of Milky Way but independent galaxies like the Milky way itself, which were subsequently referred to as "island universes" by Immanuel Kant. In the early twentieth century, astronomer Vesto M. Slipher conducted some spectroscopic observations of these nebulae and showed redshifted lines indicating that they were moving relative to the Milky Way at velocities greater than the escape velocity of our Galaxy, supporting Wright's idea. In the Great Debate, Shapley favored the argument that these nebulae were small and situated on the fringes of the Milky Way galaxy, whereas Curtis argued that they were separate galaxies, suggesting they were both extremely vast and far away. The debate was shortly resolved by Edwin Hubble's observation of Cephid variable stars, which led to the discovery of the spiral "Andromeda" as a galaxy outside the Milky Way (Hubble 1929).

In the meantime, before the quest to understand the extragalactic nature of galaxies was settled, there were hints of something unusual happening with these spiral nebulae. Edward Fath (Fath 1909) was conducting his own series of observations to test this claim by using a unique approach. He aimed at clarifying the nature of the "spiral nebulae" by testing the claim that spirals show a continuous spectrum consistent with a collection of stars, rather

than the bright line spectrum characteristic of gaseous nebulae. He analyzed the spectra of these objects and discovered a continuous spectrum featuring stellar absorption lines, indicating an unresolved cluster of solar type stars. However, in the case of NGC 1068, he observed that the "spectrum is composite, showing both bright and absorption lines". These bright lines were emission lines from NGC 1068, which were later confirmed by Vesto Slipher's observations in 1917 (Slipher 1917). Closely following it was another discovery made by H. D. Curtis of a "curious straight ray" in M87 galaxy which was connected to the nucleus by just a thin line (Curtis 1918). These were the initial moments of the discovery of Active Galactic Nuclei or AGN and extragalactic jets. However the physical nature of the jet and the host galaxy was still unknown for a few more decades.

1.2 Active Galactic Nuclei

Since Hubble's discovery, astronomers have observed hundreds of billions of galaxies in the universe, owing to the remarkable advancements that have taken place in the field of optical astronomy and instrumentation. Some of these galaxies were sufficiently peculiar to capture the attention of Carl Seyfert in 1940s (Seyfert 1943), when he observed spiral galaxies with some strongly emitting components at their centers. These galaxies, which had high-excitation emission lines were later known as Seyfert galaxies. This paved the road for the study of a particular class of galaxies known as active galactic nuclei. These galaxies are exceptionally luminous objects in the universe, emitting significant amount of energy across the electromagnetic spectrum from a compact region at their centers. This radiation is emitted from a region around the supermassive black hole (SMBH) at the center of galaxies (Kormendy and Gebhardt 2001; Merritt and Ferrarese 2001; Häring and Rix 2004) as a result of infalling material and in the presence of magnetic field.

1.2.1 Accretion Disk

Accretion classically describes the gravitationally driven inflow of matter towards a central massive object or the center of mass of an extended system. In most astrophysical systems, the inflowing gas carries a significant angular momentum, which acts as a centrifugal barrier, preventing direct infall. As a result, the gas settles into a rotationally supported, disk-like configuration, with the disk's orientation aligned with the angular momentum

vector of the accreting material. In order for the accretion onto the central object to proceed, this angular momentum must be transported outwards. In plasmas, this transport is mediated by magnetic stresses arising from magnetohydrodynamic (MHD) turbulence, especially through the magnetorotational instability (MRI; Balbus and Hawley 1991). These mechanisms effectively act as a source of "friction", helping transport angular momentum outwards and allowing mass to spiral inwards.

The structure and dynamics of the resulting accretion flow are critically dependent on the ability of the system to radiate away the generated thermal energy. Accretion flows are typically categorized into two major classes based on their radiative efficiency, ϵ, defined as

$$\epsilon = \frac{L}{\dot{M}c^2} \tag{1.1}$$

where L is the luminosity, $\dot{M}$ is the mass accretion rate, and c is the speed of light. If the dissipated energy is radiated on a timescale shorter than the accretion timescale, the gas cools efficiently and forms a geometrically thin, optically thick disk, with a vertical thickness H/R$\sim$0.01-0.03 (ratio of vertical thickness, H, to the radius, R, of the disk). These thin accretion disks (Shakura and Sunyaev 1973) are highly radiative, with efficiencies ranging from $\epsilon \sim 0.06$ to $\epsilon \sim 0.4$. This also makes them among the most efficient energy generation mechanisms in the universe, up to $\sim$50 times more efficient than nuclear fusion.

In contrast, when the cooling is inefficient and the gas cannot radiate its energy effectively, the flow becomes geometrically thick and radiatively inefficient, with $\epsilon << 1$. At low accretion rates ($\dot{M} \ll \dot{M}_{\rm Edd}$), such as in low-luminosity AGNs and quiescent X-ray binaries, the gas forms a hot, optically thin, two-temperature plasma, in which the ions are significantly at a higher temperature than the electrons (Narayan et al. 1998), here $\dot{M}_{\rm Edd}$ is the Eddington accretion rate defined as maximum steady accretion rate at which matter can fall onto a compact object (like a black hole or neutron star) without the outward force of radiation pressure (produced by the accretion itself) blowing the inflowing material away. These flows are typically modeled as Advection-Dominated Accretion Flows (ADAFs; see Figure 1.1), where most of the thermal energy is advected into the black hole rather than radiated away. Conversely, in the super-Eddington regime ($\dot{M} \gg \dot{M}_{\rm Edd}$), as proposed by Abramowicz et al. (1988), the high optical depth causes the emitted radiation to become trapped and advected with the flow. This leads to a radiation-pressure dominated, thick disk structure where photon trapping limits the radiative efficiency despite the high accretion rate. Such models apply to systems such as super-Eddington quasars and narrow line Seyfert 1 galaxies.

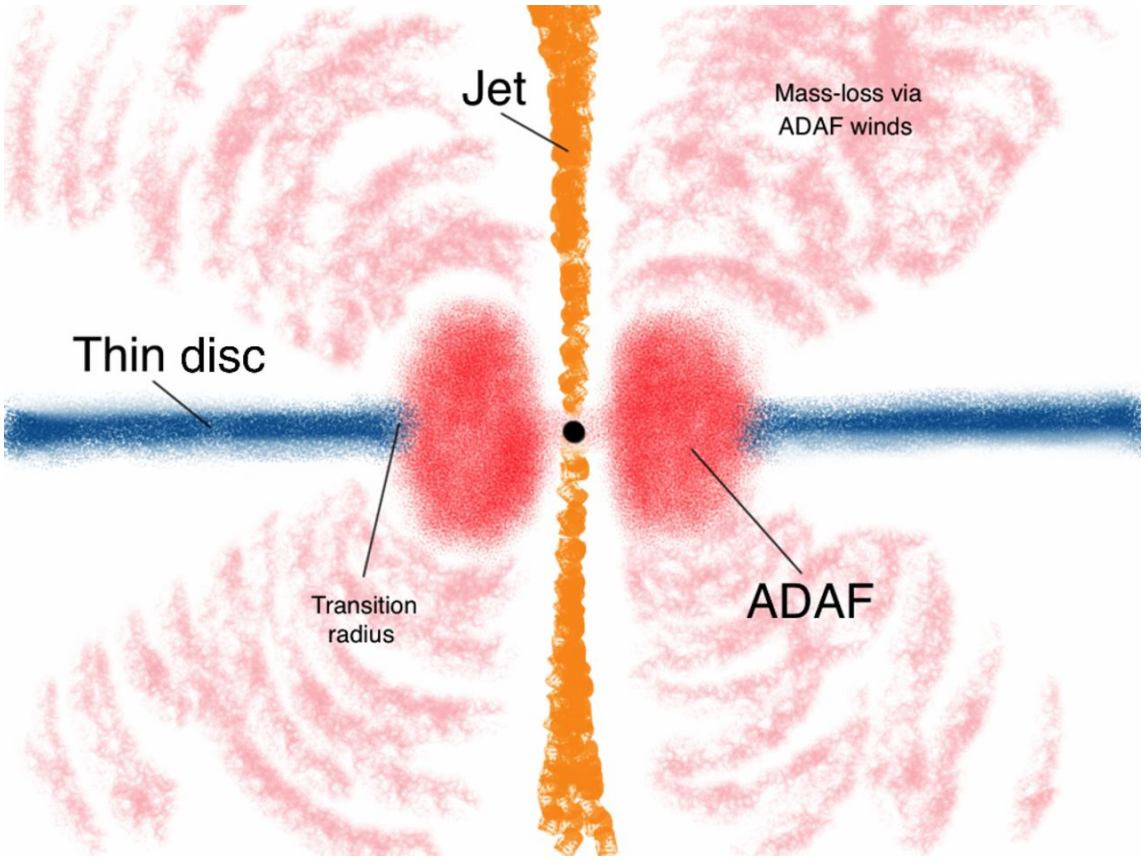

FIGURE 1.1: A cartoon version of the most favored scenario for the black hole accretion flow geometry and outflows in low-luminosity AGNs. It consists of three components: an inner ADAF, an outer truncated thin disc and a relativistic jet (NEMMEN ET AL. 2014).

When it comes to outflows from the accretion disks, one of the key player is the magnetic field configuration within the disk. This hugely determines the disk dynamics and launching of relativistic jets. The two main magnetic regimes are discussed below:

SANE (Standard and Normal Evolution): These disks have relatively weak, turbulent magnetic fields that evolve with the flow, this makes the accretion process smooth (NARAYAN ET AL. 2012; SĄDOWSKI ET AL. 2013). Jets in SANE systems are typically weaker and more variable. This scenario may describe systems like certain Seyfert galaxies or black hole binaries (BBH).

MAD (Magnetically Arrested Disk): These describe the disks where a strong poloidal magnetic flux accumulates near the horizon until it saturates. (BISNOVATYI-KOGAN AND RUZMAIKIN 1974; NARAYAN ET AL. 2003). This leads to highly energetic, stable jets. The accumulated magnetic field can become so strong close to the black hole (BH) that it can change the dynamics of the infalling matter, thereby regulating the accretion. The MAD regime is often invoked to explain powerful jets in systems such as M87, as observed by

the Event Horizon Telescope (EHT), and high-efficiency AGNs like blazars.

SMBH can sometimes launch powerful jets, driven by processes in their surrounding accretion disks. One of these mechanisms was discussed by Blandford and Znajek (1977) known as **Blandford-Znajek (BZ) process**. This theoretical mechanism explains how rotational energy can be extracted from a spinning BH to produce relativistic jets. In this model, the BH is threaded by strong, large-scale poloidal magnetic fields, which are anchored in the surrounding accretion disk or torus. As the BH rotates, it drags spacetime around it (a phenomenon known as frame dragging), twisting the magnetic field lines. This generates an outward flow of electromagnetic energy, essentially a Poynting flux that can launch powerful, collimated jets along the rotational axis of the BH. The BZ process is highly efficient in systems with strong magnetic fields, such as MAD, and is believed to be the primary engine behind the powerful jets observed in radio-loud AGNs, quasars, and blazars.

1.2.2 AGN classification

I. Quasar Mode AGN

It is also known as radiative mode AGN and is characterized by high accretion rates and efficient conversion of gravitational energy into electromagnetic radiation. This type of AGN typically accretes gas at a significant fraction of the Eddington limit in a geometrically thin, optically thick accretion disk (Shakura and Sunyaev 1973), which results in strong emission across the electromagnetic spectrum. This is in the form of thermal continuum emission spanning optical to ultraviolet (UV) regime. As material spirals inward, viscous dissipation heats the gas clouds close to the SMBH to temperatures that vary with radius: the outer disk emits in the optical, while the inner, hotter regions produce ultraviolet radiation. This stratified thermal emission creates the characteristic multi-temperature blackbody spectrum, observed as a prominent feature known as the "big blue bump" in the AGN spectral energy distribution. The corona, which is a compact high-temperature region of hot and optically thin plasma located above and/or around the inner accretion disk, upscatters the UV photons that originate from the disk and get inverse-Compton scattered to higher energies, giving rise to X-rays. This mode is further divided into the following types (Netzer 2015):

Type I AGN: The spectrum here shows all permitted line profiles and a few semi-forbidden line profiles that indicate large gas velocities of up to 5000-10,000 km/s. These

FIGURE 1.2: A fun depiction of a geometrically thick vs. thin accretion disk around a SMBH.

are objects with little or no obscuration of the central source of radiation (central disk or any other source within $\sim 1000 r_g$ of BH where r_g implies gravitational radii) and very broad lines, more than 1500 $\left(\frac{L}{10^{45}\ \mathrm{erg\ s^{-1}}}\right)^{0.2}$ km s^{-1}. Type I AGNs generally exhibit stronger X-ray and ultraviolet fluxes due to the unobstructed view of the central engine. Such objects are called narrow line Seyfert 1 galaxies and quasars.

Type II AGN: The spectrum here shows only narrow emission lines with typical full width half maximum of 400-800 km/s. These are sources with completely obscured line of sight to the center at UV, optical, and NIR wavelengths. Type II AGNs show absorbed or reprocessed emission signatures in X-ray and UV band. The central region is obscured due to the torus being seen edge-on along the line of sight.

LINERs (low-ionization nuclear emission-line regions): These are the lowest luminosity AGNs that are characterized by optical spectra dominated by emission lines from low ionization species ([OI], [NII], [SII]) and faint high-ionization emission lines. They are also further classified as Type I and Type II LINERs according to their emission line profile, with Type I having broad emission lines and Type II having narrow emission lines. LINER spectra are also known to be produced by other ionization mechanisms such as shocks (DOPITA AND SUTHERLAND 1995), post-AGB stars, or hot evolved stellar populations especially in the case of weak LINERs in ellipticals (BINETTE ET AL. 1994).

II. Radio Mode AGN

Radio mode or jet mode AGN are AGNs that produce their primary energy output in

the form of mechanical kinetic energy carried by relativistic jets rather than radiative emission. These AGNs are typically powered by low accretion rates, often below the Eddington limit, and are thought to be sustained by hot and low density gas accreted via radiatively inefficient flows (RIAF) such as ADAFs (Narayan and Yi 1995). Due to the inefficient cooling of the inflowing gas, only a small fraction of the gravitational energy is emitted as radiation, whereas most of the energy instead is chanelled towards launching large-scale jets. Such AGNs are usually found in massive elliptical galaxies or central galaxies in clusters. Unlike radiative mode AGNs, jet mode AGNs typically lack strong emission lines and exhibit relatively weak optical and UV emission. Radio mode AGNs are more pronounced in the radio band and hence are dominant in jetted radio galaxy populations such as Fanaroff and Riley (FR; Fanaroff and Riley 1974) I and some FR II radio galaxies.

1.2.3 AGN unification

Following the identification of various classes of AGNs in the latter half of the 20th century such as Seyfert galaxies, quasars, blazars, and radio galaxies, the effort to develop a unified framework to explain their diversity began to take shape. With the advent of multi-wavelength observations, particularly in the radio, X-ray, and infrared domain, it became increasingly evident that the observed differences among AGN types were not necessarily due to intrinsic physical distinctions, but rather a consequence of orientation effects and the presence of obscuring structures surrounding the central engine (Antonucci 1993; Urry and Padovani 1995; Figure 1.3). An important breakthrough came from spectropolarimetric observations of Seyfert 2 galaxies, where the broad emission lines which were normally hidden in direct light, were detected in polarized light, suggesting that the broad line region (BLR) was not absent but instead obscured from direct view (Antonucci and Miller 1985). This provided compelling evidence for the existence of a unified central structure for AGNs.

The unified model proposes that all AGN share a similar central structure: SMBH surrounded by an accretion disk, and two distinct emission line regions: the BLR and the narrow line region (NLR). Surrounding them is a geometrically and optically thick dusty torus that blocks certain lines of sight. When the system is viewed pole-on, the observer has an unobscured view of the accretion disk and BLR, resulting in the classification of a Type I AGN, characterized by both broad and narrow emission lines. When viewed edge-on, the torus obscures the BLR, and only the NLR is visible, leading to the classification of a Type II AGN (Antonucci 1993). This orientation based interpretation has also been

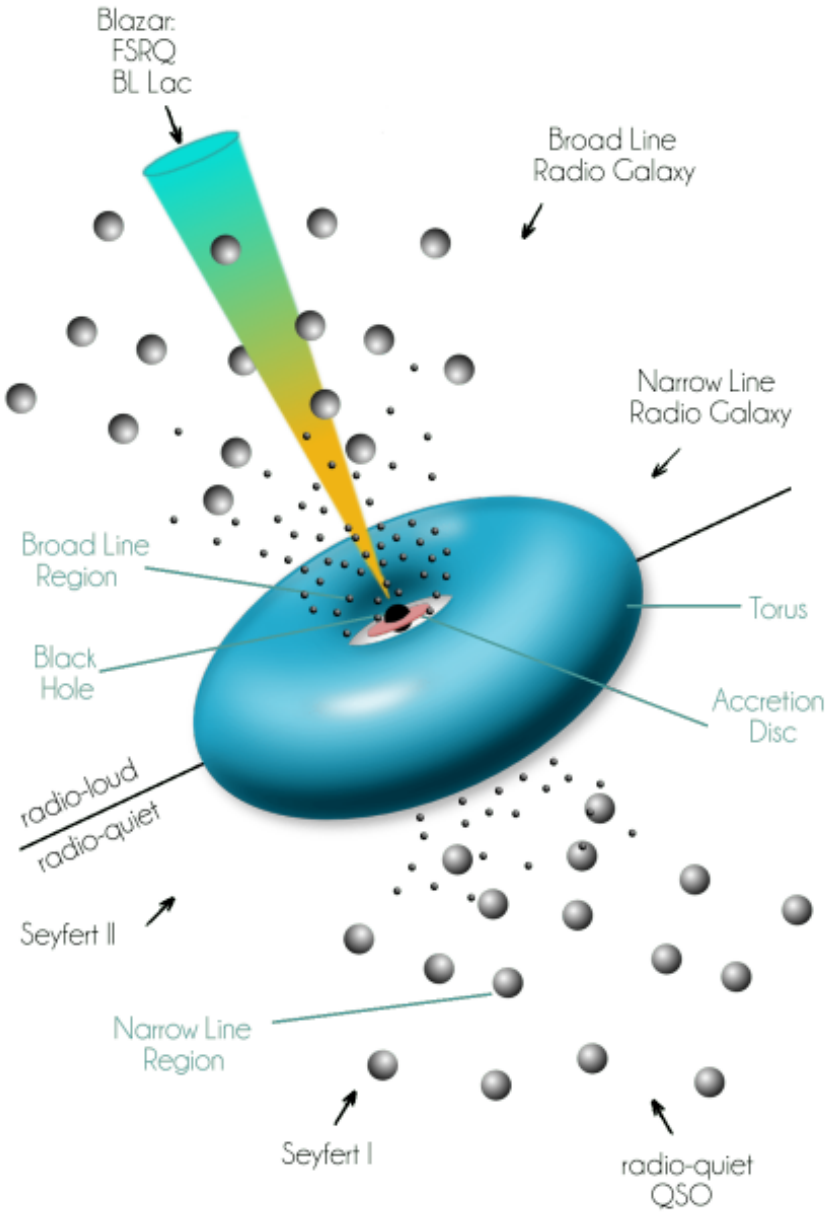

FIGURE 1.3: AGN unification scheme by URRY AND PADOVANI 1995.

extended to radio-loud AGNs such as quasars and blazars, with blazars being the jetted quasars pointed towards the line of sight of the observer. Complementarily, it can also be proposed that blazars are FR I and FR II objects seen at a very small angle to to the inner jet direction. Other classical radio loud AGNs are seen at larger angles, often from 50 degrees upto 90 degrees (Netzer 2015).

Despite its explanatory power, the AGN unified model has undergone refinements to account for exceptions and new observations. Not all AGNs fit neatly into the Type I or Type II categories. Some exhibit changing-look behavior, transitioning between types on timescales of years to decades, likely due to variability in accretion rates or dynamic changes in the obscuring material (LaMassa et al. 2015; MacLeod et al. 2016). Additionally, torus geometry and composition appear to be more complex than initially assumed, potentially clumpy or dynamic rather than uniform. The inclusion of parameters such as Eddington ratio, black hole spin, and host galaxy environment has led to a more nuanced "extended unification" framework. Nevertheless, the original unification scheme remains a cornerstone of AGN theory, framing a large body of observational data within a uniform model.

1.3 Radio Astronomy

Around early 1930s, the genesis of a completely new kind of astronomy was taking shape at the Bell Laboratories in the USA. Karl G. Jansky was a young engineer tackling a puzzling problem. He noticed a noisy static that was interfering with short wave radio transatlantic communications. After months of tracking the source, he came to the conclusion that it had an extraterrestrial origin, coming from the center of the Milky Way Galaxy. In 1933, his research culminated in one of the 20th century's most influential papers in the field of astronomy, titled "Radio Waves from Outside the Solar System" which laid the foundation for the science of radio astronomy (Jansky 1933). The subsequent advancement in the field can be majorly credited to Grote Reber, who in 1937 built a 31 foot radio antenna and published a map of the radio sky at 160 MHz. He identified a number of local maxima, notably the one located in the Cygnus constellation, which eventually became significant for AGN research later (Reber 1944). After the end of World War II, radio engineers turned their attention towards studying radio astronomy. John Bolton compiled a list of six individual radio sources, coining terms such as Cyg A, Cas A, etc (Bolton et al. 1949). Meanwhile, Ryle and Smith (Ryle and Smith 1948) presented findings from a radio interferometer at Cambridge (United Kingdom), drawing a parallel to Michelson's use

of an optical interferometer at Mt. Wilson for determining stellar diameter. Concurrently, Bolton, Stanley, and Slee (Bolton et al. 1949) got started with the optical identification of extragalactic sources. This marked the first identification of radio sources with optical hosts, such as Taurus A with the Crab Nebula supernova remnant M1 and Virgo A with the elliptical galaxy M87. Thereafter, Baade and Minkowski (1954) identified optical counterpart of Cygnus A, the first extragalactic radio source. The progress in radio surveys was also underway with Hanbury Brown, Jennison and Das Gupta imaging Cygnus A (Jennison and Das Gupta 1953) using intensity interferometer developed at Jodrell Bank, revealing its elongated structure. This structure showed two equal components that were separated by 1.5 arcmin from the optical galaxy. In the 1970s, new feature were discovered in Cygnus A that were labeled as "hotspots", regions of enhanced radio brightness, by Miley and Wade (1971) and Hargrave and Ryle (1974). Such regions were embedded in surrounding diffuse and low brightness radio emission. This feature was soon found to be a common signature of many radio sources and got commonly identified as "classical double", due to the presence of bipolar emission around either side of the host galaxy.

1.4 Morphological Classification of Radio Sources

Since the 1980s, with the advent of the National Radio Astronomy Observatory's (NRAO) Very Large Array (VLA), USA, radio astronomy has been revolutionized with the development of high-resolution and highly sensitive maps of radio sources. This breakthrough was especially significant as previous instruments, such as the east-west interferometers at Cambridge, located in United Kingdom and Westerbork in the Netherlands, were limited by long integration times and resolution that varied with declination. In contrast, the VLA's unique array configuration provided unmatched flexibility, allowing for high-resolution imaging over a broad range of declinations and with significantly shorter integration periods. This breakthrough led to the successful discovery of faint jets in Cygnus A (see Figure 1.5). Around the same time, advances in Very Long Baseline Interferometry (VLBI; Kellermann and Moran 2001) also facilitated the detection of parsec-scale jets.

The subsequent discovery and systematic cataloguing of numerous radio sources enabled their morphological classification, which was conducted by Fanaroff and Riley (1974).

Under this classification scheme the centre-brigtened sources were placed under the category of Fanaroff & Riley I (FR I) radio galaxies whereas the edge brightened sources were labelled under Fanaroff & Riley II (FR II) radio galaxies with luminosity division (Ledlow and Owen 1996) for $H_0 = 75$ km s^{-1}Mpc^{-1}, at

$$L_{178\,\mathrm{MHz}} \approx 2 \times 10^{25}\,\mathrm{W\,Hz^{-1}\,sr^{-1}}$$

Understanding the radio morphology is vital as it provides important cues into the formation dynamics of the central AGN, SMBH, the host galaxy and its surrounding intergalactic medium (IGM). Discussing further the morphological distinction:

FR I: These radio galaxies exhibit low surface brightness emission in their radio lobes, with a relatively weak jet emanating from the central AGN. In these sources, the jet typically fades and/or dissipates the further it travels from the centre of the host galaxy (Figure 1.4).

FR II: These radio galaxies show high-surface brightness radio lobes with stronger and more collimated jets. The FR II galaxy jets are more powerful, often showing a distinct termination at the lobes, often accompained with compact region of high surface brightness known as "hotspots" that are present at the edges of the lobes. These galaxies typically tend to maintain their intensity over enormous distances (Figure 1.5).

Alongside the discovery of "jet"-like features associated with the lobes of Cygnus A, Blandford and Rees (1974) and Scheuer (1974) proposed the "beam models", in which energetic electrons originating from the central region of the source were transported to the outer lobes of the radio source via twin jets. This led to the development of the current models that explain the mechanisms of energy transport over cosmic distances. In the meantime, the discovery of parsec-scale jets was facilitated by significant advancements in the field of VLBI. On the theoretical side, analysis of the spectral and polarization properties of these sources revealed that the radiation is of synchrotron origin. This form of electromagnetic radiation is emitted when ultrarelativistic charged particles undergo acceleration while moving in a curved trajectory in the presence of magnetic field. This process takes place in the vicinity of SMBHs that leads to the formation and launching of relativistic jets. The radiation emitted by a single electron covers a spectrum of frequencies, which is dictated by the electron's cyclotron frequency, its Lorentz factor, and the angle formed between its net velocity and the direction of the magnetic field. The behaviour of an ensemble of electrons is obtained by integrating the spectrum of a single

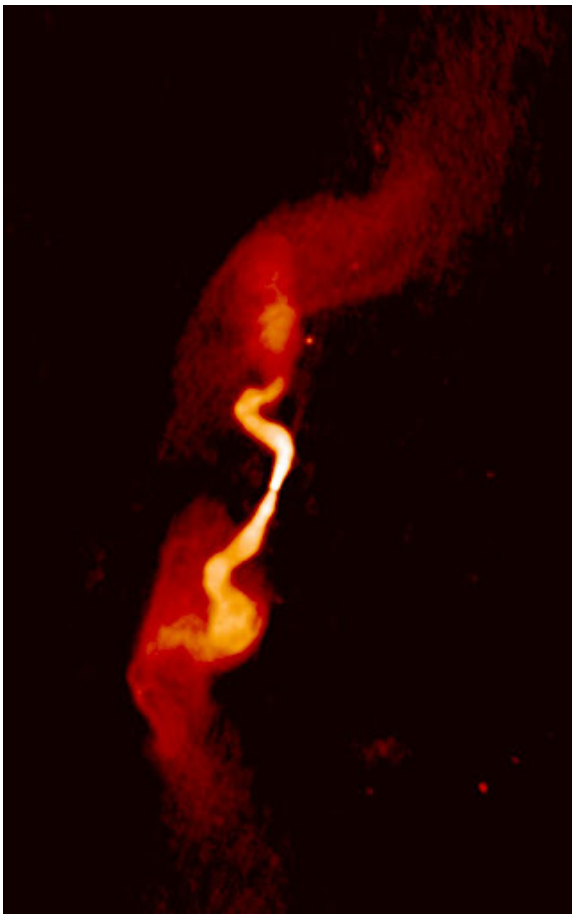

FIGURE 1.4: FR I type radio galaxy 3C31 (HARDCASTLE AND CROSTON 2020).

elctron over a suitable distribution function. The energy distribution of these electrons is given as: $\mathrm{n(E)}\,\mathrm{d}E \propto E^{-\delta}\,\mathrm{d}E$, which shows a power-law distribution, where the emissivity varies with the observing frequency ν as $\nu^{-\alpha}$, with $\alpha = \frac{\delta-1}{2}$. α is called here as the *spectral index* and can be measured when two or more different frequency maps are available for the astrophysical source.

Since the advent of deep sky surveys, various other morphological classes of radio galaxies have emerged:

FR0: These are a class of compact radio sources that feature parsec-scale radio jets and lack the extended radio structures classically seen in the FR I and FR II radio galaxies, they often also remain unresolved at parsec scales. FR0s were first identified through high-resolution radio surveys, and are typically core-dominated radio sources (BALDI 2023) generally displaying greater symmetry and mildly relativistic jets and comprising up to 80 per cent of the radio-loud AGN population, making it the most abundant population of

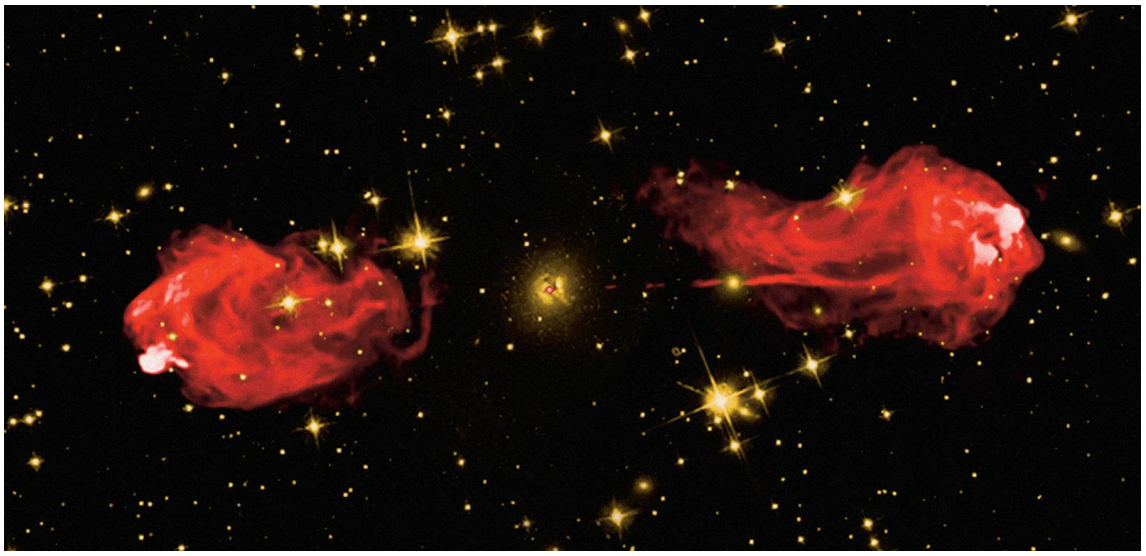

FIGURE 1.5: Multiwavelength picture of FR II type radio galaxy Cygnus A with radio lobes from VLA seen in red. Credits: NASA/STScI Radio Image: NSF/NRAO/AUI/VLA

radio galaxies. FR0s also share similar host and nuclear properties to FR Is. The mechanism underlying the origin of these galaxies is still a topic of debate in AGN studies. One theory posits that FR0s are an early stage in the evolution of radio galaxies, occurring before the formation of extensive jets and lobes. Alternatively, their compactness might also result from external conditions that hinder jet growth, or they have inherently different characteristics compared to classical FRs, like low jet kinetic power or BH spin.

Tailed Radio Galaxies: In some radio galaxies, the jets lose their straight and collimated radio morphology and display a diverse group of distortion in their radio jets. A notable class exhibiting such features are the tailed radio galaxies. While they often retain lobes resembling the classical FR I/FR II structures, their jets and lobes appear bent into characteristic C- or U-shaped forms. This bending is primarily driven by interactions with the surrounding environment, such as the intracluster medium (ICM), or by internal dynamical processes within the host galaxy. Such sources are further categorized based upon the alignment angle of their twin-tailed jetted lobes, leading to classifications such as Narrow-Angle Tailed (NAT) and Wide-Angle Tailed (WAT) radio sources (see Figure 1.6).

WAT: In WATs or C-shaped radio galaxies, the jet bending angle observed is usually very large and greater than 90 degrees (see e.g. O'DONOGHUE ET AL. 1993; O'DEA AND BAUM 2023 for a review) with wider tails spreading out from the center. Few examples of such sources are CWAT-01 (SMOLČIĆ ET AL. 2007) and 3C 465 in A 2634 (BEMPONG-MANFUL

ET AL. 2020). According to consensus, WATs are formed through the interaction between the outgoing radio jets and the dynamic, magnetized ICM of the cluster.

NAT: The sources with jets and lobes forming a small angle in the line of sight are known as NATs, or U-shaped radio galaxies (see BLITON ET AL. 1998; FERETTI AND VENTURI 2002 and references therein). The prototype of this class is NGC 1265 in the Perseus cluster (WELLINGTON ET AL. 1973; O'DEA AND OWEN 1986).

These sources are usually associated with high velocity galaxies in the gravitational potential of their clusters (MILEY 1980). In such a scenario, there is possible ram pressure bending due to the external medium, which leads to curvature/bending of the jets that sweeps the radio emitting lobe behind the moving galaxy. Consequently, it has been proposed that such bending of jets might result from large-scale motions within the ICM, triggered by mergers between clusters and sub-clusters (BLITON ET AL. 1998). An extreme form of such jet bending is often seen in the case of Head-Tail (HT) sources such as the Corkscrew Galaxy in the Abell 3627 cluster (EKERS 1969; see bottom image of Figure 1.6). Such sources travel at extremely high velcities in the ICM producing highly collimated and twisted (helical) radio tail attached to a radio head/core at the host radio galaxy position.

Double-double Radio Galaxies: DDRGs are a rare class of radio galaxies with two distinct pairs of radio lobes, signifying repeated or episodic radio activity after a period of quiescence. Such lobes are usually aligned along or almost along the same axis and emerge from a common AGN at the center of the host galaxy. The outer pair of lobes are remnants from an earlier phase of jet activity, whereas the inner lobes correspond to a more recent episode of radio emission. The older, and larger pair of lobes usually have more diffuse lobes, lack hotspots, and aged plasma due to synchrotron losses.

The formation of DDRGs is closely linked to the cyclic nature of AGN activity, where the radio jet producing AGN enters a dormant phase for a while due to probably either lack of accreting material, feedback processes or accretion disk instabilities. Following this inactive phase, availability of accreting material leads to the creation of new secondary pair of radio lobes. Some classic examples of DDRG (see Figure 1.6) include B1834+620 (SCHOENMAKERS ET AL. 2000), J0116−473 (SARIPALLI ET AL. 2003) and 3C 293, which also displays signs of recurrent jet activity with a disturbed host galaxy, possibly linked to a past merger (AKUJOR ET AL. 1996).

Winged Radio Galaxies: The galaxies that have curvature in their jets or distinctive jet bending in the form of X-, S- or Z-shaped morphology are classified under winged radio

galaxies (Rubinur et al. 2017; Cotton et al. 2020; Misra et al. 2023; Sethi et al. 2024). The "X"-shaped winged radio galaxies (see Figure 1.6) were initially documented in the works of Riley (1972), Högbom and Carlsson (1974), and it was followed by several significant studies on classic X-shaped sources by Ekers et al. (1978); Leahy and Williams (1984); Leahy and Parma (1992); Worrall et al. (1995) alongside the first major compilation of a sample of 100 X-shaped radio galaxies by Cheung (2007). The characteristic of X-shaped objects is that they possess one pair of lobes undergoing active evolution, often leading to hotspot formation, while there is an accompanying secondary pair of wings that is extended and diffuse. This pair usually lacks hotspots and showcases low surface brightness emission. These sources usually have wings where this secondary pair of lobes emanates from the central AGN with a significant angle to the primary lobe, with an average alignment angle of approximately 75°or higher (Capetti et al. 2002; Bhukta et al. 2022).

Distinguishing between the morphological class of winged radio galaxies remained a significant challenge until the advent of high-sensitivity, deep radio surveys, which provided the resolution and sensitivity necessary to reveal finer structural details. The formation of X-shaped radio galaxies is often attributed to a backflowing jet plasma that is deflected laterally by an asymmetric medium forming secondary pair of wings (Leahy and Williams 1984; Cotton et al. 2020; Giri et al. 2024) or by the sudden spin flip of an SMBH post-merger (Merritt and Ekers 2002; Rottmann 2001). The Z- and S-shaped morphology is mostly considered to be the result of underlying smooth jet precession (Gower et al. 1982; Rottmann 2001; Horton et al. 2020; Horton et al. 2023). More elaborate discussion on winged radio galaxies and specifically on "S"-shaped radio galaxies is provided in the subsequent section.

Odd Radio Circles (ORCs): These objects represent a freshly identified class of radio sources characterized by their circular morphology and low surface brightness emission alongside edge-brightened ring-like structures. Their diameters typically range from 60 to 80 arcseconds. They were first discovered in data from the Evolutionary Map of the Universe (EMU) pilot survey, conducted using the Australian Square Kilometre Array Pathfinder (ASKAP) telescope (Norris et al. 2021a). One of the examples of a best-studied ORC is named ORC1 (Norris et al. 2022a; Norris et al. 2021b), it shows a narrow ring of emission which is slightly resolved by MeerKAT's 6 arcsec beam (Norris et al. 2022b). Some of the ORCs have candiate host elliptical galaxies, while some do not. At present, the origin of ORCs reamins a mystery with several speculative origin theories such as merger shocks (Dolag et al. 2023), tidal disruption events (Omar

2022), starburst-driven shocks (Coil et al. 2023), black hole mergers (Norris et al. 2022a), precessing AGN jets (Nolting et al. 2023), jet-inflated lobes and supernova remnants (Filipović et al. 2022).

1.5 S-shaped Radio Galaxies

Radio jets are the most dominant form of outflows powered by the radiative accretion mode in the AGNs. As these kpc to Mpc size jets expand into the IGM, they mostly retain their jet axis direction for almost 10^8 yrs (Machalski et al. 2009; Machalski et al. 2021). While these jets are typically straight and collimated, some exhibit strikingly complex structures. Among them, there are S-shaped radio jets that showcase unusual bending of large-scale jets (see Figure 1.7), with inversion symmetry, making them excellent laboratories for studying the dynamic interplay between the central AGN, the jets, and the surrounding intergalactic medium. A classical example of an inversion-symmetric S-shaped radio source is PKS 2300–18, first presented by Hunstead et al. (1984). Since then, confirmed cases of such S-shaped sources have remained rare, with only a small number of individual systems studied in detail in papers such as Condon and Mitchell (1984), Nandi et al. (2017), Rubinur et al. (2017), Sethi et al. (2024) and Misra et al. (2025). Such a morphology is theorized to emerge when standard FR I/FR II jets undergo continuous precession and the jets get dragged from their initial position, creating twisted patterns (Horton et al. 2020). The precession of the jet is driven by the change in the spin-axis direction of the SMBH, which tends to gradually tilt the jet axis. This ultimately results in an S-shaped morphology over time. Some possible models for explaining this reorientation or precession include reorientation of the jets due to the presence of another SMBH in the same nucleus (Begelman et al. 1980; Britzen et al. 2001; Nandi et al. 2021; Sebastian et al. 2024) and/or a surrounding tilted accretion disc (Lu 1990; Lu and Zhou 2005; Liska et al. 2018; Chatterjee et al. 2020). Therefore studying such sources can serve as remarkable tool to gain deeper insights into the nature of SMBH and its spin evolution.

Extragalactic jets show signatures of helical morphology at scales ranging from a few parsec to a few kpc. Such jets can be observed in many astrophysical objects such as planetary nebulae (Lopez et al. 1993), AGNs (Rubinur et al. 2017; Rawes et al. 2018; Nakamura et al. 2018; Ubertosi et al. 2024) and in X-ray binaries (Hjellming and Johnston 1981). An archetypal helical jet can be described by three different jet

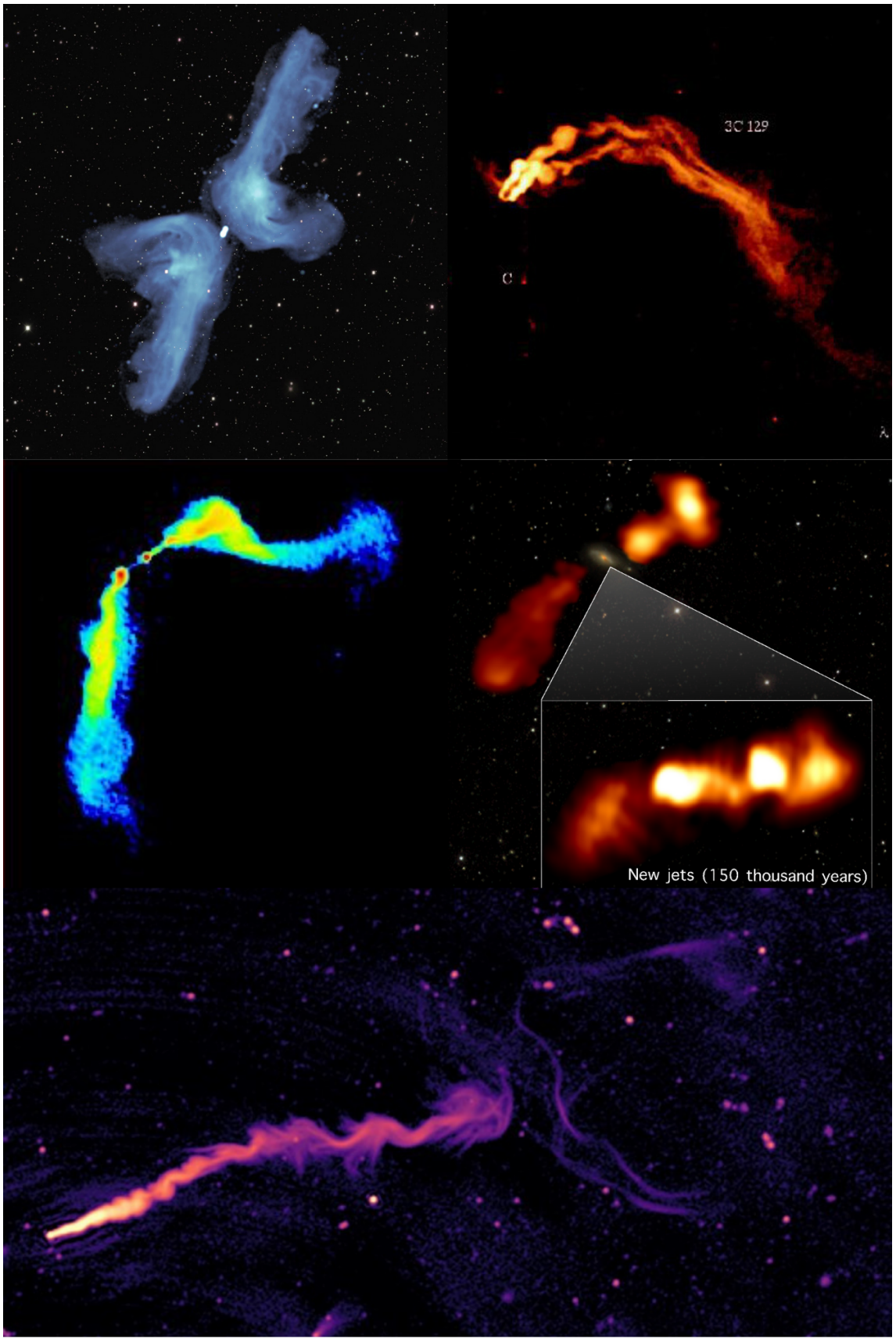

FIGURE 1.6: Montage of various radio galaxy morphologies. Top left panel: PKS 2014-55 (X-shaped), Top right panel: 3C 129 (NAT); Middle left panel: 3C 465 (WAT), Middle right panel: 3C 293 (DDRG); Bottom panel: Corkscrew galaxy (HT).

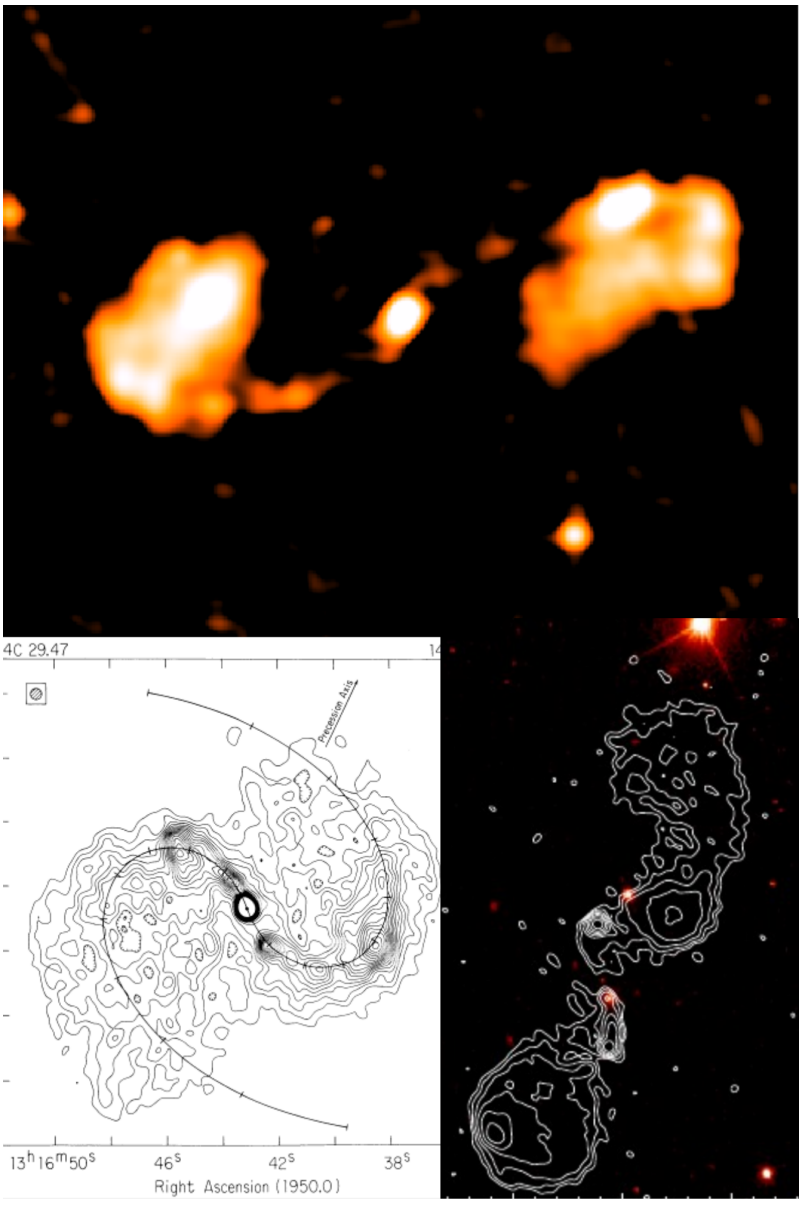

FIGURE 1.7: Compilation of S-shaped radio sources: ASKAP radio image of NGC 5972 (Top panel), VLA map of 4C 29.47 (Bottom left panel; HUNSTEAD ET AL. 1984), and GMRT map of J1328+2752 (Bottom right panel; NANDI ET AL. 2017).

structures, as elucidated by Steffen (1997), presented in the Figure 1.8 and detailed below:

Ballistic Helical Jet

This model (Figure 1.8b) consists of a ballistic helical jet, where the individual fluid elements within the jet propagate along a straight path. However, the collective morphology of the jet follows a helical structure due to periodic variations in the ejection direction of these elements, such as in the case of precessing jets. Extensive kinematic modelling of such large-scale precessing jets has been performed by Gower et al. (1982). Jet precession resulting in S-shaped radio jets is likely to occur in a binary SMBH system (Begelman et al. 1980). Within such a binary system, the spin axes of the BHs are likely to be misaligned, unless they have both accreted a significant amount of gas with fixed angular momentum. The spin axes will then subsequently undergo geodetic precession. This will result in the gradual change in the spin axis of the SMBH, producing jets which would eventually demonstrate an S-shaped morphology. A helpful analogy is of a moving water hose: while individual droplets travel outward in straight lines, changes in the hose's direction cause the overall stream to trace a curved path (see Figure 1.9). Similarly, as the spin axis of the SMBH shifts, the emitted relativistic particles change their spatial direction and create a winding or precessing jet structure imprinting on kiloparsec scales.

Sarazin et al. (1980) also proposed a model to explain the precessing jets observed in the microquasar SS 433 (see Figure 1.10). In this model, the accretion disk is tilted relative to the spin axis of the central black hole. Due to this misalignment, the Lense–Thirring effect (Lense and Thirring 1918) causes the inner part of the disk, within a certain radius to gradually align with the black hole's equatorial plane. However, the outer disk retains its original tilt and, due to its larger angular momentum, exerts a torque that causes the inner disk and the BH to precess (Bardeen and Petterson 1975). When material from the inner accretion disk is propelled along the black hole's changing spin axis, it gives rise to a precessing jet.

Helically Bent Jet

In this model (Figure 1.8c), the helical jets are bent as a whole and the fluid elements follow a common twisted trajectory that is traced by a curved jet axis. Such bending can be observed due to environmental factors such as in the case of tailed radio galaxies, as discussed in the previous section. Jet bending of this type can be seen when the jets undergo intrusion due to collision with gas clouds or interaction with transverse winds or a dense ambient medium. In radio galaxies such as 3C 433 (van Breugel et al. 1983) and

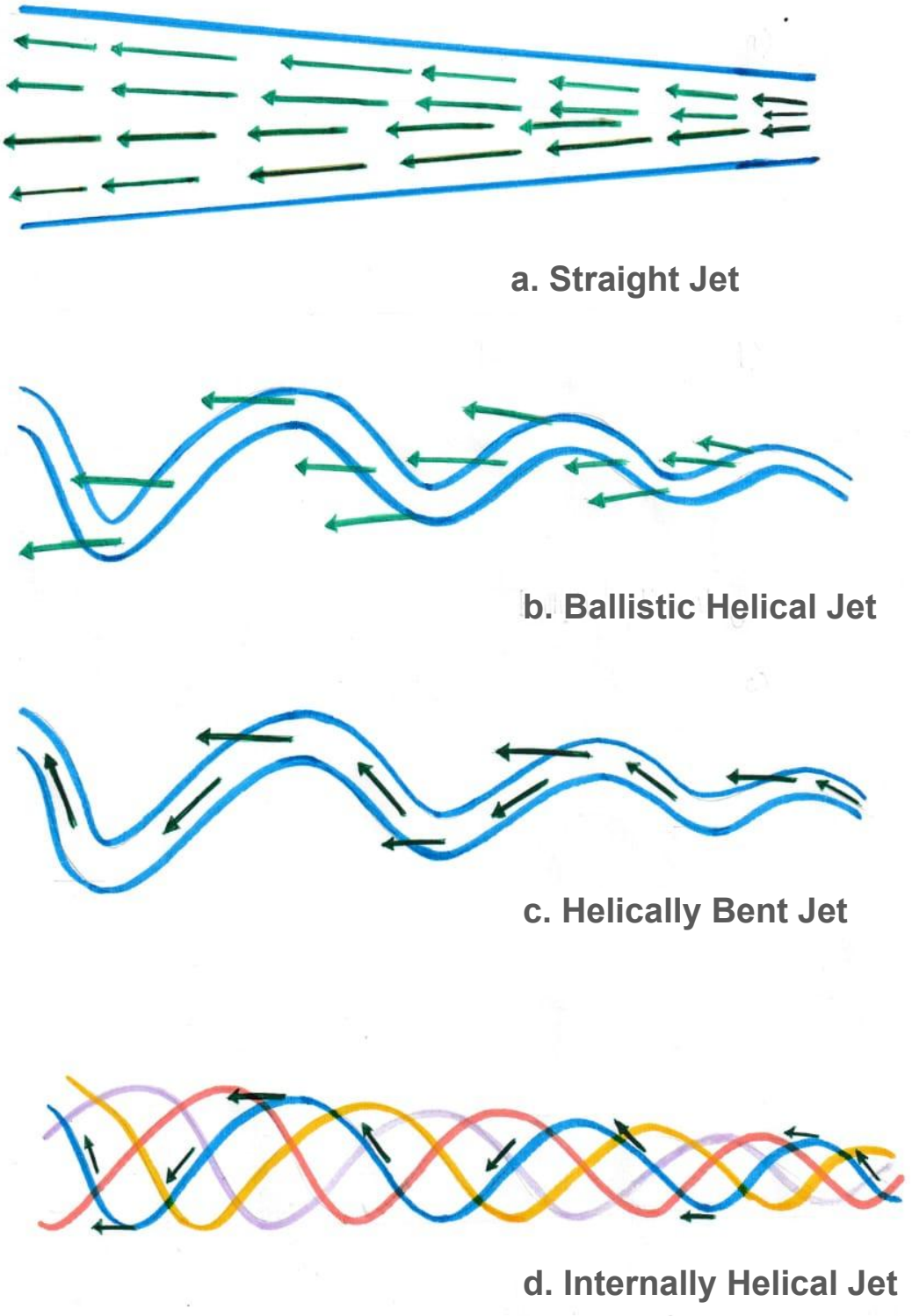

FIGURE 1.8: Schematic representation of helical jets.

FIGURE 1.9: The stream of water appears curved as the water hose moves in a clockwise direction. Each individual droplet follows a straight line path but due to the continuous motion of the hose the overall stream takes on a curved shape.

4C 65.15 (MILLER AND BRANDT 2009), which exhibit jets with a hybrid FR morphology, Chandra X-ray observations indicate that the FRI-like structure seen on one side of these sources results from a powerful jet interacting with a relatively dense external medium. Similarly, jet bending due to environmental interaction is observed in the case of 3C 321 (see Figure 1.11), where one of the jets is deflected after colliding with a nearby companion galaxy that is in the process of merging with the host (EVANS ET AL. 2008).

Internally Helical Jet

In this model (Figure 1.8d), the jets have a helical structure internally. While these jets are generally straight, they contain fluid components that move along spiral paths inside the jet. Such jets might be produced as a result of Kelvin–Helmholtz (KH) instabilities (HARDEE 1987; HARDEE AND CLARKE 1992; PERUCHO ET AL. 2006; PERUCHO ET AL. 2012). These instabilities can evolve into large-scale helical modes, significantly altering the jet structure and producing wave-like features observable from parsec to kiloparsec scales (see Figure 1.12). These instabilities can be observed in transverse oscillations in the M87 jet in the VLBA observations, where a shift of the transverse position of the jet on a quasi-periodic 10-yr time-scale was seen, consistent with KH instability (WALKER ET AL. 2017; NIKONOV ET AL. 2023). In sources like 3C 273, VLBI imaging reveals a double-helical structure consistent with KH-driven oscillations (LOBANOV AND ZENSUS 2001). In numerical simulations by PERUCHO ET AL. (2010) it was demonstrated that

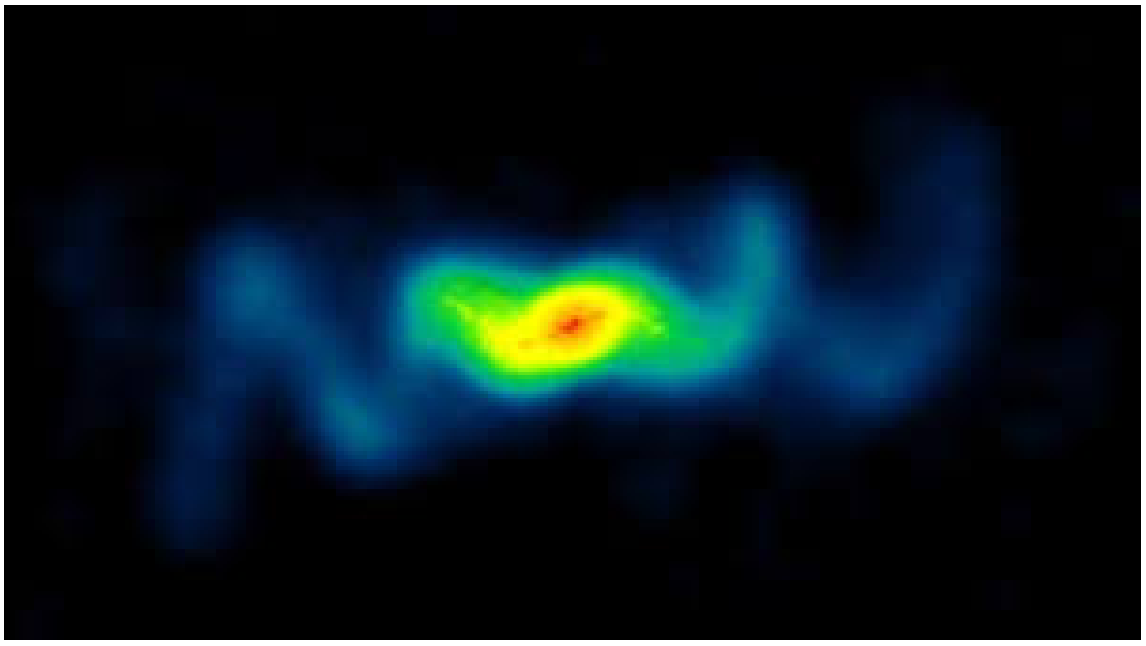

FIGURE 1.10: A VLA radio image of the jets from microquasar SS 433 forming a corkscrew pattern. The accretion disk around the black hole wobbles causing precession of the radio jets. Credit: Blundell & Bowler, NRAO/AUI/NSF

even small perturbations in jet velocity or density can amplify into visible helical patterns, as the KH modes evolve downstream.

S-shaped radio sources are relatively rare compared to their more commonly observed winged cousins, such as the X-shaped radio galaxies. These morphologically complex systems are also of interest in the context of gravitational wave astrophysics, as they are potential candidates for hosting binary supermassive black holes. The distinct S-shaped structure is often interpreted as a signature of jet precession, which can be induced by the presence of a binary companion as a result of a recent galaxy merger. Despite their significance, systematic studies of such sources, especially at low radio frequencies, have been limited. This thesis presents the first dedicated low-frequency radio study of a sample of S-shaped radio galaxies, aiming to explore their large-scale morphology, host galaxy properties, and environmental context in detail. Low-frequency observations are particularly well-suited to trace the aged, diffuse synchrotron plasma that reveals past episodes of AGN activity and directional changes in the jet axis.

The study of such sources is crucial for an in depth analysis of galaxy evolution in general as it explores growth via galaxy mergers and nuclear activity. For both the cases, the central AGN is bound to undergo perturbations, and in such case AGN jets act as an

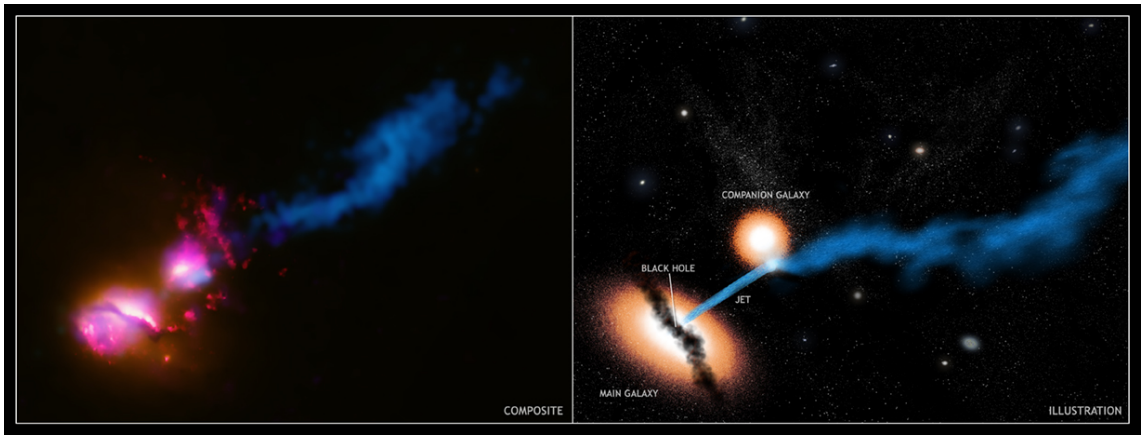

FIGURE 1.11: Composite image of 3C 321 (left) alongside the artist's illustration of the system (right) showing the main galaxy and the companion galaxy undergoing interaction. A radio jet produced by the supermassive black hole at the center of the host galaxy is striking the companion galaxy. As a result, the jet is disrupted and deflected by the impact. (Credit: Image: X-ray: NASA/CXC/CfA; Optical/UV: NASA/STScI; Radio: NSF/VLA/CfA/ STFC/JBO/MERLIN; Illustration: NASA/CXC/M. Weiss)

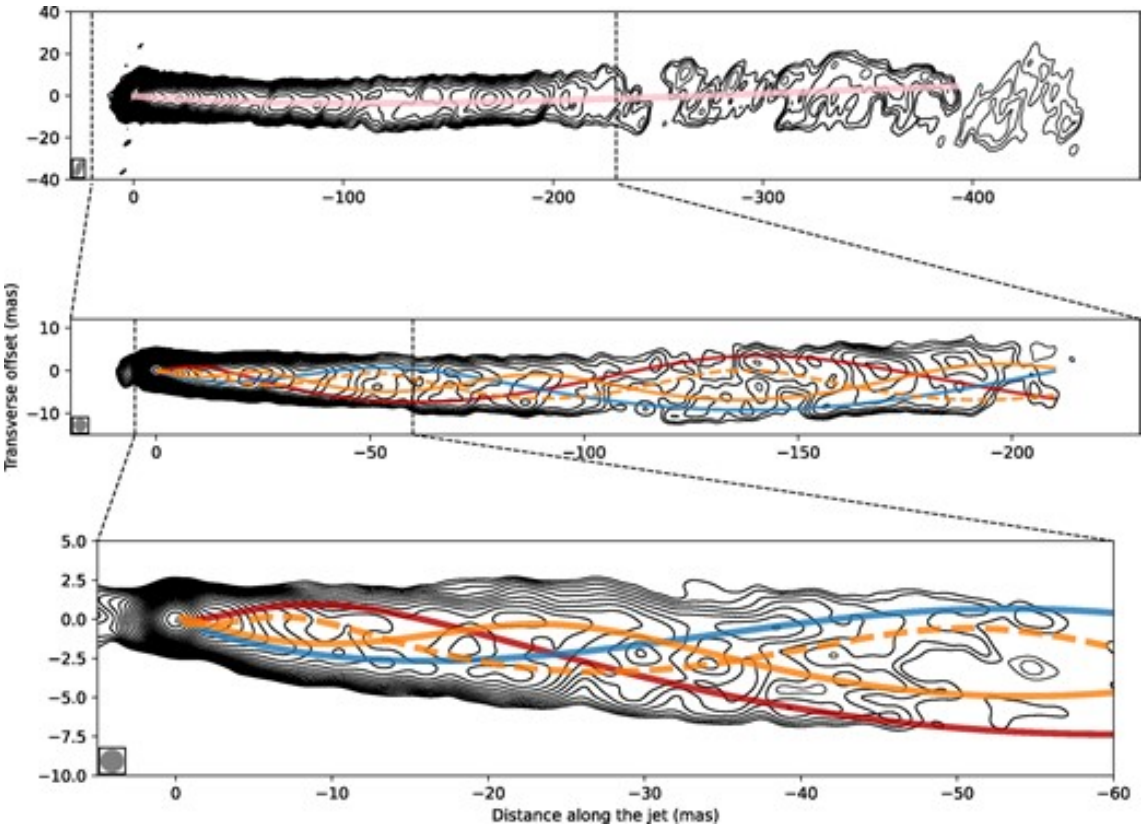

FIGURE 1.12: The oscillatory pattern observed in the M87 jet, highlighted with different colors and attributed to the Kelvin-Helmholtz instability (NIKONOV ET AL. 2023).

excellent tracer for the study of the central SMBH behaviour. These sources also remain promising targets for the indirect detection of BBHs and for improving our understanding of jet stability, precession mechanisms, and the co-evolution of galaxies and their central black holes.

1.6 Advances and Prospects in Radio Interferometry

Radio interferometry has made remarkable contributions towards our understanding of the universe across wide frequency ranges, owing to the progress in high-resolution and high-sensitivity mapping of astrophysical sources. Instruments like the the Karl G. Jansky Very Large Array (JVLA), upgraded Giant Metrewave Radio Telescope (uGMRT), and the Low-Frequency Array (LOFAR), have made major advancements in the study of galactic and extragalactic astrophysics (see Figure 1.13). With the advent of next generation facilities such as the Square Kilometre Array (SKA) and the next-generation Very Large Array (ngVLA) it will be possible to answer many more unsolved and challenging problems in astrophysics.

1.6.1 Current Generation Interferometers

Karl G. Jansky Very Large Array (JVLA)

JVLA is a radio interferrometric array situated in New Mexico, USA that comprises 27 parabolic dishes with each being 25 meters in diameter, arranged in a Y shape. This gives a configuration with a maximum baseline of 36 km. The antennas here have the ability to change their position as they move on specially adapted rails, that helps in changing the configuration from the widest separation between antennas being in A configuration, to the smallest separation between antennas being in D. The A-configuration provides the longest baselines and therefore the highest angular resolution for a given frequency, but it has limited sensitivity to surface brightness. The D-configuration provides the shortest baselines, resulting in a high surface brightness sensitivity but with a poor angular resolution. The observed frequencies range from 74 MHz to 50 GHz, with the capability to achieve subarcsecond resolution at the highest frequencies and in the most extended array configurations.

The JVLA has contributed to several major sky surveys such as Faint Images of the Radio Sky at Twenty centimeters (FIRST; Becker et al. 1995), NRAO VLA Sky Survey

(NVSS; Condon et al. 1998), and the VLA Sky Survey (VLASS; Lacy et al. 2020). FIRST at 1.4 GHz has an rms of 0.15 mJy/beam with a resolution of 5 arcsec and covers regions of sky in the north and south galactic cap. The NVSS is a 1.4 GHz with a resolution of 45 arcsec. The rms brightness fluctuations are about 0.45 mJy/beam in total power (Stokes I). VLASS is also an all-sky survey above declination –40°. It operates within a range of 2–4 GHz with an angular resolution of 2.5 arcsec and sensitivity of 69 µJy/beam. Within its operational phase, JVLA has been instrumental in making many significant discoveries such as the discovery of the most distant blazar at redshift 7 by Bañados et al. (2024) and the first direct imaging of a torus in AGN in the radio galaxy Cygnus A by Carilli et al. (2019).

Giant Metrewave Radio Telescope (GMRT)

GMRT, located near Pune, India, is a radio interferometer comprising 30 fully steerable parabolic dishes, each 45 meters in diameter, distributed across an area spanning 25 kilometers. It primarily operates in the frequency range of 150 MHz to 1450 MHz, with the highest achievable resolution of ∼3 arcseconds. GMRT is particularly sensitive to low-frequency radio waves, making it a powerful tool for studying diffuse emission and steep spectra from radio galaxies and galaxy clusters. The uGMRT has significantly enhanced its bandwidth with a wider passband of upto 400 MHz in a similar frequency range, and improved sensitivity in the range of few µJy, enabling the detection of extremely old and faint plasma from astrophysical sources.

The TIFR GMRT Sky Survey (TGSS; Intema et al. 2017) was conducted using GMRT, which is a large-scale radio survey at 150 MHz. It covered over 90 per cent of the sky north of –53° declination, with a resolution of ∼25 arcsec, and sensitivity of ∼3.5 mJy/beam. This survey helped produce a catalog of more than 620,000 radio sources. GMRT has also paved the way for groundbreaking discoveries such as the detection of first triple lobed radio galaxy hosted by a spiral by Hota et al. (2011), discovery of extremely massive supercluster by Bagchi et al. (2017), and the discovery of a giant hydrogen gas ring around a galaxy by Bait et al. (2020).

Low-Frequency Array (LOFAR)

Low Frequency Array (LOFAR; van Haarlem et al. 2013) is a distributed radio telescope network primarily based in the Netherlands, with international stations across Europe and three stations in Poland (Łazy, Borówiec and Bałdy). It consists of 24 central stations and 14 more distant stations located in Netherlands, alongside 13 international stations

operating between 10 MHz and 240 MHz. Instead of conventional parabolic dishes, LOFAR employs thousands of dipole antennas to perform interferometry, utilizing two distinct types: Low Band Antennas (LBA), which operate between 10–80 MHz, and High Band Antennas (HBA), covering the 120–240 MHz range. LOFAR, supported by international stations has an extremely large field of view which enables the possibility of imaging the sky with many beams simultaneously, as well as efficiently switching them between individual targets to perform all sky surveys in a relatively short time.

Within its operational period, LOFAR has conducted many surveys such as LOFAR LBA Sky Survey (LoLSS; de Gasperin et al. 2021), and LOFAR Two-metre Sky Survey (LoTSS; Shimwell et al. 2022). LoLSS produced maps of the entire northern sky in the frequency range 42–66 MHz, with a resolution of 15 arcsec at an average rms of 1 mJy/beam. LoTSS Data Release 2 released a sky survey ranging from 120 to 168 MHz with a 6 arcsec resolution and median rms sensitivity of 83 µJy/beam and a 20 arcsec resolution with a median rms sensitivity of 95 µJy/beam. Since its advent it has contributed towards many pioneering discoveries such as the discovery of the largest radio jets from a galaxy in our universe by Oei et al. (2024), discovery of the largest extended radio jets from the most distant radio AGN at $z > 4$ by Gloudemans et al. (2025) along with the discovery of the fastest-spinning millisecond pulsar in the Galactic field by Bassa et al. (2017).

1.6.2 Next Generation Interferometers

Square Kilometre Array (SKA)

The Square Kilometre Array is a next-generation radio interferometer designed to be the largest and most sensitive radio telescope array in the world, planned to be operational by 2029. It is being constructed in two main sites: SKA-Low in Western Australia, which will observe low radio frequencies (50–350 MHz) using over 130,000 dipole antennas; and SKA-Mid in South Africa, which will operate in the mid-frequency range (350 MHz to 15 GHz) with an array of 197 parabolic dishes. These elements will provide SKA with a combined collecting area of one square kilometer, which will notably improve the sensitivity by upto 4-10 times compared to the current sensitivity of the VLA.

The SKA is designed for exceptional angular resolution, wide instantaneous frequency coverage, and ultra-high sensitivity, making it capable of detecting extremely faint radio emissions from the early and distant universe. With a target resolution on the order of milliarcseconds at GHz frequencies, the SKA will be able to achieve imaging capabilities comparable to that of the Hubble Space Telescope, enabling detailed studies of compact

astrophysical sources. It will attempt to address questions such as: How do galaxies form and why do their fates differ so greatly? What is dark matter and how does it influence galaxy evolution?

next-generation Very Large Array (ngVLA)

The ngVLA is the proposed successor to the current VLA, planned to be fully operational by 2037. It will be operating from 1.2 to 116 GHz, and will deliver ten times the sensitivity and resolution of the current VLA. The array will comprise of 244 antennas, each 18 meters in diameter, complemented with a short baseline array of 19 antennas, each 6m in diameter, to deliver the shortest baselines. It will have a maximum baseline of over 1000 km, that will enable the array to achieve high surface brightness sensitivity and high-fidelity imaging on angular scales down to a milliarcsecond.

The planned extensions to baselines across North America and Hawaii, operable independently or integrated with the main array will make it possible to achieve angular resolutions down to 0.1 milliarcseconds, enabling microarcsecond precision astrometry. Among its key scientific goals are understanding the assembly, structure, and evolution of galaxies from the first billion years to the present, and studying the formation and evolution of stellar and supermassive black holes in the era of multi-messenger astronomy.

1.6.3 Scientific Breakthroughs Enabled by Radio Interferometry

With the advent of radio interferometry, several groundbreaking studies and discoveries have been made:

First Image of a Supermassive Black Hole: The first image of a supermassive black hole, shadow of the black hole at the center of the galaxy M87, was captured by the Event Horizon Telescope in 2019 (EHT; Event Horizon Telescope Collaboration et al. 2019). EHT is a global network of radio telescopes operating as VLBI to achieve resolution the size of the Earth, which converts to few microarcseconds. This milestone provided the first direct visual evidence of a BH and confirmed predictions of general relativity in the strong gravity regime.

Gravitational Waves from Supermassive Black Hole Binaries: The first gravitaional wave background (Agazie et al. 2023) to be ever detected was made possible in 2023 by the North American Nanohertz Observatory for Gravitational Waves

(NANOGrav), including other Pulsar Timing Array collaborations like EPTA, PPTA, and IPTA. They presented compelling evidence for a gravitational wave background at nanohertz frequencies, which is likely generated by a population of inspiraling supermassive black hole binaries, and its detection marked the beginning of low-frequency gravitational wave astronomy using radio telescopes. These findings are the result of decades of interferometric pulsar timing observations conducted at radio observatories worldwide.

HI Mapping: Radio interferometry has played a crucial role in mapping neutral hydrogen (HI) in galaxies through observations of the 21 cm line, helping trace the distribution and dynamics of atomic gas with high spatial resolution. These observations have provided key evidence for the presence of dark matter halos, revealed galaxy mergers and gas accretion processes, and offered insights into how galaxies evolve over cosmic time.

Fast Radio Bursts (FRBs): The localization of FRBs was made possible using interferometric arrays like the VLA and Canadian Hydrogen Intensity Mapping Experiment. This enabled precise localization of FRBs to their host galaxies, often to within sub-arcsecond accuracy. This has ultimately provided important clues about the possible origins of FRBs, that include magnetars and neutron stars.

1.6.4 Future Prospects

S-shaped radio galaxies remain relatively rare and poorly understood, primarily due to limitations in sensitivity and angular resolution of existing radio surveys. Many such sources may already exist but appear as amorphous or standard FR II-type radio galaxies because their internal jet morphology is unresolved. With the advent of high-resolution and high-sensitivity instruments like the SKA, particularly in the southern hemisphere, where such observations have been limited, it will be possible to detect faint, low surface brightness features that trace earlier jet orientations or precessing activity; reclassifying previously unrecognized FR IIs as S- or Z-shaped galaxies. SKA's ability to probe extended emission will serve as an exceptional tool for revealing complex radio jet morphologies, even with higher redshift sources, where mergers were more frequent.

Sub-arcsecond resolution will help with the detailed studies of jet dynamics within lobes, helping distinguish between sources shaped by genuine jet precession that are possibly due to binary SMBHs vs those bent by environmental interactions, such as dense intracluster medium or during galaxy merger processess. This will help build a statistically robust sample of truly precessing radio galaxies, offering insight into the spin evolution of SMBHs, the effects of galaxy mergers, and scenarios involving warped or tilted accretion disks

in the absence of merger signatures. By correlating radio morphology with host galaxy properties, environment, and star formation history it will be possible to study SMBH galaxy co-evolution through feedback mechanisms. Moreover, detecting jet reorientation events can provide compelling evidence for dual or recoiling supermassive black holes, offering valuable insights into BH dynamics in post-merger galaxies. As these systems are also prime candidates for the emission of low-frequency gravitational waves from inspiraling SMBH binaries, such sources will also serve as important targets to hunt for gravitational wave signatures.

SKA and ngVLA will also be instrumental in addressing several of the most fundamental astrophysical questions about the Universe's origin and evolution. These telescopes will help reveal how the first stars, galaxies, and BHs formed by detecting the faint 21-cm hydrogen signal from the epoch of reionization, shedding light on the processes that illuminated the early universe. They will also transform our understanding of cosmic magnetism by mapping magnetic fields across interstellar and intergalactic scales, helping to unravel the origin and evolution of magnetized structures from galaxies to the cosmic web. It will also play an important role in probing the nature of dark energy and the expansion history of the universe. Techniques such as HI intensity mapping will allow precise measurements of the large-scale structure of the cosmos, allowing constraints on various cosmological parameters.

1.7 Thesis Outline

The presence of S-shaped jets in radio galaxies hints at a more dynamic nature of the central AGN and poses questions about the phenomenological changes responsible for the deviation from classical FRs. The work in the thesis marks the largest sample study of S-shaped radio galaxies using multifrequency radio data in order to investigate their morphological evolution. Below is a summary of each chapter, outlining the work carried out over the course of this study. The analysis is based on radio data obtained from both dedicated observations and archival repositories, complemented by archival X-ray and optical datasets.

Chapter 2: This chapter marks the beginning of the dissertation work, where an initial sample of seven S-shaped radio sources was selected by me from the FIRST and LOFAR surveys. PKS 2300–18 was specifically included due to its prominent inversion-symmetric S-shaped morphology, likely driven by jet precession, and being the largest known example

FIGURE 1.13: Montage of radio telescopes: GMRT (Top-left corner), VLA (Top-right corner), LOFAR (Bottom-left corner), SKA (Bottom-right corner).

of such a structure. These sources were observed by me over a period of three years using the uGMRT in band 3 (300 MHz) and band 4 (700 MHz), with the aim of investigating their morphological evolution at low radio frequencies. In this chapter, I present the uGMRT radio maps of the sample of S-shaped galaxies, providing a detailed view of their morphology.

Chapter 3: Here I present my work that is published as a journal article. In this work a unique X-shaped radio galaxy was studied, J1159+5820, that has a restarting pair of inner lobes, and whose host galaxy, CGCG 292–057, displays the optical signature of a post-merger system. Multifrequency radio observations of the source were conducted, various

particle injection models were fitted to its radio spectra, and modelling of the radio spectra of the core was done using particle absorption models. Spectral ageing analysis performed on the wings and lobes of the radio source favoured a jet reorientation model. This is an exceptional source that demonstrates multiple stages of galaxy evolution at once. The evidence of a past merger, peculiar X-shaped morphology, and an AGN rebirth with a new pair of radio lobes makes it a great target for studying the evolution of galaxies and their central AGN.

Chapter 4: Here I also present my work that is published as a journal article. In this work, the first-ever detailed multiwavelegth investigations of a large-scale inversion-symmetric S-shaped radio galaxy was conducted. In this study, I used multiwavelength data to analyze the evolutionary history of the S-shaped radio quasar, PKS 2300-18, across multiple spatial scales. At parsec scales, high-resolution optical spectroscopy revealed double-peaked broad emission lines, indicating intricate gas kinematics in the broad-line region, just a few light-days from the central SMBH. X-ray observations using Chandra further uncovered signatures of photoionized gas near the SMBH, likely driven by quasar winds. At larger kiloparsec scales, detailed radio observations helped to make a kinematical model of the large-scale S-shaped jets, analyze their energetics, and perform spectral ageing studies to trace the morphological evolution of the source. This comprehensive multiwavelength approach offers fresh insights into how AGN feedback shapes the evolution of its host galaxy.

Chapter 2

Sample of S-shaped Sources: Observations and Analysis

2.1 Introduction

S-shaped radio galaxies, often observed with a striking inversion symmetry, demand a detailed study to uncover the rare astrophysical mechanisms that result in their unique and uncommom morphology; that are either intrinsic to the central engine or influenced by the surrounding environment. To advance such investigations, it is essential to compile a sample of these sources, which can help establish a broader understanding of their common characteristics and underlying formation mechanisms. The primary aim of this work and especially this thesis was to observe these sources at low radio frequencies, which are particularly effective in tracing the oldest and most diffuse plasma, thereby revealing the full extent of their morphology.

Morphological information serves as the foundation for studying the time evolution of these sources using spectral ageing analysis, a technique detailed in subsequent chapters. Additionally, the spectral ageing results can be compared with kinematical jet precession models to trace the history of jet reorientation over time. This is a novel approach that, to the best of our knowledge, has not been previously explored in the literature for directly contrasting two independent methods of estimating source ages. A comprehensive multi-wavelength investigation, incorporating all the above mentioned goals, was conducted for one selected source, PKS 2300-18, from the sample which is presented in detail in Chapter 4. In this chapter, I introduce the initial sample of seven S-shaped sources, explain the

selection criteria, and describe the observational strategies and data reduction procedures. Then I present low-frequency radio maps of these galaxies and discuss their S-shaped morphologies, highlighting precession signatures identified in each source.

As an initial step in building the sample, the catalog from Proctor (2011), which used the FIRST survey to classify radio sources by morphology, was utilized. From Proctor's list of S-shaped candidates, an initial visual inspection led to the shortlisting of a few dozen promising sources. Ultimately, three prominent S-shaped radio galaxies: J1040+5056, J1319+2938, and J1353+2809, were selected based on the following criteria: (i) clear S-shaped morphology verified using high-frequency radio images; (ii) availability of highly resolved radio maps at high frequencies (e.g., FIRST and VLASS); (iii) low to moderate redshift ($z < 0.5$), ensuring angular sizes large enough (> 1 arcmin) to resolve key structural components such as the core, jets, and lobes; and (iv) presence of at least three well-resolved archival radio maps across different frequencies to enable reliable spectral ageing analysis in subsequent investigations.

Subsequently, an additional set of three S-shaped radio galaxies: J1315+5254, J1345+5332, J1502+5304, were selected from the LoTSS DR1 survey (Shimwell et al. 2019; Pal and Kumari 2021), focusing on the declination range of 50°to 57°. This range was chosen to facilitate the use of multifrequency maps from the Apertif Survey DR1 at 1400 MHz (Adams and van Leeuwen 2019), where relatively high resolution (17 arcsec x 12 arcsec) can be achieved at higher declinations. The selected candidates were chosen as they met all the previous crtiteria mentioned before alongside few key characteristics: they were located within a narrow declination band on the sky, had moderate redshifts ($0.1 < z < 0.3$), and exhibited angular sizes larger than 2 arcmin.

To this list, one aditional source, PKS 2300–18, was added from the southern hemisphere. Although previously studied by Hunstead et al. (1984), it lacked low-frequency radio analysis. PKS 2300–18 met all the selection criteria and brought the final sample size to seven sources. The final sample of selected objects are listed in Table 2.1, alongside their projected angular sizes, observational details and total flux density values. Radio images of all sources are shown in Figures 2.1–2.9. Among them, PKS 2300–18 is studied in detail in Chapter 4; hence, this chapter presents a focused analysis of the remaining six sources. All absolute quantities in this chapter were calculated for a ΛCDM universe with $H_0 = 70$ km s^{-1}Mpc^{-1}, $\Omega_m = 0.3$, and $\Omega_\Lambda = 0.7$.

2.2 Observations

The sample of these six S-shaped radio galaxies were observed using dedicated uGMRT and JVLA observations. Here, I present only the low-frequency uGMRT observations. In this section, I individually describe the detailed observation methodology and data reduction for these sources. As mentioned earlier, PKS 2300-18, is part of this sample and has been analyzed separately as a part of a dedicated paper, which includes a multiwavelength study presented as Chapter 4 of this thesis. The six target sources were observed using the uGMRT wideband receiver (GWB) with 2048 channels in two frequency bands, band 3 (250-500 MHz) and band 4 (550-850 MHz), concurrently with the narrowband reciever (GSB) for ∼80 hrs, where I was the principal investigator in the three uGMRT proposals. The details about observations and data reduction are provided below with some additional information listed in Table 2.1. The flux density errors were calculated using the following formula:

$$\Delta S = \sqrt{(S \times \Delta S_c)^2 + \left(rms \times \sqrt{\frac{area}{beam}}\right)^2} \tag{2.1}$$

where ΔS_c is the calibration error taken as 10 per cent for the uGMRT observations.

2.2.1 J1040+5056

For the band 3 and band 4 observations, the scheme of looping the phase calibrator with the target source was adopted, with the flux density calibrator 3C 48 being observed for ∼10 mins at the beginning and flux density calibrator 3C 286 being observed for ∼15 mins at the end of observations for band 3. 3C 286 was also observed for ∼10 mins in the beginning and ∼12 mins at the end of observations for band 4. The phase calibrators for band 3 and band 4 were J0834+555 and J1035+564 respectively, and they were observed for 5 mins in loop alternation with the target source.

2.2.2 J1315+5254

For the band 3 and band 4 observations, the scheme of looping the phase calibrator with the target source was adopted, with the flux density calibrator 3C 147 being observed for ∼11 mins at the beginning for band 3, and 3C 286 observed for 11 mins at the beginning of band 4 observations. 3C 286 was observed for ∼10 mins at the end of observations for

both band 3 and band 4. J1313+675 was used as phase calibrator for band 3 and was observed for 4 mins in loop alternating with the target source. J1400+621 was used as phase calibrator for band 4 and was observed for 5 mins in a loop alternating with the target source.

2.2.3 J1319+2938

For the band 3 and band 4 observations, the scheme of looping the phase calibrator with the target source was adopted, with the flux density calibrator observed for ∼10 mins at the beginning and end of the observations. Observations of the target source for both of the bands were made using the phase and flux density calibrator 3C 286. The phase calibrator for band 3 and 4 observations were observed in a loop of 4 mins altenating with the target source.

2.2.4 J1345+5332

For the band 3 and band 4 observations, the scheme of looping the phase calibrator with the target source was adopted with the flux density calibrator 3C 147 being observed for ∼11 mins at the beginning for band 3, and 3C 286 being observed for 10 mins at the beginning of band 4 observations. 3C 286 was observed for ∼10 mins at the end of observations for both band 3 and band 4. J1313+675 was used as phase calibrator for band 3 and was observed for 4 mins in loop alternating with the target source, while J1400+621 was used as phase calibrator for band 4 and was observed for 5 mins in a loop alternating with the target source.

2.2.5 J1353+2809

For the band 3 and band 4 observations, the scheme of looping the phase calibrator with the target source was adopted with the flux density calibrator observed for ∼11 mins at the beginning and at the end of the observations for band 3, and ∼10 mins in the beginning and ∼13 mins at the end of observations for band 4. Observations of the target source for both of the bands were made using the phase and flux density calibrator 3C 286. The phase calibrator for band 3 and 4 observations was observed in a loop of 4 mins altenating with the target source.

2.2.6 J1502+5304

For the band 3 and band 4 observations, the scheme of looping the phase calibrator with the target source was adopted, with the flux density calibrator 3C 286 being observed for ∼11 mins at the beginning and end of observations for band 3 and band 4, while 3C 286 was observed for ∼11 mins and 3C 468.1 was observed for ∼10 mins at the end of observations for band 3 and band 4 respectively. J1459+716 was used as phase calibrator for band 3 and was observed for 4 mins in loop alternating with the target source while J1400+621 was used as phase calibrator for band 4 and was observed for 5 mins in a loop alternating with the target source.

2.3 Data Reduction

For all the six sources, the GSB data reduction for all the observed frequencies was carried out using the Source Peeling and Atmospheric Modeling pipeline (SPAM: Intema et al. 2009; Intema 2014). SPAM is a Python-based extension to AIPS (Greisen 2003) that reduces high-resolution, low-frequency radio interferometric observations. It follows direction-dependent calibration, modelling, and corrections for the dispersive phase delay that are primarily of ionospheric origin. The data were corrected for strong radio frequency interference followed by standard flux-density and bandpass calibration. This was followed by cleaning which was performed using the Cotton–Schwab algorithm (Schwab 1984; Cotton 1999). This algorithm is a modified version of CLEAN deconvolution (Högbom 1974; Clark 1980) and allows the deconvolution of multiple facets simultaneously, where each facet is deconvolved using a different dirty beam. The wideband GWB data were also reduced using SPAM, where the data were first split into 4–9 subbands. For the calibration of the individual subbands, a skymodel was extracted from the initial narrow-band GSB image using the python Blob Detector and Source Finder (PyBDSF: Mohan and Rafferty 2015), which is a Python-based algorithm that can decompose an image into a set of Gaussians, shapelets, or wavelets. After calibration, the final imaging was performed using the w-stacking algorithm WSclean (Offringa et al. 2014). In WSclean, a multi-scale, multi-frequency wide-band deconvolution approach (Offringa and Smirnov 2017) was used to image each band. Here the Briggs (1995) weighting scheme was used to suppress the side lobes in the point spread function. Robustness parameter of 0 was used as an optimal compromise between natural and uniform scales to preserve both large-scale structures and high-resolution details. Resultant images were primary-beam corrected using the AIPS task PBCOR. The final uGMRT maps (GWB) are presented in Figures 2.1–2.6.

TABLE 2.1: Details on the dedicated uGMRT observations of the six S-shaped sources.

Target name	Central Freq	Proposal Code	Obs Date	TOS	Resolution	PA	RMS	Total Flux Density
	(MHz)			(hrs)	($''\times''$)	(°)	(mJy/beam)	(mJy)
(1)	(2)	(3)	(4)	(5)	(6)	(7)	(8)	(9)
J1040+5056	400	40_016	2021-05-06	1.5	7.47 x 5.43	5.77	0.045	488±49
J1040+5056	700	39_018	2021-03-11	4.65	3.95 x 3.72	152.76	0.010	369±26
J1315+5254	400	41_025	2022-01-04	1.8	9.14 x 5.44	46.58	0.037	89±9
J1315+5254	650	41_025	2022-02-26	2.4	5.35 x 3.96	139.08	0.012	62±4
J1319+2938	317	40_016	2021-05-12	1.5	9.09 x 7.68	-42.04	0.119	3220±322
J1319+2938	650	39_018	2021-03-28	1.7	4.20 x 3.81	8.49	0.025	1879±131
J1345+5332	383	41_025	2022-01-04	2.3	9.71 x 5.61	43.48	0.051	773±77
J1345+5332	650	41_025	2022-03-04	3.6	5.80 x 3.83	151.51	0.014	559±39
J1353+2809	400	40_016	2021-06-11	1.8	10.74 x 5.15	74.71	0.041	653±65
J1353+2809	700	39_018	2021-03-17	3.0	3.97 x 3.21	41.16	0.016	470±33
J1502+5304	400	41_025	2022-01-16	1.8	8.15 x 5.49	19.50	0.027	66±7
J1502+5304	650	41_025	2022-02-25	2.9	4.82 x 3.77	151.47	0.011	46±3

(1) The first row next to each target represents the band 3 observations followed by the band 4 observations in the second row (5) TOS refers to the Time on Source, (7) PA refers to the Position Angle, (8) RMS refers to Root Mean Square noise. (9)The flux density values were calculated for the entire target source at the frequency given in col (2).

2.4 Source Description

2.4.1 J1040+5056

The radio morphology of the source, as observed with uGMRT band 3 and band 4 map (given in Figure 2.1) and archival LOFAR map (Figure 2.7) reveals lobes aligned along the north–south axis. The northern jet exhibits a distinct eastward bend, while the southern jet displays a westward bend, imparting an S-shaped curvature to the overall structure. The source with coordinates RA: $10^{h}\,40^{m}\,22.45^{s}$ DEC : $+50^{\circ}\,56'\,22.9''$ (J2000.0) , is located at a redshift z = 0.153, and has an angular extent of $\sim$ 1.5 arcmin, corresponding to a projected linear size of $\sim$ 240 kpc. The host of the radio source is an elliptical galaxy.

The source's large-scale morphology is broadly consistent with that of an FR I-type radio galaxy. The southern lobe features diffuse, wing-like emission that curves strongly westward, suggesting that the jets may have undergone significant reorientation, from a previous configuration to the current north south alignment. Similarly, in the northern lobe, diffuse emission extends eastward from the main jet axis, reinforcing the impression of an S-shaped structure.

FR I jets are typically narrow and collimated, often showing small-scale bends due to environmental interactions. This strong characteristic bending in the opposite directions, with large trail of diffuse emission behind the jet, makes it a likely case of jet reorientation. Precession indicators include curved jets and S-shaped symmetry. However, there still remains the likelihood of this structure being an FR I jet being extremely bent due to environmental factors, that is resulting in an S-shaped morphology, which can only be confirmed with high-resolution radio observations and further multi-wavelength studies.

2.4.2 J1315+5254

The radio structure observed in uGMRT band 3, band 4, and archival LOFAR maps (see Figure 2.2 and 2.7) reveals a prominent S-shaped large-scale morphology. The source exhibits narrow, well-collimated jets extending along the east–west axis, accompanied by tail/wing like extensions in the north-south direction. A bright knot is observed in the western lobe, while a much fainter counterpart appears in the eastern lobe. The host galaxy located at coordinate RA: $13^{h}\,15^{m}\,29.9^{s}$ DEC : $+52^{\circ}\,54'\,37.8''$ (J2000.0), is an elliptical galaxy with a redshift of z = 0.121. These east–west jets show extended emission toward

the north and south, imparting an FR I-like morphology to the source. The southern, tail-like extension connected to the western lobe is slightly thinner than the broader northern feature associated with the eastern lobe. In the uGMRT band 3 and band 4 maps, the total angular size of the source is $\sim$ 3 arcmin. However, in the LOFAR 150 MHz archival map, due to the telescope's better low-frequency sensitivity and resolution, the structure extends beyond 5 arcminutes, corresponding to a projected linear size of $\sim$ 654 kpc.

This larger extent at low frequencies suggests the presence of aged synchrotron plasma in the outer tails, visible only in deep, sensitive and low-frequency observations. The thin, oppositely twisted wings indicate a rapid reorientation of the FR I-like jets, possibly due to precession or a dynamical interaction, with the jets being dragged from their previous orientation in an anti-clockwise direction. The primary indicators of jet precession in this source are its large-scale curved morphology and the clear S-shaped symmetry.

2.4.3 J1319+2938

The source observed in the low-frequency band 3 and band 4 uGMRT map and archival LOFAR map (see Figure 2.3 and 2.8) exhibits inversion-symmetric S-shaped jets oriented along the east–west axis. These jets are embedded in a cocoon of low surface brightness diffuse emission that extends along the north–south direction, forming a structure $\sim$ 4 arcmin and 330 kpc in linear size. The extended emission mirrors the S-shaped morphology, continuing outward from the edges of the east–west aligned curved jets. The western jet shows a morphology resembling an FR II type, whereas the eastern jet displays characteristics more typical of an FR I jet. Notably, the eastern jet appears more collimated compared to the western jet. The radio core is coincident with an elliptical galaxy located at the coordinate RA: $13^{\rm h}\,19^{\rm m}\,04.17^{\rm s}$ DEC : $+29^\circ\,38'\,35.3''$ (J2000.0) , with a redshift of 0.073, accompanied by a companion spiral or disk galaxy at a similar redshift.

Enhanced radio emission is evident near the core and towards the western extremity of the S-shaped jet. At the outer edges, the diffuse wings of the S-shaped jets show a slight elongation along the north–south direction. This feature hints at a previous jet orientation, suggesting that the current configuration results from a reorientation event. The inversion-symmetric S-shaped jets strongly indicate that the source is undergoing jet precession. The overall morphology of the source can be attributed to the source undergoing continuous precession in the clockwise direction. The precession indicators here include large-scale curved morphology and clear inversion symmetric S-shaped jets.

2.4.4 J1345+5332

The radio morphology observed in the uGMRT band 3 and band 4 maps and archival LOFAR map (see Figure 2.4 and 2.8) reveals a compact radio core accompanied by two-sided, S-shaped jets. In the band 3 image, we identify bright emission regions: a central core and two prominent, hotspot-like features (compact region of enhanced brightness) aligned along the east–west direction. The eastern hotspot appears notably extended and curved, which in the higher-resolution uGMRT band 4 image resolves into knot-like features comprising two distinct components. The inner eastern and western lobes, connected through the central core and passing through the hotspots in each lobe, collectively form a distinct S-shaped curved morphology. These eastern and western lobes are surrounded by diffuse emission extending in the southwestern and northeastern directions. The total extent of the radio source is $\sim$ 370 kpc, corresponding to an angular size of $\sim$ 3 arcmin in the uGMRT low-frequency maps. The host galaxy is a blazar located at coordinate RA: $13^{\rm h}\,45^{\rm m}\,45.2^{\rm s}$ DEC : $+53^{\circ}\,32'\,52.6''$ (J2000.0), with a redshift of 0.135.

The eastern jet contains a prominent knot located about 30 kpc from the core. Interestingly, knots are observed only on the eastern side, which could be explained by Doppler boosting, suggesting that the eastern jet is directed towards our line of sight. The diffuse extension from the western lobe towards the south is substantially more pronounced than the northern extension from the eastern lobe. These asymmetrical diffuse wings, southwestern and northeastern, may represent relic emission from earlier jet orientations, indicating a possible reorientation of the jet axis in an anti-clockwise direction. The observed S-shaped curvature, presence of multiple or complex knots, and asymmetric diffuse emission are strong indicators of jet precession in this source.

2.4.5 J1353+2809

The radio source exhibits a prominent double-lobed structure aligned along the north-east–southwest direction, characterized by an S-shaped morphology (see Figure 2.5 and 2.9) in the uGMRT band 3, band 4 map and LOFAR map. The angular size of the source is $\sim$ 2 arcmin and it is located at the coordinate RA: $13^{\rm h}\,53^{\rm m}\,08.36^{\rm s}$ DEC : $+28^{\circ}\,09'\,08.9''$ (J2000.0) , with a redshift of z = 0.4, which makes the projected linear size of the source as $\sim$ 670 kpc. In the uGMRT band 3 map, both the northeastern and southwestern lobes display bright, hotspot-like features. The southeastern hotspot appears larger and brighter and extends towards the south, while the northern hotspot is more compact but also shows a extension towards the north.

In the higher-resolution uGMRT band 4 map, the southeastern lobe reveals a well-defined jet that bends sharply, almost perpendicularly, indicating significant jet deflection that was just previously seen as a large bright hotspot in low resolution band 3 map. In contrast, while the northern hotspot remains visible in band 4, there is no clearly defined jet-like feature associated with it. Instead, a faint, misaligned trail of emission extends northward from the hotspot, forming an S-shaped curve.

The sharp bending of the jet in the southwestern lobe, coupled with the misaligned and curved emission trail in the northeastern lobe hotspot, hints toward change in the jet-axis direction or reorientation. The opposite bending of the lobes relative to the core strongly suggests a scenario of jet-axis precession. Key indicators of precession in this source include the large-scale curvature of the jets, S-shaped symmetry, the presence of hotspots at the edges of the lobe, and the appearance of multiple or broad hotspots.

2.4.6 J1502+5304

The radio galaxy exhibits bright central emission in both uGMRT band 3, band 4 and LOFAR maps (see Figure 2.6 and 2.9), accompanied by extended, twisted radio lobes oriented along the north–south direction. Both the northern and southern lobes display hotspot-like features. Notably, the southern lobe hosts a knot-like region of enhanced emission closer to the core. The core itself appears extended in the band 3 image and, in the higher-frequency band 4 map, resolves into an additional compact, knot-like feature extended towards the eastern lobe.

The source with coordinate RA: $15^{\mathrm{h}}\,02^{\mathrm{m}}\,09.7^{\mathrm{s}}$ DEC : $+53^{\circ}\,04'\,19.9''$ (J2000.0), has an angular size of ~ 2 arcmin, corresponding to a projected physical size of ~ 260 kpc at the redshift of z = 0.287. The host is an elliptical and bright cluster galaxy. The northern lobe also exhibits an elongation in the form of a diffuse, wing-like extension towards the right of the hotspot present at the edge of the lobe, suggesting a twisting or dragging of the jet in an anti-clockwise direction. Meanwhile, the southern lobe shows an abrupt bend of nearly 90 degrees near the first knot present towards the right side of the radio core.

Overall, the source displays an FR I-like morphology, with jets that undergo dramatic bending, almost perpendicular, towards the north and south. The observed flattening at the lobe edges and the pronounced curvature of the jets support the idea of a reorientation of the jet axis in an anti-clockwise direction. The key indicators of jet precession in this source include the curved large-scale morphology, S-shaped symmetry, and the presence of broad hotspot.

uGMRT Radio Maps

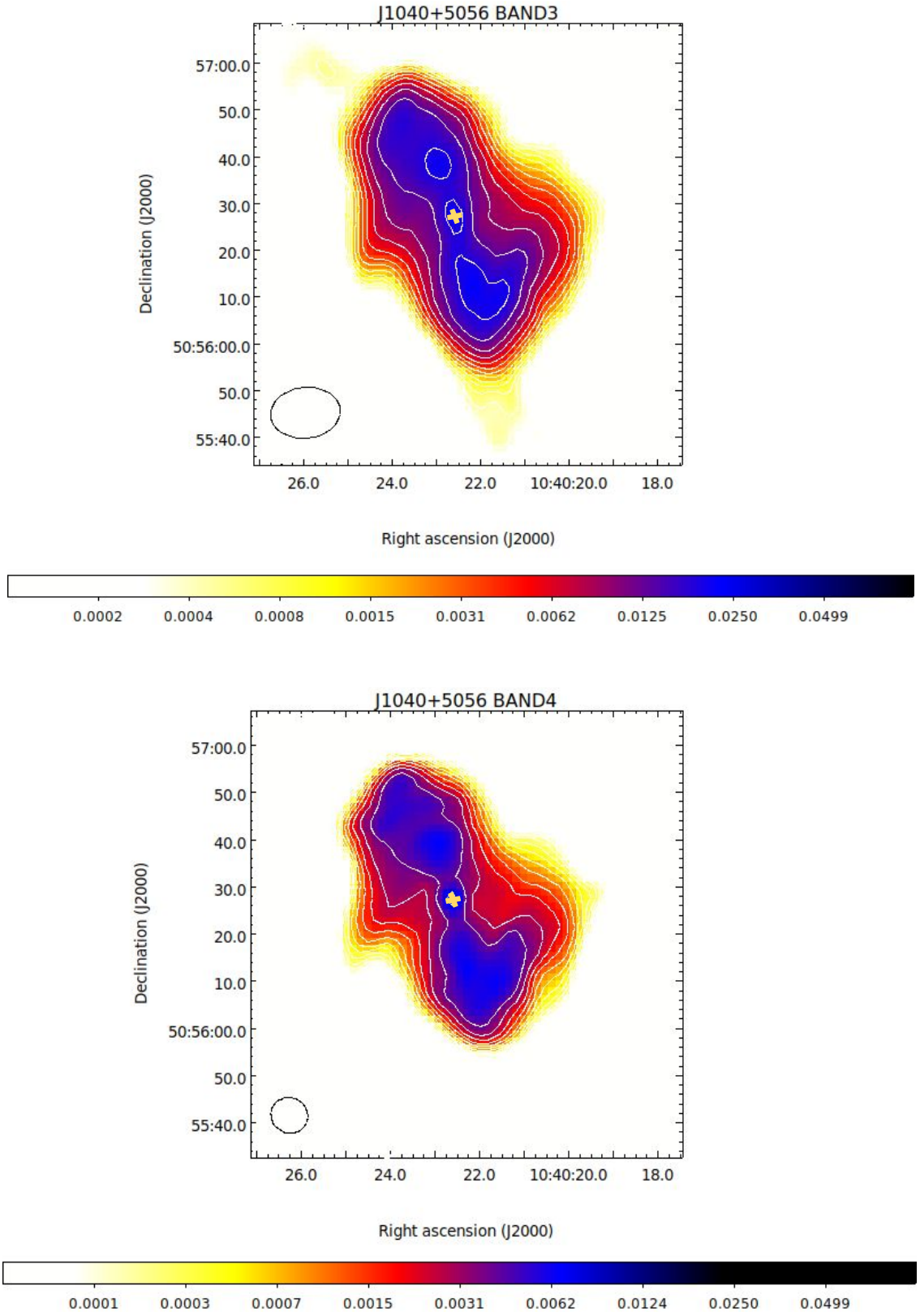

FIGURE 2.1: Low-frequency map of J1040+5056 obtained from uGMRT observations at band 3 (Top panel) and band 4 (Bottom panel). The yellow crosshair marks the position of the radio core. The contour levels are spaced by a factor of $\sqrt{2}$ and the first contour is at 3 $\times$ RMS level. The RMS values and beam sizes of all the uGMRT maps are given in Table 2.1. The relative sizes of the beam are indicated by the ellipse at the bottom left corner of each image. The colour gradient represents flux density values in Jy beam^{-1}.

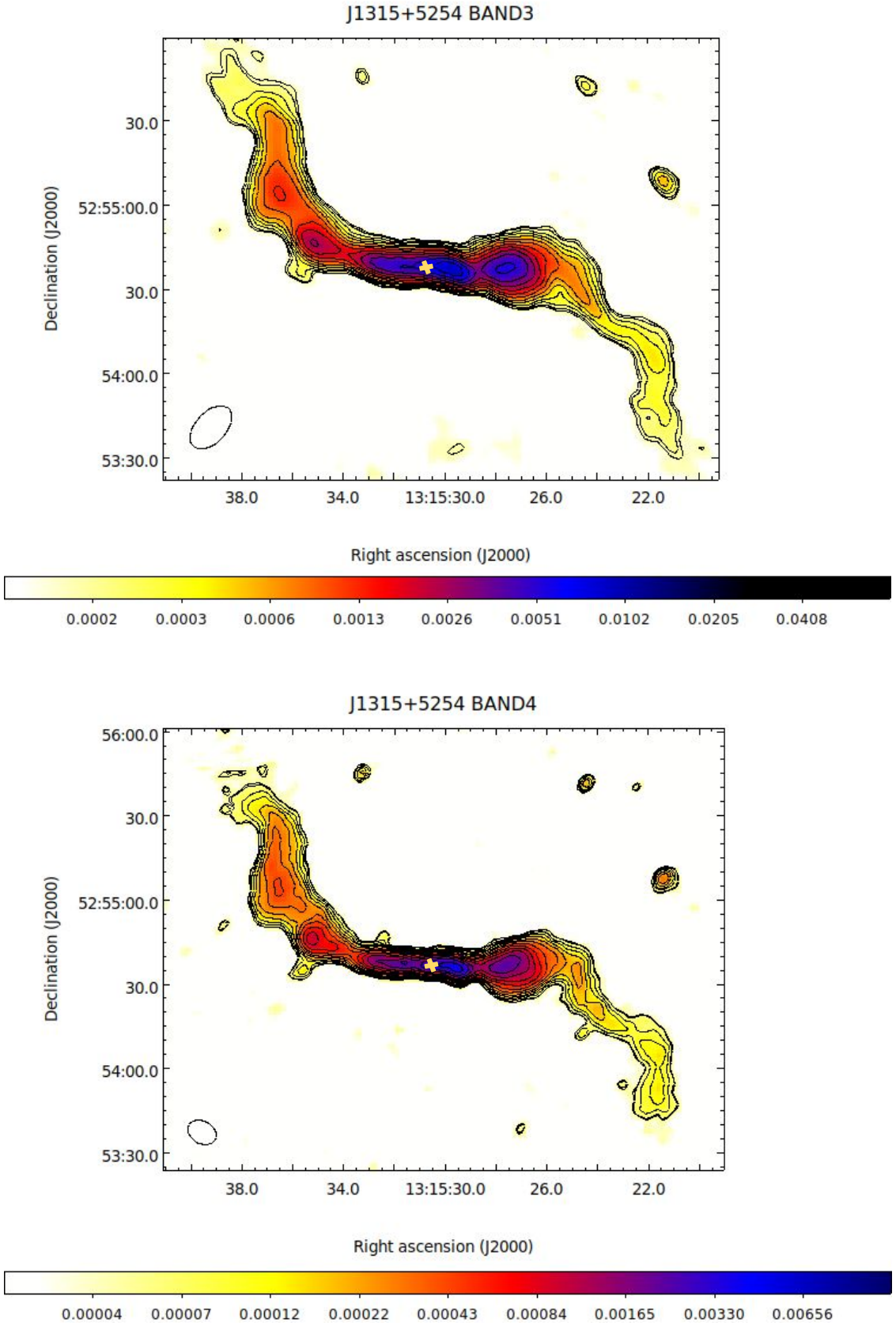

FIGURE 2.2: Low-frequency map of J1315+5254 obtained from uGMRT observations at band 3 and band 4. The map details are identical to those provided in the caption of Figure 2.1.

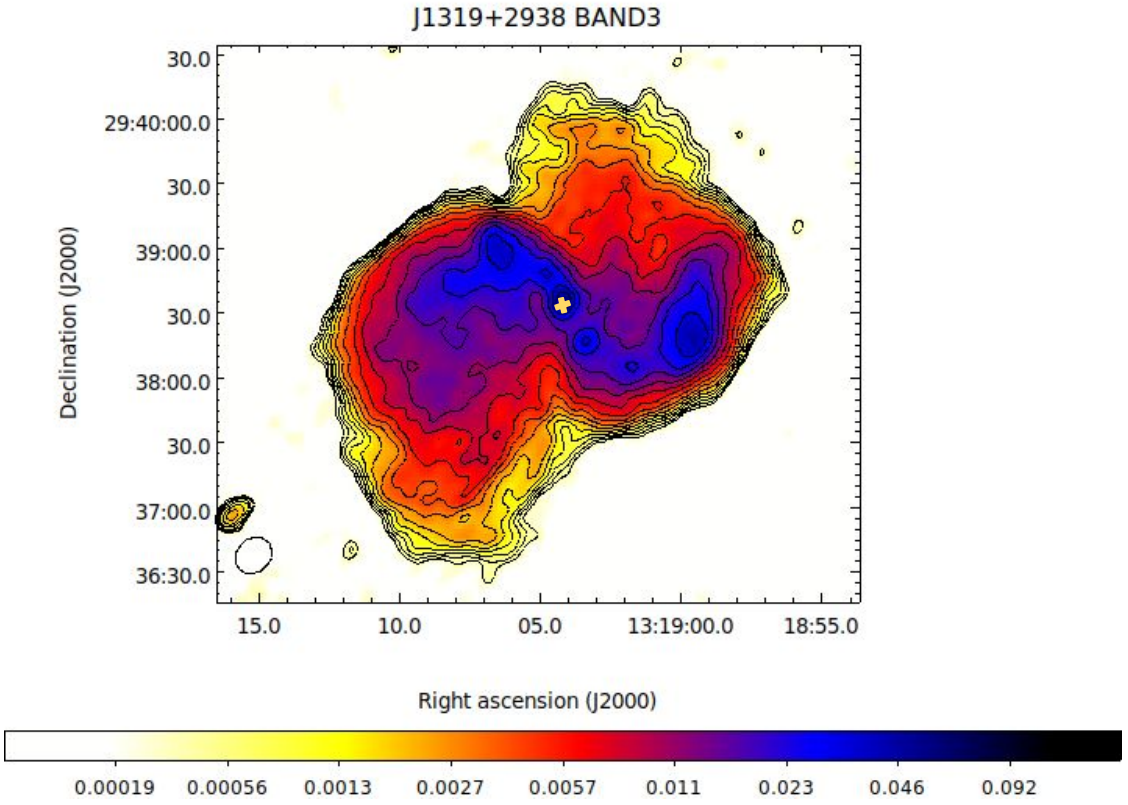

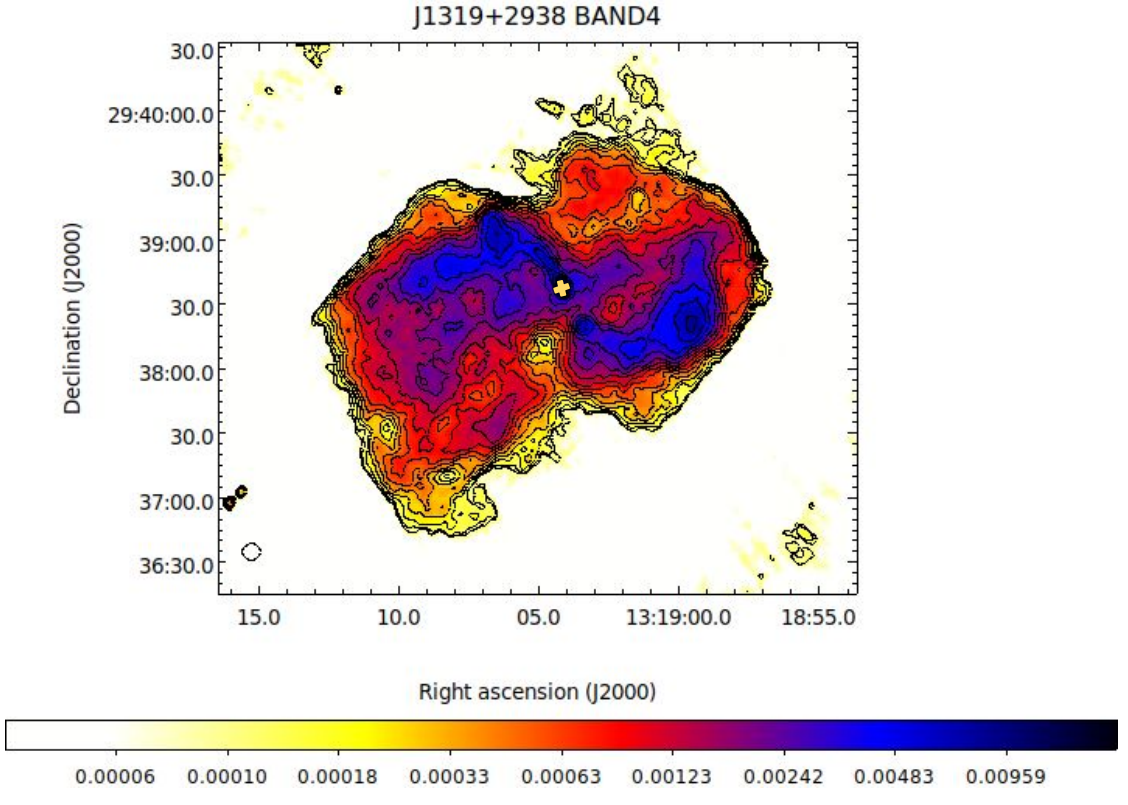

FIGURE 2.3: Low-frequency map of J1319+2938 obtained from uGMRT observations at band 3 and band 4. The map details are identical to those provided in the caption of Figure 2.1.

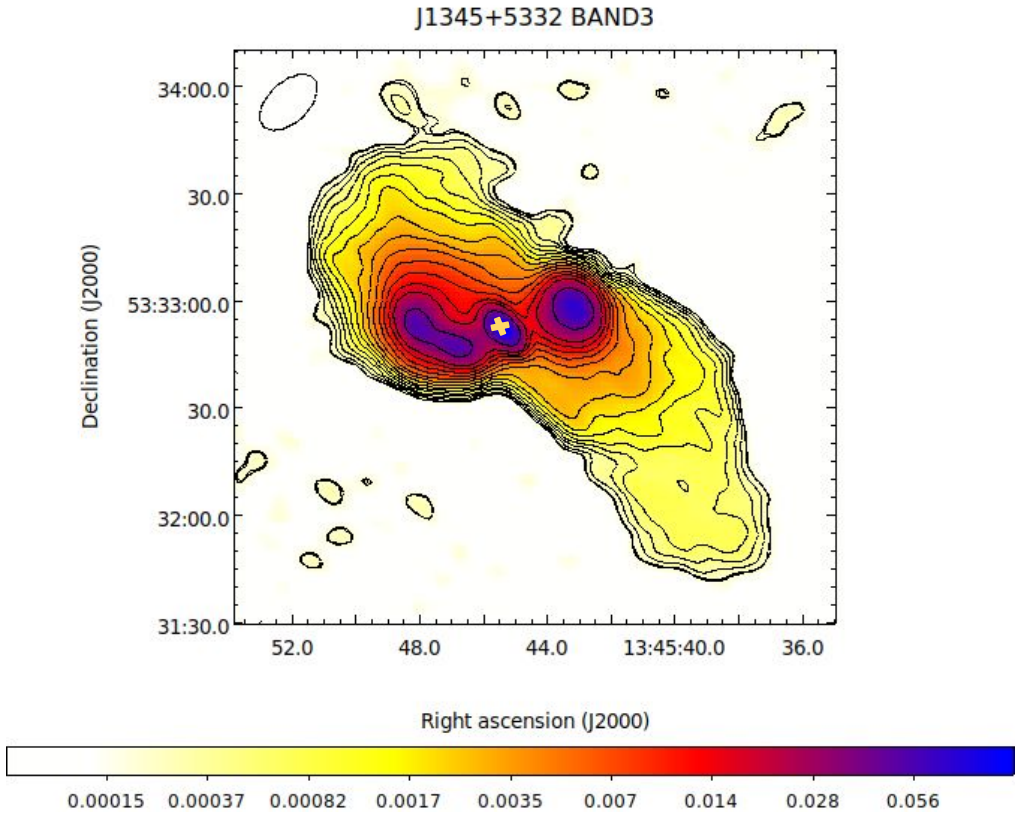

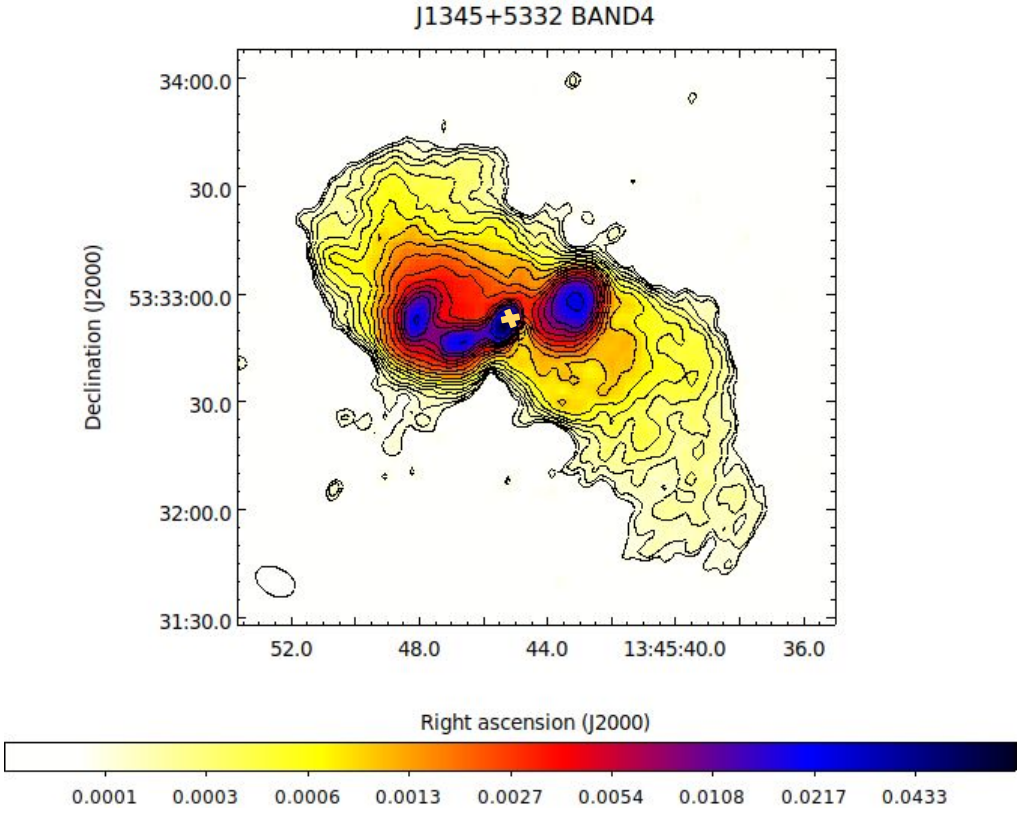

FIGURE 2.4: Low-frequency map of J1345+5332 obtained from uGMRT observations at band 3 and band 4. The map details are identical to those provided in the caption of Figure 2.1.

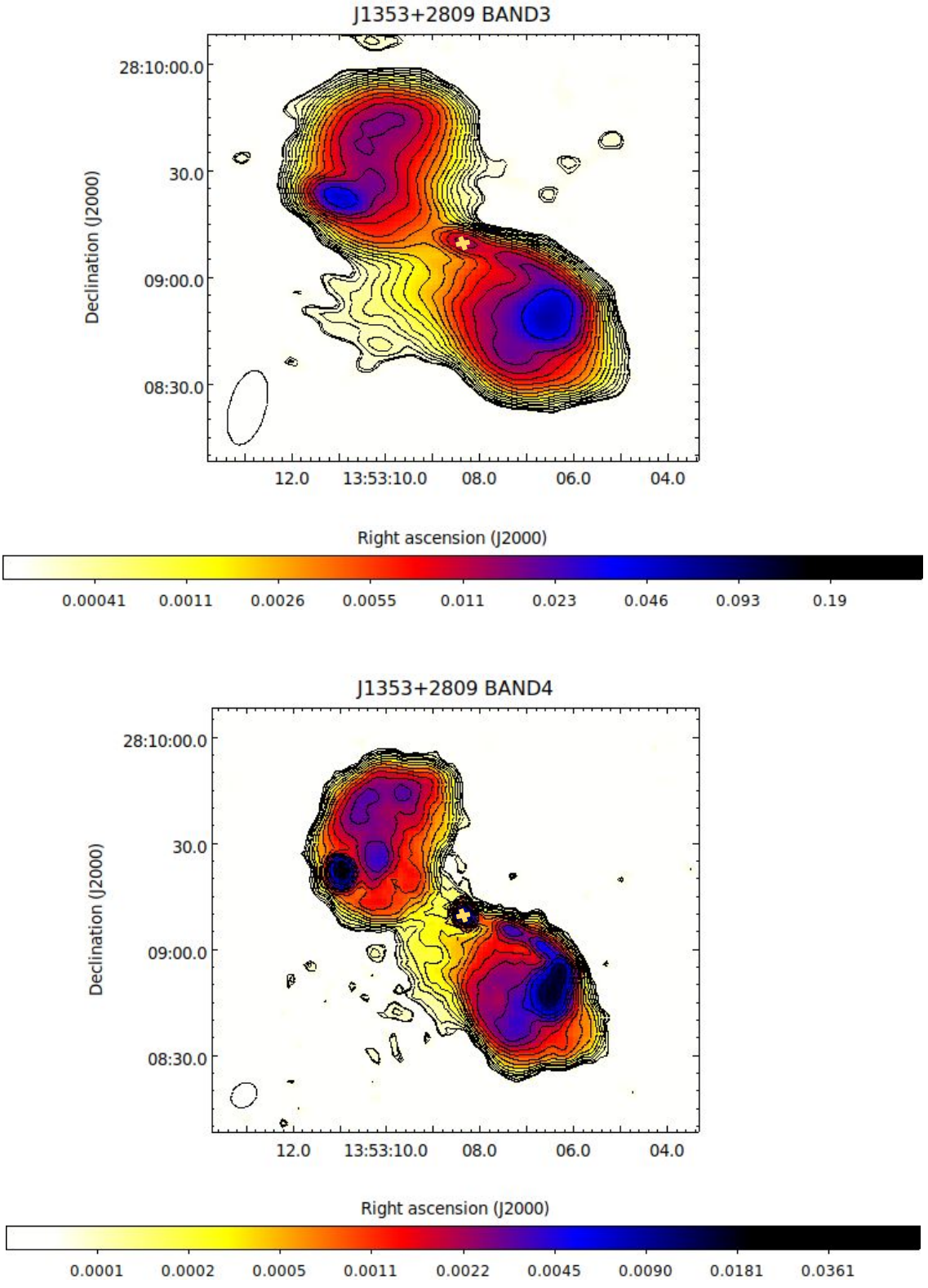

FIGURE 2.5: Low-frequency map of J1353+2809 obtained from uGMRT observations at band 3 and band 4. The map details are identical to those provided in the caption of Figure 2.1.

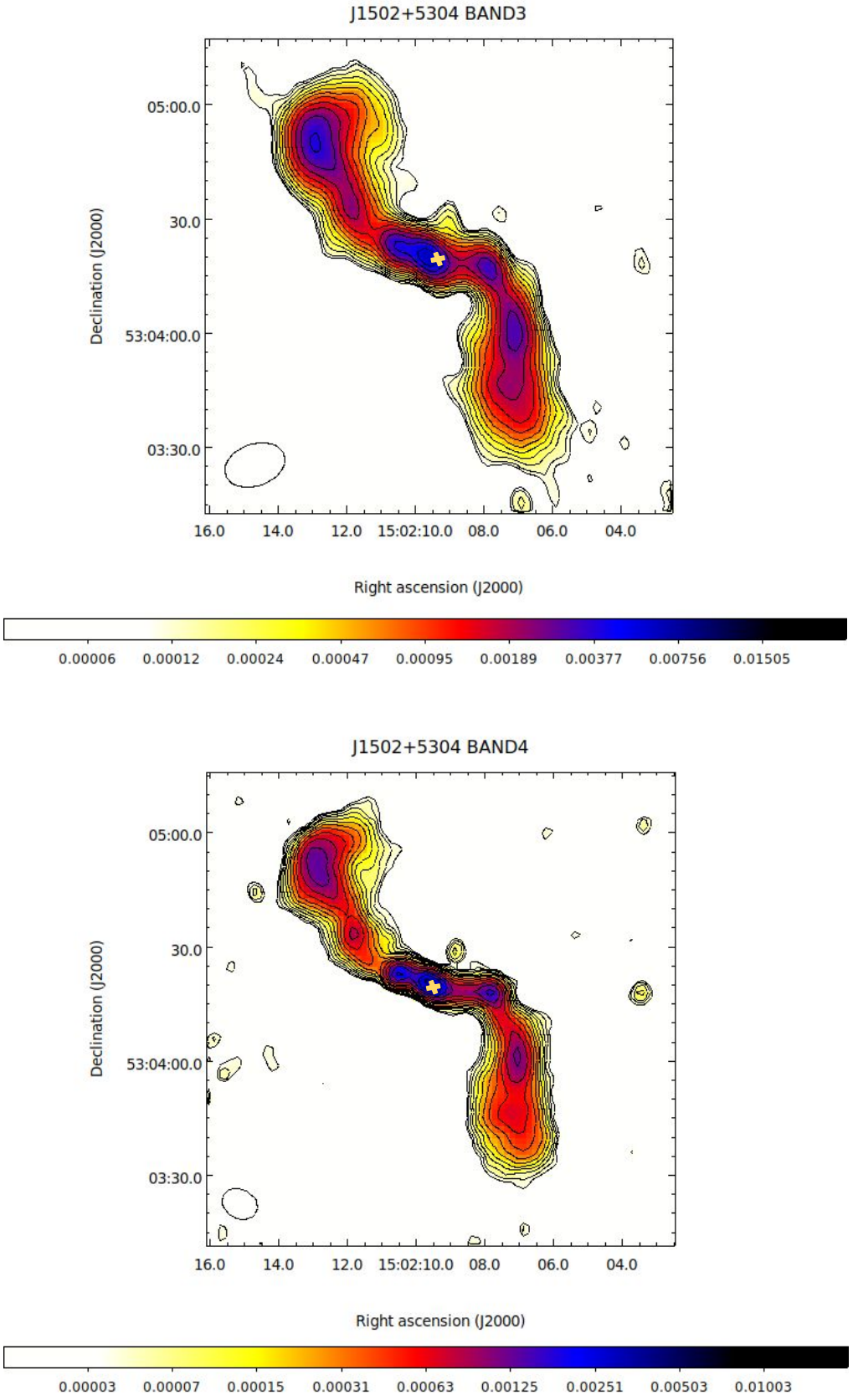

FIGURE 2.6: Low-frequency map of J1502+5304 obtained from uGMRT observations at band 3 and band 4. The map details are identical to those provided in the caption of Figure 2.1.

Archival LOFAR Radio Maps

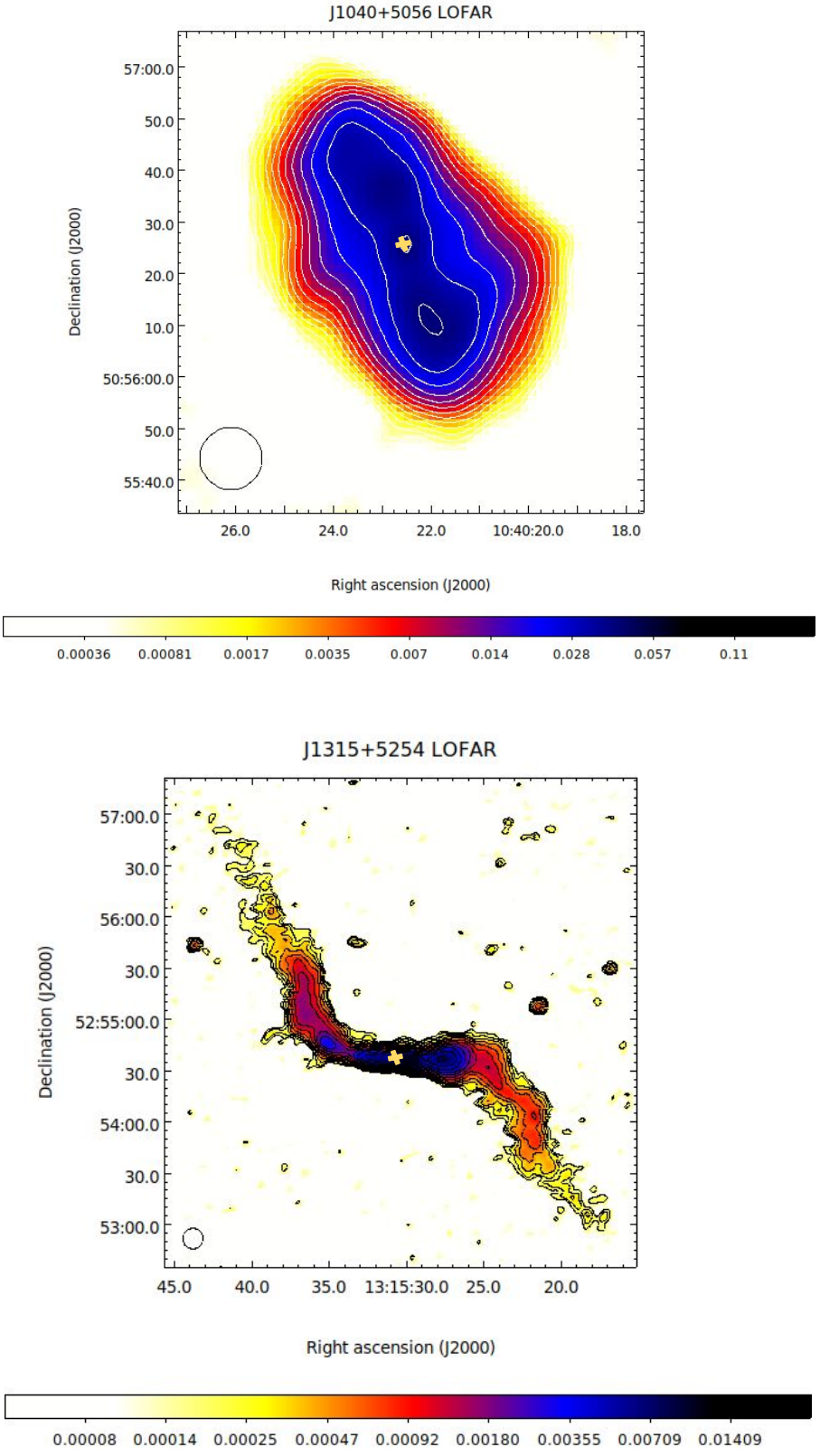

FIGURE 2.7: Archival low-frequency LOFAR maps of J1040+5056 (upper panel) and J1315+5254 (lower panel). The beam size is 6 arcsec × 6 arcsec. The yellow crosshair marks the position of the radio core. The RMS noise values for J1040+5056 and J1315+5254 are 1.5×10^{-4} and 5.4×10^{-5} Jy beam^{-1} respectively. The contour levels are spaced by a factor of $\sqrt{2}$ and the first contour is at 3 × RMS level. The relative sizes of the beam are indicated by the ellipse at the bottom left corner of each image. The colour gradient represents flux density values in Jy beam^{-1}.

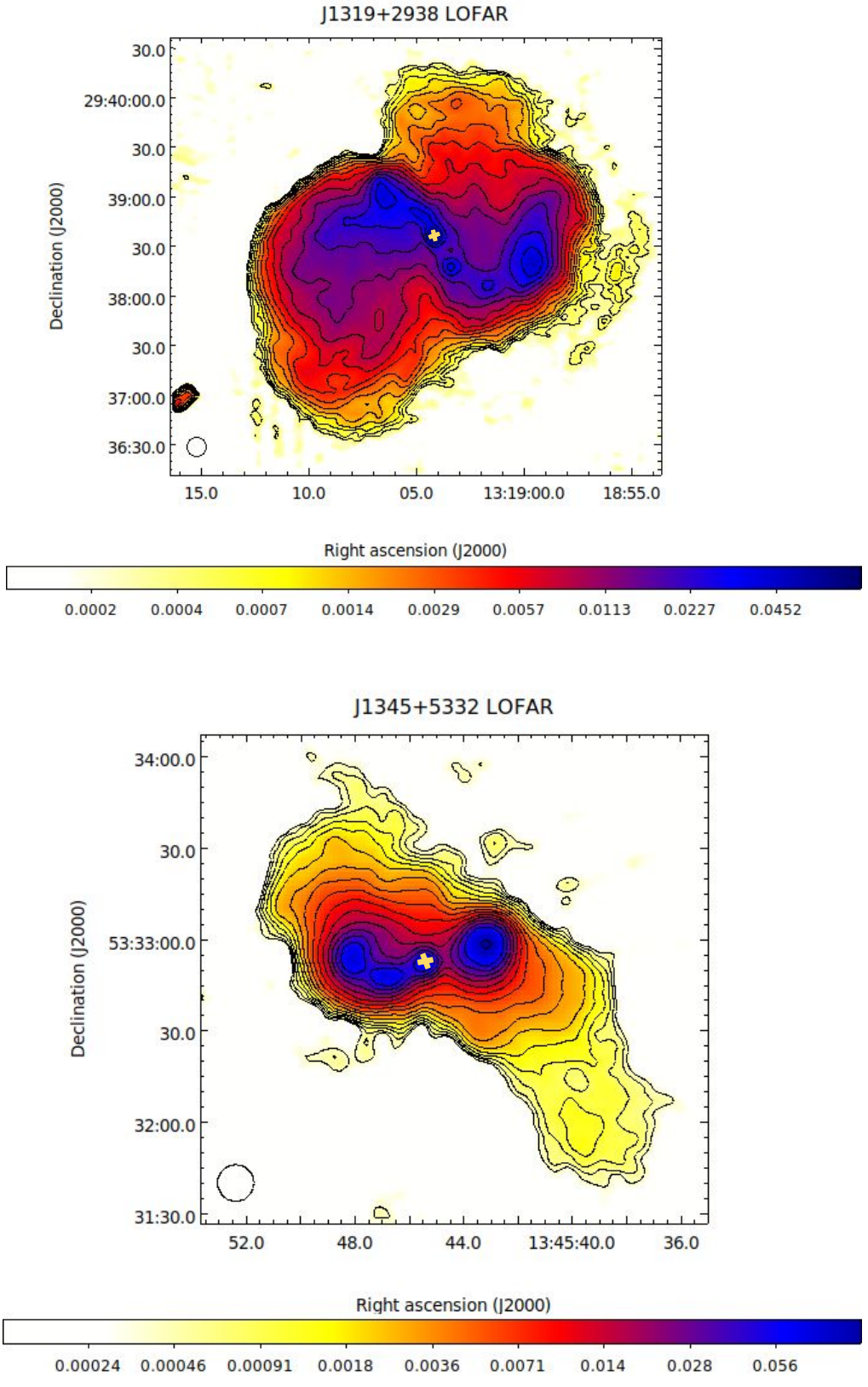

FIGURE 2.8: Archival low-frequency LOFAR maps of J1319+2938 (upper panel) and J1345+5332 (lower panel). The RMS noise values for J1319+2938 and J1345+5332 are 8.5×10^{-5} and 1.3×10^{-4} Jy beam^{-1} respectively. The map details are identical to those provided in the caption of Figure 2.7.

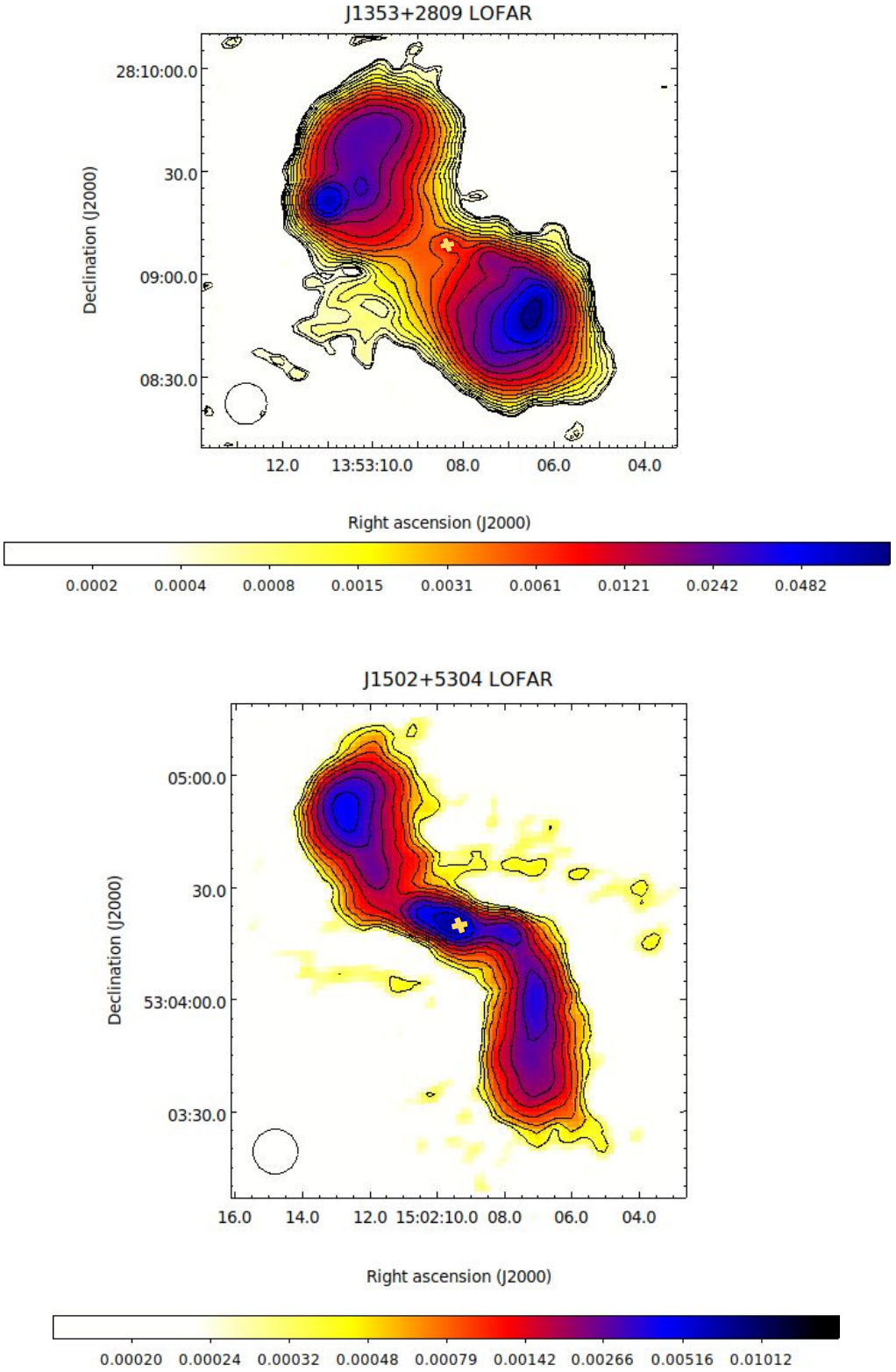

FIGURE 2.9: Archival low-frequency LOFAR maps of J1353+2809 (upper panel) and J1502+5304 (lower panel). The RMS noise values for J1353+2809 and J1502+5304 are 1.1×10^{-4} and 8.3×10^{-5} Jy beam^{-1} respectively. The map details are identical to those provided in the caption of Figure 2.7.

Chapter 3

Multifrequency analysis of the radio emission from a post-merger galaxy CGCG 292-057

Monthly Notices of the ROYAL ASTRONOMICAL SOCIETY

MNRAS **523,** 1648–1660 (2023) https://doi.org/10.1093/mnras/stad1533
Advance Access publication 2023 May 22

Multifrequency analysis of the radio emission from a post-merger galaxy CGCG 292-057

Arpita Misra,* Marek Jamrozy and Marek Weżgowiec
Astronomical Observatory, Jagiellonian University, Orla 171, PL-30-244 Krakow, Poland

Accepted 2023 May 15. Received 2023 May 13; in original form 2023 January 6

ABSTRACT

Galaxies exhibiting a specific large-scale extended radio emission, such as X-shaped radio galaxies, belong to a rare class of winged radio galaxies. The morphological evolution of these radio sources is explained using several theoretical models, including galaxy mergers. However, such a direct link between a perturbed radio morphology and a galaxy merger remains observationally sparse. Here, we investigate a unique radio galaxy J1159+5820, whose host CGCG 292-057 displays the optical signature of a post-merger system with a distinct tidal tail feature, and an X-shaped radio morphology accompanied by an additional pair of inner lobes. We observed the target on a wide range of radio frequencies ranging from 147 to 4959 MHz, using dedicated GMRT and VLA observations, and supplemented it with publicly available survey data for broad-band radio analysis. Particle injection models were fitted to radio spectra of lobes and different parts of the wings. Spectral ageing analysis performed on the lobes and the wings favours a fast jet realignment model with a reorientation time-scale of a few million years. We present our results and discuss the possible mechanisms for the formation of the radio morphology.

Key words: radiation mechanisms: non-thermal – galaxies: active – galaxies: individual: CGCG 297-057 – galaxies: jets – galaxies: peculiar – radio continuum: galaxies.

1 INTRODUCTION

Highly collimated large-scale radio galaxy (RG) jets are formed from the relativistic outflows of charged particles and magnetic fields from the synchrotron-emitting plasma of the active galactic nucleus (AGN). These jets ranging from a few kpc to Mpc in size are known to strikingly maintain their jet axis direction for almost 10^8 yr (Machalski, Jamrozy & Saikia 2009; Machalski, Kozieł-Wierzbowska & Goyal 2021), or even 10^9 yr, as in the case of some giant RGs (Hurley-Walker et al. 2015; Shulevski et al. 2019). The typical hosts for RGs are giant ellipticals, and the most common mechanism for growing massive galaxies is galaxy mergers. Mergers invigorate galaxies with a fresh supply of gas and dust and can trigger AGN activity around the supermassive black hole (SMBH), ultimately playing a key rôle in explaining the growth of the SMBH at the centre of most active galaxies (Bessiere et al. 2012; Cotini et al. 2013; Ellison et al. 2019). A subset of such interactions can also take place in galaxies containing AGNs with radio jets, leading to non-standard radio morphologies as seen in the case of e.g. 3C 321 (Evans et al. 2008), an FRII (Fanaroff & Riley 1974) type RG where one of the jets undergoes bending after interacting with a nearby companion galaxy going through a merger with its host. A similar but more severe bending of the jets is observed in the case of 3C 433 (van Breugel et al. 1983), which is a part of an interacting galaxy pair. During the merger process, the central AGN is bound to undergo disturbances and perturbations, and studying radio jets associated with such galaxies can act as an excellent tracer for understanding the central SMBH behaviour.

The discovery of X-shaped radio sources (Florido, Battaner & Sanchez-Saavedra 1990; Leahy & Parma 1992; Capetti et al. 2002) poses a challenge towards understanding the dynamic interplay between radio jets, the central active region, and the intergalactic medium. The class of X-shaped RGs mainly consists of two misaligned pairs of lobes, the second pair having a relatively different orientation than the primary lobe, with the typical examples being 3C 223.1 and 3C 403 (Dennett-Thorpe et al. 2002). There are a few models that account for the formation of such sources, including (i) hydrodynamical backflow, where the secondary pair of lobes are formed by the backflow of the primary lobe that is deflected by the hot gas halo of the host galaxy (Leahy & Williams 1984; Worrall, Birkinshaw & Cameron 1995; Cotton et al. 2020); (ii) spin flip of the primary black hole and quick realignment in a post-merger system (Merritt & Ekers 2002; Rottmann 2002); (iii) presence of a dual AGN with two independent pairs of jets (Lal & Rao 2005; Cheung 2007; Yang et al. 2022); (iv) the projection due to a precessing beam (Ekers et al. 1978; Parma, Ekers & Fanti 1985); and (v) the jet–shell interaction in a merged galaxy (Gopal-Krishna., et al. 2012). The list of such objects has so far constituted a small fraction of radio sources (Cheung 2007; Mezcua et al. 2012; Saripalli & Roberts 2018; Yang et al. 2019) but with new highly resolved deep-sky surveys, X-shaped sources are found at an ever-increasing rate.

RGs usually go through an initial phase of jet activity, lasting between $\sim 10^7$ and $\sim 10^9$ yr (Cordey 1986; Parma et al. 1999, 2007), followed by a period of quiescence. However, in some RGs, nuclear activity can be classified as intermittent, where a

* E-mail: arpita.misra@doctoral.uj.edu.pl

Table 1. Details of GMRT and the VLA dedicated observations of J1159+5820 analysed in this paper.

Frequency (MHz) (1)	Telescope (2)	Proposal code (3)	Date of observation (4)	TOS (hrs) (5)	Bandwidth (MHz) (6)	Channel (7)	Size (arcsec × arcsec) (8)	PA (°) (9)	rms (mJy beam^{-1}) (10)
147	GMRT	20_009	2011 May 14	7.30	16.6	256	29.1 × 16.5	28.0	1.279
240	GMRT	18_026	2010 May 21	5.26	16.0	128	13.0 × 10.3	27.4	0.843
323	GMRT	20_009	2011 Aug 22	5.55	33.3	256	15.0 × 7.8	20.7	0.229
611	GMRT	18_026	2010 May 21	5.26	33.3	512	5.6 × 4.0	23.4	0.067
1570	VLA L band C-conf	10B-127	2010 Nov 02	0.53	256	128	18.4 × 14.0	63.1	0.204
1635	VLA L band A-conf	10C-130	2011 Jul 08	0.47	256	128	2.2 × 1.0	−52.9	0.040
4959	VLA C band CNB-conf	10C-130	2011 Feb 20	2.25	256	128	2.0 × 1.4	−85.2	0.011
4959	VLA C band C-conf*	10B-127	2010 Nov 02	1.40	256	n/a	n/a	n/a	n/a
4959	VLA C band D-conf*	11B-051	2011 Nov 08	1.35	256	n/a	n/a	n/a	n/a

Note. *The VLA *C*-band observations in C and D configurations were imaged simultaneously with a resulting resolution of 15.6 arcsec × 11.9 arcsec, PA of −4.9° and the rms of 0.06 mJy beam^{-1}.

new pair of radio lobes is visible along with the older pair, tracing plasma from a previous episode of jet activity. This suggests a short dormant phase followed by restarting nuclear activity, leading to a double–double radio morphology (DDRG; Schoenmakers et al. 2000; Saikia & Jamrozy 2009; Kuźmicz et al. 2017; Mahatma et al. 2019). Identifying and studying the radio spectra of such galaxies is of great importance for understanding the duty cycle of RGs.

In this paper, we examine radio data of CGCG 292-057, host of J1159+5820, which is a unique RG that presents a non-standard X-shaped radio morphology and also shows a restarting pair of radio lobes as a DDRG. The target source displays low-surface-brightness radio wings that span ∼7 arcmin and high-surface-brightness lobes that span to 5 arcmin. First described in the paper of Kozieł-Wierzbowska et al. (2012), this object at RA $= 11^{\rm h}59^{\rm m}05\overset{\rm s}{.}7$, Dec $= +58^{\circ}20'36''$ (J2000.0) with $z = 0.0537$ (Adelman-McCarthy et al. 2008) is classified as a low-ionization nuclear emission-line region (LINER) galaxy, based on its emission-line fluxes. The host galaxy morphology was determined by the concentration index of about 2.81 ± 0.03, which places it almost exactly at the separation line between elliptical and spiral galaxies. In the optical observations performed by Kozieł-Wierzbowska et al. (2012), a face-on galaxy with a clear tidal tail feature was revealed, indicating traces of a merging event in the past. Skipper & Browne (2018) found an offset of 291 mas in the optical position of the CGCG 292-057 galaxy centre given by the SDSS catalogue and 8.46 GHz radio position of core given by the Cosmic Lens All-Sky Survey (CLASS; Browne et al. 2003; Myers et al. 2003) catalogue. Taking into account the velocity dispersion of 242 ± 13.6 km s^{-1}, the mass of the central black hole was calculated as $\log(M_{BH}/M_{\odot}) = 8.47 \pm 0.32$ (Kozieł-Wierzbowska et al. 2012). The target is also fairly isolated as it is not associated with any nearby group or cluster. The star formation rate was calculated by Singh et al. (2015), with the use of mid-IR and UV emission, to be 2.89 and 1.50 $M_{\odot}$ per year, respectively, with evolved stellar composition at the centre of the host galaxy. X-ray studies conducted by Balasubramaniam et al. (2020) detected an excess of X-ray emission in the bulge from a thermal plasma and the presence of a Fe XXV K α line. From the SDSS spectrum, doubly peaked emission lines were observed which might be considered as an indicator for an SMBH binary (Kozieł-Wierzbowska et al. 2012).

In this paper, we present a multifrequency radio analysis of J1159+5820, which exhibits a rare combination of DDRG along with an X-shaped morphology. The presence of all of these features makes the target an ideal source for studying X-shaped RGs connected with galaxy mergers. We used archival and dedicated radio data at a range of frequencies between 54 and 8440 MHz, revealing its compact (a few kpc) and extended (several hundred kpc) radio structure. By analysing its radio spectra, we estimate the ageing of the electron population at different sections of the source and try to give an account of its morphological evolution. In Section 2, we present radio observations and data reduction procedure in detail. In Section 3, we present our results which are followed by a discussion in Section 4. Final conclusions are drawn in Section 5.

All absolute quantities in this paper were calculated for a Lambda cold dark matter universe with $H_0 = 70$ km s^{-1} Mpc^{-1}, $\Omega_{\rm m} = 0.3$, and $\Omega_{\Lambda} = 0.7$. The host galaxy is referred to as CGCG 292–057 and the related radio source is called J1159+5820 throughout the paper. Using the host galaxy redshift, the conversion scale translates to 1.045 kpc arcsec^{-1}, used in the paper.

2 RADIO OBSERVATIONS

To understand the radio morphology of J1159+5820, high-resolution and multifrequency radio maps of the diffuse lobes, centre, and the overall structure of the radio source were obtained from dedicated observations with the Giant Metrewave Radio Telescope (GMRT) at low-frequency, the Karl G. Jansky Very Large Array (VLA) at high-frequency, and publicly available survey data. The shortest baselines from both telescopes could successfully sample the largest scales of the source. In the following subsections, we describe in detail the surveys used, the observation schemes, and the data reduction techniques used to obtain GMRT and the VLA maps.

2.1 GMRT observations

J1159+5820 was observed with the GMRT in four frequency bands centred at 147, 240, 323, and 611 MHz. All observations were performed within projects 18_026 and 20_009 in 2010 May and between 2011 May and August, respectively (details are given in Table 1). The usual scheme of observations of looping the phase calibrator with the target source was adopted with the flux density calibrators observed for ∼10–20 min at the beginning and at the end of observations. For the observation of the target source centred at 147 and 323 MHz, 3C 286 was observed as both the phase and flux density calibrator. At 147 MHz, 3C 286 as the phase calibrator was observed for 5 min alternating with the target source in the loop. At 323 MHz, 3C 286 was observed as the flux density calibrator and also as the phase calibrator for 4 min between cycles. Observations at 240 and 611 MHz were conducted in dual-frequency mode (Swarup et al. 1991). This mode allows the recording of data at two frequency bands simultaneously but with a single polarization for each band only, thereby reducing the sensitivity by a factor of ∼1.41. In this case, flux density calibrators 3C 48 and 3C 147 were observed at

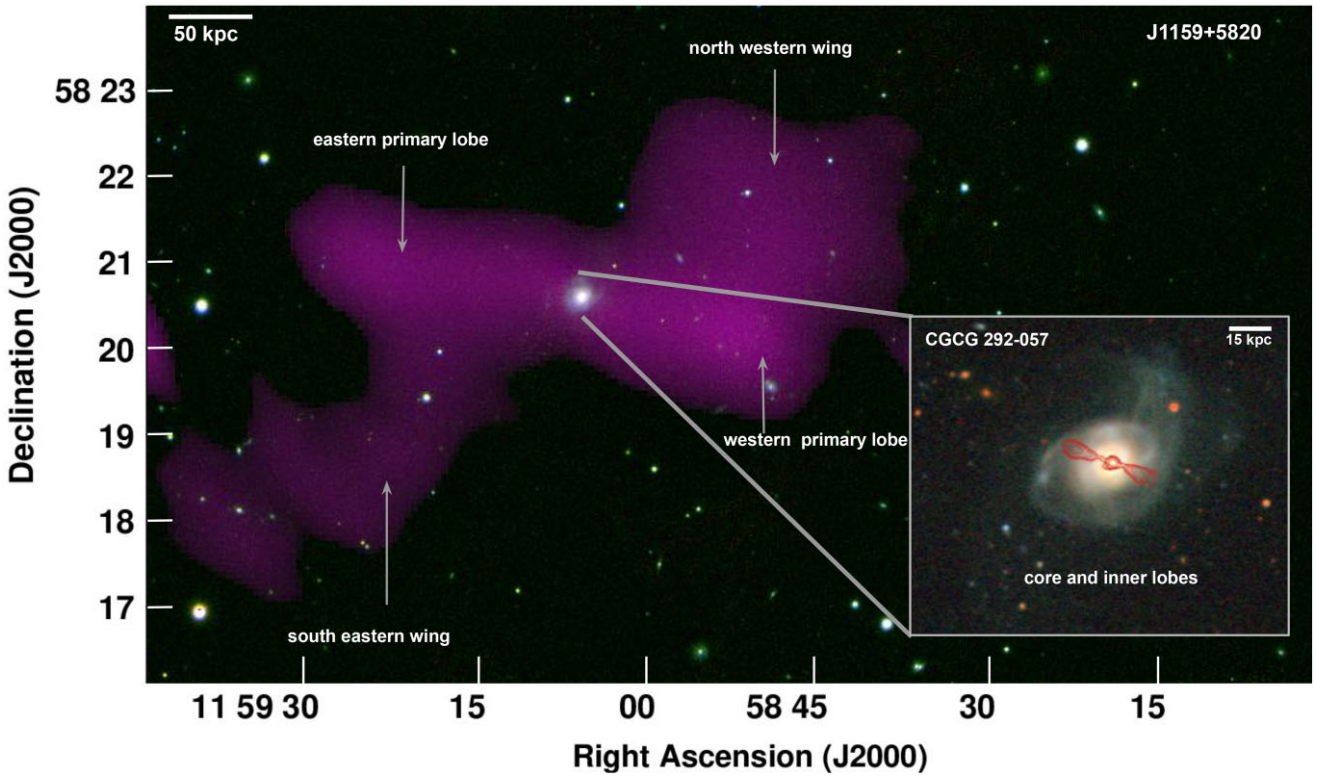

Figure 1. 147 MHz GMRT radio map of J1159+5820 overlaid on PanSTARRS (Chambers et al. 2016) optical image. The right panel insert shows VLA contours at 4959 MHz of inner lobes and core (red contours) overlaid on the host galaxy CGCG 292–057 optical image from BASS (Zou et al. 2019) with distinct tidal tail and shell features.

the beginning and 3C 286 at the end of the observations. The phase calibrator for this set of observations was J1313+675, which was observed for 5 min in a loop with the target source.

The data reduction for all observed frequencies was completed using the Source Peeling and Atmospheric Modeling (SPAM) pipeline (Intema et al. 2009; Intema 2014). It is a Python-based extension to AIPS (Greisen 2003), and is aimed at reducing high-resolution, low-frequency radio interferometric observations. It contains direction-dependent calibration, modelling, and corrections for dispersive phase delay, mainly of ionospheric origin. The data were corrected for strong radio frequency interference (RFI) and then standard flux density, phase, and bandpass calibrations were applied to the source. Cleaning was performed using the Cotton–Schwab algorithm (Schwab 1984; Cotton 1999), which is a variant of CLEAN deconvolution (Högbom 1974; Clark 1980) that allows for the simultaneous deconvolution of multiple facets, using a different dirty beam for each facet. The resultant images were then primary beam corrected, using the AIPS task PBCOR (see Figs 1–3).

2.2 VLA observations

J1159+5820 was observed with the VLA between 2010 November and 2011 November in *C* and *L* bands using various array configurations. C and D configurations allowed for proper sampling of the largest scale emission from the source. The more compact structure of the inner lobes could be efficiently studied with the use of CNB configuration at *C* band and A configuration at *L* band, both allowing for detecting structures as extended as 30 arcsec at resolutions of few arcseconds. The details of the observations are presented in Table 1. All observations were performed in single scheduling blocks consisting of calibrator (both flux and phase) and source scans.

The data were reduced with the COMMON ASTRONOMY SOFTWARE APPLICATIONS (CASA) package[1] (CASA Team et al. 2022). All data affected by shadowed antennas or RFI were flagged manually. The radio source 3C 286 was used for the flux density scale in all observations, and phase calibration was done with the use of the radio source J1148+5924 in the case of *L* band observations in A-configuration and the radio source J1219+4829 for all other observations.

All data sets, as presented in Table 1, were calibrated separately, resulting in five calibrated data sets (for each band and configuration). To deconvolve the point spread function of the interferometer from the dirty map, we used the CASA task TCLEAN, which performs the Clark CLEAN algorithm. The two *C* band observations in compact configurations C and D were merged prior to cleaning to increase the uv-coverage of the data and allow for a more precise deconvolution. To produce the best-quality images we used the robust weighting of the data (robust parameter set to one) and the multiscale CLEAN. Due to a very strong point source just east of J1159+5820 (details on this source are given in Section 3.5), in all of the obtained maps, severe interference from its sidelobes was still present. Therefore, the maps were self-calibrated both in phases (initial runs) and in amplitudes (final runs). The final images were restored with elliptical beams and then convolved into a circular beam. This allowed for better identification of components of the radio source,

[1] http://casa.nrao.edu

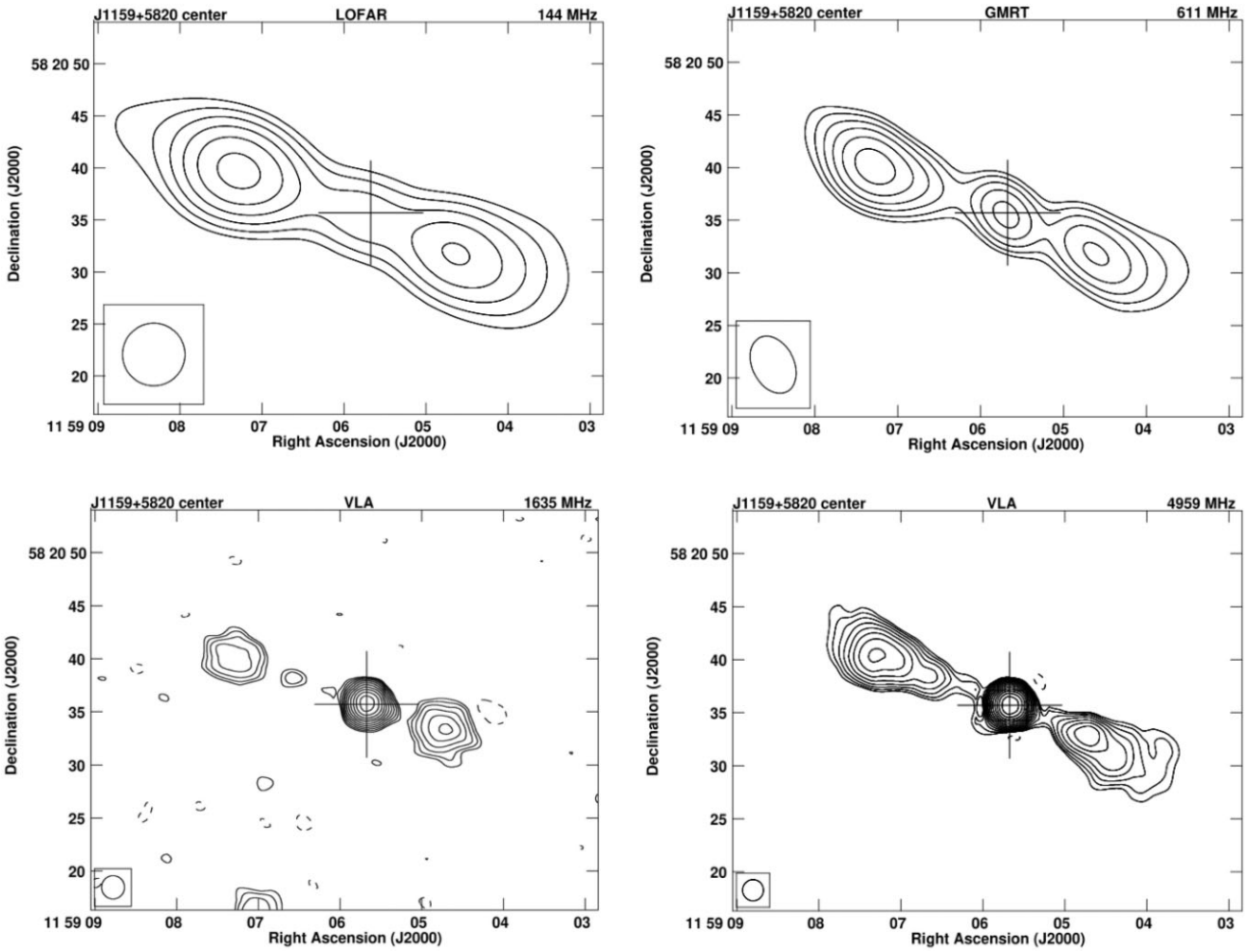

Figure 2. Contour maps of the central part of J1159+5820 (within the host galaxy), obtained from LOFAR, GMRT, and the VLA observations at 144, 611, 1635, and 4959 MHz (see also right panel of Fig. 1). The contour levels are spaced by a factor of $\sqrt{2}$ and the first contour is at 3 × rms level (rms values are given in Table 1). The first negative 3 × rms level is marked with a dashed contour. The relative sizes of the beam are indicated by the ellipse at the bottom left corner of each image. The position of the core is marked with a cross.

as well as to improve the signal-to-noise ratio of the faint extended emission.

2.3 Data extracted from surveys

Low-frequency surveys used in the multifrequency analysis of the source include LOw-Frequency ARray (LOFAR; van Haarlem et al. 2013), LBA Sky Survey (LoLSS; de Gasperin et al. 2021), and LOFAR Two-metre Sky Survey (LoTSS; Shimwell et al. 2022). LoLSS maps the entire northern sky in the frequency range 42–66 MHz, with a resolution of 15 arcsec at an average rms of 1 mJy beam^{-1}. LoTSS Data Release 2 is an ongoing sky survey ranging from 120 to 168 MHz with a 6 arcsec resolution and median rms sensitivity of 83 μJy beam^{-1} and a 20 arcsec resolution with a median rms sensitivity of 95 μJy beam^{-1}. The VLA surveys that were used for high-frequency analysis include Faint Images of the Radio Sky at Twenty centimeters (FIRST; Becker, White & Helfand 1995), NRAO VLA Sky Survey (NVSS; Condon et al. 1998), and the VLA Sky Survey (VLASS; Lacy et al. 2020). FIRST at 1.4 GHz has an rms of 0.15 mJy beam^{-1} with a resolution of 5 arcsec and covers regions of sky in the north and south galactic cap. The NVSS is a 1.4 GHz continuum survey covering the entire sky north of −40° declination with a resolution of 45 arcsec. The rms brightness fluctuations are about 0.45 mJy beam^{-1} in total power (Stokes I). VLASS is an all-sky survey above declination −40°. It operates within a range of 2–4 GHz with an angular resolution of 2.5 arcsec and sensitivity of 69 μJy beam^{-1}. In Table 2, we show the flux density values obtained from dedicated observations and surveys.

3 RESULTS

3.1 Radio morphology

In the large-scale emission seen in the low-frequency maps presented in Figs 1 and 3, J1159+5820 displays a pair of well-defined axially symmetric lobes labelled as eastern primary lobe (EPL) and western primary lobe (WPL), accompanied by two extended and diffuse wings, labelled as north western wing (NWW) and south eastern wing (SEW; marked in Fig. 1). The LOFAR 20 arcsec × 20 arcsec resolution map overlaid on the LOFAR 6 arcsec × 6 arcsec contour map at 144 MHz, given in Fig. 3 (upper left panel), shows the extent of the diffuse SEW elongated much further in the

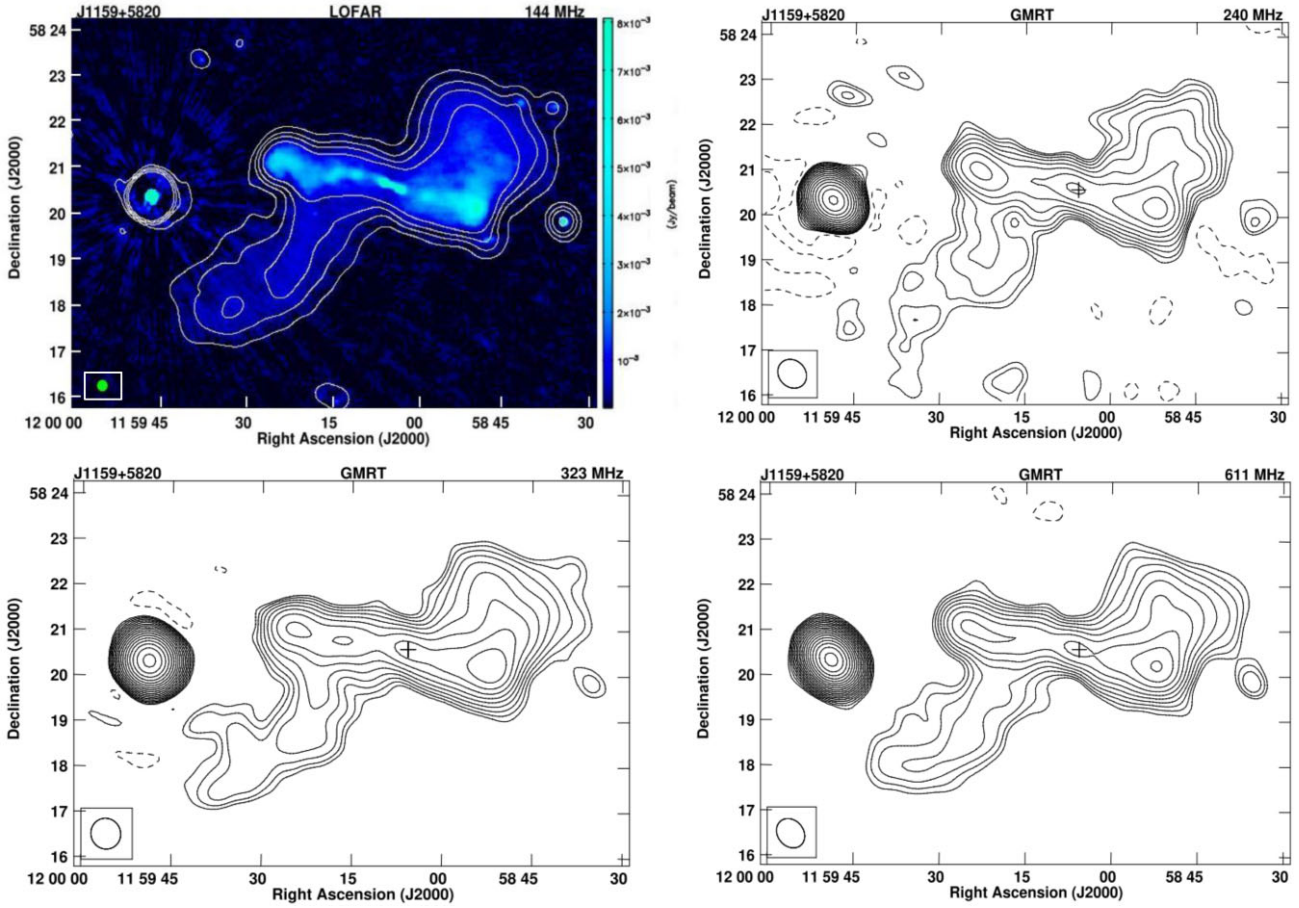

Figure 3. Low-frequency maps of J1159+5820 obtained from LOFAR and GMRT observations at 144, 240, 323, and 611 MHz. The contour levels are spaced by a factor of $\sqrt{2}$ and the first contour is at 3 × rms level (rms values given in Table 1). The first negative 3 × rms level is marked as a dashed contour. The relative sizes of the beam are indicated by the ellipse at the bottom left corner of each image. The position of the core is marked with a cross. The top left corner map is LOFAR 144 MHz 6 arcsec high-resolution map (given in blue) overlaid with LOFAR 20 arcsec low-resolution contours. The bright source in the background is an independent compact steep-spectrum (CSS) source.

Table 2. Flux densities of different components of J1159+5820.

Frequency (MHz) (1)	Core (mJy) (2)	Inner eastern lobe (mJy) (3)	Inner western lobe (mJy) (4)	Eastern primary lobe (mJy) (5)	Western primary lobe (mJy) (6)	Total structure (mJy) (7)	References (8)
54						3530 ± 700	I
144	2.6 ± 0.2	45.8 ± 2.3	40.3 ± 2.0	404 ± 65	556 ± 94	1660 ± 95	II
147						1677 ± 294	This paper
240				258 ± 48	338 ± 73	1264 ± 223[b]	This paper
323	5.2 ± 0.7	28.8 ± 2.9[a]	42.6 ± 4.5[a]	276 ± 49	375 ± 71	1220 ± 197[b]	This paper
611	4.8 ± 0.4	15.6 ± 1.3[a]	13.2 ± 1.1[a]	168 ± 30	225 ± 45	798 ± 98[b]	This paper
1400	1.8 ± 0.2	3.9 ± 0.5	1.8 ± 0.4			338 ± 57[c]	III, IV
1570				84 ± 14	139 ± 25		This paper
1635	4.1 ± 0.2	1.3 ± 0.4	1.6 ± 0.5				This paper
3000	5.6 ± 0.5	7.1 ± 1.5	6.3 ± 1.2				V
4959	7.3 ± 0.4	3.2 ± 0.8	2.4 ± 0.6	51 ± 9[d]	65 ± 13[d]	166 ± 17[d]	This paper
8440	9.2 ± 0.6						VI

Note. References* (I) de Gasperin et al. (2021); (II) Shimwell et al. (2022); (III) Becker et al. (1995); (IV) Condon et al. (1998); (V) Lacy et al. (2020); (VI) Healey et al. (2007) [a] flux of inner lobes with shorter baselines flagged to get the compact emission. [b] flux of total structure with longer baselines flagged to obtain extended emission. [c] total flux taken from NVSS. [d] values from C band C and D configuration.

south-eastern direction with the high-resolution map clearly showing jet bending in the EPL, unseen before. The WPL displays a hotspot-like feature around RA = $11^{h}58^{m}50\overset{s}{.}6$, Dec. = $+58^{\circ}20'04''$ (J2000.0), with a spectral index (SI) value of about 0.5, which is typical for a hotspot. In the GMRT 610 MHz and high-frequency VLA maps in Fig. 2, the central structure is clearly resolved. The core, along with the inner lobes, prominently show an FRII-type mini-double. Thus, the target source exhibits a double–double morphology. J1159+5820

is also close to a bright compact steep spectrum (CSS) source, which is discussed in detail in Section 3.5.

J1159+5820 resembles an FRII-type winged RG; however, the radio power of the primary lobes, $P_{1400\mathrm{MHz}} \simeq 2 \times 10^{24}\mathrm{W\,Hz^{-1}}$, places the source at the FRI/FRII transition boundary. The primary lobes are symmetric with respect to the radio core and the source displays an almost X-symmetric structure with the two low surface brightness wings emerging outwards from the high surface brightness lobes with the estimated inclination of the structure of $\sim 80^{\circ}$. This structure shares a strong similarity to the source NGC 507 (Murgia et al. 2011; Brienza et al. 2022). WISEA J130225+514911 is another source found in the LoTSS DR2 survey that also demonstrates morphological resemblance to our target source but at a much larger distance of $z_{\mathrm{phot}} = 0.9$. The host galaxy is seen face-on and its centre coincides with the radio core. This makes the linear size of the source from the EPL to WPL of ∼330 kpc and of the inner pair of lobes ∼30 kpc. The formation of distinct outer and inner lobes traced at least two different epochs of the jet cycle, with the outer lobes being formed at a different cycle of jet activity than the inner pair, hinting at recent changes in the level of nuclear activity of the source.

3.2 Spectral index analysis

The profile of radio spectra conveys important information regarding the evolution of plasma in the source. A steep spectrum hints at old plasma that is devoid of fresh energetic electrons, unlike a flatter spectrum where fresh particles might still be injected. In radio lobes, synchrotron and inverse-Compton losses cause steepening of the spectra over time, with more energetic electrons losing energy faster than the less energetic ones. In this case, the SI provides crucial information about the past activity of a radio source. The SI map of J1159+5820 was obtained using the LOFAR 144 MHz and the VLA 4959 MHz map. The VLA map was first tapered to a resolution similar to the LOFAR 144 MHz map and was then convolved to 20 arcsec × 20 arcsec , that is, the resolution of the original LOFAR map. AIPS task HGEOM and COMB were used, respectively, to align the geometry of both of the maps and to finally produce the SI map as shown in Fig. 4. All the other pre-described GMRT and VLA maps were similarly transformed before using them for further spectral analyses of the different regions of J1159+5820. The SI map ($S_\nu \propto \nu^{-\alpha}$) reveals a relatively flat core and steep spectra wings. The spectrum in the lobes is quite different from that of the wings, with the north-western wing showing a strong gradient going from steeper to flatter spectra along a clockwise direction. This shows the concentration of energetic electrons in the WPL, in comparison to the wings. In the SEW, the spectra are steep, but with much less gradient, indicating the presence of old and low energetic electrons. The EPL shows relatively flat spectra, similar to WPL, although it flattens further out than EPL. There is a small region of flat spectra around the edges of the EPL and WPL, which might be a result of an image artefact. The steeper spectra next to the inner lobes are caused by the backward-flowing lobe plasma, where aged plasma accumulates. The SEW looks narrower than the counter NWW, as the former is much weaker and has a relatively lower surface brightness. The strong gradient of the flux density contours in the EPL, as seen in Fig. 4, could also be a hint of missing flux in the region between the EPL and the bright background source. Nevertheless, the lack of significant steepening of the SI throughout the edges of the source confirms that no large-scale emission was lost in the high-frequency VLA observations.

To acutely understand the movement of plasma across the wings, they were further divided into four separate regions based on the same/similar SI values (W1–W4; Fig. 4). As the gradient shows a trend in relative plasma ages, it will help to estimate when particles were last accelerated in these regions. It is also evident that the total flux of the primary lobes is mostly affected by the brightest compact nodes of the flat-spectrum emission, and as such is not representative of the true lobe age. To estimate the ages of the primary lobes it would be much proper to measure the spectral age with the particle injection model fitted to the inner edge of the primary lobes (IEPL) and to the EPL and WPL. The spectral age of the EPL/WPL will give the mean age of the lobes, whereas the spectral age of the IEPL will constitute the oldest plasma from primary lobes and should give the true age of the lobes. However, since the IEPL might include contamination from the old plasma from the wings, it could return an age comparatively older than the true age of the primary lobes. Therefore, ages estimated from IEPL and EPL/WPL will be more likely the upper and lower constraints for the ages of the primary lobes. Further analyses are presented in more detail in the next sections.

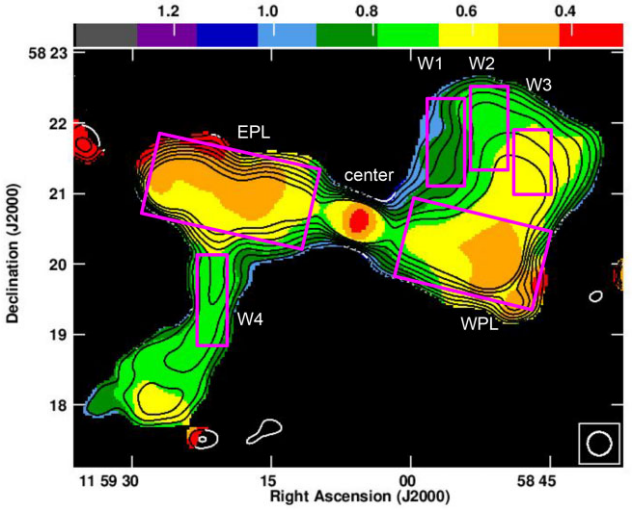

Figure 4. The SI map between 144 and 4959 MHz. The VLA 4959 MHz contours are spaced by a factor of $\sqrt{2}$ with the first contour starting at 3 × rms level. The size of the beam is indicated by a circle in the bottom right corner of the image. Four different regions in the wings (W1-W4), as well as the regions of the primary lobes (WPL and EPL) are marked with magenta rectangles. The centre region includes both the core and the inner lobes. In further sections, these regions are used to perform multifrequency ageing analysis.

The flux densities of all components of the source are listed (Table 2 and Table 4) and have been used to model the individual components comprising the pair of inner lobes, the core, the primary lobes, and different sections of the wings. The resulting spectra fitted using different particle injection models to the primary lobes and wings, and absorption models to the core are displayed in Figs 5–7.

3.3 Radio core

The core spectrum is plotted from 144 to 8440 MHz in Fig. 5, using the flux density values given in Table 2. The spectrum steeply rises from 144 MHz and then falls rapidly by 1400 MHz; it then rises steadily again around 1635 MHz and continues to rise till 8440 MHz. The first low-frequency turnover, below 500 MHz, implies a low-frequency absorption. Such low-frequency absorption is also seen in the case of CSS sources. The turnover frequency observed is closely associated with the absorption of synchrotron radiation in the source,

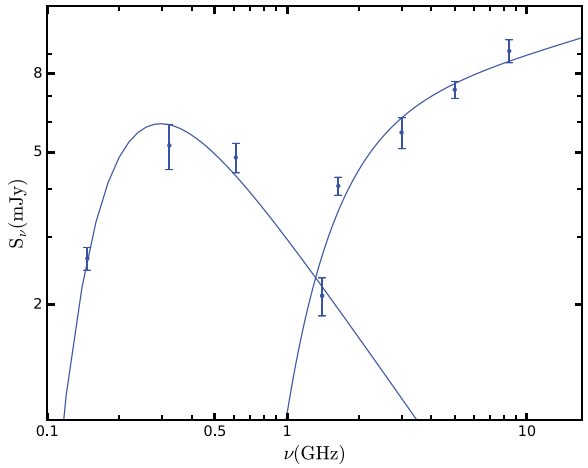

Figure 5. Radio spectra of the core with the double homogeneous FFA model fit as discussed in Section 3.3.

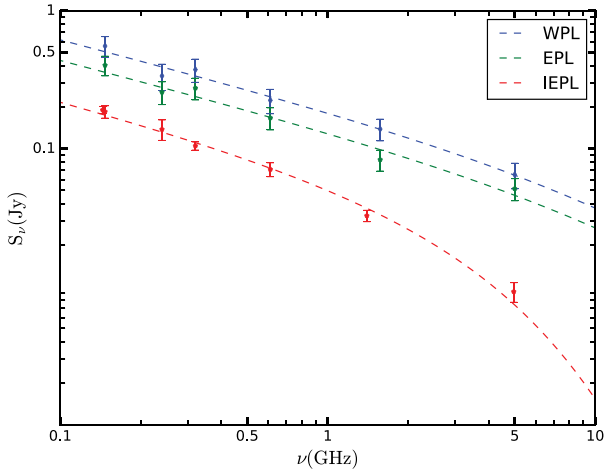

Figure 6. Radio spectra of the eastern and western primary lobes (EPL; WPL) fitted with the CI model and the IEPL fitted with the JP model.

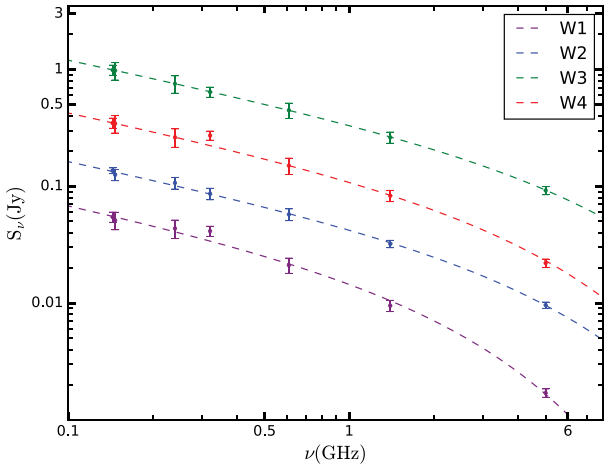

Figure 7. Radio spectra of regions W1, W2, W3, and W4 (marked in Fig. 3) fitted with the JP model. The spectra of particular regions are arbitrarily shifted in the ordinate axis to give the appropriate picture of the curvature of the spectra.

Table 3. Model fit parameters for the core with double homogeneous FFA model.

Frequency range (GHz) (1)	a (2)	ν_t (GHz) (3)	α (4)	χ^2_{red} (5)
0.14–1.4	3.06 ± 0.22	0.198 ± 0.01	0.89 ± 0.13	0.87
1.4–8.4	5.98 ± 1.47	1.305 ± 0.17	-0.18 ± 0.14	4.91

which is either in the form of synchrotron self-absorption (SSA) or free–free absorption (FFA) (Kellermann 1966). To understand this mechanism we tested the SSA and FFA models to describe the core spectra similar to Callingham et al. (2015). All models gave a similar fit including the homogeneous FFA model which provided the least χ^2_{red} value. This particular model describes an external homogeneous ionized screen around a synchrotron-emitting plasma that attenuates the radiation. The absorbing medium can be described by

$$S_\nu = a\nu^{-\alpha} e^{-\tau_\nu}, \quad (1)$$

where a and α are the amplitude and SI of the synchrotron spectrum and τ_ν is the optical depth. The optical depth is given by $\tau_\nu = (\frac{\nu}{\nu_t})^{-2.1}$, where ν_t is the turnover frequency at which the optical depth is equal to 1. A single model fit to the spectrum was not possible, hence two separate homogeneous FFA models were fit, the first one starting from 144 to 1400 MHz and the second fit starting from 1400 to 8440 MHz. This led to two independent model fits for the core spectra as given in Fig. 5. The fitting parameters are given in Table 3. The values of the turnover frequency and SI in the second model fit are similar to the ones obtained by Ledlow et al. (2001) in their study of the core spectrum of the radio source B0313-192, which is also associated with a disc galaxy.

According to O'Dea (1998), the turnover frequency and the projected linear size of the radio source can give crucial information regarding the source's linear evolution. This correlation is given by

$$log(\nu_t) = -0.21(\pm 0.05) - 0.65(\pm 0.05) log(l), \quad (2)$$

where l is the linear size of the source in kpc and ν_t is the turnover frequency in GHz. Making use of two different turnover frequencies from the model fit, we estimate two different linear sizes, ∼5 kpc corresponding to the first turnover at 0.2 GHz and ∼320 pc corresponding to the second turnover at 1.3 GHz. The electron density in these regions was calculated using the emission measure for FFA (O'Dea 1998) as follows:

$$(n_e)^2 l \simeq 3.05 \times 10^6 \tau \left(\frac{T}{10^4 K}\right)^{1.35} \left(\frac{\nu}{1 GHz}\right)^{2.1} cm^{-6} pc, \quad (3)$$

where n_e is the electron density, τ is the optical depth at frequency ν in GHz, and T is the temperature in K. Using the two different turnover frequency values, we arrive at two different electron density values, that is, for the turnover at 0.2 GHz, n_e is ∼5 cm^{-3} and for the turnover corresponding to 1.3 GHz, n_e is ∼126 cm^{-3}. The two different electron density values most likely correspond to different regions of the central nuclear region through which the radiation is absorbed as it passes. It initially passes through the denser inner parsec-scale region of ∼320 pc with a higher electron density of about 126 cm^{-3}, which is comparable to the value of ∼200 cm^{-3} that Emonts et al. (2005) obtained from the central kpc region of 3C 293, before entering a less opaque region of the ISM at around 5 kpc, where n_e drops to about 5 cm^{-3}.

Table 4. Flux densities of wing regions and the inner edge of primary lobes.

Frequency (MHz) (1)	W1 (mJy) (2)	W2 (mJy) (3)	W3 (mJy) (4)	W4 (mJy) (5)	IEPL (mJy) (6)
144	54.5 ± 4.3	135.9 ± 7.6	107.4 ± 6.3	79.2 ± 7.9	191.5 ± 11.5
147	51.1 ± 7.6	125.4 ± 13.7	89.1 ± 10.5	57.4 ± 9.8	186.2 ± 19.0
240	43.5 ± 7.2	106.8 ± 12.1	74.8 ± 9.4	68.6 ± 12.3	138.6 ± 23.4
323	41.3 ± 7.2	86.3 ± 9.7	64.5 ± 7.8	68.7 ± 7.5	105.2 ± 7.1
611	21.1 ± 3.1	57.4 ± 6.2	46.7 ± 5.2	33.2 ± 5.3	71.1 ± 8.2
1400	9.5 ± 1.7	32.1 ± 2.3	23.1 ± 2.0	17.4 ± 2.0	32.8 ± 3.1
4959	1.7 ± 0.3	9.6 ± 0.6	9.5 ± 0.6	5.2 ± 0.4	9.2 ± 1.5

Table 5. Break frequency values for the primary lobes and wing regions.

Lobe/Region (1)	Model (2)	Break frequency (ν_{br} in GHz) (3)	χ^2_{red} (4)
EPL	CI	$8.4^{+>100}_{-5.9}$	0.65
WPL	CI	$8.1^{+>100}_{-6.9}$	0.30
IEPL	JP	$4.8^{+>100}_{-0.7}$	1.16
W1	JP	$3.8^{+1.9}_{-0.8}$	0.45
W2	JP	$8.5^{+6.5}_{-1.7}$	0.14
W3	JP	$13.2^{+>100}_{-2.2}$	1.11
W4	JP	$7.7^{+6.5}_{-2.7}$	2.31

3.4 Lobes and wings

3.4.1 Source energetics

The spectrum of J1159+5820 was fitted with the Jaffe & Perola (JP; Jaffe & Perola 1973) and continuous injection (CI; Pacholczyk 1970) models for calculating the radiative losses that compute time evolution using the initial power-law energy distribution. This is performed using the emission spectrum of particles specified by their injection SI (α_{inj}) distributed isotropically in pitch angle relative to the direction of the magnetic field. In the case of both the primary lobes, the CI model provided the best fit to the data with minimum χ^2_{red} values. The NWW was divided into three different regions based on the spectral gradient using the SI map (see Fig. 4) and the SEW was made into a single vertical region due to a lack of clear gradient across the lobe. All the regions of the northern wing and the southern wing were best fit with the JP model, possibly due to the lack of any compact hotspots along with the presence of steep spectra in the wings. The same is the case of the IEPL region. The SYNAGE package (Murgia 1996) was used to fit the CI and JP models to the radio spectra. The best-fitting models are given in Figs 6 and 7 and the fit parameters are given in Table 5. With the application of the JP and CI model, the following assumptions were made: (i) the particles follow a constant power-law energy distribution without any re-acceleration of radiating particles after entering the lobes, (ii) the magnetic field lines are intertwined and the field strength is constant throughout the energy-loss process, and (iii) the time of isotropization is short compared to the radiative lifetime for the pitch angles for the injected particles. We address that the assumptions made here are an idealization of the physical processes that are actually taking place in the lobes, for instance, the supposition of a constant magnetic field. However, since the dominant loss mechanism in these regions is inverse-Compton, therefore it is reasonable to assume a constant magnetic field here.

3.4.2 Primary lobes and wings

The break frequency values obtained for the EPL and WPL are given in Table 5, for a fixed value of $\alpha_{inj} = 0.5$. Since from the pre-fitting results α_{inj} was close to 0.5, the α_{inj} therefore was fixed at that particular value. The ν_{br} values for both primary lobes obtained via the CI model give comparable results with ν_{br} lying slightly above the highest radio frequency data presented in the paper. As visible in Fig. 4, the close vicinity of the central region, IEPL, is characterized by a steeper spectrum than the rest of the primary lobes, and its emission is best fitted with the JP model (see Fig. 6). The JP model fit for the wing regions W1, W2, W3, and W4 is given in Table 5. The spectra of the primary lobes, as given in Fig. 6, appear flatter than the steep spectra wings, given in Fig. 7, implying the absence of recent particle injection processes in the wings. In the regions W1, W2, and W3, we see a clear gradient in the break frequency values. which seems consistent with the SI map. This shows that the oldest plasma is in region W1 followed by regions W2 and W3. This directs the movement of the flow of plasma and the jet in the clockwise direction in the NWW.

We estimate the magnetic field strength and synchrotron age for the primary lobes, IEPL, and the regions W1, W2, W3, and W4 of the wings. The spectral age is calculated using the following formula:

$$\tau_{rad} = 50.3 \frac{B_{eq}^{0.5}}{B_{eq}^2 + B_{CMB}^2} (\nu_{br}(1+z))^{-0.5} \mathrm{Myr} \quad (4)$$

$B_{CMB} = 0.318(1+z)^2$ is the magnetic field strength analogous to the cosmic microwave background (CMB) radiation at the redshift of the target. Here B, the magnetic field strength of the lobes, and B_{CMB} are expressed in units of nT, ν_{br} the spectral break frequency in GHz above which the radio spectrum steepens from the initial power-law spectrum is given by $\alpha_{inj} = (\gamma - 1)/2$. The magnetic field was calculated using the minimum energy arguments following Longair (2011). The magnetic field strength can be directly estimated when a radio source is detected at radio and X-ray frequencies simultaneously. X-ray emission in the lobes of RGs most likely originate from inverse-Compton scattering between the same relativistic electrons that produce the observed radio synchrotron radiation, and the CMB (Harris & Grindlay 1979). For the calculation of magnetic field, with the lack of adequate X-ray observations, using the equipartition assumption is the most general practice. However, it is also often found that in the lobes of active FRII sources, the magnetic field is generally within a factor of a few (2–3) lower than those implied by equipartition (e.g. Hardcastle et al. 2002; Croston et al. 2005; Kataoka & Stawarz 2005; Migliori et al. 2007; Ineson et al. 2017; Turner, Shabala & Krause 2018). For inactive (outer) lobes of double–double radio galaxies that were analysed by Konar et al. (2019), it was found that their magnetic field values were

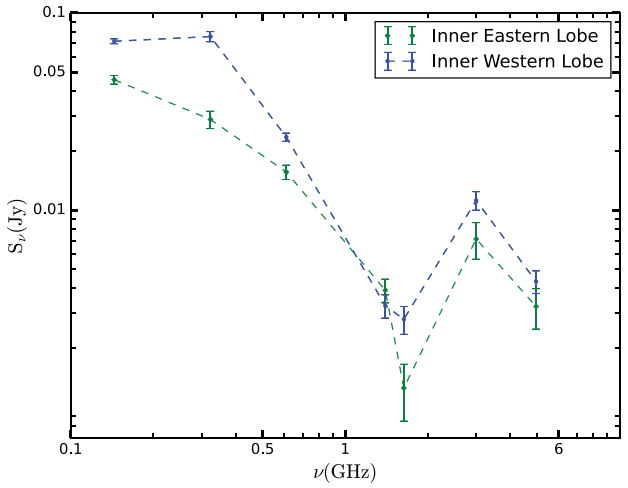

Figure 8. Radio spectra of the inner lobes. The spectrum of the inner western lobe is shifted arbitrarily in the ordinate axis to give the appropriate picture of the spectra.

close to the ones obtained by equipartition. In addition, Parma et al. (1999) showed (see their fig. 4) how the radiative lifetime depends on the ratio of magnetic field $B/B_{\rm eq}$. They proved that for $0.5 < B_{\rm eq}/B_{\rm CMB} < 2$, deviations from equipartition have a small effect on the computed lifetime if $B \leq 2\,B_{\rm eq}$. Furthermore, in the case of our target, inverse-Compton losses to the CMB seem to dominate over synchrotron losses. Therefore, the equipartition assumption to calculate the magnetic field is reasonable for the analysis that we conducted. Our assumptions included the cut-off frequencies of $\nu_{\rm min}$ = 10 MHz and $\nu_{\rm max}$ = 100 GHz, the filling factor of 1, and the pure electron–positron plasma. The volume of the lobes and different regions of the wings was estimated using a cylindrical shape. This led to the magnetic field strength values for the eastern and western primary lobe as B = 0.10 ± 0.01 nT and B = 0.11 ± 0.01 nT, respectively. The spectral ages of the EPL and WPL are calculated as 39.4 and 41.7 Myr, respectively. For IEPL, B = 0.14 ± 0.01 nT and the spectral age is 58.2 Myr.

For the NWW regions W1, W2, and W3, B = 0.11 ± 0.01, 0.17 ± 0.01, 0.16 ± 0.01 nT, respectively; for the SEW region W4, B = 0.14 ± 0.01 nT. Taking into account the break frequencies calculated by the model and the magnetic field strength estimated above from a cylindrical geometry, the spectral ages of NWW are 61.8, 45.1, and 36.0 Myr for regions W1, W2, and W3, respectively; for SEW region W4 it is 45.6 Myr. This shows that the oldest plasma is in the region W1, followed by W2 and W3. The ages of W2 and W4 are similar, which is in accordance with the SI map in Fig. 3. The decreasing gradient in the SI map and the spectral ages of different wing regions in the NWW confirm the clockwise movement of plasma. The mean spectral age of the primary lobes is ∼40 Myr; however, the actual age of these lobes considering the oldest plasma from IEPL is ∼60 Myr (as detailed in Section 3.2).

3.4.3 Inner lobes

The flux density of the inner lobes is plotted in Fig. 8. The spectrum shows a convex pattern with an unusual bump at 3000 MHz and a slight resemblance to some GPS sources described in Callingham et al. (2017). Upon fitting, the CI and JP models for the data from 144 to 4959 MHz, to the inner lobes, the break frequency values obtained from the fit were unreasonable, giving spectral ages much older than the steep spectra wings. This discrepancy could arise due to strong absorption in the ISM as the inner lobes expand through them. Therefore, we could not provide accurate spectral ages of the inner lobes. However, for dynamical age, considering a lobe expansion speed of 0.2c (Murgia 2003), we estimate the inner lobes should not be younger than ∼0.2 Myr.

Table 6. Flux density values for the CSS source.

Frequency (MHz)	147	240	323	611	1400	3000	4959
Flux density (Jy)	0.74	1.72	2.04	1.74	1.14	0.58	0.37
Error (Jy)	±0.06	±0.17	±0.16	±0.14	±0.06	±0.03	±0.02

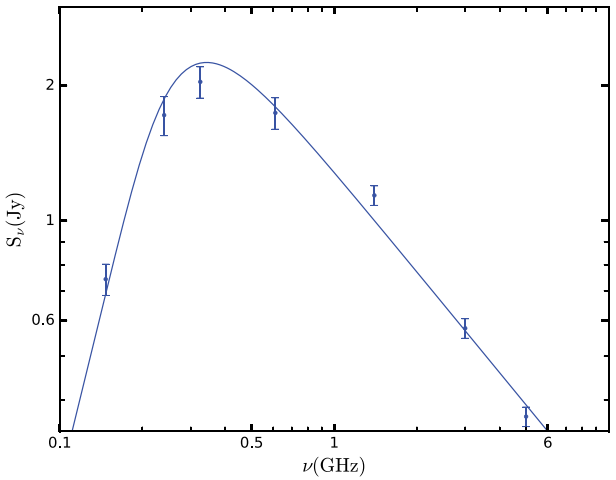

Figure 9. Radio spectrum of the CSS source next to J1159+5820 modelled using SSA.

3.5 Background CSS source

The CSS source located at RA = $11^{\rm h}59^{\rm m}48\overset{\rm s}{.}7$, Dec. = $+58^\circ20'20''$(J2000.0), next to the EPL of the target source is at a redshift of $z = 1.27$ (Tremblay et al. 2016). The measured flux density values at different frequencies are given in Table 6. Its radio spectrum fitted with the SSA model is given in Fig. 9. Also, to check for any discrepancies with the flux density values of the maps, we fitted the CSS source next to the target with the SSA model which returned a reasonable fit with a turnover frequency of ∼270 MHz as given in Fig. 9.

4 DISCUSSION

To give an account of the extended radio morphology of J1159+5820, we proceed by discussing some possible scenarios:

4.1 Hydrodynamic backflow

The radio jets from luminous RGs usually evolve to become inversion symmetric about their host galaxies. In some cases however, the backward-flowing plasma from the primary lobes interacts with the ISM of the host galaxy and starts expanding laterally. When there is a misaligned hot gas halo around the host galaxy, it can bend the backward-flowing plasma in opposite directions creating secondary wings (Leahy & Williams 1984; Cotton et al. 2020). These wings

are therefore a result of a single AGN outburst, with the backward-flowing plasma from the jets being diverted along the direction of the steepest pressure gradient of the surrounding medium. However, if this is the case for our target source, it will be difficult to explain wings that are larger than the primary lobes. This is due to the fact that energetic jets are usually expected to drive through the surrounding medium supersonically, and wings will have to expand completely under buoyancy, which is usually subsonic. The SI map also shows a gradation in the distribution of plasma in the wings (especially in the NWW), instead of a perfectly steep spectra expected from a backward-flowing cocoon, due to quasi-simultaneous evolution. The SEW is very extended in the low-frequency maps; however, in the high-frequency VLA map (see Fig. 3), no such emission is found implying a much steeper emission. In the *Chandra* X-ray studies conducted by Balasubramaniam et al. (2020), the presence of an X-ray halo around the host was not observed, but this could result from a limited sensitivity of *Chandra* to large-scale diffuse emission.

4.2 Spin flip of SMBH

Galaxy mergers most likely take place in galaxy groups and clusters. CGCG 292-057 does not reside in such an environment, but upon closer inspection approximately seven galaxies were found within a radius of around 1 Mpc with similar redshift. Although the number of galaxies within a megaparsec distance to our host is few, this nevertheless does not rule out the possibility that there might be other galaxies at a similar redshift not discovered or catalogued by surveys. However, at an angular separation of 17.5 arcsec from CGCG 292–057, an edge-on galaxy MCG +10-17-123 at RA $= 12^{\rm h}00^{\rm m}04\overset{\rm s}{.}0$, Dec $= +58^{\circ}36'20''$ (J2000.0) with $z = 0.0541$, obscured by an S-shaped dust lane is located. This disturbed galaxy has a comparable projected angular size, brightness, and redshift to our target galaxy. To explore further the possibility of whether these two galaxies might have interacted via a close flyby event in the past, we considered a typical velocity of 250 km s^{-1} (Bean et al. 1983) for each galaxy and a distance of 500 kpc (assuming the flyby might have occurred mid-way to the current distance separating them). The time to reach the current separation was calculated as $\sim$2 Gyr.

The binary SMBHs formed through galaxy mergers mostly coalesce following a regime of slow approach as a result of dynamical friction and gravitational radiation. As discussed by Merritt & Ekers (2002), galaxy mergers can lead to a dramatic change in the SMBH spin axis direction, subsequently leading to a sudden flip in the direction of the associated jet, post-merger of the system. This mechanism will lead to a distinct X-shaped morphology, e.g. J1513+2607 (Springmann & Cheung 2006). The two pairs of jets here would be formed from two different episodes of nuclear activity, with the new lobes formed before the older lobes disappear. To produce such a pronounced X-shaped morphology would require a large spin-flip angle, which would lead to the creation of active primary lobes post-spin flip of SMBH. However, in the case of J1159+5820, we do not see two prominent pairs of lobes passing symmetrically through the core of the associated galaxy; instead, they appear to be emerging rather radially from the primary lobes.

4.3 Independent jets from dual AGN

Furthermore, as first proposed by Lal & Rao (2005), there might exist a class of binary co-orbiting SMBHs with independent jets undergoing a merger, e.g. 3C 75 (Merritt & Milosavljević 2005), which due to poor resolution or orientation effects appear to generate an X-shaped morphology. From the optical maps of CGCG 292–057, we cannot resolve a second nuclear core, and neither in the radio maps and/or X-ray maps there is a distinct dual radio core. This either hints that the binary SMBH pair have merged or has fallen below kpc scale separation. A third possibility could be that the secondary SMBH is not active at the present time of observation. All of these scenarios are difficult to be explored currently in the confines of this paper.

4.4 Jet precession

As discussed in Begelman, Blandford & Rees (1980), a natural way for a black hole to undergo precession at a significant rate is while orbiting in a binary system. As mentioned by Kaastra & Roos (1992), the apparent shape of any jet generated by the black holes will be modified by the binary's orbital motion, which can motivate the helical motion of jets or precession. These wiggles in jets are observed in the quasar 1928+738 and are successfully modelled by Roos, Kaastra & Hummel (1993). In 3C 273, Romero et al. (2000) showed that the precession of the inner jets results from tidal perturbation of the accretion disc produced by the non-coplanar orbit of the secondary black hole. The exact morphology according to Merritt & Ekers (2002) however would depend on the time-scale of jet axis reorientation. A slow realignment would lead to an FRI source with S-shaped morphology, with rapid realignment producing an intermediate-luminosity X-shaped source, with radio power near the FRI/FRII break. Relatively slowly precessing jets can also lead to an X-shaped morphology in projection, as shown by hydrodynamical simulations performed by Horton, Krause & Hardcastle (2020).

In the optical study conducted by Kozieł-Wierzbowska et al. (2012), the SDSS nuclear spectrum revealed a doubly peaked profile, which hints at two possibilities: it could be either due to narrow line region (NLR) kinematics or as a result of an SMBH binary. The NLR can be both associated with AGN outflows and galaxy mergers (Comerford et al. 2018). The lack of an optically detectable companion galaxy here can imply that we are observing the post-merger stage where the black hole separation has shrunk below the kpc scale. There still remains the possibility of the jet precession being induced by a tilted accretion disc, as suggested by Lu (1990). As elaborated by Pringle (1997), the accretion disc can become wrapped due to non-uniform irradiation from AGN, causing instabilities of the accretion disc and leading to precession. But a wrapped accretion disc cannot explain the NLR kinematics. But since we cannot resolve two separate optical cores, it is hard to rule out one of the above precession models. In the LOFAR map given in Fig. 3 (upper left panel), one can clearly see the wiggles or waves in the eastern jet, which can hint at an underlying precession in progress.

4.5 Jet–shell interaction

In the jet–shell interaction model for the formation of X-shaped radio galaxies proposed by Gopal-Krishna et al. (2012), the radio morphology arises from the interaction of jets with gaseous shells in a merged galaxy system. According to the model, the merger between galaxies leads to the formation of a sequence of shells, and the wings are formed as a result of the interruption faced by the jets trying to pass through rotating shells. These temporary deflections can be triggered by a lighter jet colliding with a few times wider massive cloud. This model can well account for the observed Z-shaped wings, since also in the optical map (given in Fig. 1) there seems to be a shell-like structure associated with the host galaxy almost exactly along the direction of the north-western wing. There

might be a possibility that the shells are formed as the galaxy moves during the merger from an inclined position almost clockwise in the sky plane to its current face-on position, and thereby the jets coming from SMBH interact with the shells and undergo bending until the galaxy settles to its current orientation.

Among all the models discussed here, it might be possible that more than one phenomenon is at play behind the origin of the radio morphology. However, the model that most likely explains the relative spectral ages in the different regions of the wings and primary lobes is the precessing jet model. It is favoured by the decreasing gradient of the spectral ages in the different regions of the NWW, directing at a clockwise movement of plasma driven by a fast reorientation of the jets, and it is also further supported by the wiggles in the jet, distinctly visible in the EPL of the LOFAR 144 MHz map (see Fig. 3).

5 CONCLUSION

CGCG 292–057 is an exceptional source that demonstrates multiple stages of galaxy evolution at once. The evidence of a past merger, peculiar X-shaped morphology, and an AGN rebirth with a new pair of radio lobes makes it a great source for studying the evolution of galaxies.

To analyse the source properties, we conducted multifrequency observations using GMRT and the VLA. The conclusion we draw is that the most likely explanation for the X-shaped morphology is the jet reorientation following the orbital motion of a binary SMBH pair causing a rapid jet precession in the time-scale of a few million years.

(i) We have supplemented the flux density measurements from our observational data with a large number of radio sky surveys that helped us to build the spectra from 54 to 8440 MHz. Using the above, we modelled the lobes and different sections of the wings and were able to deduce the break frequency and conduct an ageing analysis.

(ii) The core was modelled using a double homogeneous FFA model as a single FFA could not fit the spectra. This is most likely caused due to the presence of two different ionizing screens around the synchrotron-emitting relativistic plasma, which could be due to the result of the past merger activity.

(iii) The inner pair of lobes produced unrealistic break frequency values with various particle injection models, ultimately giving much larger ages than the steep spectra wings. We reason that the strong absorption caused during the expansion of the inner pair of lobes inside the ISM of the host galaxy could cause such an unusual behaviour of the radio flux.

(iv) The spectral age of primary lobes was found to be between 40 and 58 Myr. We also found the ages of the different sections of the steep spectra wings to be 61.8, 45.1, and 36.0 Myr for regions W1, W2, and W3, respectively, and 45.6 Myr for region W4. This decreasing gradient of the spectral ages of the wing regions agrees well with that of the SI map.

The multiwavelength study of this one-of-kind post-merger double–double source with a peculiar morphology opens up a new window for thorough investigations of the origins of such class of radio galaxies. Future observations with ALMA will allow the detection of cool molecular gas and possible outflows in the galaxy, which can shed light on the unusual behaviour of the core and the inner lobes. This can subsequently lead to a better understanding of the effects of AGN feedback on the host galaxy and SMBH-galaxy coevolution.

ACKNOWLEDGEMENTS

The authors thank the anonymous Reviewer for her/his valuable comments and suggestions. We thank Subhrata Dey and Dorota Kozieł-Wierzbowska for their help. MJ acknowledges access to the SYNAGE software kindly provided by M. Murgia. We thank the GMRT staff for their assistance with observations. The GMRT is a national facility operated by the NCRA, TIFR. The National Radio Astronomy Observatory is a facility of the National Science Foundation operated under a cooperative agreement by Associated Universities Inc. This research work was partially supported by the National Science Center OPUS-15 grant, nr UMO-2018/29/B/ST9/01793. AM also acknowledges the Jagiellonian University grant N17/MNS/000055.

LOFAR data products were provided by the LOFAR Surveys Key Science project (LSKSP; https://lofar-surveys.org/) and were derived from observations with the International LOFAR Telescope (ILT). LOFAR (van Haarlem et al. 2013) is the LowFrequency Array designed and constructed by ASTRON. It has observing, data processing, and data storage facilities in several countries, which are owned by various parties (each with their own funding sources), and which are collectively operated by the ILT foundation under a joint scientific policy. The ILT resources have benefited from the following recent major funding sources: CNRS-INSU, Observatoire de Paris and Université d'Orléans, France; BMBF, MIWF-NRW, MPG, Germany; Science Foundation Ireland (SFI), Department of Business, Enterprise and Innovation (DBEI), Ireland; NWO, The Netherlands; The Science and Technology Facilities Council, UK; Ministry of Science and Higher Education, Poland; The Istituto Nazionale di Astrofisica (INAF), Italy.

This research used the Dutch national e-infrastructure with support of the SURF Cooperative (e-infra 180169) and the LOFAR e-infra group. The Jülich LOFAR Long Term Archive and the German LOFAR network are both coordinated and operated by the Jülich Supercomputing Centre (JSC), and computing resources on the supercomputer JUWELS at JSC were provided by the Gauss Centre for Supercomputing e.V. (grant CHTB00) through the John von Neumann Institute for Computing (NIC).

This research used the University of Hertfordshire high-performance computing facility and the LOFAR-UK computing facility located at the University of Hertfordshire and supported by STFC [ST/P000096/1], and of the Italian LOFAR IT computing infrastructure supported and operated by INAF, and by the Physics Department of Turin university (under an agreement with Consorzio Interuniversitario per la Fisica Spaziale) at the C3S Supercomputing Centre, Italy.

The National Radio Astronomy Observatory running the VLA is a facility of the National Science Foundation operated under a cooperative agreement by Associated Universities, Inc.

This research has used BASS DR3 images. BASS is a key project of the Telescope Access Program (TAP), which has been funded by the National Astronomical Observatories of China, the Chinese Academy of Sciences (the Strategic Priority Research Program 'The Emergence of Cosmological Structures' Grant No. XDB09000000), and the Special Fund for Astronomy from the Ministry of Finance. The BASS is also supported by the External Cooperation Program of Chinese Academy of Sciences (Grant No. 114A11KYSB20160057), and Chinese National Natural Science Foundation (Grant No. 12120101003, No. 11433005).

The Pan-STARRS1 Surveys (PS1) and the PS1 public science archive have been made possible through contributions by

the Institute for Astronomy, the University of Hawaii, the Pan-STARRS Project Office, the Max-Planck Society and its participating institutes, the Max Planck Institute for Astronomy, Heidelberg and the Max Planck Institute for Extraterrestrial Physics, Garching, The Johns Hopkins University, Durham University, the University of Edinburgh, the Queen's University Belfast, the Harvard-Smithsonian Center for Astrophysics, the Las Cumbres Observatory Global Telescope Network Incorporated, the National Central University of Taiwan, the Space Telescope Science Institute, the National Aeronautics and Space Administration under Grant No. NNX08AR22G issued through the Planetary Science Division of the NASA Science Mission Directorate, the National Science Foundation Grant No. AST-1238877, the University of Maryland, Eotvos Lorand University (ELTE), the Los Alamos National Laboratory, and the Gordon and Betty Moore Foundation.

DATA AVAILABILITY

The data underlying this paper will be shared on reasonable request to the corresponding author.

REFERENCES

Adelman-McCarthy J. K. et al., 2008, ApJS, 175, 297
Balasubramaniam K., Stawarz L., Marchenko V., Sobolewska M., Cheung C. C., Siemiginowska A., Thimmappa R., Kosmaczewski E., 2020, ApJ, 905, 148
Bean A. J., Ellis R. S., Shanks T., Efstathiou G., Peterson B. A., 1983, MNRAS, 205, 605
Becker R. H., White R. L., Helfand D. J., 1995, ApJ, 450, 559
Begelman M. C., Blandford R. D., Rees M. J., 1980, Nature, 287, 307
Bessiere P. S., Tadhunter C. N., Ramos Almeida C., Villar Martín M., 2012, MNRAS, 426, 276
Brienza M. et al., 2022, A&A, 661, A92
Browne I. W. A. et al., 2003, MNRAS, 341, 13
Callingham J. R. et al., 2015, ApJ, 809, 168
Callingham J. R. et al., 2017, ApJ, 836, 174
Capetti A., Zamfir S., Rossi P., Bodo G., Zanni C., Massaglia S., 2002, A&A, 394, 39
CASA Team et al., 2022, PASP, 134, 114501
Chambers K. C. et al., 2016, preprint (arXiv:1612.05560)
Cheung C. C., 2007, AJ, 133, 2097
Clark B. G., 1980, A&A, 89, 377
Comerford J. M., Nevin R., Stemo A., Müller-Sánchez F., Barrows R. S., Cooper M. C., Newman J. A., 2018, ApJ, 867, 66
Condon J. J., Cotton W. D., Greisen E. W., Yin Q. F., Perley R. A., Taylor G. B., Broderick J. J., 1998, AJ, 115, 1693
Cordey R. A., 1986, MNRAS, 219, 575
Cotini S., Ripamonti E., Caccianiga A., Colpi M., Della Ceca R., Mapelli M., Severgnini P., Segreto A., 2013, MNRAS, 431, 2661
Cotton W. D. et al., 2020, MNRAS, 495, 1271
Cotton W. D., 1999, in Taylor G. B., Carilli C. L., Perley R. A.eds, ASP Conf. Ser. Vol. 180, Active Galaxies. Synthesis Imaging in Radio Astronomy II. Astron. Soc. Pac., San Francisco, p. 357
Croston J. H., Hardcastle M. J., Harris D. E., Belsole E., Birkinshaw M., Worrall D. M., 2005, ApJ, 626, 733
de Gasperin F. et al., 2021, A&A, 648, A104
Dennett-Thorpe J., Scheuer P. A. G., Laing R. A., Bridle A. H., Pooley G. G., Reich W., 2002, MNRAS, 330, 609
Ekers R. D., Fanti R., Lari C., Parma P., 1978, Nature, 276, 588
Ellison S. L., Viswanathan A., Patton D. R., Bottrell C., McConnachie A. W., Gwyn S., Cuillandre J.-C., 2019, MNRAS, 487, 2491
Emonts B. H. C., Morganti R., Tadhunter C. N., Oosterloo T. A., Holt J., van der Hulst J. M., 2005, MNRAS, 362, 931
Evans D. A. et al., 2008, ApJ, 675, 1057
Fanaroff B. L., Riley J. M., 1974, MNRAS, 167, 31P
Florido E., Battaner E., Sanchez-Saavedra M. L., 1990, Ap&SS, 164, 131
Gopal-Krishna, Biermann P. L., Gergely L. Á., Wiita P. J., 2012, Res. Astron. Astrophys., 12, 127
Greisen E. W., 2003, in Heck A.ed., Astrophysics and Space Science Library, Vol. 285, Information Handling in Astronomy – Historical Vistas. Springer-Verlag, Berlin, p. 109
Hardcastle M. J., Birkinshaw M., Cameron R. A., Harris D. E., Looney L. W., Worrall D. M., 2002, ApJ, 581, 948
Harris D. E., Grindlay J. E., 1979, MNRAS, 188, 25
Healey S. E., Romani R. W., Taylor G. B., Sadler E. M., Ricci R., Murphy T., Ulvestad J. S., Winn J. N., 2007, ApJS, 171, 61
Högbom J. A., 1974, A&AS, 15, 417
Horton M. A., Krause M. G. H., Hardcastle M. J., 2020, MNRAS, 499, 5765
Hurley-Walker N. et al., 2015, MNRAS, 447, 2468
Ineson J., Croston J. H., Hardcastle M. J., Mingo B., 2017, MNRAS, 467, 1586
Intema H. T., 2014, Astrophysics Source Code Library, record ascl:1408.006
Intema H. T., van der Tol S., Cotton W. D., Cohen A. S., van Bemmel I. M., Röttgering H. J. A., 2009, A&A, 501, 1185
Jaffe W. J., Perola G. C., 1973, A&A, 26, 423
Kaastra J. S., Roos N., 1992, A&A, 254, 96
Kataoka J., Stawarz Ł., 2005, ApJ, 622, 797
Kellermann K. I., 1966, Aust. J. Phys., 19, 195
Konar C., Hardcastle M. J., Croston J. H., Jamrozy M., Hota A., Das T. K., 2019, MNRAS, 486, 3975
Kozieł-Wierzbowska D., Jamrozy M., Zola S., Stachowski G., Kuźmicz A., 2012, MNRAS, 422, 1546
Kuźmicz A., Jamrozy M., Kozieł-Wierzbowska D., Weżgowiec M., 2017, MNRAS, 471, 3806
Lacy M. et al., 2020, PASP, 132, 035001
Lal D. V., Rao A. P., 2005, MNRAS, 356, 232
Leahy J. P., Parma P., 1992, in Roland J., Sol H., Pelletier G.eds, Extragalactic Radio Sources. From Beams to Jets. Cambridge University Press, New York. p. 307
Leahy J. P., Williams A. G., 1984, MNRAS, 210, 929
Ledlow M. J., Owen F. N., Yun M. S., Hill J. M., 2001, ApJ, 552, 120
Longair M. S., 2011, High Energy Astrophysics, 3rd edn.Cambridge Univ.Press, Cambridge
Lu J. F., 1990, A&A, 229, 424
Machalski J., Jamrozy M., Saikia D. J., 2009, MNRAS, 395, 812
Machalski J., Kozieł-Wierzbowska D., Goyal A., 2021, ApJS, 255, 22
Mahatma V. H. et al., 2019, A&A, 622, A13
Merritt D., Ekers R. D., 2002, Science, 297, 1310
Merritt D., Milosavljević M., 2005, Living Rev. Relativ., 8, 8
Mezcua M., Chavushyan V. H., Lobanov A. P., León-Tavares J., 2012, A&A, 544, A36
Migliori G., Grandi P., Palumbo G. G. C., Brunetti G., Stanghellini C., 2007, ApJ, 668, 203
Murgia M. et al., 2011, A&A, 526, A148
Murgia M., 1996, Laurea thesis, University of Bologna
Murgia M., 2003, Publ. Astron. Soc. Aust., 20, 19
Myers S. T. et al., 2003, MNRAS, 341, 1
O'Dea C. P., 1998, PASP, 110, 493
Pacholczyk A. G., 1970, Radio Astrophysics. Nonthermal Processes in Galactic and Extragalactic Sources. Freeman & Co., San Francisco
Parma P., Ekers R. D., Fanti R., 1985, A&AS, 59, 511
Parma P., Murgia M., de Ruiter H. R., Fanti R., Mack K. H., Govoni F., 2007, A&A, 470, 875
Parma P., Murgia M., Morganti R., Capetti A., de Ruiter H. R., Fanti R., 1999, A&A, 344, 7
Pringle J. E., 1997, MNRAS, 292, 136
Romero G. E., Chajet L., Abraham Z., Fan J. H., 2000, A&A, 360, 57
Roos N., Kaastra J. S., Hummel C. A., 1993, ApJ, 409, 130
Rottmann H., 2002, PhD thesis, Univ. Bonn
Saikia D. J., Jamrozy M., 2009, Bull. Astron. Soc. India, 37, 63

Saripalli L., Roberts D. H., 2018, ApJ, 852, 48
Schoenmakers A. P., de Bruyn A. G., Röttgering H. J. A., van der Laan H., Kaiser C. R., 2000, MNRAS, 315, 371
Schwab F. R., 1984, AJ, 89, 1076
Shimwell T. W. et al., 2022, A&A, 659, A1
Shulevski A. et al., 2019, A&A, 628, A69
Singh V., Ishwara-Chandra C. H., Sievers J., Wadadekar Y., Hilton M., Beelen A., 2015, MNRAS, 454, 1556
Skipper C. J., Browne I. W. A., 2018, MNRAS, 475, 5179
Springmann A., Cheung C. C., 2007, U.S. Department of Energy Journal of Undergraduate Research, 7, 97
Swarup G., Ananthakrishnan S., Kapahi V. K., Rao A. P., Subrahmanya C. R., Kulkarni V. K., 1991, Curr. Sci., 60, 95
Tremblay S. E., Taylor G. B., Ortiz A. A., Tremblay C. D., Helmboldt J. F., Romani R. W., 2016, MNRAS, 459, 820
Turner R. J., Shabala S. S., Krause M. G. H., 2018, MNRAS, 474, 3361
van Breugel W., Balick B., Heckman T., Miley G., Helfand D., 1983, AJ, 88, 40
van Haarlem M. P. et al., 2013, A&A, 556, A2
Worrall D. M., Birkinshaw M., Cameron R. A., 1995, ApJ, 449, 93
Yang X. et al., 2019, ApJS, 245, 17
Yang X. et al., 2022, ApJ, 933, 98
Zou H. et al., 2019, ApJS, 245, 4

This paper has been typeset from a TEX/LATEX file prepared by the author.

Chapter 4

Multiwavelength investigations of PKS 2300-18: S-shaped radio quasar with precessing jets and double-peaked broad emission-line spectrum

Monthly Notices of the ROYAL ASTRONOMICAL SOCIETY

MNRAS **536,** 2025–2045 (2025) https://doi.org/10.1093/mnras/stae2639
Advance Access publication 2024 November 26

Multiwavelength investigations of PKS 2300−18: S-shaped radio quasar with precessing jets and double-peaked broad emission-line spectrum

Arpita Misra,[1,2]★ Marek Jamrozy,[1]★ Marek Weżgowiec[3] and Dorota Kozieł-Wierzbowska[1]

[1]*Department of Stellar and Extragalactic Astronomy, Astronomical Observatory, Jagiellonian University, Orla 171, PL-30-244 Krakow, Poland*
[2]*Jagiellonian University, Doctoral School of Exact and Natural Sciences, PL-30-348 Krakow, Poland*
[3]*Department of Radioastronomy and Space Physics, Astronomical Observatory, Jagiellonian University, Orla 171, PL-30-244 Krakow, Poland*

Accepted 2024 November 21. Received 2024 November 17; in original form 2024 September 3

ABSTRACT

S-shaped radio galaxy jets are prime sources for investigating the dynamic interplay between the central active galactic nucleus (AGN), the jets, and the ambient intergalactic medium. These sources are excellent candidates for studying jet precession, as their S-shaped inversion symmetry strongly indicates underlying precession. We present a multiwavelength analysis of the giant inversion-symmetric S-shaped radio galaxy PKS 2300−18, which spans 0.76 Mpc. The host is a quasar at a redshift of 0.128, displaying disturbed optical morphology due to an ongoing merger with a companion galaxy. We conducted a broad-band radio spectral study using multifrequency data ranging from 183 MHz to 6 GHz, incorporating dedicated observations with the upgraded Giant Metrewave Radio Telescope (uGMRT) and Karl G. Jansky Very Large Array (JVLA) alongside archival radio data. A particle injection model was fitted to the spectra of different regions of the source to perform ageing analysis, which was supplemented with a kinematic jet precession model. The ageing analysis revealed a maximum plasma age of $\sim$ 40 Myr, while the jet precession model indicated a precession period of $\sim$ 12 Myr. *ROentgen SATellite* (*ROSAT*) data revealed an X-ray halo of Mpc size, and from *Chandra* the AGN X-ray spectrum was modelled using thermal and power-law components. The optical spectrum displaying double-peaked broad emission lines was modelled, indicating complex broad-line region kinematics at the centre with the possibility of a binary SMBH. We present the results of our multiwavelength analysis of the source, spanning scales from a few light-days to a few Mpc, and discuss its potential evolutionary path.

Key words: radiation mechanisms: non-thermal – galaxies: active – galaxies: individual: PKS 2300−18 – galaxies: jets – galaxies: peculiar – radio continuum: galaxies.

1 INTRODUCTION

Supermassive black holes (SMBHs) play a key role in the formation and evolution of active galactic nuclei (AGNs) at the centres of galaxies. SMBHs accrete surrounding gas and matter, forming an accretion disc where a fraction of the gravitational binding energy is converted into thermal energy and radiation. This process, at times, leads to the production of bipolar relativistic jets that align with the SMBH's spin axis and extend millions of light years before eventually spreading into large-scale radio-emitting lobes (Blandford & Rees 1974). The jets of these radio galaxies (RGs) penetrate deep into the intergalactic medium, gradually fading in luminosity with increasing distance from the host galaxy or terminating in hotspots at the edges of the diffuse lobes. Standard RGs display a 'core–jet–lobe' structure, characterized by symmetric, double-sided radio lobes extending from a central radio core.

RGs are known to exhibit a wide variety of morphological shapes, including twin-tailed jet lobes bent into C-, U-, or V-shaped structures, commonly classified as wide-angle tail and narrow-angle tail galaxies (Miley et al. 1972; Owen & Rudnick 1976; Sebastian, Lal & Pramesh Rao 2017; Das et al. 2021; O'Dea & Baum 2023; Pal & Kumari 2023). These structures result primarily from ram pressure stripping as the galaxies move through a cluster environment (Gunn & Gott 1972; Bhukta, Mondal & Pal 2022b). Furthermore, some RGs display morphologies resembling X-, S-, or Z-shaped structures, which are classified within the broader class of winged RGs (Florido, Battaner & Sanchez-Saavedra 1990; Gopal-Krishna et al. 2012; Lal et al. 2019; Cotton et al. 2020; Misra, Jamrozy & Weżgowiec 2023; Giri et al. 2024; Sebastian et al. 2024). Among these, the S- or Z-shaped radio morphology is comparatively rarer (Bera et al. 2022; Ndung'u et al. 2023), with clear examples of S-shaped morphology observed in sources such as 4C 29.47 (Condon & Mitchell 1984), 2MASXJ12032061 + 1319316 (Rubinur et al. 2017), J0644 + 1043 (Sethi et al. 2024), and RBS 797 (Ubertosi et al. 2024b).

The atypical inversion-symmetric 'S-shape' in RGs is thought to emerge when standard Fanaroff–Riley type I (FRI) and/or Fanaroff–Riley type II (FRII: Fanaroff & Riley 1974) jets undergo continuous precession and the jets get dragged from their initial position, creating twisted patterns (Horton, Krause & Hardcastle 2020). The precession of the jet, driven by a change in the spin-axis direction of an SMBH, gradually tilts the jet axis and ultimately results in an S-shaped morphology over time. A range of possible models for explaining

★ E-mail: arpita.misra@doctoral.uj.edu.pl (AM); marek.jamrozy@uj.edu.pl (MJ)

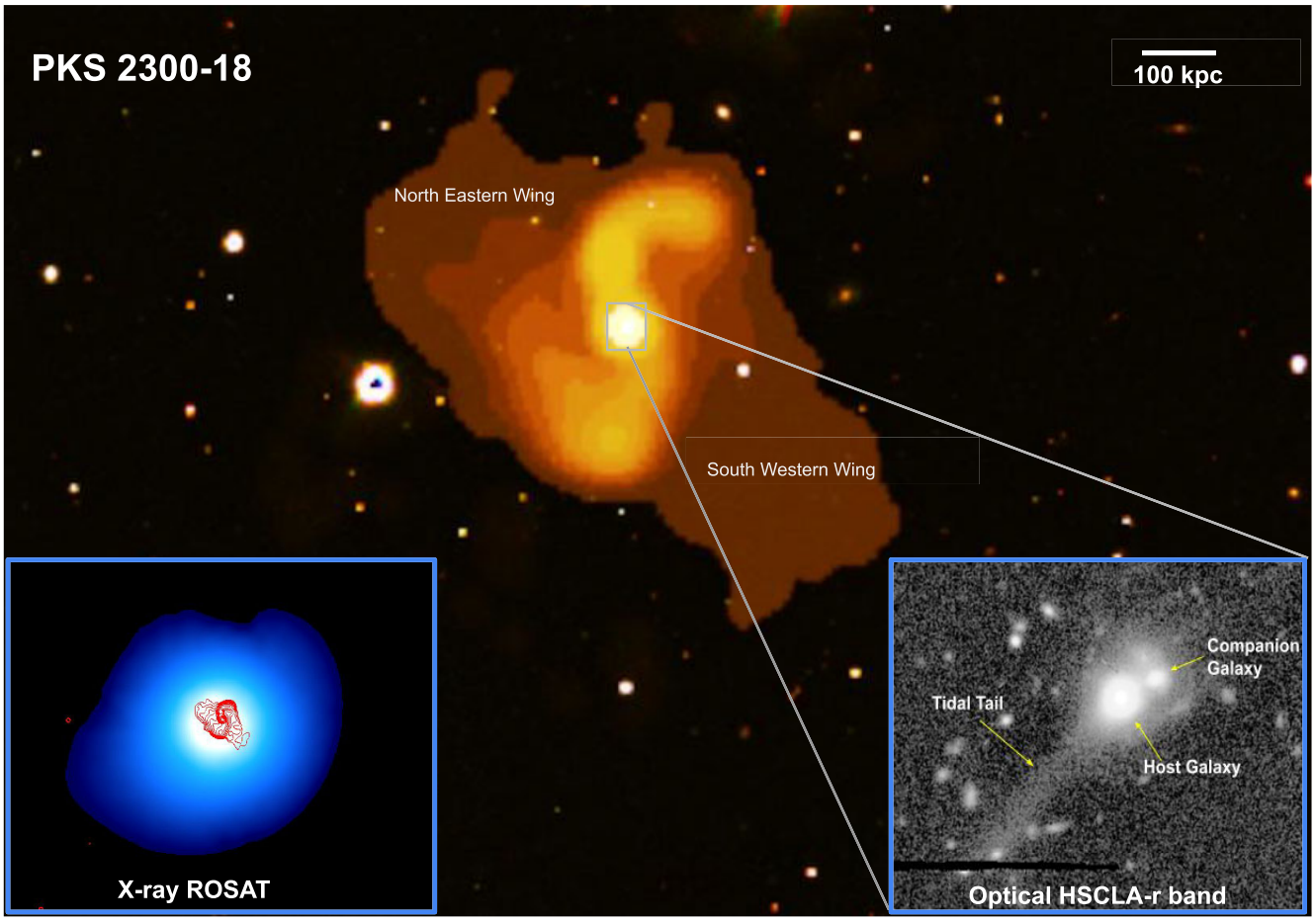

Figure 1. 1.4-GHz RACS radio map of PKS 2300−18 (in orange) overlaid on the PanSTARRS (Chambers et al. 2016) optical image. The right panel inset is the HSCLA *r*-band optical image of the host quasar at the centre of the radio source interacting with a companion galaxy and consequentially forming an extended tidal tail. The left inset is the *ROSAT* map of the quasar, showing extended X-ray emission (in blue) with 3σ emission above the noise level, overlaid with contours (in red) from the RACS map at 1.4 GHz (main figure in orange).

this reorientation or precession have been proposed that include reorientation of the jets due to the presence of another SMBH in the same nucleus (Begelman, Blandford & Rees 1980; Britzen et al. 2001; Nandi et al. 2021; Sebastian et al. 2024) and/or a surrounding tilted accretion disc (Lu 1990; Lu & Zhou 2005; Liska et al. 2018; Chatterjee et al. 2020). Galaxy mergers, which are a common evolution trajectory for most galaxies following hierarchical structure formation (e.g. Ostriker & Hausman 1977; Lacey & Cole 1993), have an important role behind forming such radio morphologies. Mergers drive the processes that lead naturally to the formation of SMBH binaries and complex gas dynamics at the centres of galaxies, which contribute to jet precession.

One of the most compelling examples linking S-shaped radio jets to precession is the quasar PKS 2300−18 (other names PKS B2300−189, QSO 2300–189, and J2303−1841). This source is notable for its striking inversion symmetry in radio wavelengths and is considered one of the clearest examples of precessing jets observed in quasars (Hunstead et al. 1984). PKS 2300−18 has S-shaped jets surrounded by diffuse low surface brightness wings that contain old plasma. In RGs, such emission can be detected, as the phase of nuclear activity in a radio AGN can range from several million to several billion years. Over time, particles in the radio lobes lose energy through synchrotron radiation and inverse Compton scattering, leading to the gradual fading of the lobes and jets. However, these radio sources still remain traceable long after their emitting electrons were last accelerated to relativistic energies, thus preserving a comprehensive historical record of jet activity.

In this article, we examine the radio emission of PKS 2300−18, which features low surface brightness radio wings that span ~ 5 arcmin and S-shaped jets that extend ~ 3 arcmin in the plane of the sky. Identified by Bolton & Ekers (1966), the source displays a concave radio spectrum, i.e. steep at low frequencies and flat at high frequencies (Hunstead et al. 1984). This spectrum is typically observed in sources with a compact, flat-spectrum core surrounded by steep-spectrum extended emission. PKS 2300−18 is located at RA $23^{\rm h}03^{\rm m}02\overset{\rm s}{.}97$ and Dec. $-18^\circ41'25\overset{''}{.}8$ (J2000.0) with a redshift of $z = 0.1283$ (Hunstead, Murdoch & Shobbrook 1978). The quasar, with an absolute *B*-band magnitude of −20.51, is identified by its broad emission lines. Optical *i*-band images from the Hyper Suprime-Cam Legacy Archive (HSCLA: Tanaka et al. 2021) reveal a companion galaxy located 14 kpc away, with both galaxies embedded in a common envelope of gas and dust (Hunstead et al. 1984). The quasar and its companion are undergoing a merger, resulting in a long tidal tail extending from the host and a small c-shaped tidal arm wrapped around the companion galaxy, as seen in Fig. 1 (bottom right insert). This source is not associated with any known galaxy group or cluster. The quasar shows optical variability, as observed in the All-Sky Automated Survey for Supernovae (ASAS:

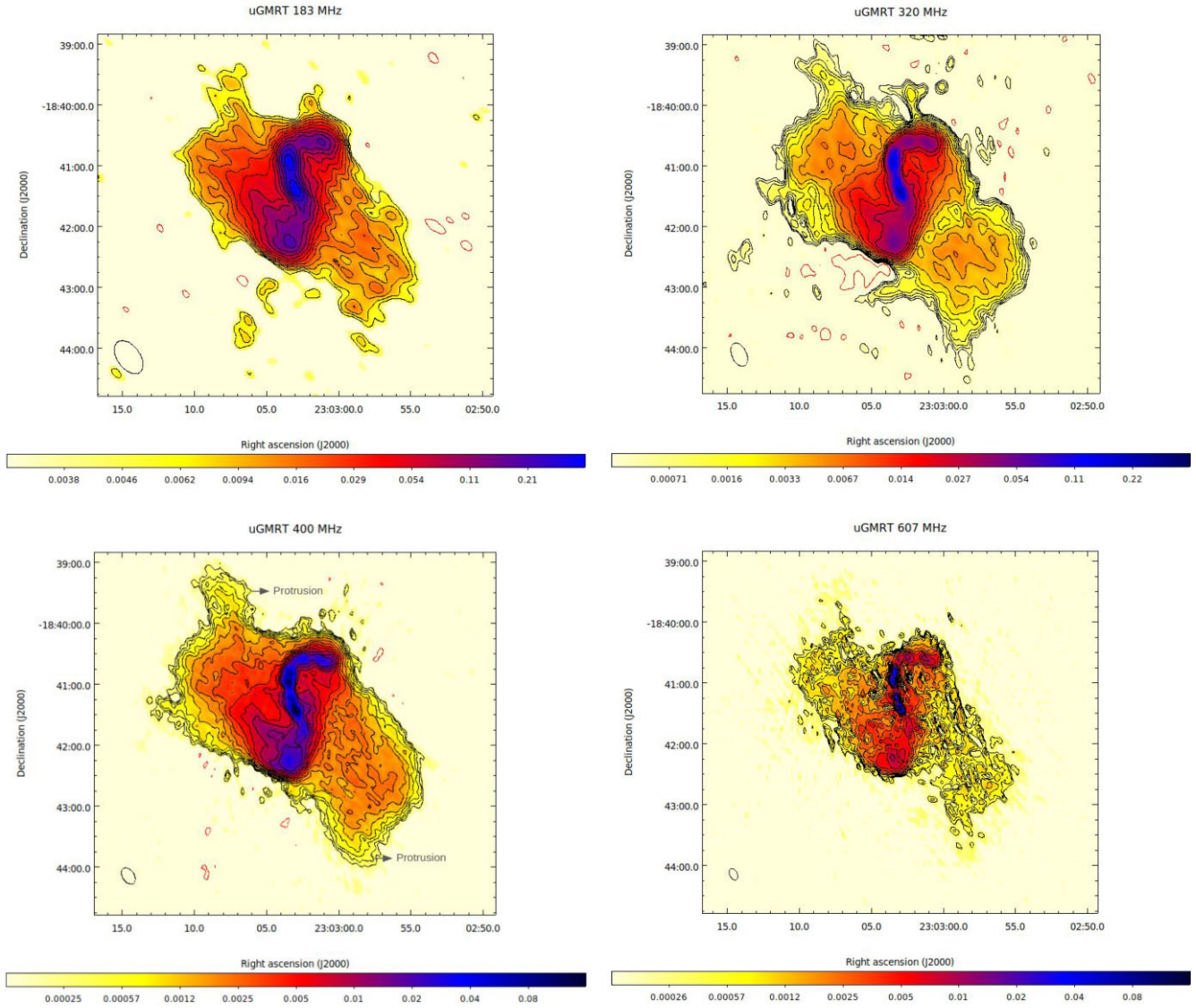

Figure 2. Low-frequency maps of PKS 2300−18 obtained from uGMRT observations at 183, 320, 400, and 607 MHz. The contour levels are spaced by a factor of $\sqrt{2}$ and the first contour is at 3 × rms level. The first negative 3 × rms level is marked with red contours. The rms values and beam sizes of all the above maps are given in Table 1. The relative sizes of the beam are indicated by the ellipse at the bottom left corner of each image. The colour gradient represents flux-density values in Jy beam^{-1}.

Jayasinghe et al. 2020) from 2013–2018 and in Zwicky Transient Facility monitoring (Bellm et al. 2019). Furthermore, the radio core of PKS 2300−18 also shows strong variability between 5 and 40 GHz, seen in the Planck Australian Telescope Compact array (Planck-ATCA) Co-eval Observations (PACO: Bonaldi et al. 2013). A more detailed discussion of this is presented in Section 3.3. The host is also identified as a gamma-ray-emitting RG, as detected by the *Fermi* satellite in 4FGL-DR2 (Abdollahi et al. 2020; Ballet et al. 2020; Chen et al. 2023). A source morphologically similar to PKS 2300−18, J1257+1228, was discussed in Kozieł-Wierzbowska, Goyal & Żywucka (2020) and has an X-shaped radio morphology.

In this study, we performed a multiwavelength analysis of PKS 2300−18, examining its radio emission, optical spectrum, and X-ray emission. We used archival and dedicated radio observations covering frequencies from 183 MHz to 40 GHz to investigate the galaxy in detail. By analysing its radio spectra, we assessed the ageing of the electron population in various regions of the source and gave an account of its structural evolution. In addition, we modelled the optical and X-ray spectra of the AGN. In this work, Section 2 provides a comprehensive overview of the radio observations along with details of the optical and X-ray observations. Sections 3, 4, and 5 present the results of our radio, optical, and X-ray analyses, respectively. A detailed discussion is presented in Section 6 and conclusions are drawn in Section 7.

All absolute quantities in this work were calculated for a ΛCDM universe with $H_0 = 70$ km s^{-1}Mpc^{-1}, $\Omega_m = 0.3$, and $\Omega_\Lambda = 0.7$. Using the host galaxy redshift, the conversion scale translates to 2.291 kpc arcsec^{-1} as used in Wright (2006).

2 OBSERVATIONS AND DATA REDUCTION

2.1 Radio observations

To elucidate the radio morphology of PKS 2300−18, high-resolution multifrequency radio maps were obtained using dedicated observations from the upgraded Giant Metrewave Radio Telescope

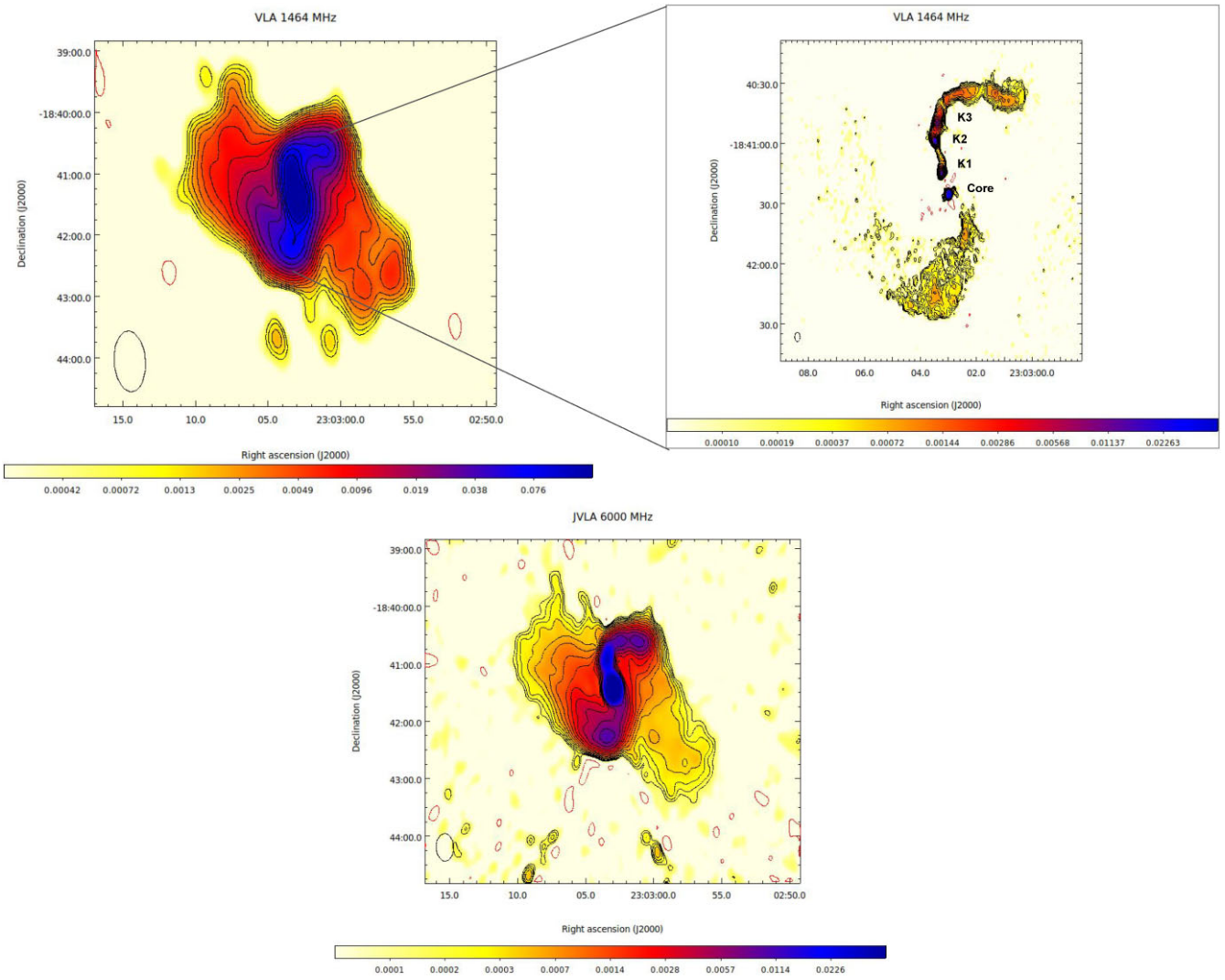

Figure 3. High-frequency maps of PKS 2300−18 obtained from VLA observations at 1.4 GHz (archival) and 6 GHz (dedicated). The contour levels are spaced by a factor of $\sqrt{2}$ and the first contour is at 3 × rms level. The first negative 3 × rms level is marked with red contours. The beam size of the archival VLA 1464-MHz (C config) map is 29.7×15.2 arcsec^2 and rms value is 0.27 mJy beam^{-1} (rms values and beam sizes of 6000-MHz map and 1464-MHz A and C configuration maps are given in Tables 1 and 2). The relative sizes of the beam are indicated by the ellipse at the bottom left corner of each image. The colour gradient represents the flux-density values in Jy beam^{-1}.

(uGMRT), the Karl G. Jansky Very Large Array (JVLA), and publicly available survey data. In the following subsections, we provide a detailed overview of the observation methodologies, the surveys utilized, and the data processing techniques implemented to generate the uGMRT and JVLA maps presented in Figs 2 and 3.

2.1.1 uGMRT observations

PKS 2300−18 was observed using the uGMRT wide-band receiver (GWB) with 2048 channels in three frequency bands, band 2 (125−250 MHz), band 3 (250−500 MHz), and band 4 (550−850 MHz), concurrently with the narrow-band receiver (GSB); details are given in Table 1. For the observations, the usual scheme of looping the phase calibrator with the target source was adopted, with the flux-density calibrators observed for ∼10 min at the beginning and the end of observations. Observations of the target source from bands 2–4 were made using the flux-density calibrator 3C 48. In band 4, J2246−121 as the phase calibrator was observed for 5 min alternating with the target source in the loop. In bands 2 and 3, J2225−049 was observed as the phase calibrator for 5 min between cycles.

The reduction of GSB narrow-band data for all observed frequencies was carried out using the Source Peeling and Atmospheric Modeling pipeline (SPAM: Intema et al. 2009; Intema 2014). SPAM is a PYTHON-based extension to AIPS (Greisen 2003) that reduces high-resolution, low-frequency radio interferometric observations. It follows direction-dependent calibration, modelling, and corrections for the dispersive phase delay that are mainly of ionospheric origin. The data were corrected for strong radio frequency interference (RFI) followed by standard flux-density and bandpass calibration. Subsequent cleaning was performed using the Cotton–Schwab algorithm (Schwab 1984; Cotton 1999). This algorithm is a modified version of CLEAN deconvolution (Högbom 1974; Clark 1980) and enables the deconvolution of multiple facets simultaneously, where each facet is deconvolved using a different dirty beam. The wide-band GWB data were also reduced using SPAM, where the data were first split into 6–9 subbands. For the calibration of the individual

Table 1. Details of uGMRT and JVLA dedicated observations of PKS 2300−18 analysed in this work.

Telescope	Frequency range (MHz)	Central freq. (MHz)	Proposal code	Date of observation	TOS (hrs)	Resolution (arcsec×arcsec)	PA (°)	rms (mJy beam^{-1})
(1)	(2)	(3)	(4)	(5)	(6)	(7)	(8)	(9)
uGMRT Band–2	120–250	183	40_016	2021 Aug 14	4.1	18.6×11.2	36.8	1.28
uGMRT Band–3	250–500	320	40_016	2021 Aug 17	4.0	12.2×7.2	23.7	0.10
uGMRT Band–3	250–500	400	40_016	2021 Aug 17	4.0	8.9×5.6	32.8	0.09
uGMRT Band–4	550–850	607	39_018	2020 Dec 11	4.0	6.0×3.7	27.3	0.11
JVLA C band D–conf	4000–8000	6000	22A_091	2022 Aug 31	0.2	14.4×9.0	1.8	0.03

subbands, a skymodel was extracted from the initial narrow-band image using the PYTHON Blob Detector and Source Finder (PyBDSF: Mohan & Rafferty 2015), which is a Python-based algorithm that can decompose an image into a set of Gaussians, shapelets, or wavelets. After calibration, the final imaging was performed using the w-stacking algorithm WSclean (Offringa et al. 2014), which is an alternative to the w-projection algorithm in which the uv samples are not convolved with a w-term correcting kernel before the fast Fourier transform (FFT), but are instead corrected with a multiplication after the FFT. In WSclean, a multi-scale, multi-frequency wide-band deconvolution approach (Offringa & Smirnov 2017) was used to image each band. The multi-frequency deconvolution feature for wide-band enables the simultaneous cleaning of channels by considering spectral variation and using each channel's specific point spread function (PSF) for deconvolution. Here the Briggs (1995) weighting scheme was used to suppress the side lobes in the PSF. A robustness parameter of 0 was used as an ideal between natural and uniform scales to preserve both large-scale structures and high-resolution details. The resultant images were primary-beam corrected using the AIPS task PBCOR. The final uGMRT maps are presented in Fig. 2.

2.1.2 *VLA observations*

Dedicated observations of PKS 2300−18 were performed in the *C* band using the D configuration of the JVLA, with a bandwidth of 4096 MHz and 2048 channels. A single scheduling block was used, consisting of calibrator (both flux and phase) and source scans. The data were processed with the Common Astronomy Software Applications (CASA: CASA Team et al. 2022) package version 6.5.6.22. All data affected by RFI were flagged manually. The radio sources 3C 286 and J2246−1206 were used for the flux-density scale and phase calibrations, respectively. The deconvolution of the interferometer PSF from the dirty map was performed with the use of the CASA task TCLEAN. Within this task, the Clark CLEAN algorithm was used and to ensure the best dynamic range, that is, the sensitivity to faint large-scale emission; multiscale clean with Briggs weighting was used (robust parameter set to 0). Due to the significant brightness of the source core region, as well as its complex structure, severe interference from the side lobes caused the need for self-calibration (a total of three runs), which was performed in phases only.

To obtain high angular resolution maps of PKS 2300−18, necessary for the analysis presented in Section 3, *L*- and *C*-band data of the target from the VLA archive were retrieved and reduced using AIPS (Greisen 1990) following standard procedures. Observations in the A-array configuration were carried out with a bandwidth of 50 MHz and with the pointing centre at RA $23^{h}03^{m}03\overset{s}{.}0$, Dec. $-18^{\circ}41'25\overset{''}{.}87$ (J2000.0) and a total integration time of 168 (spread out on 12 scans) and 46 min (spread out on 5 scans), respectively. For flux and phase calibration, sources 3C 286 and J2246−121 were used, respectively. Observations in the C-array configuration were carried out with a bandwidth of 50 MHz. The observations were performed with the same pointing as mentioned above with a total integration time of 10 min. For the flux and phase calibration, the sources 3C 48 and J0202−172 were used, respectively. After the initial data reduction, the two *L*-band data sets were merged using the task DBCON. After preliminary CLEANing of the *L*- and *C*-band maps with the routine IMAGR, several self-calibrations were performed to improve their quality. The two resultant maps were corrected for primary beam attenuation and the images were finally convolved with circular Gaussians. The flux density was on the Baars et al. (1977) scale. The resulting maps are presented in Fig. 3. Details about the observations and resultant maps are given in Table 2.

2.1.3 *VLBA observations*

To study the nuclear jet kinematics of PKS 2300−18, the archival multi-epoch X-band data observed with the Very Long Baseline Array (VLBA) and published by Beasley et al. (2002), Schinzel et al. (2015), and Gordon et al. (2016) were analysed. The five epoch maps, i.e. 1997.499, 1997.652, 2014.411, 2015.441, and 2017.222, used in our analysis were acquired from the Astrogeo Very-Long-Baseline Interferometry (VLBI) Flexible Image Transport System (FITS) image data base (https://astrogeo.org/vlbi_images/). The synthesized beam size of all these maps is similar and varies from 1.94 mas × 0.83 mas to 2.75 mas × 1.03 mas; the map pixel size is 0.2 mas × 0.2 mas. Details of our analysis are given in Section 3.2 and information about the observations and resultant maps is given in Table 2.

2.1.4 *Data extracted from surveys*

This work made use of the Rapid Australian Square Kilometre Array Pathfinder (ASKAP) Continuum Survey (RACS: Hale et al. 2021) for low-frequency radio data analysis. RACS-low is a large-sky survey using ASKAP, covering the sky south of Dec. $+41^{\circ}$ in the low band at a central frequency of 887.5 MHz. The images are convolved to a common resolution of 25 arcsec with a root-mean-square (rms) sensitivity of 0.25–0.3 mJy beam^{-1}.

High-frequency analysis was conducted using the data from the National Radio Astronomy Observatory (NRAO) Very Large Array (VLA) Sky Survey (NVSS: Condon et al. 1998) RACS-mid (Duchesne et al. 2023) and VLA Sky Survey (VLASS; Lacy et al. 2020). NVSS is a continuum survey that covers the entire sky north of declination -40° at 1.4 GHz with a resolution of 45 arcsec. The rms brightness fluctuations in total power are about 0.45 mJy beam^{-1} (Stokes I). RACS-mid is a large sky survey using ASKAP that comprises images covering the whole sky south of declination $+49^{\circ}$ in the mid band at 1367.5 MHz. The rms sensitivity is ∼0.15–0.4 mJy beam^{-1} at a resolution of 8.1–47.5 arcsec. VLASS is an all-sky survey above declination -40°. It operates within the range

Table 2. Details of archival and survey data of PKS 2300–18 analysed in this work.

Telescope/Survey	Frequency range (MHz)	Central freq. (MHz)	Proposal code	Date of observations	TOS (mins)	Resolution (arcsec × arcsec)	PA (°)	rms (mJy beam^{-1})
(1)	(2)	(3)	(4)	(5)	(6)	(7)	(8)	(9)
ASKAP/RACS-low	744−1032	888	AS110	2019 Apr–2020 Jun	15	25 × 25	–	0.352
ASKAP/RACS-mid	1224−1512	1368	AS110	2021 Jan 21	15	8.80 × 7.40	72.03	0.181
VLA-D/NVSS	1344−1456[a]	1400	AC308	1993 Sep 20	0.7	45 × 45	–	0.45
VLA-A	1440−1490	1465	COND	1982 Jun 25	168	2.25 × 1.38[b]	0.05[b]	0.033[b]
VLA-C	1440−1490	1465	MITC	1981 Dec 15	10	2.25 × 1.38[b]	0.05[b]	0.033[b]
JVLA-B/VLASS	2000−4000	3000	VLASS	2019 Jul 06	–	2.90 × 1.77	56.29	0.158
VLA-A	4860−4910	4885	COND	1982 Jun 25	46	0.7 × 0.7	–	0.059
VLBA	7392−7840	7624	BS241	2015 Jun 11	1.9	0.0028 × 0.0010	2.51	0.15
VLBA	8155−8555	8340	BB023	1997 Jul 02	5.4	0.0024 × 0.0009	−7.9	0.374
VLBA	8155−8555	8340	BB023	1997 Aug 27	5.4	0.0022 × 0.0010	−9.09	0.614
VLBA	8428−8876	8668	UF001	2017 Mar 23	4.9	0.0019 × 0.0008	−3.46	0.178
VLBA	8444−8892	8668	BG219	2014 May 31	2.5	0.0021 × 0.0008	−1.32	0.171

Note. (a) NVSS frequency ranges: 1344–1386 MHz and 1414–1456 MHz, (b) values for the merged A and C configuration data.

2–4 GHz with an angular resolution of 2.5 arcsec. Details about the observations and resultant maps are given in Table 2. Throughout the work, the flux-density errors were calculated using the following formula:

$$\Delta S = \sqrt{(S \times \Delta S_c)^2 + \left(rms \times \sqrt{\frac{area}{beam}}\right)^2}, \quad (1)$$

where ΔS_c is the calibration error, taken as 10 per cent for the uGMRT observations and 5 per cent for the VLA observations. The calibration error for the radio surveys was taken as 5 per cent.

2.2 Optical observations

Spectral observations of PKS 2300−18 were obtained from the Isaac Newton Group of Telescopes archives. The target was observed using the William Herschel Telescope (WHT) and the Intermediate-dispersion Spectrograph and Imaging System (ISIS). The observations were taken on 1994 July 4, with gratings R158B and R158R, slit width 1.″34, and 900 sec of exposure. During the observations, seeing (0.″9) was smaller than the slit width, ensuring that none of the quasar emission was missed. The spectrum was taken at two position angles (measured from north to east), 167° and 162°; however, neither of these positions reached the companion galaxy. The spectrum was wavelength-calibrated using CuNe + CuAr arc lamp exposures, and photometrically calibrated using exposures of Feige 34 and Feige 92 standard spectrophotometric stars taken on the same night.

2.3 X-ray observations

To investigate the properties of the hot gas associated with the host galaxy of PKS 2300−18, as well as its AGN, we used archival X-ray data from the *ROentgen SATellite* (*ROSAT*: Truemper 1982) All Sky Survey (RASS: Voges et al. 1999) and from the *Chandra* X-ray Observatory Data Archive.[1]

2.3.1 ROSAT *data*

In this work we used the broad-band image from the sequence rs932061n00, smoothed to a resolution of 2 arcmin, which is the PSF of the Position Sensitive Proportional Counter (PSPC) instrument. The resulting image was used only to estimate the extent of the X-ray emission associated with our studied source, which will be discussed in Section 6.4.2.

2.3.2 Chandra data

PKS 2300−18 was observed with *Chandra* on 2021 September 11 for a total of 9.57 ks, using an ACIS-S camera. In this work, we use the pipeline data obtained from the Chandra Data Archive. However, the data were reprocessed with the $chandra-repro$ script for the most accurate and up-to-date calibration. Due to the high brightness of the source associated with the PKS 2300−18 host galaxy, the data included a readout streak, which was removed using the $acisreadcorr$ script. Next, we produced a broad-band (0.2–7 keV) image and smoothed it with the PSF of the instrument. The extended emission visible in the *ROSAT* map (left insert in Fig. 1) was not detected, likely due to the short time of the observations and overall lower sensitivity to diffuse structures of the *Chandra* telescope. A circular region of 4 arcsec radius around the brightest emission associated with the host galaxy of PKS 2300−18 was used to extract the spectrum. The background spectrum was also extracted from a rectangular source-free area close to the studied source. Further, for both spectra, response files were created. The final background-subtracted source spectrum was grouped (25 counts in an energy bin) to increase the signal-to-noise ratio. The spectrum of PKS 2300−18 was analysed with XSPEC12 (Arnaud 1996). The results of the model fitting are presented in Section 5.

3 MULTIFREQUENCY RADIO ANALYSIS

3.1 Comprehensive radio morphology

The source displays a pair of S-shaped, inversion-symmetric jets oriented along the north–south direction, extending over 240 kpc, as observed in the low-frequency uGMRT maps shown in Fig. 2 and the high-frequency VLA maps shown in Fig. 3. These jets are embedded within low surface brightness diffuse emission that extends along the southwest and northeast direction, forming a structure of total length ∼5 arcmin. The S-shaped jets resemble an FRI-type morphology with $P_{1.4\mathrm{GHz}} \simeq 5.5 \times 10^{25}$ W Hz^{-1}, calculated using a spectral-index value of 0.7 and total flux density measured at 1.4 GHz NVSS of 1.38 Jy, using equation (1) of Brown, Webster & Boyle (2001). The high-resolution *L*-band map at 1.4 GHz and *C*-band map at 6 GHz in

[1] https://cxc.harvard.edu/cda/

Table 3. Flux-density values of radio knots at different frequencies given in mJy (see Fig. 3).

Region	1367 MHz	1464 MHz	3000 MHz	4885 MHz
K1	72.9±6.3	32.5±1.6	15.5±2.4	11.2±0.6
K2	77.8±3.9	53.4±2.7	33.9± 5.1	16.0±0.8
K3	59.4±3.0	50.0± 2.4	29.7±4.9	11.5±0.6

Note. The flux-density values of columns (2)–(5) are from the RACS survey, archival VLA observations, the VLASS survey, and archival VLA observations, respectively, as detailed in Section 2.

the A configuration seen in Fig. 3 have a well-resolved view of the core and the jets, where the radio core is observed to have enhanced emission at higher frequencies. The core also coincides perfectly with the position of the optical host at the centre. In Fig. 3, it can be observed that the northern jet is pronounced and well collimated compared with the southern jet. The northern jet features three distinct knots labelled K1, K2, and K3, with K1 being the brightest, followed by K2 and K3; their flux-density values are given in Table 3. The southern jet is much fainter and quite diffuse in comparison with the northern jet, and lacks any complementary knot-like features. This could most likely result from relativistic Doppler beaming of the jets.

The diffuse wings are aligned in the northeast and southwest directions relative to the central S-shaped jets. Notably, the upper part of the northeastern wing features a prominent protrusion that resembles an inverted U, as clearly depicted in the uGMRT 400-MHz map (Fig. 2). A subtler complementary protrusion is observed in the lower part of the southwestern wing near its bottom edge. This pattern suggests an earlier orientation of the jets, indicating that the current structure is the result of a jet reorientation. From the current inversion-symmetric S-shaped jets we can hence deduce that the source is going through precession. The overall morphology of the source can be attributed to jet reorientation taking place in the counterclockwise direction, due to continuous jet precession. The jet precession not only occurs in a counterclockwise direction but also involves the northern jet approaching our line of sight, causing Doppler boosting of its components, while the southern jet is receding. This may explain the presence of knots in the northern jet and their absence in the southern jet. The total extent of the source, taking into account the extended wings, is ∼760 kpc in linear size.

3.1.1 Spectral-index analysis

The evolution of plasma in the radio lobes as a result of synchrotron and inverse-Compton losses is traced well on the spectral index (SI) map. The SI map for PKS 2300−18 was produced using uGMRT band 3 (400 MHz) and the large-scale low-resolution JVLA *C*-band (6-GHz) maps with similar uv coverage. These maps were convolved to a resolution of 15 arcsec × 15 arcsec, which is comparable with the original resolution of the uGMRT and the JVLA maps. AIPS tasks HGEOM and COMB were subsequently used to align the geometry of the maps and masking of three times above the root-mean-square noise level was applied to produce the SI map shown in Fig. 4. The SI map ($S_\nu \propto \nu^{-\alpha}$) distribution displays remarkable variation within the source and shows a smooth gradient that runs from the core to the extended wing regions. The S-shaped jets emerging from the flat-spectrum radio core are distinctively visible on the SI map and have a uniform $\alpha\sim$ 0.7. The small regions on either side of the jets, with comparatively flatter spectra, could be due to in situ reacceleration of particles (Gopal-Krishna & Wiita 2024) where the jet experiences bending. The extended wings surrounding the jet and the core have steeper spectra and show an evolution in their SI, with the steepest plasma being present at the edge of the wings. The low surface brightness wings have steeper spectra compared with the central S-shaped structure. The gradient in the SI map traces the location of the oldest to the youngest plasma, tracking the motion of the radio jets over a period of time.

The current trend in the SI map hints at an anticlockwise movement of the radio jet, moving from the extended wings to the S-shaped jets, with the north jet bending towards the western side and the south jet bending towards the eastern side, forming an inversion-symmetric S-shape. This implies a previous southwest and northeast alignment of the radio jets, where we currently see steep spectra. The jets gradually moved in the anticlockwise direction to their current north–south alignment, where we now see comparatively flatter spectra. The SI layout of this source shares similarities with the X-shaped radio source J0113 + 0106 (Lal et al. 2019), diverging from the typical radio lobes characteristic of classical FRII or FRI sources. This unusual morphology prompts several questions about the formation, dynamics, and evolution of the source. Hence, the SI pattern and structure of PKS 2300−18 will provide valuable insights into the nature of precessing jet radio galaxies in general.

3.1.2 Polarization

Maps of the linearly polarized intensity and fractional polarization were created by combining the NVSS Stokes *Q* and *U* maps using the AIPS task COMB. These maps allow for the determination of the polarized flux density, fractional polarization, and polarization angle of the $\boldsymbol{E}$ vector. The total intensity NVSS map with the electric field $\boldsymbol{E}$ vectors (rotated by 90°) superimposed is shown in Fig. 5(a), and Fig. 5(b) shows the linearly polarized intensity map with the vectors of fractional linear polarization superimposed. It is observed that the whole structure is polarized. The total integrated polarized flux intensity of this source is 96.2 ± 5.1 mJy, which gives m = 6.9 per cent for the mean fractional polarization (m is the ratio of polarized flux to total flux). Simard-Normandin, Kronberg & Button (1981b) presented a polarization study at 2695 and 8085 MHz, where the fractional polarization was found to be $m = 5.3 \pm 0.5$ per cent and 2.0± 1.2 per cent, respectively. There is a clear trend here showing a monotonic decrease in the degree of polarization with increasing wavelength. As anticipated, steep-spectrum radio galaxies typically exhibit a reduction in the degree of polarization at lower frequencies. (e.g. Saikia & Salter 1988; Klein et al. 2003). However, Simard-Normandin, Kronberg & Button (1981a) have shown (in their fig. 1) some exceptions, where the degree of polarization of a source first increases and then decreases with increasing wavelength. The authors explain such a behaviour as due to the existence of two or more polarized components with different rotation measures within the source. Another possible reason could be connected to the spectral index differences between less- and more-polarized components. To determine precisely the phenomenon taking place in PKS 2300−18, additional sensitive polarimetric observations are necessary. In the NVSS maps, most of the polarized flux is concentrated in the central part of the source. However, fractional polarization is larger in the diffuse wings. The magnetic field vectors in the central part of the source, which contain the core and the S-shaped jets, are aligned in the north–south direction. The magnetic field vectors also follow the direction of the jet path closely in the diffuse wings, which is traced by the S-shaped jets. Reid, Kronberg & Perley (1999) showed a high-resolution (∼3 arcsec) map of the central part of this source at

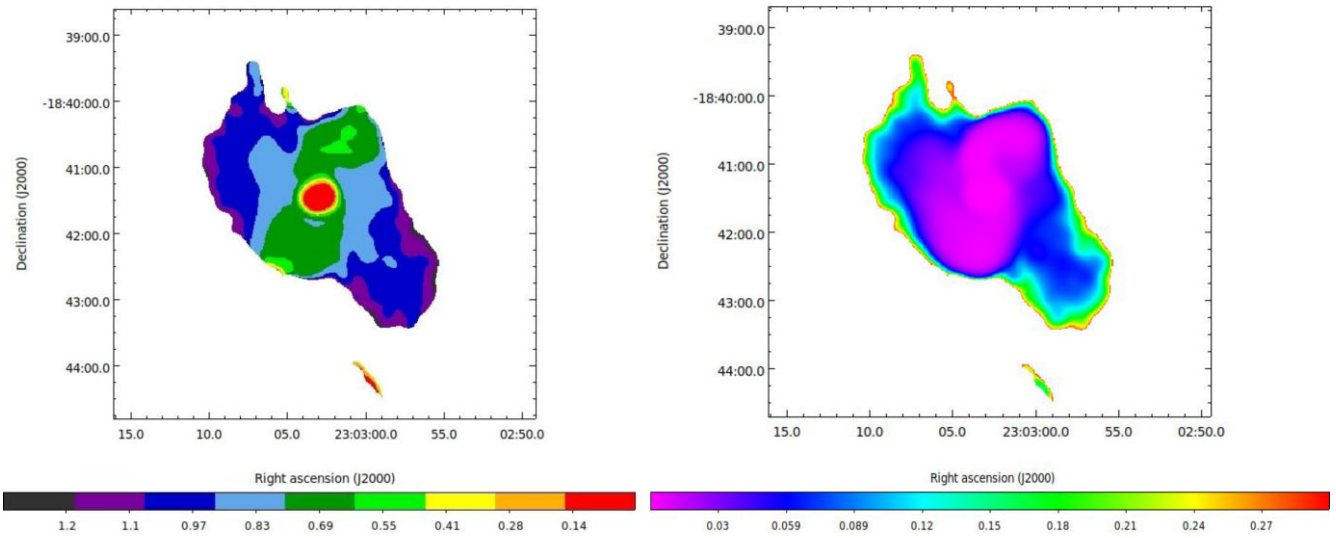

Figure 4. Left: the spectral-index map of PKS 2300−18 between GMRT 400 MHz and JVLA 6 GHz. The colour bar shows the spectral-index values. Right: the spectral-index error map between GMRT 400 MHz and JVLA 6 GHz with the colour bar showing the error associated with the spectral-index values.

4735.1 MHz where the core, the northern blobs, and the S-structure were visibly polarized.

3.2 VLBI pc-scale jets

The milliarcsecond radio structure from VLBA observations of the central part of PKS 2300−18 is shown in Fig. 6. The brightness distribution reveals a compact core and an extended and weaker one-sided jet component of more than 10 mas length in the north-east direction of the core. The jet exhibits a multi-blob structure. A prominent component located at the head of the jet, visible in all epochs, is marked with a red 'X' sign in Fig. 6. The exact positions of the core and the 'X' blob were determined using the AIPS task JMFIT. The position angle of the X blob with respect to the core in epoch 2017.222 is about 34°. For comparison, the position angle of K1 is 20°. We estimated the apparent proper motion by tracking the positional changes in the 'X' component with respect to the core, identified across five different epochs covering a period of 20 years. According to An & Baan (2012), for example, the apparent transverse velocity $v_{\rm app}$ in the rest frame of the source, in units of c, can be obtained as $v_{\rm app} = 0.0158 \mu D_{\rm A}(1+z)$, where $D_{\rm A}$ is the angular size distance of the source in Mpc and μ is the angular separation velocity of the 'X' blob with respect to the central core. $D_{\rm A}$ to PKS 2300−18 is 472.6 Mpc, while μ is in mas yr^{-1} and is defined as $\mu = \theta_{\rm X-Core}/\Delta t$. The angular separation velocity and apparent proper motion obtained in the source rest frame of X are $\mu = 0.3486 \pm 0.0158$ mas yr^{-1} and $v_{\rm app} = (2.31 + / - 0.10)c$. The kinematical age in the source rest frame, calculated from $\theta_{\rm X-Core}/\mu(1+z)$, is 26.1 yr.

The jets of PKS 2300−18 show mildly superluminal speeds at $2.3c$ on the parsec (pc) scale. Such superluminal motions in AGNs were predicted by Rees (1966). The first detection of a source moving with an apparent velocity higher than the speed of light was the quasar 3C 279 (Gubbay et al. 1969). To date, apparent speeds observed in AGNs range from subluminal speeds to a maximum of about $50c$ (QSO PKS J0808−0751: Lister et al. 2009), although common values are 1–10c. Assuming intrinsically symmetric jets and having the apparent proper motion in the source rest frame calculated above, following e.g. Ghisellini et al. (1993), we estimated the inclination angle of the pc-scale jet, i, with respect to the observer's line of sight as

$$v_{\rm app} = \left[c\beta_{\rm j}\sin(i)\right] / \left[1 - \beta_{\rm j}\cos(i)\right], \quad (2)$$

where $\beta_{\rm j}$ is the velocity of the jet in units of c. Using the above value of $v_{\rm app}$, we can write the above equation as

$$\beta_{\rm j} = 2.31/\left[\sin(i) + 2.31\cos(i)\right], \quad (3)$$

further, following e.g. Hocuk & Barthel (2010),

$$\beta_{\rm j} = a/\cos(i), \quad (4)$$

where $a = [s-1]/[s+1]$, $s = J^{1/(2+\alpha)}$, J is the jet-to-counterjet flux-density ratio, and α is the spectral index of the jet. The graphical solution of the above two equations for $\beta_{\rm j}$ and i for three values of $a = 0.95$, 0.8, and 0.684 is shown in Fig. 7. The intersection of the solid black line with the three different dashed lines gives a solution to the above equations. Therefore, we infer that the current angle to the line of sight of PKS 2300−18 cannot be larger than 46°.9, and this is valid for $a = 0.684$ (when $\beta_{\rm j} = 1$). The above limiting value of a corresponds to $J = 65.6$ (for $\alpha = 0.5$). From the X-band epoch 2017.222 map, we obtained the 'X'-blob peak flux density of 8.3 ± 0.17 mJy beam^{-1} and, since there was no counter-blob visible on the map where the rms value is 0.2 mJy beam^{-1}, the lower limit of J was calculated as ~ 41.7.

3.3 Radio core

The radio core of PKS 2300−18 was first observed by Thompson et al. (1980) in 1979 using the VLA at 4885 MHz, and the flux density was found to be 342±14 mJy. Concurrently, the core flux density was measured by Hunstead et al. (1984) between 1978–1979 as 287 ± 30 mJy at 2695 MHz and 304 ± 45 mJy at 8085 MHz. Follow-up observations in 1982 using the VLA in the A configuration revealed a core flux density of 253 ± 8 mJy at 1465 MHz and 417 ± 17 mJy at 4885 MHz. This measured flux at 5 GHz was significantly higher than the value obtained in 1979. This indicated a flat-spectrum radio core at higher frequencies, which usually implies synchrotron self-absorption. The radio core at higher frequencies also shows an inverted spectrum, which influences the total flux of the source at higher frequencies.

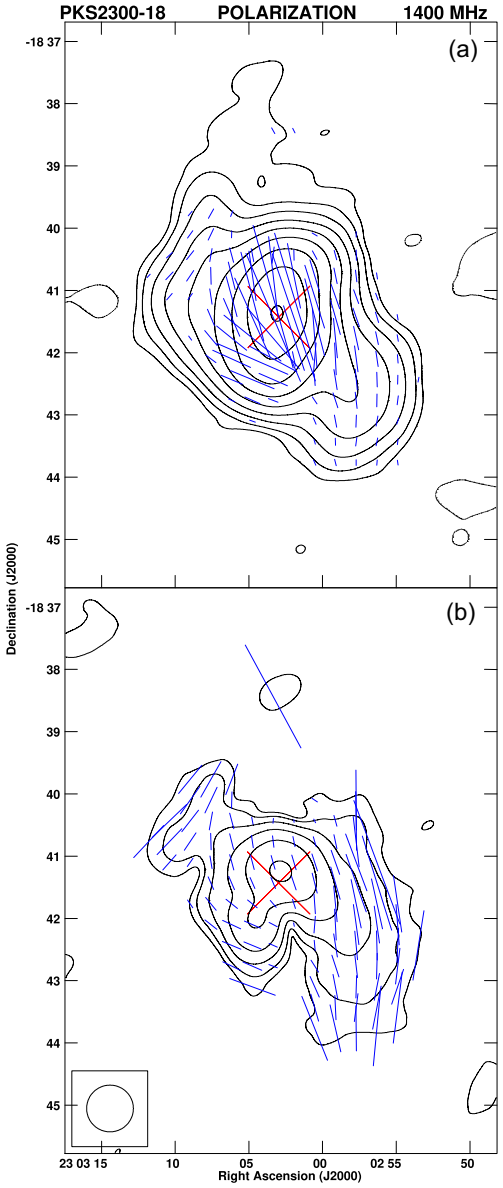

Figure 5. 1400-MHz NVSS polarimetric images. (a) Total intensity contours spaced by a factor of $\sqrt{2}^n$ starting at 1.8 mJy beam^{-1}. Superimposed are ***E***-vectors rotated by 90° with their lengths proportional to the polarized intensity, where 1 arcmin corresponds to a 12 mJy beam^{-1}. (b) Linearly polarized intensity contours spaced by a factor of $\sqrt{2}^n$ starting with 0.9 mJy beam^{-1}, with the vectors of the fractional linear polarization superimposed. A length of 1 arcmin corresponds to 30 per cent of the fractional linear polarization. The red X sign marks the central position of the host galaxy. The size of the convolved beam is indicated by a circle in the bottom left corner of the image.

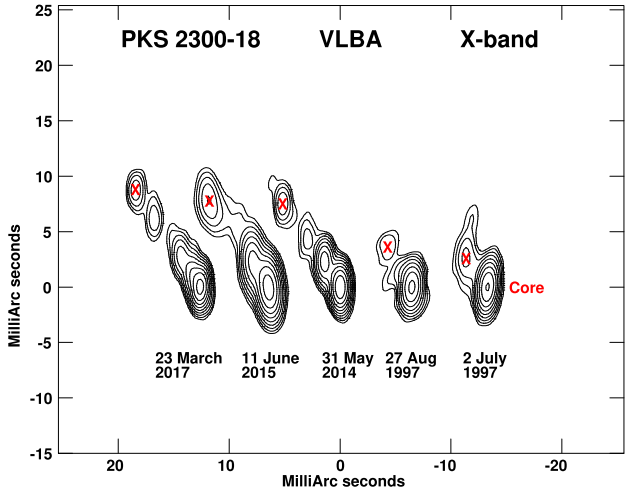

Figure 6. Apparent superluminal motion in the nucleus of the quasar PKS 2300−18. VLBA *X*-band five-epoch images of the variable pc-scale structure of the jet are shown. Positions of the core and a bright component named as the 'X' blob at the forefront of the jet are marked in red.

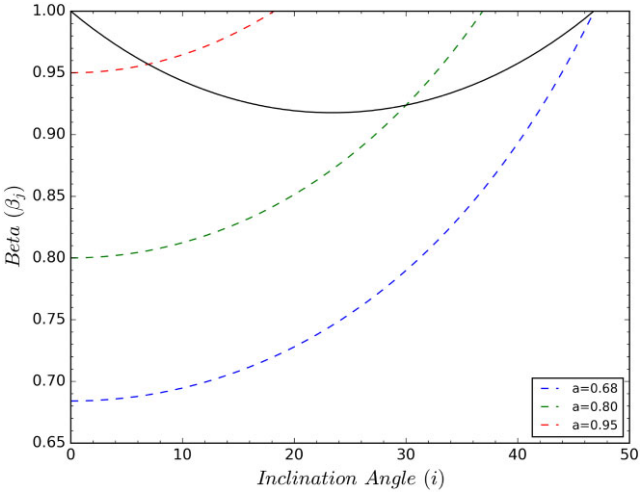

Figure 7. The dependence of the jet velocity β_j on the pc-scale jet inclination angle i in degrees for PKS 2300−18. The black solid line represents equation (2) and the dashed lines represent equation (3) for three different values of a: 0.95 (red), 0.8 (green), and 0.684 (blue), as detailed in Section 3.2.

The source was re-observed to study spectral behaviour and variability between 5 and 40 GHz as part of a sample of galaxies for the PACO project in several epochs between 2009 and 2010. The epoch 1 observations were conducted on 2009 November 11, epoch 2 on 2009 December 4, epoch 3 on 2010 June 14, and epoch 4 on 2010 June 19. The flux-density values of all four epochs are plotted in Fig. 8. The core spectrum shows a consistent pattern throughout the four epochs, with the core displaying an inverted spectrum up to 10 GHz followed by a steepening of the spectrum up to 40 GHz. The observations between epoch 1 and epoch 2, which were taken a few weeks apart, reveal considerable variations in the flux-density values across the observed spectral range. A similar pattern is observed between epochs 3 and 4, with these observations spaced less than a week apart. There are noticeable variations in the flux-density values, particularly at higher frequencies from 22 GHz upwards, where prominent changes are observed between epochs.

The variability of radio quasars is particularly noticed and studied in the case of blazars such as 3C 466 (Bregman et al. 1988), OJ 287 (Komossa et al. 2023), and S5 0716 + 714 (Rani et al. 2013). There are several factors that can cause such variability, including Doppler boosting in blazars or jets with a low inclination angle to the line of sight. Additionally, relativistic beaming can also lead to anisotropic emission, as noted by Woltjer (1966). Extrinsic factors often include interstellar scintillations that can cause flux-density variations on time-scales of a few hours or days (Koay et al. 2018). In the case of PKS 2300−18, the observed variations occur over periods

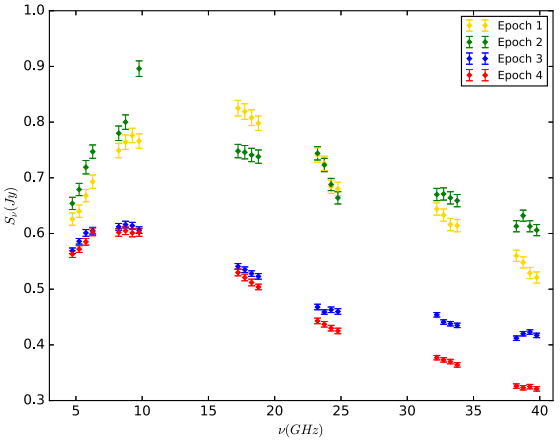

Figure 8. Flux-density values of the radio core of PKS 2300−18 in the frequency range 5–40 GHz showing variability (details in Section 3.3).

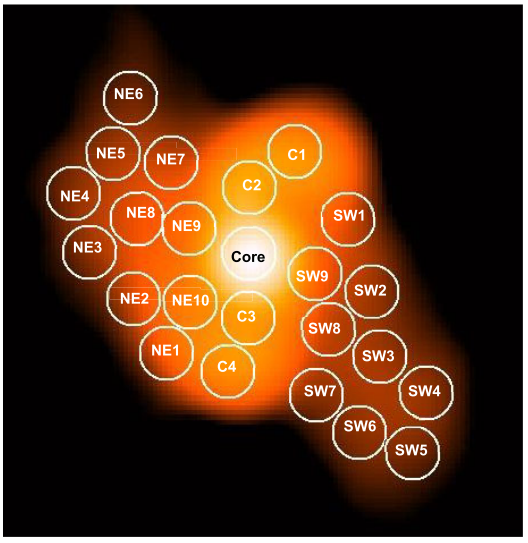

Figure 9. JVLA 6-GHz map displaying different regions of the source selected for fitting the particle injection model and ageing analysis.

ranging from a few weeks to several years, with minimal indications of fluctuation during these observation windows. A possible cause for this variability could also be inherent to the source itself, as suggested by Wagner & Witzel (1995), potentially arising from (a) a change in the accretion rate due to disc instabilities and thus jet power and brightness, (b) propagation of shocks along the jets, or (c) precessing jets that could vary the Doppler beaming of the ejected jet components. As the core variability seen in the case of PKS 2300−18 is on a time-scale of a few days to months, it is likely to have a point of origin very close to the core, possibly due to either some variation in the accretion rate or propagation of shocks in pc-scale jets. However, other scenarios might also contribute simultaneously towards it (Ricci & Trakhtenbrot 2023).

3.4 Analysis of radio spectra of the wings

3.4.1 Source energetics

Electrons present inside a fixed magnetic field emit radiation primarily via synchrotron processes. At higher frequencies, this leads to higher energy electrons losing energy much faster than their lower energy counterparts. This produces spectra that are increasingly curved over time when there is no further reacceleration of particles. To trace the movement of plasma over time and track the jet reorientation in PKS 2300−18, the north-eastern (NE) wing was divided into 10 separate circular regions and the south-western (SW) wing was divided into nine separate circular regions (see Fig. 9), based on the spectral gradient seen in Fig. 4, with the sampling region size similar to the radio beam (28 arcsec). The flux-density values of those regions are provided in Table 4. To calculate the radiative losses over time in these regions, the Jaffe & Perola (JP: Jaffe & Perola 1973) model was used to fit the spectrum of PKS 2300−18. All regions of the NE and SW wings were fitted with the JP model, due to their steep spectra and the absence of any compact hotspots in the wings. This model uses an initial power-law energy distribution to determine the time evolution of the radiative loss incurred by high-energy electrons as a result of synchrotron and inverse-Compton processes. This results in a higher degree of curvature in the spectrum consisting of older plasma.

Model fitting was carried out by analysing the emission spectrum of the particles, characterized by their injection spectral index ($\alpha_{\rm inj}$), distributed uniformly in pitch angle with respect to the direction of the magnetic field. The JP model was applied with the following assumptions: (i) the particles adhere to a constant power-law energy distribution without any reacceleration of radiating particles once they enter the regions, (ii) the magnetic field is constant in time and uniform in space and the field lines are tangled, with the field intensity remaining constant during the energy dissipation, (iii) the isotropization time is small compared with the radiative lifetime for the pitch angles of the injected particles.

The SYNAGE package (Murgia 1996) was used to fit the JP model to the radio spectra. The best-fitting models are shown in Figs 10 and 11. The resulting break-frequency values of the NE and SW wing regions obtained with the model fit are given in Table 5 and, from the pre-fitting results, $\alpha_{\rm inj}$ was observed to be close to 0.5, therefore it was fixed at 0.5. The $\nu_{\rm br}$ values for both the NE and SW wing regions obtained by the JP model gave $\nu_{\rm br}$ values comparable with or slightly higher than the highest radio frequency data presented in the article.

In the radio spectra of the NE wing, as given in Fig. 10, we see a clear gradient from regions NE1–NE6, with NE6 showing the steepest spectrum and NE1 showing a relatively flatter spectrum. This also indicates the anticlockwise movement of plasma where the jet moves from region NE6 to region NE1 while sweeping an S-like pattern in the plane of the sky. The regions NE7–NE10 are much flatter than the regions NE2–NE6, as also seen from the spectral-index map in Fig. 4. This is most likely the result of these regions being closer to the current direction of the southern jet, containing younger plasma. In Fig. 11, we have the spectra from the regions of the SW wing plotted, and a gradient similar to that previously seen in the case of the NW wing appears. In the spectra from SW1–SW7, the gradient becomes much steeper as we move from regions SW1 to SW7, with SW4–SW7 showing a similar steepening. Here, the spectra of SW8 and SW9 are comparatively flat, which is also consistent with the SI map. This aligns with a northward sweep of the jet in the anticlockwise direction. We therefore observe from the spectra that the jets have undergone reorientation, coming to the current north–south alignment after depositing plasma in the southwestern region, moving through SW7 to SW1, and correspondingly in the northeastern regions moving through NE6 to NE1. This gives an overall view of the trajectory of the precessing jet, moving in an anticlockwise direction along the NE and SW wings.

Table 4. Flux-density values (mJy) of different segmented regions of PKS 2300−18.

Region/Freq. (1)	183 MHz (2)	322 MHz (3)	400 MHz (4)	607 MHz (5)	888 MHz (6)	1367 MHz (7)	6000 MHz (8)
Total	4638±464	3325±332	2929±293	2301±161	1976±99	1364±68	805±40
NE1	8.7±2.1	7.0±0.7	5.6±0.6	4.0±0.4	3.5±0.4	3.0±0.4	0.9±0.1
NE2	8.5±2.1	6.6±0.7	5.7±0.6	3.6±0.4	3.2±0.4	2.6±0.4	0.5±0.1
NE3	4.7±2.0	2.9±0.4	3.2±0.4	2.3±0.4	1.9±0.4	1.3±0.4	0.2±0.1
NE4	4.5±1.9	4.1±0.5	3.4±0.4	2.5±0.4	1.8±0.4	1.3±0.4	0.2±0.1
NE5	4.5±1.9	4.9±0.5	3.9±0.4	2.5±0.4	2.2±0.4	1.3±0.4	0.3±0.1
NE6	2.9±1.9	3.3±0.4	2.5±0.3	1.5±0.4	1.4±0.4	0.8±0.4	0.2±0.1
NE7	5.9±2.0	5.3±0.6	5.0±0.5	3.0±0.4	2.7±0.4	1.9±0.4	0.4±0.1
NE8	10.1±2.1	6.4±0.7	6.8±0.7	5.0±0.5	3.9±0.4	2.8±0.4	0.6±0.1
NE9	16.3±2.5	10.8±1.1	10.2±1.0	6.9±0.6	6.2±0.5	5.0±0.5	1.5±0.1
NE10	26.1±3.2	19.9±2.0	16.1±1.6	11.2±0.9	10.0±0.6	8.1±0.6	2.3±0.2
SW1	5.9±2.0	6.1±0.7	4.5±0.5	2.8±0.4	2.9±0.4	2.0±0.4	0.5±0.1
SW2	4.2±1.9	2.7±0.4	3.5±0.4	2.5±0.4	2.0±0.4	1.4±0.4	0.3±0.1
SW3	5.5±2.0	4.6±0.5	3.6±0.4	2.6±0.4	2.1±0.4	1.2±0.4	0.3±0.1
SW4	4.2±1.9	4.2±0.5	3.5±0.4	2.7±0.4	2.2±0.4	1.1±0.4	0.2±0.1
SW5	3.8±1.9	2.8±0.4	2.6±0.3	1.6±0.4	1.5±0.4	0.8±0.4	0.2±0.1
SW6	3.4±1.9	3.5±0.4	3.0±0.4	2.2±0.4	1.8±0.4	1.0±0.4	0.2±0.1
SW7	3.8±1.9	4.0±0.5	2.7±0.3	1.5±0.4	1.6±0.4	1.3±0.4	0.2±0.1
SW8	6.0±2.0	3.9±0.5	4.2±0.5	3.3±0.4	2.7±0.4	1.8±0.4	0.4±0.1
SW9	11.8±2.2	9.9±1.0	7.6±0.8	5.4±0.5	5.6±0.5	3.8±0.4	1.5±0.1
C1	34.8±4.0	22.9±2.3	20.6±2.1	13.6±1.0	14.0±0.8	11.2±0.7	3.8±0.2
C2	68.5±7.1	47.1±4.7	42.1±4.2	28.8±2.0	28.0±1.4	22.5±1.2	7.6±0.4
C3	48.1±5.2	34.2±3.4	29.8±3.0	20.2±1.5	18.8±1.0	14.3±0.8	5.1±0.3
C4	34.1±3.9	23.0±2.3	20.1±2.0	14.2±1.1	12.5±0.7	10.0±0.6	3.3±0.2

Note. The flux-density values of columns (2)−(5) and (8) are taken from dedicated observations as detailed in Sections 2.1.1 and 2.1.2 and the flux-density values of columns (6) and (7) are taken from the RACS survey, as detailed in Section 2.1.4. The regions are defined in Fig. 9.

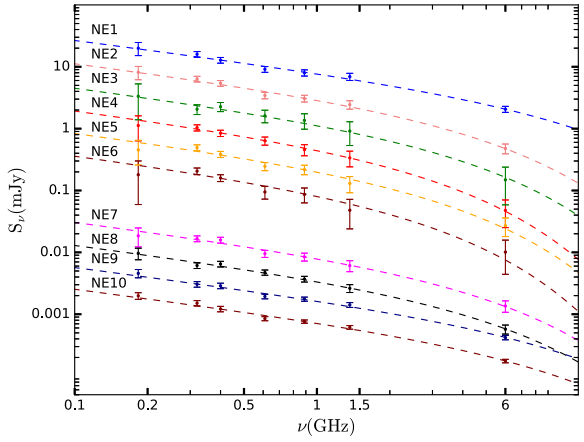

Figure 10. Radio spectra of the different regions from the NE wing (NE1–NE10) fitted with the JP model. The spectra of particular regions are shifted arbitrarily on the ordinate axis to give the appropriate picture of the curvature of the spectra. For details of the flux-density values see Table 4.

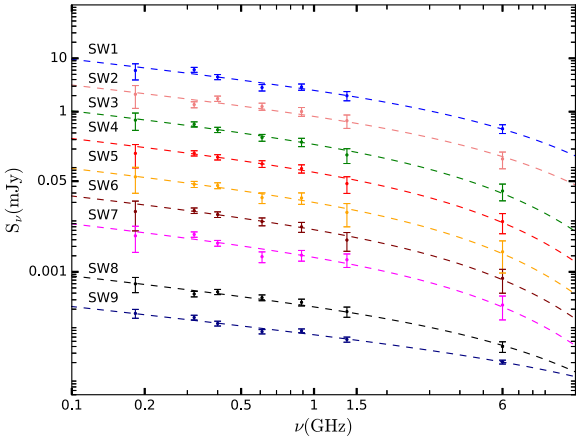

Figure 11. Radio spectra of the different regions from the SW wing (SW1–SW9) fitted with the JP model. The spectra of particular regions are shifted arbitrarily on the ordinate axis to give the appropriate picture of the curvature of the spectra. For details of the flux-density values see Table 4.

3.4.2 Spectral ageing

We estimate here the magnetic field strength and synchrotron age of the NE and SW wing regions from NE1–NE10 and SW1–SW9, respectively. The spectral age is calculated using Miley (1980) as follows:

$$\tau_{\rm rad} = 1590 \frac{B_{\rm eq}^{0.5}}{B_{\rm eq}^2 + B_{\rm CMB}^2} [\nu_{\rm br}(1+z)]^{-0.5} \,{\rm Myr}. \quad (5)$$

$B_{\rm CMB} = 3.18(1+z)^2$ is the magnetic field strength analogous to the cosmic microwave background radiation. The magnetic field strengths of the wings, i.e. $B_{\rm eq}$ and $B_{\rm CMB}$, are expressed in units of μG. The spectral break frequency $\nu_{\rm br}$ (in GHz), above which the radio spectrum steepens from the initial power-law spectrum, is given by $\alpha_{\rm inj} = (\gamma - 1)/2$. The magnetic field calculations ($B_{\rm eq}$) were done in accordance with the revised equipartition arguments provided by Beck & Krause (2005, see equation 3 therein). Magnetic field strength can be estimated directly for a source if it is detected simultaneously at radio and X-ray frequencies. Although our radio source was observed with *ROSAT*, its angular resolution is insufficient to distinguish the emission originating from the

Table 5. Break-frequency values and spectral ages of circular regions computed using the JP particle injection model.

Region	Break freq. (GHz)	$\chi^2_{\rm red}$	α^*	$B_{\rm eq}$ (μG)	Spectral age (Myr)
(1)	(2)	(3)	(4)	(5)	(6)
SW1	$9.2^{+>100}_{-2.9}$	1.13	0.88	$1.06^{+0.20}_{-0.11}$	$29.00^{+6.04}_{->20.93}$
SW2	$8.4^{+5.3}_{-5.2}$	1.25	0.97	$1.05^{+0.19}_{-0.11}$	$30.24^{+21.71}_{-7.55}$
SW3	$5.4^{+>100}_{-1.7}$	0.28	1.10	$1.13^{+0.21}_{-0.10}$	$38.74^{+10.77}_{->30.27}$
SW4	$5.2^{+9.2}_{-2.3}$	0.27	1.10	$1.11^{+0.20}_{-0.10}$	$39.22^{+16.31}_{-16.46}$
SW5	$5.0^{+>100}_{-2.6}$	0. 25	1.06	$0.99^{+0.18}_{-0.09}$	$38.32^{+20.50}_{->30.27}$
SW6	$5.2^{+18.7}_{-2.5}$	0.18	1.04	$1.03^{+0.19}_{-0.10}$	$38.15^{+18.10}_{-21.05}$
SW7	$5.3^{+>100}_{-2.0}$	1.22	1.00	$1.05^{+0.20}_{-0.10}$	$38.07^{+13.22}_{->29.85}$
SW8	$9.3^{+5.1}_{-5.3}$	0.65	0.91	$1.18^{+0.23}_{-0.11}$	$29.97^{+18.36}_{-6.63}$
SW9	$30.7^{+>100}_{-16.3}$	1.10	1.10	$1.50^{+0.28}_{-0.14}$	$17.74^{+9.15}_{->9.37}$
NE1	$19.5^{+>100}_{-9.4}$	0.48	0.92	$1.21^{+0.24}_{-0.12}$	$20.87^{+9.78}_{->12.74}$
NE2	$7.7^{+41}_{-2.2}$	0.54	1.00	$1.25^{+0.24}_{-0.12}$	$33.58^{+8.26}_{-21.21}$
NE3	$6.6^{+5.6}_{-3.8}$	0.45	1.10	$1.16^{+0.21}_{-0.11}$	$35.36^{+20.61}_{-10.27}$
NE4	$4.8^{+12.4}_{-2.1}$	0.11	1.00	$1.05^{+0.20}_{-0.10}$	$40.00^{+16.71}_{-19.66}$
NE5	$5.5^{+>100}_{-1.6}$	0.69	1.03	$1.08^{+0.21}_{-0.10}$	$37.76^{+9.90}_{->29.45}$
NE6	$4.3^{+>100}_{-2.1}$	0.57	0.92	$0.88^{+0.15}_{-0.10}$	$39.43^{+19.23}_{->31.82}$
NE7	$8.0^{+47.1}_{-2.6}$	0.53	1.00	$1.16^{+0.22}_{-0.11}$	$32.12^{+9.22}_{-20.31}$
NE8	$8.2^{+5.0}_{-3.2}$	0.36	0.90	$1.17^{+0.23}_{-0.11}$	$31.82^{+11.32}_{-7.61}$
NE9	$17.7^{+51.7}_{-7.7}$	0.57	0.80	$1.26^{+0.26}_{-0.12}$	$22.20^{+8.99}_{-11.36}$
NE10	$15.5^{+33.4}_{-4.7}$	0.88	0.83	$1.46^{+0.29}_{-0.14}$	$24.79^{+6.17}_{-11.23}$
C1	$33.1^{+>100}_{-20.4}$	2.09	0.62	$1.82^{+0.39}_{-0.19}$	$17.81^{+11.53}_{->9.12}$
C2	$28.6^{+30}_{-16.4}$	1.49	0.64	$2.19^{+0.45}_{-0.23}$	$19.54^{+10.26}_{-6.02}$
C3	$26.6^{+>100}_{-7.8}$	0.92	0.73	$1.94^{+0.39}_{-0.20}$	$20.05^{+4.02}_{->11.02}$
C4	$21.3^{+>100}_{-6.2}$	0.65	0.63	$1.76^{+0.37}_{-0.19}$	$22.07^{+4.78}_{->13.04}$

Note. ∗The alpha (α), i.e the mean spectral-index values of the individual regions, were estimated from the SI map in Fig. 4.

wings from the strong X-ray emission generated by the radio core.

For the calculation, the following assumptions were made: (i) the ratio of proton-to-electron number densities $K = 0$ (a relativistic electron–positron plasma), (ii) the polarized emission originates from a regular magnetic field with all possible inclinations, and (iii) the degree of polarization is 7 per cent (for details see Section 3.1.2). We made use of the BFIELD program developed by Beck & Krause (2005) to apply their revised calculations and obtained the magnetic field strength of 23 different regions within the radio structure as marked in Fig. 9. The volume of the circular regions in the wings was estimated using a cylindrical geometry. The calculated values of magnetic field strength and spectral age of the respective regions are given in Table 5. It is also observed that the magnetic fields in the wing regions are mostly uniform, ranging between 0.88 and 2.19 μG, and the median value is ∼2.1 times lower than the minimum magnetic field value of $B_{\rm CMB}/\sqrt{3} = 2.34$ μG, which minimizes the radiative losses and maximizes the lifetime of the source, providing an upper limit. In the case of the SW wing, the spectral age from SW1–SW7 ranges between 29 and 39 Myr, with the youngest plasma being in region SW1, which is closest to the current location of the northern jet, with SW7 containing comparatively older plasma. We see a similar gradient in the ageing of the NW wing between NE1 and NE6, ranging from 21–40 Myr, with NE6 containing the oldest plasma of 39 Myr and NE1 containing the youngest plasma of 21 Myr. NE6 is furthest from the southern jet, whereas NE1 is closest to the southern jet, so this trend in spectral age confirms the anticlockwise movement of plasma in the wings. C1, C2, C3, and C4, located in the northern and southern jet regions, have spectral ages between 17 and 22 Myr and magnetic field in the range 1.8–2.2 μG. The magnetic field is higher in these regions compared with the NE and SW wings and the spectral ages are lower, given that it is along the current north–south orientation of the jets. Nonetheless, these ages might still be overestimated because of the presence of diffuse background plasma originating from earlier emission due to the former orientation of the jets during precession.

We hence observe that the oldest plasma in both the NE and SW wings is of similar age, supporting our assessment of jet reorientation taking place in the source. Based on our analysis, we interpret that the NE wing was formed as the southern jet gradually moved from its earliest position at NE6 to its current position at NE1. Similarly, the northern jet progressed from SW7 to SW1, resulting in the formation of the SW wing.

4 OPTICAL PROPERTIES OF THE CENTRAL AGN

The rest-frame optical spectrum shown in Fig. 12 clearly exhibits a quasar spectrum, characterized by a power-law continuum and a combination of broad and narrow emission lines. In particular, the Hα and Hβ lines feature broad double-peaked components. The power law (PL) and the iron continuum (Fe) were fitted with PyQSOFit (Guo, Shen & Wang 2018). The emission lines measured in the residual spectrum presented extended wings and therefore were fitted with a Lorentzian profile. The Hα and Hβ lines were fitted with a combination of one narrow and two broad components. The Hα line was fitted simultaneously with [N II]λλ6548,6583 and [O I]λ6300 narrow lines that were blended with Hα. [S II]λλ6717,6731 lines were affected by the telluric sky line and were not taken into account. The Hβ line was fitted with [O III]λλ4959,5007 lines and He II λ4687. [O III]λ5007 was affected by the bright sky line and therefore was not taken into account in further analysis. The fits obtained for both Balmer lines were consistent and they were used to obtain information about the central AGN. The fluxes, widths, and shifts of the broad components with respect to the narrow ones are presented in Table 6. The optical quasar outshines the host galaxy; therefore, it was not possible to extract the host galaxy's contribution from the optical spectrum.

Monochromatic luminosity at 5100 Å is often used to estimate the virial mass of the SMBH, size of the broad-line region (BLR), AGN bolometric luminosity, and Eddington ratio. The measured flux density at 5100 Å $= (22.83\pm0.55) \times 10^{-17}$ erg s^{-1} cm^{-2} Å^{-1} and the source luminosity distance, $D_L = 601.7$ Mpc, gives the monochromatic luminosity $\lambda L_\lambda(5100) = (5.04\pm0.13) \times 10^{43}$ erg s^{-1}. Using the virial mass–luminosity relation of Greene & Ho (2005, equation 5 therein) and the width of the broad component Hβ = 9020 km s^{-1}, derived according to the procedure described by Peterson et al. (2004), the total black hole (BH) mass in PKS 2300−18 is $= (2.31\pm1.02) \times 10^8$ M$_\odot$. The size of the BLR, estimated based on the Greene & Ho (2005) relation, is 13.9±0.2 light-days.

Total bolometric luminosity can be calculated assuming a simple relation between monochromatic luminosity $\lambda L_\lambda(5100)$ and AGN bolometric luminosity in the form $L_{\rm bol} = C_\lambda \lambda L_\lambda$. With the value of $C_{5100} = 9$ adopted after Kaspi et al. (2000), the bolometric luminosity

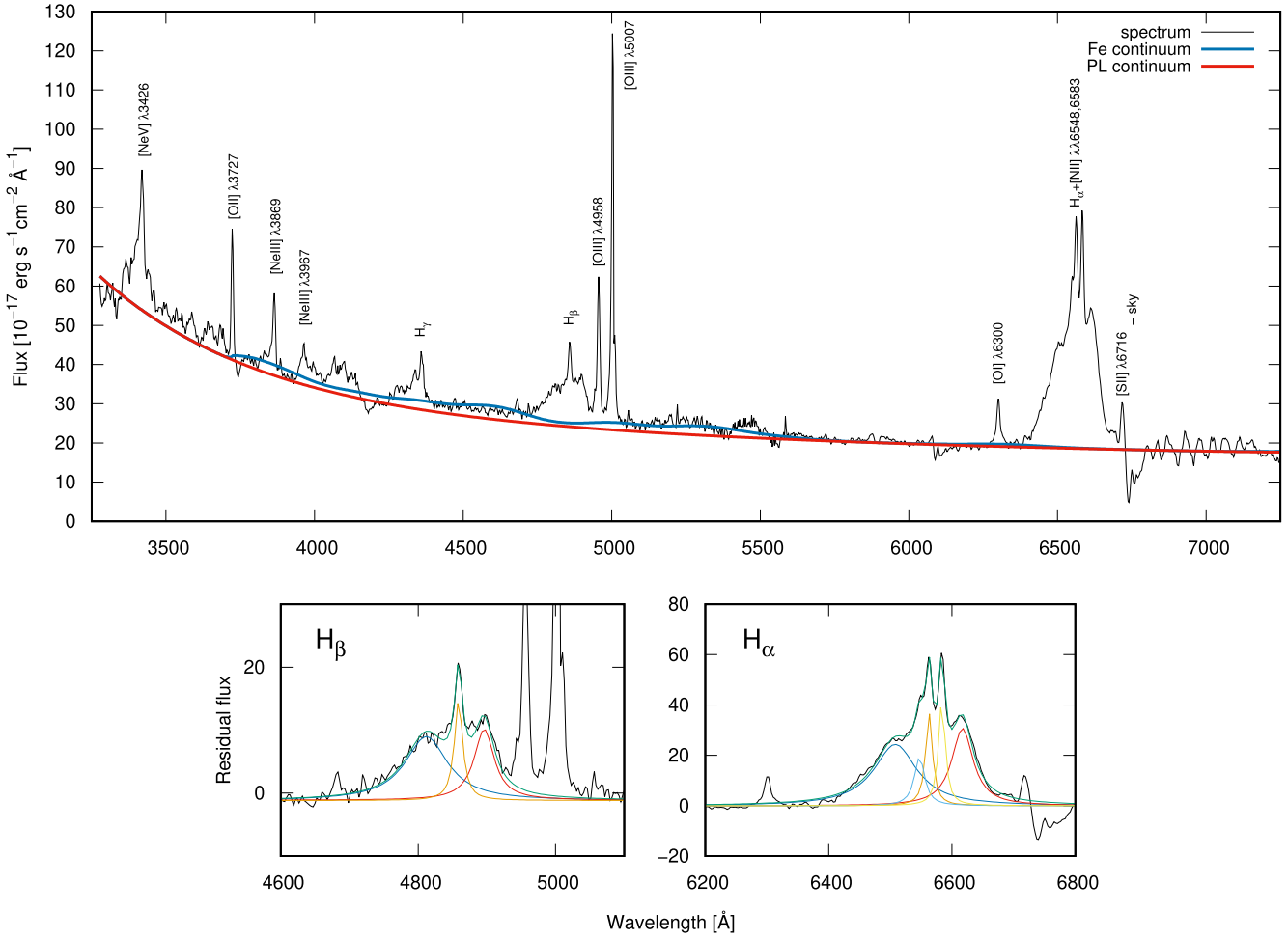

Figure 12. Optical spectrum of PKS 2300−18 obtained from WHT observations. The top panel shows the rest-frame observed spectrum (in black) with power-law continuum (in red) and Fe continuum (in blue). The bottom panels show Hβ and Hα regions modelled using a Lorentzian profile. The total fitted flux is shown in green, blue broad components are shown in blue, red broad components are shown in red, and narrow components are shown in orange. [N II] λ6548 and [N II] λ6583 lines in the bottom right panel are shown in light blue and yellow, respectively.

Table 6. The Hα and Hβ parameters of the rest-frame optical emission lines of PKS 2300−18.

Line	Component	Flux (10^{-15} erg s^{-1} cm^{-2})	FWHM (km s^{-1})	Shift v_d (km s^{-1})
	broad blue	13.19±0.84	5490±1300	−2840±96
Hβ	narrow	3.44±0.23	820±110	
	broad red	6.28±0.08	2130±540	2331±8
	total broad	19.47±0.92	9020±1890	
	broad blue	32.8±3.0	3970±400	−2520±250
Hα	narrow	7.0±1.3	470±280	
	broad red	21.78±1.5	2000±280	2457±46
	total broad	54.6±4.5	8015±950	

of PKS 2300−18 $= (4.54\pm0.1) \times 10^{44}$ erg s^{-1} and the Eddington ratio is 0.015±0.007.

Double-peaked broad emission lines are a rare feature among AGNs, and radio sources in particular. They are often explained by the presence of a binary black hole (BBH: e.g. Gaskell 1983; Popović 2012), irradiated disc (Eracleous & Halpern 1994), or irradiated disc with a spiral perturbation (Chakrabarti & Wiita 1994; Gilbert et al. 1999). With only one-epoch spectral data, these scenarios cannot be easily distinguished. However, in the case of PKS 2300−18, where precession of the jets and radio and optical variability are observed, the assumption about the presence of a BBH system seems plausible.

There may be different configurations of the BBH system, with (1) both BHs active and having their own BLRs, (2) both BHs active but with a common BLR, and (3) only one BH active (see e.g. Popović 2012). With the available data, the first scenario could be tested.

As shown by Greene & Ho (2005), $\lambda L_\lambda(5100)$ correlates well with the Hα and Hβ luminosities. Assuming that the double-peaked broad emission lines result from the presence of a BBH with separate BLRs, each broad component can be interpreted as being emitted by a different AGN. In that case, the ratio of the luminosities of broad-line components should be the same as the ratio of $\lambda L_\lambda(5100)$ of each AGN. BLR radii would be then 15.2±1.1 and 9.5±0.1 light-days based on Hβ (14.1±1.3 and 10.8±0.7 light-days based on Hα). From the separation of broad components, the separation of the BHs in the system can be found as follows (Sebastian et al. 2024):

$$d_{\rm BBH} \leq \frac{G * (M_{\rm BH1} + M_{\rm BH2})}{\Delta v_{\rm d}^2}. \quad (6)$$

This separation from Hβ measurements would be equal to 17.4 light-days and 10.1 light-days according to Hα data. These values

are smaller than the sum of the BLR radii, and thus BHs would be surrounded by a common BLR. With these simple estimates, the scenario about separate BLRs contributing to the double-peaked broad emission lines in PKS 2300−18 can be ruled out. However, the remaining two other possibilities cannot be easily distinguished, as PKS 2300−18 is a variable source (see Sections 1 and 3.3) and many quasars also show variations in broad emission lines; therefore, estimates based on one-epoch observations can be biased. Visual comparison with previously published data from Hunstead et al. (1984) and Eracleous & Halpern (1994) may suggest spectral variability, and future systematic spectral observations and reverberation mapping can help to clarify the scenario of the structure of the line-emitting gas and help to distinguish further between a single irradiated disc and the SMBH binary scenario (e.g. Shen & Loeb 2010).

5 X-RAY STUDY

In the X-ray broad-band (0.2−7 keV) *Chandra* image of PKS 2300−18 (Fig. 13), the radio core coincides with a bright point-like source, the extent of which reaches 8 arcsec, which is significantly larger than the PSF of the Advanced CCD Imaging Spectrometer (ACIS) instrument (Fig. 14). This suggests that the X-ray image captures not only the central AGN but also the hot interstellar medium of the host galaxy. Toward the north, a few more compact X-ray sources are visible that coincide well with the radio knots K1–K3 in the *Chandra* image as seen in Fig. 13. The knot K1 is also visible in the optical HSCLA *r*-band image, as seen in the insert in Fig. 13, making it the first multiwavelength detection of a knot in an S-shaped RG jet. The radio to optical emission (and X-rays in some cases) can be attributed to synchrotron radiation from the jet extended at higher frequencies, produced by relativistic electrons interacting with the jet's magnetic field. However, such X-ray emission in the knots can also stem from the inverse Compton scattering of cosmic microwave background (CMB) photons, while the optical emission might originate from upscattered CMB photons when they interact with the relativistic electrons in the jet. An interesting observation here is that a visible lag can be seen between the radio contour and the X-ray peak, seen most clearly in knot K1 and to a lesser extent in knots K2 and K3.

We extracted spectra of all four sources (knots and centre), but only in the case of the host galaxy (or core region) was a more detailed spectral analysis possible. For this spectrum, we used a model consisting of a thermal and a power-law component accounting for the hot gas in the host galaxy/core region and the central source, respectively. The thermal component is described by the *mekal* model (Mewe, Gronenschild & van den Oord 1985; Kaastra 1992) of thermal bremsstrahlung with additional emission lines. The metallicity in this model was set to solar. The absorption in our Galaxy was taken into account via the *wabs* model with a fixed value of column density towards the source.

The derived model describes the spectrum of the core region well, except for the energy range between 1 and 1.5 keV, in which a significant excess of X-ray emission over the model can be observed. This could suggest that an additional thermal component of very high temperature (describing the hot gas in the core region) is needed. However, such a modification of the model did not improve the fit and the new parameter could not be constrained. Much better results were obtained by allowing the metallicity of the *mekal* model to vary. In this case, however, a good model fit to the spectrum required metallicity to be as low as around 3 per cent solar. Such a level of metal abundance certainly needs explanation. We note here that the radius of our spectral region of 4 arcmin corresponds to around 9 kpc, which means that we probe the conditions in the direct vicinity of the AGN. Recently, Russell et al. (2024) found similar low metallicity at the core of a low-redshift quasar (within 10 kpc), which they explained as a potential result of photo-ionization of the hot atmosphere by quasar emission. We argue that this might also be the case for PKS 2300−18. In Table 7 and Fig. 14 we present the parameters of the fitted models (both variable and solar metallicity) and their plots with residuals, respectively.

6 DISCUSSION

6.1 Formation of S-shaped jet morphology

The characteristic curvature of radio jets in the case of winged radio galaxies is observed in the form of X-, S-, and Z-shaped morphologies (Rubinur et al. 2017; Cotton et al. 2020; Bhukta, Pal & Mondal 2022a; Misra et al. 2023; Sethi et al. 2024). In most of these sources, one pair of lobes undergoes active evolution, often leading to hotspot formation, while the accompanying pair of wings or the secondary pair of lobes have low surface brightness emission and are relatively diffuse and extended. Until recently, distinctively recognizing winged morphologies in low-resolution observations was challenging; however, with the advent of high-sensitivity and deep radio surveys, it has become easier to distinguish between different classes of winged RGs. X-shaped sources are typically formed as a result of backflowing jet plasma deflected laterally by an asymmetric medium (Leahy & Williams 1984; Capetti et al. 2002; Cotton et al. 2020; Giri et al. 2024) or by the sudden spin flip of an SMBH post-merger (Merritt & Ekers 2002; Rottmann 2002), whereas Z- and S-shaped radio sources are often considered to be the result of underlying jet precession (Gower et al. 1982; Rottmann 2002; Horton et al. 2020, 2023). As marked by Krause et al. (2019), the best indicators of jet precession are (i) a jet at the edge of the lobe, (ii) curvature in the jet path, (iii) S-shaped symmetry, and (iv) multiple or complex hotspots. These indicators make the S-shaped morphology one of the most suitable classes among winged RGs for studying jet precession.

When studying such S-shaped sources, it is important to be cautious of environmental factors other than conventional jet precession that might lead to an S-shaped morphology. Sources displaying helical jets have been found in X-ray binaries (Hjellming & Johnston 1981b), planetary nebulae (Lopez, Meaburn & Palmer 1993), and AGN jets (Rawes, Birkinshaw & Worrall 2018; Ubertosi et al. 2024). A prototypical helical jet can be described by three different jet structures, as elucidated by Steffen (1997). The first model consists of a ballistic helical jet, where the individual jet fluid elements follow a straight path but the overall structure becomes helical as the direction of ejection of the fluid elements changes periodically; these jets demonstrate precession. In the second model, the helical jets are bent as a whole and the fluid elements follow a common twisted trajectory, delineated by a curved jet axis. Jet bending of this type can be seen when the jets undergo intrusion due to collision with gas clouds or interaction with transverse winds or a dense ambient medium. In RGs like 3C 433 and 4C 65.15, which exhibit jets with a hybrid FR morphology, *Chandra* observations reveal that the FRI structure observed on one side of these hybrid sources arises from a powerful jet interacting with a comparatively dense medium (van Breugel et al. 1983; Miller & Brandt 2009). Also, such jet bending can be observed in the case of 3C 321 (Evans et al. 2008), where one of its jets bends after interacting with a neighbouring companion galaxy that is undergoing a merger with the host galaxy. In the

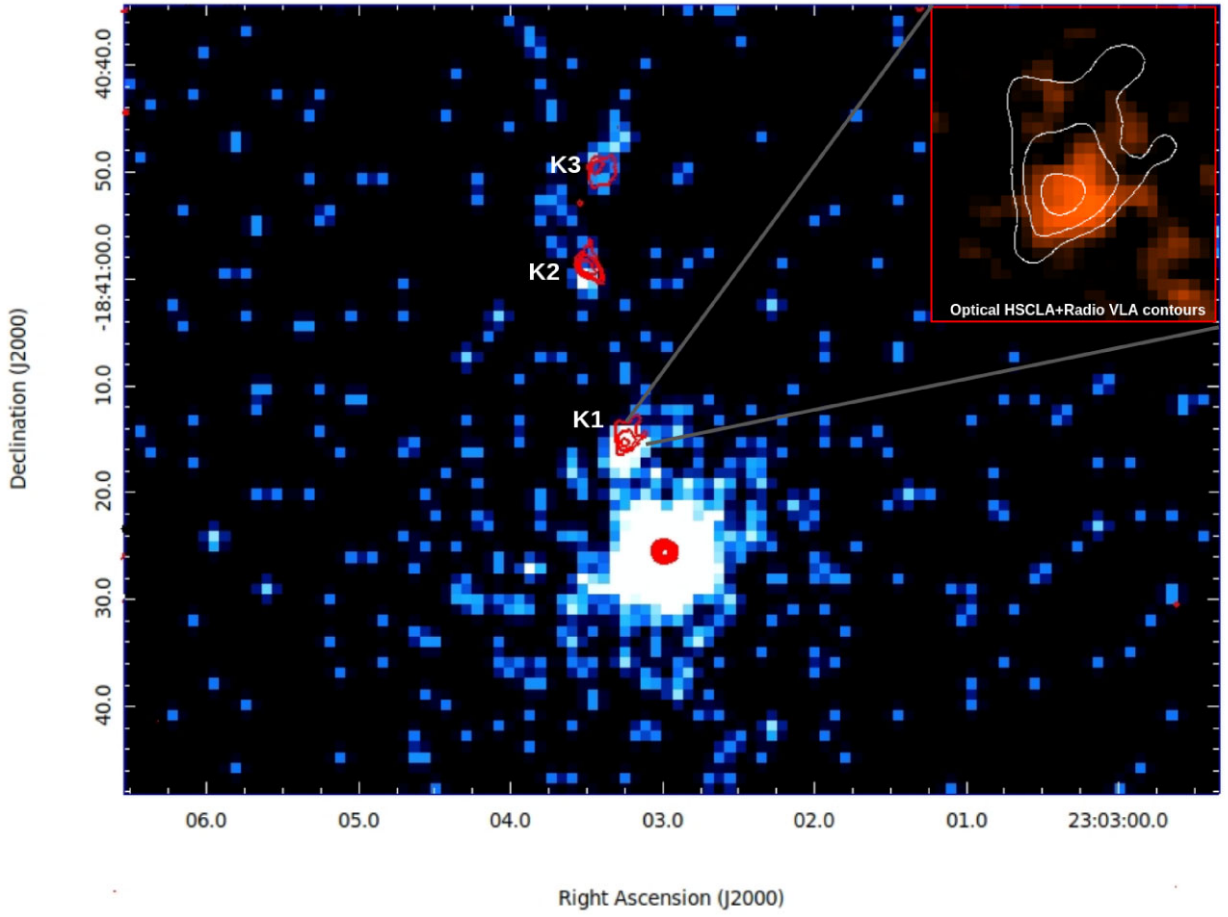

Figure 13. X-ray image from *Chandra* of the host PKS 2300−18 as seen in blue. The red contours overlaid on top of the X-ray map are VLA contours at 5 GHz with 0.7-arcsec resolution. The radio contours show the location of the core and three knots of the northern jet. The radio knots coincide with points of enhanced X-ray emission. In the inset towards the top-right corner we have the first radio knot, K1, as seen in the HSCLA *r*-band image in orange, overlaid with radio VLA 5-GHz contours.

third model, the jets have a helical structure internally. Such jets are straight as a whole, but have fluid elements flowing along helical trajectories within the jet. This type of jet might be produced as a result of Kelvin–Helmholtz instabilities (Hardee 1987; Hardee & Clarke 1992; Perucho et al. 2006, 2012). These instabilities can be observed in transverse oscillations in the M87 jet during VLBA observations, where a shift of the transverse position of the jet on a quasi-periodic 10-yr time-scale was seen, consistent with Kelvin–Helmholtz instability (Walker et al. 2018; Nikonov et al. 2023). The VLBI observations of M87 jet also showed 1-yr period wiggles in multi-epoch observations (Ro et al. 2023).

We first consider the case where the S-shaped jets of PKS 2300−18 are bent as a result of local environment interaction and discuss other scenarios thereafter. The S-shaped jets, which are currently orientated in the north–south direction, show inversion-symmetric jet bending. It is statistically unlikely that the northern and southern jet encounter and are obstructed by gas clouds within the confines of the host galaxy located on an axis of about 180°. Furthermore, such obstruction by clouds that are aligned in opposite directions on either side of the galaxy will likely cause jet bending/curvature much closer to the periphery of the host galaxy, however we only see strong jet curvature at a scale of more than 150 kpc. The formation of multiple jet knots (see Fig. 3), much further than the confines of the host galaxy, in the case of the northern jet also hints that the jet is not getting obstructed by gas clouds, which would lead to a jet with a diffuse structure rather than a collimated structure as seen in the case of the northern jet. The presence of diffuse emission around the S-shaped jets also indicates that the jets were previously oriented in the northeast and southwest direction and have gone through jet reorientation. Therefore, given the above arguments, the helical jets of our target seem unlikely to be a result of collision with gas clouds.

We now consider the possibility that the observed bending is a result of the pressure gradient within the hot gas halo surrounding the host galaxy. In such a case, the halo should lead to a plane-symmetric effect for both jets (e.g. 3C 98) and an uneven curvature of the jets, rather than the S-shaped inversion symmetry seen in the case of PKS 2300−18. Another potential explanation could be that Kelvin–Helmholtz instability in the jets is responsible for the observed bending. This instability would most likely give rise to 'wiggles' or sharp small bends in the jets. However, we observe a well-collimated curved jet, which is visible in the case of the northern side of the jet and completely absent on the southern side of the jet. The jets also appear to be curved and not straight as a whole. Therefore, Kelvin–Helmholtz instability seems to be an unlikely explanation for the S-shaped jets seen in our target. The

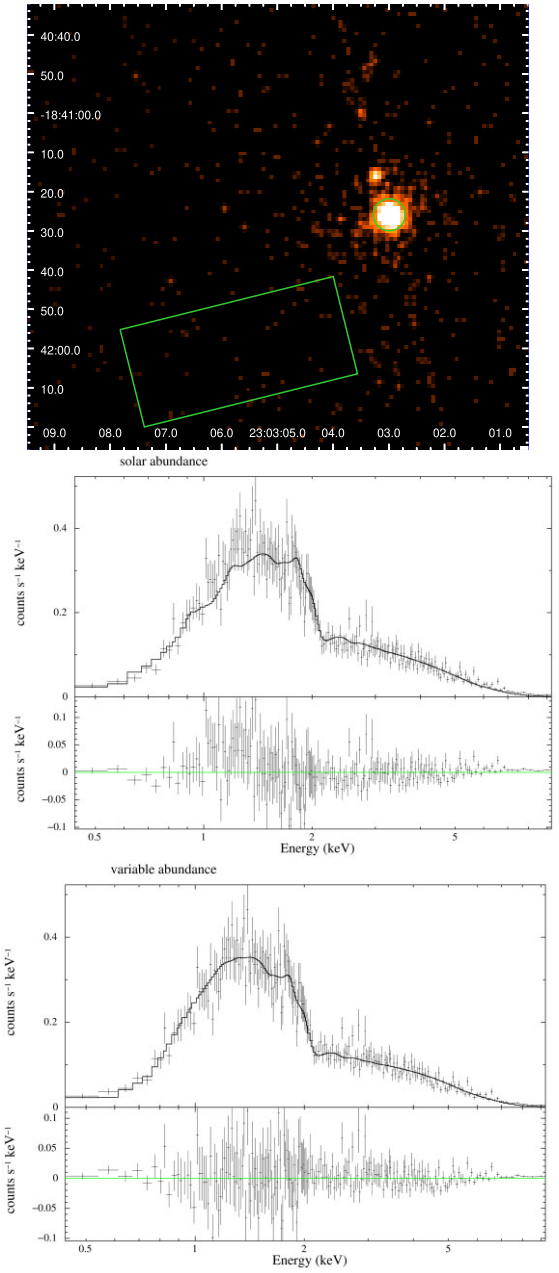

Figure 14. Top: regions used in the spectral analysis of the core of PKS 2300−18 from *Chandra* X-ray data. The core region is marked with a green circle and the background region with a green rectangle. Bottom: extracted *Chandra* X-ray spectrum of the core region with fitted solar abundance and variable abundance model and residuals. For detailed discussion see Section 5.

most plausible scenario here remains a ballistic helical jet that arises due to jet precession. In the high-resolution VLA *L*-band map, as seen in Fig. 3, the three jet knots that are visible in the northern jet are seen moving along curved trajectories, which is strongly indicative of plasmoids being ejected in different directions. Furthermore, there is low surface brightness extended emission along the north-eastern and south-western side of the S-shaped jets that is caused by jet reorientation. Such large-scale jet reorientation can only be explained by jet precession.

Table 7. Parameters of the model fit to the spectrum of the core region.

	low Z	solar Z
kT [keV]	$0.61^{+0.22}_{-0.16}$	$0.32^{+0.28}_{-0.04}$
S_{kT} [10^{-12} erg cm^{-2} s^{-1}]	$4.83^{+5.85}_{-2.49}$	$2.73^{+2.19}_{-1.15}$
Γ	$1.04^{+0.15}_{-0.19}$	1.41 ± 0.05
S_Γ [10^{-12} erg cm^{-2} s^{-1}]	$14.4^{+11.3}_{-6.3}$	$14.7^{+2.3}_{-2.0}$
red. χ^2	1.096	1.328
d.o.f.	193	194

Note. In our model fits we used the weighted average value of $N_{\rm H} = 1.88\times10^{20}$ cm^{-2} after the HI4PI survey (HI4PI Collaboration et al. 2016). The fluxes are derived in the range 0.3–10 keV.

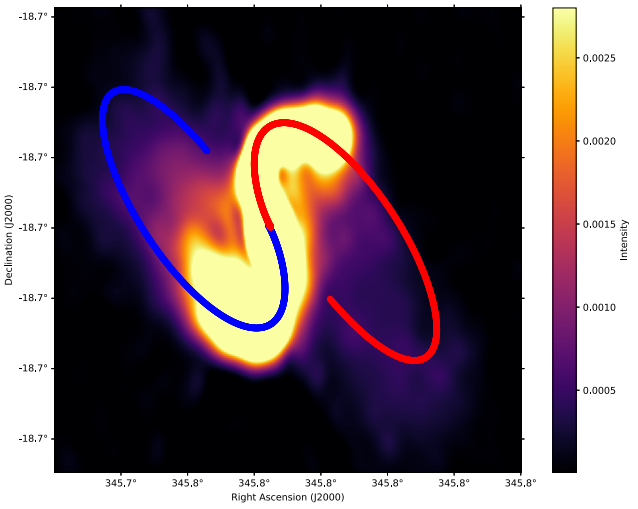

Figure 15. Kinematic jet precession model overlaid on top of the JVLA 6-GHz map. The colour gradient represents flux density in units of Jy beam^{-1}. The red and blue lines represent the jet and counterjet, respectively.

6.2 Kinematical modelling of jet precession

In this section, we proceed towards modelling the precession of the radio jet in the case of PKS 2300−18. We modelled the jet using the kinematic jet precession model of Gower et al. (1982), originally developed by Hjellming & Johnston (1981a) to model the jets of the SS 433 microquasar. In this model, symmetric jets are launched along an axis that traces a cone throughout a precession period P. The model parameters primarily include the following: the precession cone half opening angle (ψ), the cone inclination angle (i), the position angle (θ), and the jet advance speed (β). The proper-motion plots were derived from a visual inspection, by varying the values of the model parameters to match the radio map of PKS 2300−18 at JVLA 6 GHz, given in Fig. 15. The best-fitting model values, which were fitted to multiple high-resolution maps including the VLA *L*-band A and C configuration maps with the highest resolution for constraining the degeneracy, are $i = 67^\circ$, $\psi = 66^\circ$, $\theta = 119^\circ$; note that these values are similar to the ones obtained by Hunstead et al. (1984). To determine the errors associated with our precession model, we estimated the range of parameters that can fit the radio morphology by fixing all parameters except one, and then subsequently varying it until the visual fit became noticeably worse (Steenbrugge & Blundell 2008); this step was then followed for the rest of the parameters. The parameter ranges obtained using this method are $i = 67^\circ \pm 4^\circ$, $\psi = 66^\circ \pm 4^\circ$, $\theta = 119^\circ \pm 4^\circ$. This gave a best fit for P in the range

12 ± 8 Myr. The β here was confined to be below $0.2c$, as values higher than that lead to asymmetric lobes, making one side lobe much larger than the other. The lower limit was set as $0.01c$. The precession period obtained here is a few Myr lower than the maximum spectral age obtained for the source, which might hint that the jets have gone through more than one precession cycle. The upper limit of β is much lower than the ones obtained from the analysis of the VLBA pc-scale jets in Section 3.2. This may be attributed to changes in the large-scale precessing jets, which have been observed to decelerate as they interact with the intergalactic medium in simulation studies (Giri et al. 2022). As a result, while the pc-scale precessing jets might still have relativistic speeds, their bulk motion at the kpc scale can remain mildly relativistic.

6.3 Mechanisms for jet precession

Jet precession resulting in S-shaped radio jets is likely to occur in a binary SMBH system (Begelman et al. 1980). Within such a binary system, the spin axes of the BHs are likely to be misaligned, unless they have both accreted a significant amount of gas with fixed angular momentum. The spin axes will then subsequently undergo geodetic precession and, for the more massive BH, the precession period $P_{\rm prec}$ can be given by the following:

$$P_{\rm prec} \sim 600 r_{16}^{5/2} \left(\frac{M}{m}\right) {M_8}^{-3/2}\ {\rm yr}, \tag{7}$$

where r_{16} is the separation in units of 10^{16} cm, M_8 is the mass of the primary SMBH in units of 10^8 $M_\odot$, and (M/m) is the mass ratio of the primary to the secondary SMBH (Begelman et al. 1980). Considering a scenario where BH mass ratios lie between 1 and 10, a primary BH mass of 2.31×10^8 $M_\odot$ (from Section 4), and the precession period of 12 Myr from the kinematical model in Section 6.2, we obtain binary separation values of $\sim$ 335 and $\sim$ 133 light-days, respectively. This indicates the possibility that the binary has shrunk to a sub-pc scale separation, due to which, even in the VLBI observations (as seen in Fig. 6), it would be impossible to separate two different components at the centre. The orbital period of such a BBH, assuming a Keplerian orbit, can be given by the following:

$$P_{\rm orb} \sim 1.6 r_{16}^{3/2} {M_8}^{-1/2}\ {\rm yr}. \tag{8}$$

This results in orbital periods of $\sim$ 856 and $\sim$ 212 years for binary SMBH mass ratios of 1 and 10 respectively, and can be categorized as a wide binary system. Besides a BBH system, a single AGN model can also explain the helical motion of BH jets. Based on the Sarazin, Begelman & Hatchett (1980) model for SS 433, a tilted accretion disc can also cause jet precession. According to this model, if the accretion disc is tilted with respect to the equator of the central SMBH, i.e. the rotation axis does not align with the central BH spin, then the Lens–Thirring effect (Lense & Thirring 1918) can cause the disc material inside a specific inner radius to align with the BH's equatorial plane. Meanwhile, the outer part of the disc, which possesses significant angular momentum, will preserve its orientation and induce precession of both the central BH and the inner disc (Bardeen & Petterson 1975). Some material of the inner disc is assumed to be ejected out along the BH's spin axis, forming a precessing jet. This model of a tilted accretion disc around a single AGN also gives a relation between the precession period and optical luminosity, as given by Lu (1990).

We have used this period–luminosity relation, where the absolute B-band magnitude of our target is $M_{\rm abs} = -20.51$, to give an estimated precession period in the range of $\sim$ 6–20 Myr. This does agree well with the dynamical age from the jet precession model, but differs by a few Myr from the maximum spectral age of 40 Myr. It also remains a possibility that the accretion disc, in the case of PKS 2300−18, becomes wrapped or tilted due to non-uniform irradiation from the AGN, which can lead to jet precession (Pringle 1997). As we have not resolved two separate optical cores and VLBI observations are limited by their resolution, it is hard to rule out one of the above precession scenarios. Therefore, jet precession in PKS 2300−18 might be caused either by a SMBH binary or by a wrapped/tilted accretion disc.

6.4 Cohorent multiwavelength picture

This work delves into the radio, optical, and X-ray properties of the S-shaped radio quasar PKS 2300−18 to probe the origin and evolution of such enigmatic sources through a comprehensive multiwavelength approach. In this section, we provide a concise summary of the insights gained from our analysis of the system across various spatial scales, beginning from the vicinity of the quasar core and extending up to a few Mpc distance.

6.4.1 Light-days to pc scale

Optical observations revealed that the host displays a quasar spectrum characterized by double-peaked broad Hα and Hβ emission lines. Analysing the luminosity of the spectral lines, we were able to investigate the source on a scale of a few light-days and calculate the mass of the SMBH as 2.31×10^8 $M_\odot$, along with the size of the BLR as 14 light-days. Given the precessing nature of the source and optical variability, we considered the idea of the double-peaked lines being due to the result of a binary SMBH at the centre carrying its own system of BLR clouds. However, such an analysis gave us separation between the binary SMBHs smaller than or nearly the same as the radius of the BLRs, implying that in such a scenario both BLRs should exist as a circumbinary BLR or single BLR. This led us to rule out the hypothesis of a dual SMBH carrying its own BLR clouds and conclude that it is most likely the kinematics of the BLR clouds that leads to such a double-peaked spectral shape. Nevertheless, this does not dismiss the possibility of a binary SMBH system co-orbiting at the centre. Based on our calculations of the precession period, it is conceivable that a binary system exists with a separation of approximately $\sim$ 130–340 light-days. The variability in the spectra of the optical data and the assumptions for modelling of the radio jets might be responsible for the inconsistencies in the estimated BBH separation between the optical and radio studies. Hence, to determine accurately the mechanism at the centre that results in the double-peaked broad emission-line spectrum, comprehensive studies such as spectral monitoring and reverberation mapping are essential. These methods will provide precise measurements of the central BH mass(es) and help distinguish between the presence of a dual SMBH system and the complex dynamic behaviour of BLR clouds.

Moving to pc scale with the milliarcsec (mas) resolution VLBI radio observations, as seen in Fig. 6, we see a single-component core of the radio source along with a one-sided jet. Using multi-epoch observations conducted over a period of 20 years, we could clearly track the positional changes of the topmost blob in five different observations and estimate the proper motion of the pc-scale radio jet as $2.3c$, indicating superluminal motion. Also, from multi-epoch observations of the radio core from 5–40 GHz, radio variability was detected, due to either some variation in the accretion rate or propagation of shocks in the pc-scale jets.

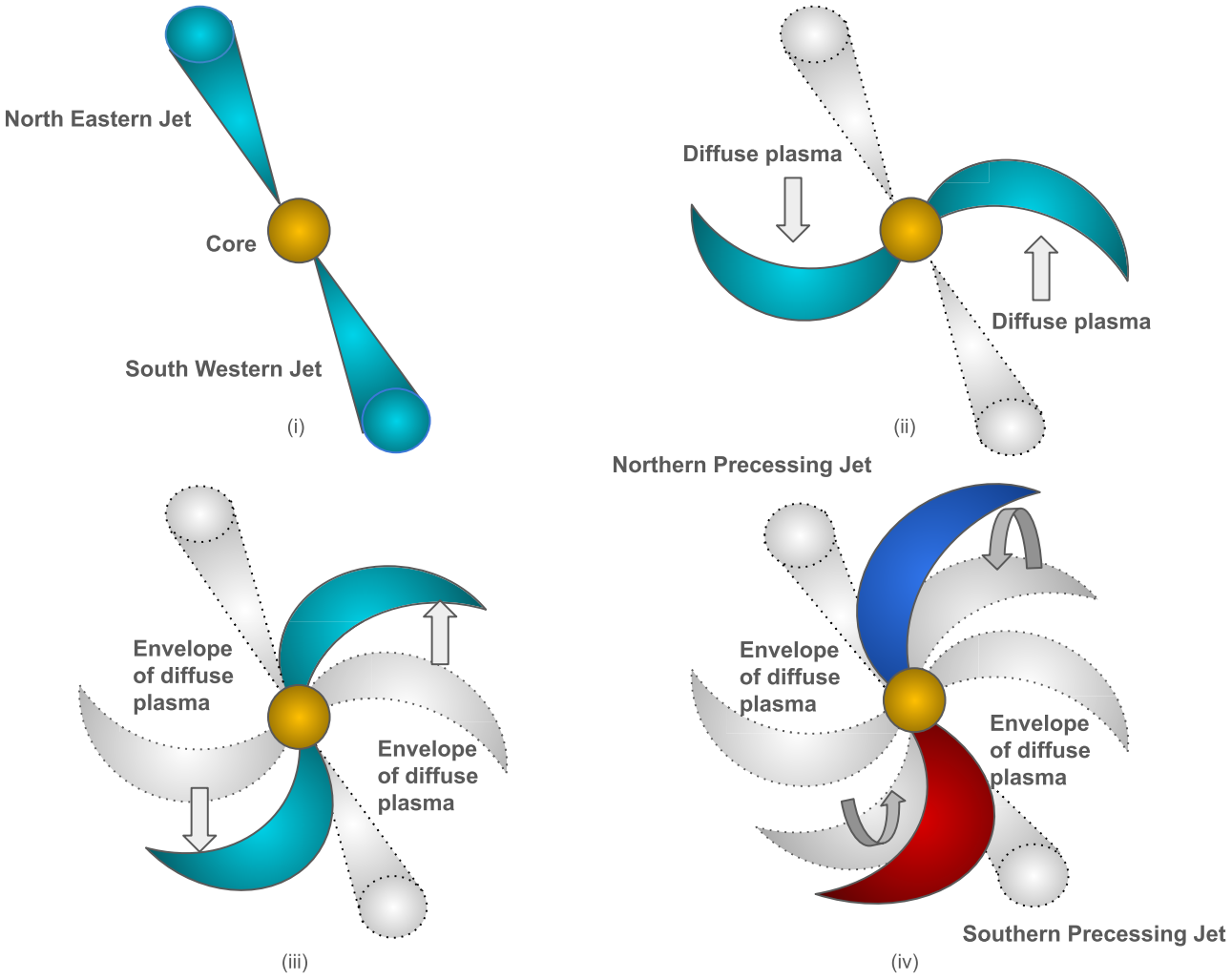

Figure 16. Precessing jet model illustration showing the movement of the jets in PKS 2300−18. Panels (ii) and (iii) encapsulate the anticlockwise movement of the precessing jets, and panel (iv), following the anticlockwise motion, showcases the motion of the northern precessing jet towards the line of sight (blue) and the southern precessing jet away from the line of sight (red).

6.4.2 Kpc to Mpc scale

In the optical map shown in Fig. 1 (right bottom insert), the host quasar is seen merging with a companion galaxy at a separation of 14 kpc. This merger is characterized by a tidal tail and a shared envelope of dust and gas surrounding the system. Considering the possibility of the quasar already hosting an SMBH binary system at its centre, this may also make it a case of a triple merger system (Hoffman & Loeb 2007; Darg et al. 2011; Liu et al. 2019); alternatively, it is also possible that the host quasar captured the SMBH from the companion galaxy during a previous close interaction while merging, leading to a binary SMBH at the centre. In the high-resolution VLA *L*-band map in Fig. 3, we see inversion-symmetric S-shaped jets that are around 200 kpc in size displaying significant curvature/bending of jets. The northern jet has three distinct knots, whereas the southern jet is much more diffuse, possibly due to the Dopper-boosting effect. As seen in Figs 2 and 3, this S-shaped jet is embedded in low surface brightness diffuse emission comprising a 5-arcmin structure that is 760 kpc in linear size, making it a giant S-shaped radio quasar.

Given the S-shaped morphology of the source, to study the time evolution of the radio source and trace the movement of the lobes over a period of time we segregated the source into multiple circular regions to conduct spectral ageing analysis. From the ageing analysis, the spectral age of the oldest plasma found in the diffuse wings was ∼40 Myr, and the youngest plasma in the jets was ∼20 Myr. The spectral ages throughout the source closely followed the gradient seen in the spectral-index map in Fig. 4, with the steepest plasma found in the wings that are oriented in the northeast and southwest direction and the youngest plasma in the core and the S-shaped jets that are oriented in the north–south direction. This implies a jet reorientation taking place in the anticlockwise direction, on a time-scale of a few million years (see illustration in Fig. 16). The precession was also modelled using a kinematical jet precession model, where the precession was estimated to be 12±8 Myr. The discrepancy between the precession period from modelling and the oldest plasma age from the ageing analysis could hint that the source has undergone multiple cycles of precession, with the oldest plasma from the oldest episode being found in the wings. It is also possible that the spectral ages represent upper limits and that the true age could be significantly less; nevertheless, this discrepancy is still considerably small. The mechanism responsible for jet precession was studied in detail, where

the possibility of a binary SMBH causing geodetic precession and a tilted accretion disc remain equally plausible explanations.

The spectrum of the X-ray emission observed by *Chandra* was modelled with a combination of thermal and power-law models. The hot gas detected in the central ∼10 kpc is likely present not only in the core, but also within the entire host galaxy. Nevertheless, in one of the models fitted to the spectrum, the metallicity of this gas was found to be as low as 3 per cent solar, which could be a result of the photo-ionization of the gas in the direct vicinity of the AGN/SMBHs due to quasar emission. The *Chandra* X-ray map in Fig. 13 revealed three radio knots, K1 being the most prominent. This knot is also identified on the optical map, resulting in a simultaneous multiwavelength detection of the radio knot. The X-ray emission in the knot is possibly due to the inverse Compton radiation of CMB photons, whereas the optical emission could be due to upscattered CMB photons as a result of their interaction with the relativistic electrons present in the jet. In the *ROSAT* X-ray map, the X-ray emission extends up to a size of 2.5 Mpc. Such large-scale X-ray halos are associated with some massive galaxy clusters, e.g. the Coma cluster (Bonamente, Lieu & Bulbul 2009), and can possibly be linked to cluster radio halos. However, exact reasons for the formation of such halos remain largely unknown.

7 CONCLUSION

PKS 2300−18 is a unique S-shaped radio quasar that is among the clearest examples of large-scale precessing jets in radio galaxies. The source exhibits large-scale diffuse wings along with a misaligned pair of collimated S-shaped jets, making it an excellent source to trace the morphological evolution of precessing jets. To analyse the source properties, we conducted multifrequency radio observations using uGMRT and the JVLA and carried out multiwavelength investigations of the source using optical and X-ray data. We conclude that the S-shaped radio morphology is the result of continuous jet precession with a precession period of $\sim 12 \pm 8$ million years, possibly caused by either a binary SMBH system at the core or a tilted accretion disc.

(i) We supplemented the flux-density measurements from our dedicated observations with archival radio data, allowing us to construct spectra ranging from 183 MHz to 6 GHz. Using these spectra, we fitted a particle injection model to different sections of the wings and the jet to determine their break-frequency values.

(ii) In the polarization studies, it was observed that the entire source was strongly polarized, with the central part showing a high degree of polarization. Additionally, the fractional polarization was found to be higher in the wings.

(iii) In the X-ray studies using *Chandra*, the host galaxy and its hot interstellar medium were detected. The core spectrum was modelled with both a thermal and a power-law component. Furthermore, a strong X-ray knot coinciding with the radio and optical knot K1 was discovered, along with two fainter X-ray knots corresponding to the radio knots K2 and K3.

(iv) Variability was detected in the radio core observations over multiple epochs. The observed variability, which occurred over a span of a few days to weeks, was attributed to changes in the accretion rate or changes in the pc-scale jets close to the radio core.

(v) The broad, double-peaked optical emission lines from the quasar spectrum were fitted with Lorentzian profiles, which yielded a central SMBH mass of 2.31×10^8 $M_\odot$ and a BLR size of 14 light-days. This double-peaked emission-line spectrum indicated complex gas kinematics within the quasar's BLR.

(vi) The jets and the diffuse emission of the source were modelled using a kinematical jet precession model, which determined the precession period to be 12 ± 8 million years.

(vii) The spectral age of the oldest plasma found in the diffuse wings was ∼40 Myr and that of the youngest plasma in the jets ∼20 Myr. The spectral ages throughout the source closely followed the gradient observed in the spectral-index map, with the steepest plasma located in the wings oriented along the northeast and southwest directions, and the youngest plasma found in the core and the S-shaped jets oriented along the north–south direction.

(viii) The source morphology results from jet reorientation taking place in the anticlockwise direction over a span of a few million years. The discrepancy between the precession period and the maximum plasma age suggests that the source may have undergone multiple precession cycles.

The multiwavelength study of the S-shaped radio quasar PKS 2300−18 presented in this work is among the most extensive investigations on such a select class of radio galaxies. Studying these sources is vital for an in-depth understanding of galaxy evolution through nuclear activity, as changes at the scale of the central AGN manifest as large-scale perturbations, seen in the case of radio jets. This can provide novel insights into the dynamic behaviour of the central SMBH. Multiwavelength studies also play a key role in building a comprehensive picture of the host galaxy and the central SMBH, from subpc to Mpc scales. Given that these objects are also prime candidates for hosting BBHs at their centre, in their final evolutionary stages they are expected to generate nanoHertz gravitational wave (GW) emission. Such emission can be observed by pulsar timing arrays, which regularly monitor millisecond pulsars (Agazie et al. 2023) to track GWs from SMBH mergers, and also by other novel methods, as suggested by Stegmann et al. (2024). Consequently, radio galaxies exhibiting S-shaped morphology can serve as an ideal resource for identifying BBHs, investigating galaxy mergers, and analysing dynamic behaviour of AGNs.

ACKNOWLEDGEMENTS

The authors thank the anonymous reviewer for valuable comments and suggestions and Urszula Pajdosz-Śmierciak for her contribution to the radio proposals. DKW thanks Agnieszka Kuźmicz and Bożena Czerny for discussions. AM thanks Rubinur Khatun, Martin Hardcastle, Kamil Wolnik, and Subhrata Dey for scientific discussions. MJ acknowledges access to the SYNAGE software kindly provided by Matteo Murgia. We acknowledge support from the National Science Centre research grants 2021/43/B/ST9/03246 [DKW, AM].

The GMRT is a national facility operated by the NCRA, TIFR. The National Radio Astronomy Observatory is a facility of the National Science Foundation operated under a cooperative agreement by Associated Universities Inc. The National Radio Astronomy Observatory running the VLA is a facility of the National Science Foundation operated under a cooperative agreement by Associated Universities, Inc. The Astrogeo VLBI FITS image database is maintained by L. Petrov, and the particular maps were contributed by Y. Y. Kovalev, A. Pushkarev, and L. Petrov.

The Pan-STARRS1 Surveys (PS1) and the PS1 public science archive have been made possible through contributions by the Institute for Astronomy, the University of Hawaii, the Pan-STARRS Project Office, the Max-Planck Society and its participating institutes, the Max Planck Institute for Astronomy, Heidelberg and the Max Planck Institute for Extraterrestrial Physics, Garching, the Johns Hopkins University, Durham University, the University of Edinburgh, the Queen's University Belfast, the Harvard-Smithsonian

Center for Astrophysics, the Las Cumbres Observatory Global Telescope Network Incorporated, the National Central University of Taiwan, the Space Telescope Science Institute, the National Aeronautics and Space Administration under Grant No. NNX08AR22G issued through the Planetary Science Division of the NASA Science Mission Directorate, the National Science Foundation Grant No. AST-1238877, the University of Maryland, Eotvos Lorand University (ELTE), the Los Alamos National Laboratory, and the Gordon and Betty Moore Foundation.

This research has made use of data obtained from the *Chandra* Data Archive and the *Chandra* Source Catalog, and software provided by the *Chandra* X-ray Center (CXC) in the application packages CIAO and SHERPA. This research has made use of the NASA/IPAC Extra- galactic Database (NED), which is funded by the National Aeronautics and Space Administration and oper- ated by the California Institute of Technology.

ZTF is a fully-automated, wide-field survey aimed at a systematic exploration of the optical transient sky. Supported by the National Science Foundation under Grants No. AST-1440341 and AST-2034437 and a collaboration including current partners Caltech, IPAC, the Oskar Klein Center at Stockholm University, the University of Maryland, University of California, Berkeley, the University of Wisconsin at Milwaukee, University of Warwick, Ruhr University, Cornell University, Northwestern University, and Drexel University. Operations are conducted by COO, IPAC, and UW.

DATA AVAILABILITY

The data underlying this work will be shared on reasonable request to the corresponding author.

REFERENCES

Abdollahi S. et al.. 2020, ApJS, 247, 33
Agazie G. et al., 2023, ApJ, 952, L37
An T., Baan W. A., 2012, ApJ, 760, 77
Arnaud K. A., 1996, in Jacoby G. H., Barnes J., eds, ASP Conf. Ser. Vol. 101, Astronomical Data Analysis Software and Systems V. Astron. Soc. Pac., San Francisco, p. 17
Baars J. W. M., Genzel R., Pauliny-Toth I. I. K., Witzel A., 1977, A&A, 61, 99
Ballet J., Burnett T. H., Digel S. W., Lott B., 2020, preprint (arXiv:2005.11208)
Bardeen J. M., Petterson J. A., 1975, ApJ, 195, L65
Beasley A. J., Gordon D., Peck A. B., Petrov L., MacMillan D. S., Fomalont E. B., Ma C., 2002, ApJS, 141, 13
Beck R., Krause M., 2005, Astron. Nachr., 326, 414
Begelman M. C., Blandford R. D., Rees M. J., 1980, Nature, 287, 307
Bellm E. C. et al., 2019, PASP, 131, 018002
Bera S., Sasmal T. K., Patra D., Mondal S., 2022, ApJS, 260, 7
Bhukta N., Mondal S. K., Pal S., 2022b, MNRAS, 516, 372
Bhukta N., Pal S., Mondal S. K., 2022a, MNRAS, 512, 4308
Blandford R. D., Rees M. J., 1974, MNRAS, 169, 395
Bolton J. G., Ekers J., 1966, Australian Journal of Physics, 19, 559
Bonaldi A., Bonavera L., Massardi M., De Zotti G., 2013, MNRAS, 428, 1845
Bonamente M., Lieu R., Bulbul E., 2009, ApJ, 696, 1886
Bregman J. N. et al., 1988, ApJ, 331, 746
Briggs D. S., 1995, BAAS, 27, 1444
Britzen S., Roland J., Laskar J., Kokkotas K., Campbell R. M., Witzel A., 2001, A&A, 374, 784
Brown M. J. I., Webster R. L., Boyle B. J., 2001, AJ, 121, 2381
Capetti A., Zamfir S., Rossi P., Bodo G., Zanni C., Massaglia S., 2002, A&A, 394, 39
CASA Team et al., 2022, PASP, 134, 114501
Chakrabarti S. K., Wiita P. J., 1994, ApJ, 434, 518
Chambers K. C. et al., 2016, preprint (arXiv:1612.05560)
Chatterjee K. et al., 2020, MNRAS, 499, 362
Chen Y., Gu Q., Fan J., Yu X., Ding N., Xiong D., Guo X., 2023, ApJS, 265, 60
Clark B. G., 1980, A&A, 89, 377
Condon J. J., Cotton W. D., Greisen E. W., Yin Q. F., Perley R. A., Taylor G. B., Broderick J. J., 1998, AJ, 115, 1693
Condon J. J., Mitchell K. J., 1984, ApJ, 276, 472
Cotton W. D. et al., 2020, MNRAS, 495, 1271
Cotton W. D., 1999, in Taylor G. B., Carilli C. L., Perley R. A., eds, ASP Conf. Ser. Vol. 180, Synthesis Imaging in Radio Astronomy II. Astron. Soc. Pac., San Francisco, p. 357
Darg D. W., Kaviraj S., Lintott C. J., Schawinski K., Silk J., Lynn S., Bamford S., Nichol R. C., 2011, MNRAS, 416, 1745
Das S., Kharb P., Morganti R., Nandi S., 2021, MNRAS, 504, 4416
Duchesne S. W. et al., 2023, PASA, 40, e034
Eracleous M., Halpern J. P., 1994, ApJS, 90, 1
Evans D. A. et al., 2008, ApJ, 675, 1057
Fanaroff B. L., Riley J. M., 1974, MNRAS, 167, 31P
Florido E., Battaner E., Sanchez-Saavedra M. L., 1990, Ap&SS, 164, 131
Gaskell C. M., 1983, in Swings J.-P.ed., IN: Quasars and gravitational lenses; Proceedings of the Twenty-fourth Liege International Astrophysical Colloquium, Quasars as Supermassive Binaries. Universite de Liege, Cointe-Ougree, Belgium, p. 473
Ghisellini G., Padovani P., Celotti A., Maraschi L., 1993, ApJ, 407, 65
Gilbert A. M., Eracleous M., Filippenko A. V., Halpern J. P., 1999, in Gaskell C. M., Brandt W. N., Dietrich M., Dultzin-Hacyan D., Eracleous M., eds, ASP Conf. Ser. Vol. 175, Structure and Kinematics of Quasar Broad Line Regions. Astron. Soc. Pac., San Francisco, p. 189
Giri G., Dubey R. P., Rubinur K., Vaidya B., Kharb P., 2022, MNRAS, 514, 5625
Giri G., Fendt C., Thorat K., Bodo G., Rossi P., 2024, Frontiers in Astronomy and Space Sciences, 11, 1371101
Gopal-Krishna, Biermann P. L., Gergely L. Á., Wiita P. J., 2012, Res. Astron. Astrophys., 12, 127
Gopal-Krishna, Wiita P. J., 2024, JA&A, 45, 12
Gordon D. et al., 2016, AJ, 151, 154
Gower A. C., Gregory P. C., Unruh W. G., Hutchings J. B., 1982, ApJ, 262, 478
Greene J. E., Ho L. C., 2005, ApJ, 630, 122
Greisen E. W., 2003, in Heck A.ed., Astrophysics and Space Science Library Vol. 285, Information Handling in Astronomy – Historical Vistas. Kluwer Academic Publishers, Dordrecht p.109
Greisen E. W. 1990, in Acquisition, Processing and Archiving of Astronomical Images, 125–142
Gubbay J., Legg A. J., Robertson D. S., Moffet A. T., Ekers R. D., Seidel B., 1969, Nature, 224, 1094
Gunn J. E., Gott J. Richard I., 1972, ApJ, 176, 1
Guo H., Shen Y., Wang S., 2018, Astrophysics Source Code Library, record ascl:1809.008
Hale C. L. et al., 2021, PASA, 38, e058
Hardee P. E., 1987, ApJ, 318, 78
Hardee P. E., Clarke D. A., 1992, ApJ, 400, L9
HI4PI Collaboration et al., 2016, A&A, 594, A116
Hjellming R. M., Johnston K. J., 1981a, ApJ, 246, L141
Hjellming R. M., Johnston K. J., 1981b, Nature, 290, 100
Hocuk S., Barthel P. D., 2010, A&A, 523, A9
Hoffman L., Loeb A., 2007, MNRAS, 377, 957
Högbom J. A., 1974, A&AS, 15, 417
Horton M. A., Krause M. G. H., Hardcastle M. J., 2020, MNRAS, 499, 5765
Horton M. A., Krause M. G. H., Hardcastle M. J., 2023, MNRAS, 521, 2593
Hunstead R. W., Murdoch H. S., Condon J. J., Phillips M. M., 1984, MNRAS, 207, 55
Hunstead R. W., Murdoch H. S., Shobbrook R. R., 1978, MNRAS, 185, 149
Intema H. T., 2014, Astrophysics Source Code Library, record ascl:1408.006

Intema H. T., van der Tol S., Cotton W. D., Cohen A. S., van Bemmel I. M., Röttgering H. J. A., 2009, A&A, 501, 1185
Jaffe W. J., Perola G. C., 1973, A&A, 26, 423
Jayasinghe T. et al., 2020, MNRAS, 491, 13
Kaastra J. S., 1992, An X-Ray Spectral Code for Optically Thin Plasmas, Internal SRON-Leiden Report, updated version 2.0
Kaspi S., Smith P. S., Netzer H., Maoz D., Jannuzi B. T., Giveon U., 2000, ApJ, 533, 631
Klein U., Mack K. H., Gregorini L., Vigotti M., 2003, A&A, 406, 579
Koay J. Y. et al., 2018, MNRAS, 474, 4396
Komossa S. et al., 2023, ApJ, 944, 177
Kozieł-Wierzbowska D., Goyal A., Żywucka N., 2020, ApJS, 247, 53
Krause M. G. H. et al., 2019, MNRAS, 482, 240
Lacey C., Cole S., 1993, MNRAS, 262, 627
Lacy M. et al., 2020, PASP, 132, 035001
Lal D. V., Sebastian B., Cheung C. C., Pramesh Rao A., 2019, AJ, 157, 195
Leahy J. P., Williams A. G., 1984, MNRAS, 210, 929
Lense J., Thirring H., 1918, Phys. Z., 19, 156
Liska M., Hesp C., Tchekhovskoy A., Ingram A., van der Klis M., Markoff S., 2018, MNRAS, 474, L81
Lister M. L. et al., 2009, AJ, 138, 1874
Liu X. et al., 2019, ApJ, 887, 90
Lopez J. A., Meaburn J., Palmer J. W., 1993, ApJ, 415, L135
Lu J. F., 1990, A&A, 229, 424
Lu J.-F., Zhou B.-Y., 2005, ApJ, 635, L17
Merritt D., Ekers R. D., 2002, Science, 297, 1310
Mewe R., Gronenschild E. H. B. M., van den Oord G. H. J., 1985, A&AS, 62, 197
Miley G. K., Perola G. C., van der Kruit P. C., van der Laan H., 1972, Nature, 237, 269
Miley G., 1980, ARA&A, 18, 165
Miller B. P., Brandt W. N., 2009, ApJ, 695, 755
Misra A., Jamrozy M., Weżgowiec M., 2023, MNRAS, 523, 1648
Mohan N., Rafferty D., 2015, Astrophysics Source Code Library, record ascl:1502.007
Murgia M., 1996, Laurea thesis, University of Bologna
Nandi S., Caproni A., Kharb P., Sebastian B., Roy R., 2021, ApJ, 908, 178
Ndung'u S., Grobler T., Wijnholds S. J., Karastoyanova D., Azzopardi G., 2023, New Astron. Rev., 97, 101685
Nikonov A. S., Kovalev Y. Y., Kravchenko E. V., Pashchenko I. N., Lobanov A. P., 2023, MNRAS, 526, 5949
O'Dea C. P., Baum S. A., 2023, Galaxies, 11, 67
Offringa A. R. et al., 2014, MNRAS, 444, 606
Offringa A. R., Smirnov O., 2017, MNRAS, 471, 301
Ostriker J. P., Hausman M. A., 1977, ApJ, 217, L125
Owen F. N., Rudnick L., 1976, ApJ, 205, L1
Pal S., Kumari S., 2023, JA&A, 44, 17
Perucho M., Lobanov A. P., Martí J. M., Hardee P. E., 2006, A&A, 456, 493
Perucho M., Martí-Vidal I., Lobanov A. P., Hardee P. E., 2012, A&A, 545, A65
Peterson B. M. et al., 2004, ApJ, 613, 682
Popović L. Č., 2012, New Astron. Rev., 56, 74
Pringle J. E., 1997, MNRAS, 292, 136
Rani B. et al., 2013, A&A, 552, A11
Rawes J., Birkinshaw M., Worrall D. M., 2018, MNRAS, 480, 3644
Rees M. J., 1966, Nature, 211, 468
Reid R. I., Kronberg P. P., Perley R. A., 1999, ApJS, 124, 285
Ricci C., Trakhtenbrot B., 2023, Nat. Astron., 7, 1282
Ro H. et al., 2023, Galaxies, 11, 33
Rottmann H., 2002, PhD thesis, University of Bonn
Rubinur K., Das M., Kharb P., Honey M., 2017, MNRAS, 465, 4772
Russell H. R. et al., 2024, MNRAS, 528, 1863
Saikia D. J., Salter C. J., 1988, ARA&A, 26, 93
Sarazin C. L., Begelman M. C., Hatchett S. P., 1980, ApJ, 238, L129
Schinzel F. K., Petrov L., Taylor G. B., Mahony E. K., Edwards P. G., Kovalev Y. Y., 2015, ApJS, 217, 4
Schwab F. R., 1984, AJ, 89, 1076
Sebastian B. et al., 2024, MNRAS, 530, 4902
Sebastian B., Lal D. V., Pramesh Rao A., 2017, AJ, 154, 169
Sethi S., Kuźmicz A., Jamrozy M., Slavcheva-Mihova L., 2024, ApJ, 969, 156
Shen Y., Loeb A., 2010, ApJ, 725, 249
Simard-Normandin M., Kronberg P. P., Button S., 1981a, ApJS, 45, 97
Simard-Normandin M., Kronberg P. P., Button S., 1981b, ApJS, 46, 239
Steenbrugge K. C., Blundell K. M., 2008, MNRAS, 388, 1457
Steffen W., 1997, Vistas in Astronomy, 41, 71
Stegmann J., Zwick L., Vermeulen S. M., Antonini F., Mayer L., 2024, Nature Astron., 8, 1321
Tanaka M., Ikeda H., Murata K., Takita S., Mineo S., Koike M., Okura Y., Harasawa S., 2021, PASJ, 73, 735
Thompson A. R., Clark B. G., Wade C. M., Napier P. J., 1980, ApJS, 44, 151
Truemper J., 1982, Adv. Space Res., 2, 241
Ubertosi F. et al., 2024, A&A, 688, A86
Ubertosi F. et al., 2024b, A&A, 688, A86
van Breugel W., Balick B., Heckman T., Miley G., Helfand D., 1983, AJ, 88, 40
Voges W. et al., 1999, A&A, 349, 389
Wagner S. J., Witzel A., 1995, ARA&A, 33, 163
Walker R. C., Hardee P. E., Davies F. B., Ly C., Junor W., 2018, ApJ, 855, 128
Woltjer L., 1966, ApJ, 146, 597
Wright E. L., 2006, PASP, 118, 1711

This paper has been typeset from a TEX/LATEX file prepared by the author.

Chapter 5

Conclusions and future work

5.1 Conclusions

Since the serendipitous discovery of radio galaxies in the early 1950s, the field of radio astronomy has grown tremendously, with millions of such sources now catalogued. A major milestone in their understanding came with the morphological classification introduced by Fanaroff and Riley in 1974, which divided radio galaxies into two categories: FR I (center-brightened) and FR II (edge-brightened) based on the distribution of radio brightness along their jets and lobes. The advent of large-scale radio surveys soon led to the identification of additional morphological classes, such as Wide-Angle Tailed and Narrow-Angle Tailed radio galaxies. These sources emphasized the role of the galaxy environment in shaping radio structures, and they have since become valuable tracers of galaxy clusters.

With the development of more sensitive and high resolution radio telescopes, more complex structures such as Double-double radio galaxies were identified. These sources displayed two pairs of lobes from separate episodes of jet activity, providing some of the first evidence for the episodic, or cyclic, nature of AGN-driven radio emission. Subsequent deep radio observations led to the discovery of X-shaped radio galaxies, a class of winged radio galaxies that have a secondary set of lobes or wings, which are considered as evidence of jet reorientation as a result of processes such as backflow deflection by an asymmetric medium or a flip in the SMBH spin axis following a galactic merger. These discoveries introduced the idea that the jet direction could be influenced by the merger history of the host galaxy.

A notable subclass of winged radio galaxies are the "S"-shaped radio galaxies. These sources are extremely rare and are distinguished by striking features such as curved jets, inversion-symmetric S-shaped morphology, and in some cases, multiple or broad hotspots, and jet terminations at the edges of the lobes. Such morphology are often believed to result from continuous jet reorientation or precession, driven by changes in the spin axis of the central supermassive black hole. Due to their rareness they demand detailed investigation to uncover their formation mechanisms and trace the evolutionary history of their host galaxies. The striking inversion symmetry also offers valuable insights into the evolution of the supermassive black holes spin axis, particularly in the context of jet reorientation and precession. Studying their optical hosts and surrounding environments, such as presence of a companion galaxy and any disturbance of the optical host galaxy indicating a possible merger can help in understanding the conditions that give rise to this distinctive morphology. Despite these exceptional characteristics, S-shaped radio galaxies remain significantly understudied, and no dedicated sample-based investigation had been conducted prior to this work. This thesis presents the first dedicated low frequency radio study of a sample of S-shaped radio galaxies, aiming to explore their large-scale morphology, host galaxy properties, and environmental context in detail.

In this thesis, a carefully selected sample of radio sources having S-shaped morphology and bent jets were analyzed using high-resolution observations from the uGMRT and the VLA, and one among these sources, PKS 2300-18, is complemented with archival radio data from telescopes such as LOFAR, ASKAP, WENSS. The decision to study using low frequency surveys is motivated by the fact that low frequency observations are particularly well suited to trace the aged and diffuse synchrotron plasma that reveals past episodes of AGN activity and directional changes in the jet axis. In our study, analysis such as morphological study, spectral ageing, and jet precession modelling were performed to characterise the evolutionary stages and physical mechanisms governing the observed structures.

In Chapter 2, a sample of six S-shaped radio galaxies, selected from the FIRST and LOFAR surveys, is presented. These sources were observed with the uGMRT in band 3 and band 4 to investigate their morphological evolution at low radio frequencies. The resulting uGMRT maps reveal detailed radio structures, allowing for comprehensive morphological analysis. Several sources display trails of diffuse and low-frequency plasma, alongside distinct indicators of jet precession, such as curved jets, S-shaped symmetry, multiple or broad hotspots, and jets terminating at the edges of lobes. Among the sample, three sources showed three precession indicators, while one source showed all four of them. This chapter

marks the first systematic study of a sample of S-shaped radio galaxies, emphasizing their morphological complexity and the potential link to reorientation triggered by jet precession.

In Chapter 3, a detailed multifrequency study is presented of an X-shaped radio galaxy, CGCG 292-057, that uniquely showcases multiple stages of galaxy evolution. This source exhibits compelling features that include evidence of a past merger, X-shaped radio morphology, double-peaked optical emission lines, and a newly formed inner pair of radio lobes, making it an excellent source for exploring the connection between galactic mergers and AGN activity. Such direct observational links between disturbed radio morphologies and merger events are extremely rare. The galaxy was observed across a broad range of radio frequencies using dedicated GMRT and VLA observations. Morphological and spectral analyses were performed which revealed a gradient in the northwestern wing indicative of jet reorientation.

The radio core displayed a double-peaked spectrum with turnovers at 200 MHz and 1.3 GHz, best modelled using a double homogeneous free-free absorption model. This model suggested that the synchrotron radiation was absorbed by two ionized regions: a dense inner parsec-scale screen and a more diffuse, kiloparsec-scale ISM. Spectral ageing analysis of the primary lobes yielded ages between 40 and 58 Myr, while the wings showed decreasing spectral ages from 60 to 30 Myr, consistent with the spectral index gradient. Attempts to model the inner lobes returned unrealistically high ages, likely due to absorption during the expansion of the lobes through the host galaxy's dense ISM. Overall, this study provides key insights into how galaxy mergers can influence AGN jet behavior, showing strong evidence of jet reorientation and restarting activity driven by changes in the central SMBH dynamics.

In Chapter 4, a comprehensive multiwavelength study is presented for the giant inversion-symmetric S-shaped radio galaxy PKS 2300–18 (part of the initial sample of S-shaped sources), hosted by a quasar undergoing interaction with a companion galaxy. The host displays disturbed optical morphology, suggesting an ongoing merger. A broad-band radio spectral analysis was carried out using dedicated uGMRT and JVLA observations. The source was observed to be strongly polarized, with a notably high degree of polarization concentrated near the core. Chandra X-ray observations revealed both the quasar's core and its surrounding hot ISM. The core X-ray spectrum was modelled with thermal and power-law components. Radio monitoring across multiple epochs showed variability in the core on timescales of days to weeks, likely caused by fluctuations in accretion or changes in parsec-scale jet structures. VLBI observations confirmed superluminal motion in the jets, with an apparent velocity of 2.3c.

Optical spectroscopy revealed broad, double-peaked emission lines, modelled with Lorentzian profiles, indicating complex kinematics in the quasar's broad line region. A kinematical jet precession model applied to the jets and diffuse radio emission yielded a precession period of ∼12 million years. Spectral ageing analysis showed that the oldest plasma, located in the extended wings, is ∼40 Myr old, while the youngest plasma in the S-shaped jets near the core is ∼20 Myr old. These results were found to be consistent with the spectral index map, which showed steep spectrum plasma along the NE–SW wings and flatter spectrum, younger plasma along the N–S oriented jets. The findings suggest that the S-shaped morphology arises from gradual jet reorientation in an anticlockwise direction over several million years. This study of PKS 2300–18 stands as one of the most detailed investigations of an S-shaped radio quasar to date, offering valuable insights into jet dynamics, AGN variability, and host galaxy interactions.

5.2 Scope for future work

This thesis presents the first systematic effort to study S-shaped radio galaxies in detail and compile a sample of such morphologically distinct sources. One of the sources was subjected to a comprehensive multiwavelength analysis, revealing several intriguing features that highlight the dynamic nature of jet activity and the host galaxy environment. Similar in-depth investigations are planned for the remaining sources in the sample. Future work will include detailed spectral ageing analyses and jet precession modeling for the rest of the sample, allowing for a broader comparative understanding of their evolutionary stages. These efforts will be further supplemented with 3D hydrodynamical simulations to model jet reorientation and test precession scenarios.

Given the relatively small sample size, expanding the current dataset will be crucial and would be made possible using upcoming deep and wide-area radio surveys such as SKA, EMU, and upgraded LOFAR surveys. These offer promising opportunities for identifying more S-shaped radio galaxies and enhancing the statistical robustness of such studies. This will also provide a clearer picture on the diversity and frequency of these sources. Alongside this deeper optical and X-ray follow-up observations are essential, particularly for sources with ambiguous or poorly resolved host galaxies. High-resolution facilities like Chandra, XMM-Newton, and optical instruments such as Very Large Telescope (VLT) or James Webb Space Telescope (JWST) can help uncover merger signatures and detailed gas kinematics linked to AGN activity. Since jet precession is often associated with binary SMBHs, future work will also be aimed towards identifying such systems through high

resolution imaging studies like VLBA and spectroscopic investigations. Confirming binary SMBHs in S-shaped radio galaxies would provide direct evidence linking galactic mergers to the dynamic reorientation of jets. Finally, binary SMBHs, especially in the final stages of their merger, are among the most promising sources of gravitational waves. These S-shaped sources can therefore serve as key targets for pulsar timing arrays (PTAs), which monitor millisecond pulsars to detect the low frequency gravitational wave background generated as a result of such mergers.

Bibliography

Abramowicz, M. A., Czerny, B., Lasota, J. P., and Szuszkiewicz, E. (1988). Slim Accretion Disks. , 332:646.

Adams, E. A. K. and van Leeuwen, J. (2019). The first data release from the apertif imaging surveys. *Nature Astronomy*, 3:188–193.

Agazie, G., Anumarlapudi, A., Archibald, A. M., Arzoumanian, Z., Baker, P. T., Bécsy, B., Blecha, L., Brazier, A., Brook, P. R., Burke-Spolaor, S., Burnette, R., Case, R., Charisi, M., Chatterjee, S., Chatziioannou, K., Cheeseboro, B. D., Chen, S., Cohen, T., Cordes, J. M., Cornish, N. J., Crawford, F., Cromartie, H. T., Crowter, K., Cutler, C. J., Decesar, M. E., Degan, D., Demorest, P. B., Deng, H., Dolch, T., Drachler, B., Ellis, J. A., Ferrara, E. C., Fiore, W., Fonseca, E., Freedman, G. E., Garver-Daniels, N., Gentile, P. A., Gersbach, K. A., Glaser, J., Good, D. C., Gültekin, K., Hazboun, J. S., Hourihane, S., Islo, K., Jennings, R. J., Johnson, A. D., Jones, M. L., Kaiser, A. R., Kaplan, D. L., Kelley, L. Z., Kerr, M., Key, J. S., Klein, T. C., Laal, N., Lam, M. T., Lamb, W. G., Lazio, T. J. W., Lewandowska, N., Littenberg, T. B., Liu, T., Lommen, A., Lorimer, D. R., Luo, J., Lynch, R. S., Ma, C.-P., Madison, D. R., Mattson, M. A., McEwen, A., McKee, J. W., McLaughlin, M. A., McMann, N., Meyers, B. W., Meyers, P. M., Mingarelli, C. M. F., Mitridate, A., Natarajan, P., Ng, C., Nice, D. J., Ocker, S. K., Olum, K. D., Pennucci, T. T., Perera, B. B. P., Petrov, P., Pol, N. S., Radovan, H. A., Ransom, S. M., Ray, P. S., Romano, J. D., Sardesai, S. C., Schmiedekamp, A., Schmiedekamp, C., Schmitz, K., Schult, L., Shapiro-Albert, B. J., Siemens, X., Simon, J., Siwek, M. S., Stairs, I. H., Stinebring, D. R., Stovall, K., Sun, J. P., Susobhanan, A., Swiggum, J. K., Taylor, J., Taylor, S. R., Turner, J. E., Unal, C., Vallisneri, M., van Haasteren, R., Vigeland, S. J., Wahl, H. M., Wang, Q., Witt, C. A., Young, O., and Nanograv Collaboration (2023). The NANOGrav 15 yr Data Set: Evidence for a Gravitational-wave Background. , 951(1):L8.

Akujor, C. E., Leahy, J. P., Garrington, S. T., Sanghera, H., Spencer, R. E., and Schilizzi, R. T. (1996). A two-sided jet structure in the 'steep-spectrum core' of 3C293. , 278(1):1–5.

and and and (2012). On the origin of x-shaped radio galaxies. *Research in Astronomy and Astrophysics*, 12(2):127.

Antonucci, R. (1993). Unified models for active galactic nuclei and quasars. *Annual Review of Astronomy and Astrophysics*, 31:473–521.

Antonucci, R. R. J. and Miller, J. S. (1985). Spectropolarimetry and the nature of ngc 1068. *The Astrophysical Journal*, 297:621–632.

Bañados, E., Khusanova, Y., Decarli, R., Momjian, E., Walter, F., Connor, T., Carilli, C. L., Mazzucchelli, C., Rojas-Ruiz, S., and Venemans, B. P. (2024). [C II] Properties and Far-infrared Variability of a z = 7 Blazar. , 977(2):L46.

Baade, W. and Minkowski, R. (1954). Identification of the radio source cygnus a with a distant galaxy. *The Astrophysical Journal*, 119:206.

Bagchi, J., Sankhyayan, S., Sarkar, P., Raychaudhury, S., Jacob, J., and Dabhade, P. (2017). Saraswati: An extremely massive 200 megaparsec scale supercluster. *The Astrophysical Journal*, 844(1):25.

Bait, O., Kurapati, S., Duc, P.-A., Cuillandre, J.-C., Wadadekar, Y., Kamphuis, P., and Barway, S. (2020). Discovery of a large H I ring around the quiescent galaxy AGC 203001. , 492(1):1–7.

Balbus, S. A. and Hawley, J. F. (1991). A powerful local shear instability in weakly magnetized disks. i. linear analysis. *The Astrophysical Journal*, 376:214–233.

Baldi, R. D. (2023). The nature of compact radio sources: the case of FR 0 radio galaxies. , 31(1):3.

Bardeen, J. M. and Petterson, J. A. (1975). The Lense-Thirring Effect and Accretion Disks around Kerr Black Holes. , 195:L65.

Bassa, C. G., Pleunis, Z., Hessels, J. W. T., Ferrara, E. C., Breton, R. P., Gusinskaia, N. V., Kondratiev, V. I., Sanidas, S., Nieder, L., Clark, C. J., Li, T., van Amesfoort, A. S., Burnett, T. H., Camilo, F., Michelson, P. F., Ransom, S. M., Ray, P. S., and Wood, K. (2017). LOFAR Discovery of the Fastest-spinning Millisecond Pulsar in the Galactic Field. , 846(2):L20.

Becker, R. H., White, R. L., and Helfand, D. J. (1995). The FIRST Survey: Faint Images of the Radio Sky at Twenty Centimeters. , 450:559.

Begelman, M. C., Blandford, R. D., and Rees, M. J. (1980). Massive black hole binaries in active galactic nuclei. , 287(5780):307–309.

Begelman, M. C., Blandford, R. D., and Rees, M. J. (1980). Massive black hole binaries in active galactic nuclei. *Nature*, 287(5780):307–309.

Bempong-Manful, E., Hardcastle, M. J., Birkinshaw, M., Laing, R. A., Leahy, J. P., and Worrall, D. M. (2020). A high-resolution view of the jets in 3c 465. *Monthly Notices of the Royal Astronomical Society*, 496(1):676–688.

Bhukta, N., Pal, S., and Mondal, S. K. (2022). Search for X/Z-shaped radio sources from TGSS ADR 1. , 512(3):4308–4323.

Binette, L., Magris, C. G., Stasińska, G., and Bruzual, A. G. (1994). Photoionization in elliptical galaxies by old stars. *Astronomy and Astrophysics*, 292:13–24.

Bisnovatyi-Kogan, G. S. and Ruzmaikin, A. A. (1974). The accretion of matter by a collapsing star in the presence of a magnetic field. *Astrophysics and Space Science*, 28:45–59.

Blandford, R. D. and Rees, M. J. (1974). A 'twin-exhaust' model for double radio sources. *Monthly Notices of the Royal Astronomical Society*, 169(3):395–415.

Blandford, R. D. and Znajek, R. L. (1977). Electromagnetic extraction of energy from Kerr black holes. , 179:433–456.

Bliton, M., Rizza, E., Burns, J. O., Owen, F. N., and Ledlow, M. J. (1998). Cluster-subcluster mergers and the formation of narrow-angle tailed radio sources. , 301(3):609–625.

Bolton, J. G., Stanley, G. J., and Slee, O. B. (1949). Positions of three discrete sources of cosmic radio radiation. *Nature*, 164(4157):101–102.

Briggs, D. S. (1995). High Fidelity Interferometric Imaging: Robust Weighting and NNLS Deconvolution. In *American Astronomical Society Meeting Abstracts*, volume 187 of *American Astronomical Society Meeting Abstracts*, page 112.02.

Britzen, S., Witzel, A., Krichbaum, T. P., and et al. (2001). Evidence for orbital motion in the radio jet of the bl lacertae object 1803+784? *Astronomy & Astrophysics*, 374(3):784–794.

Capetti, A., Zamfir, S., Rossi, P., Bodo, G., Zanni, C., and Massaglia, S. (2002). On the origin of x-shaped radio-sources: New insights from the properties of their host galaxies. *Astronomy Astrophysics*, 394(1):39–45.

Carilli, C. L., Perley, R. A., Dhawan, V., and Perley, D. A. (2019). Imaging the Active Galactic Nucleus Torus in Cygnus A. , 874(2):L32.

Chatterjee, K., Liska, M., Tchekhovskoy, A., and Markoff, S. (2020). Observational signatures of disk and jet misalignment in images of accreting black holes. *Monthly Notices of the Royal Astronomical Society*, 499(3):3622–3635.

Cheung, C. C. (2007). First "winged" and x-shaped radio source candidates. *The Astronomical Journal*, 133(6):2097–2121.

Clark, B. G. (1980). An efficient implementation of the algorithm 'CLEAN'. , 89(3):377.

Coil, A. L. et al. (2023). Revealing the origin of orcs with lem: A lucky cloverleaf at z 0.05. *Bulletin of the AAS*, 55(4):110.12. `https://baas.aas.org/pub/2023n4i110p12`.

Condon, J. J., Cotton, W. D., Greisen, E. W., Yin, Q. F., Perley, R. A., Taylor, G. B., and Broderick, J. J. (1998). The NRAO VLA Sky Survey. , 115(5):1693–1716.

Condon, J. J. and Mitchell, K. J. (1984). 4C 29.47 : Quasi-periodic outbursts recorded by precessing jets ? , 276:472–475.

Cotton, W. D. (1999). Special Problems in Imaging. In Taylor, G. B., Carilli, C. L., and Perley, R. A., editors, *Synthesis Imaging in Radio Astronomy II*, volume 180 of *Astronomical Society of the Pacific Conference Series*, page 357.

Cotton, W. D., Thorat, K., Condon, J. J., Frank, B. S., Józsa, G. I. G., White, S. V., Deane, R., Oozeer, N., Atemkeng, M., Bester, L., Fanaroff, B., Kupa, R. S., Smirnov, O. M., Mauch, T., Krishnan, V., and Camilo, F. (2020). Hydrodynamical backflow in x-shaped radio galaxy pks 201455. *Monthly Notices of the Royal Astronomical Society*, 495(1):1271–1281.

Croom, S. M., Smith, R. J., Boyle, B. J., Shanks, T., Miller, L., Outram, P. J., and Loaring, N. S. (2004). The 2dF QSO Redshift Survey - XII. The spectroscopic catalogue and luminosity function. , 349(4):1397–1418.

Curtis, H. D. (1918). Descriptions of 762 Nebulae and Clusters Photographed with the Crossley Reflector. *Publications of Lick Observatory*, 13:9–42.

de Gasperin, F., Williams, W. L., Best, P., Brüggen, M., Brunetti, G., Cuciti, V., Dijkema, T. J., Hardcastle, M. J., Norden, M. J., Offringa, A., Shimwell, T., van Weeren, R., Bomans, D., Bonafede, A., Botteon, A., Callingham, J. R., Cassano, R., Chyży, K. T., Emig, K. L., Edler, H., Haverkorn, M., Heald, G., Heesen, V., Iacobelli, M., Intema, H. T., Kadler, M., Małek, K., Mevius, M., Miley, G., Mingo, B., Morabito, L. K., Sabater, J., Morganti, R., Orrú, E., Pizzo, R., Prandoni, I., Shulevski, A., Tasse, C., Vaccari, M., Zarka, P., and Röttgering, H. (2021). The LOFAR LBA Sky Survey. I. Survey description and preliminary data release. , 648:A104.

Dolag, K. et al. (2023). Insights on the origin of odd radio circles from cosmological simulations. *The Astrophysical Journal*, 945(1):74.

Dopita, M. A. and Sutherland, R. S. (1995). Spectral signatures of fast shocks. ii. optical diagnostic diagrams. *The Astrophysical Journal*, 455:468–479.

Ekers, R. D. (1969). The radio galaxy in the abell 3627 cluster. *Australian Journal of Physics*, 22(4):399–407.

Ekers, R. D., Fanti, R., Lari, C., and Parma, P. (1978). Inversion symmetry of radio lobes in extragalactic sources. *Nature*, 276(5690):588–590.

Evans, D. A., Fong, W.-F., Hardcastle, M. J., Kraft, R. P., Lee, J. C., Worrall, D. M., Birkinshaw, M., Croston, J. H., and Muxlow, T. W. B. (2008). A Radio through X-Ray Study of the Jet/Companion-Galaxy Interaction in 3C 321. , 675(2):1057–1066.

Event Horizon Telescope Collaboration, Akiyama, K., Alberdi, A., Alef, W., Asada, K., Azulay, R., Baczko, A.-K., Ball, D., Baloković, M., Barrett, J., Bintley, D., Blackburn, L., Boland, W., Bouman, K. L., Bower, G. C., Bremer, M., Brinkerink, C. D., Brissenden, R., Britzen, S., Broderick, A. E., Broguiere, D., Bronzwaer, T., Byun, D.-Y., Carlstrom, J. E., Chael, A., Chan, C.-k., Chatterjee, S., Chatterjee, K., Chen, M.-T., Chen, Y., Cho, I., Christian, P., Conway, J. E., Cordes, J. M., Crew, G. B., Cui, Y., Davelaar, J., De Laurentis, M., Deane, R., Dempsey, J., Desvignes, G., Dexter, J., Doeleman, S. S., Eatough, R. P., Falcke, H., Fish, V. L., Fomalont, E., Fraga-Encinas, R., Freeman, W. T., Friberg, P., Fromm, C. M., Gómez, J. L., Galison, P., Gammie, C. F., García, R., Gentaz, O., Georgiev, B., Goddi, C., Gold, R., Gu, M., Gurwell, M., Hada, K., Hecht, M. H., Hesper, R., Ho, L. C., Ho, P., Honma, M., Huang, C.-W. L., Huang, L., Hughes, D. H., Ikeda, S., Inoue, M., Issaoun, S., James, D. J., Jannuzi, B. T., Janssen, M., Jeter, B., Jiang, W., Johnson, M. D., Jorstad, S., Jung, T., Karami, M., Karuppusamy, R., Kawashima, T., Keating, G. K., Kettenis, M., Kim, J.-Y., Kim, J., Kim, J., Kino, M., Koay, J. Y., Koch, P. M., Koyama, S., Kramer, M., Kramer, C., Krichbaum, T. P.,

Kuo, C.-Y., Lauer, T. R., Lee, S.-S., Li, Y.-R., Li, Z., Lindqvist, M., Liu, K., Liuzzo, E., Lo, W.-P., Lobanov, A. P., Loinard, L., Lonsdale, C., Lu, R.-S., MacDonald, N. R., Mao, J., Markoff, S., Marrone, D. P., Marscher, A. P., Martí-Vidal, I., Matsushita, S., Matthews, L. D., Medeiros, L., Menten, K. M., Mizuno, Y., Mizuno, I., Moran, J. M., Moriyama, K., Moscibrodzka, M., Müller, C., Nagai, H., Nagar, N. M., Nakamura, M., Narayan, R., Narayanan, G., Natarajan, I., Neri, R., Ni, C., Noutsos, A., Okino, H., Olivares, H., Ortiz-León, G. N., Oyama, T., Özel, F., Palumbo, D. C. M., Patel, N., Pen, U.-L., Pesce, D. W., Piétu, V., Plambeck, R., PopStefanija, A., Porth, O., Prather, B., Preciado-López, J. A., Psaltis, D., Pu, H.-Y., Ramakrishnan, V., Rao, R., Rawlings, M. G., Raymond, A. W., Rezzolla, L., Ripperda, B., Roelofs, F., Rogers, A., Ros, E., Rose, M., Roshanineshat, A., Rottmann, H., Roy, A. L., Ruszczyk, C., Ryan, B. R., Rygl, K. L. J., Sánchez, S., Sánchez-Arguelles, D., Sasada, M., Savolainen, T., Schloerb, F. P., Schuster, K.-F., Shao, L., Shen, Z., Small, D., Sohn, B. W., SooHoo, J., Tazaki, F., Tiede, P., Tilanus, R. P. J., Titus, M., Toma, K., Torne, P., Trent, T., Trippe, S., Tsuda, S., van Bemmel, I., van Langevelde, H. J., van Rossum, D. R., Wagner, J., Wardle, J., Weintroub, J., Wex, N., Wharton, R., Wielgus, M., Wong, G. N., Wu, Q., Young, K., and Young, A. (2019). First M87 Event Horizon Telescope Results. I. The Shadow of the Supermassive Black Hole. , 875(1):L1.

Fanaroff, B. L. and Riley, J. M. (1974). The morphology of extragalactic radio sources of high and low luminosity. , 167:31P–36P.

Fath, E. A. (1909). The spectra of some spiral nebulae and globular star clusters. *Lick Observatory Bulletin*, 149:71–77.

Feretti, L. and Venturi, T. (2002). Radio galaxies and their environment. In Plionis, M. and Georgantopoulos, I., editors, *The Universe at Low Radio Frequencies*, volume 199, pages 163–+. Kluwer Academic Publishers. ASSL, Vol. 272.

Filipović, M. D. et al. (2022). Mysterious odd radio circle near the large magellanic cloud. *Monthly Notices of the Royal Astronomical Society*, 512(1):265–274.

Giri, G., Fendt, C., Thorat, K., Bodo, G., and Rossi, P. (2024). X-shaped radio galaxies: probing jet evolution, ambient medium dynamics, and their intricate interconnection. *Frontiers in Astronomy and Space Sciences*, 11:1371101.

Gloudemans, A. J., Sweijen, F., Morabito, L. K., Farina, E. P., Duncan, K. J., Harikane, Y., Röttgering, H. J. A., Saxena, A., and Schindler, J.-T. (2025). Monster radio jet (gt;66 kpc) observed in quasar at z 5. *The Astrophysical Journal Letters*, 980(1):L8.

Gower, A. C., Gregory, P. C., Unruh, W. G., and Hutchings, J. B. (1982). Relativistic precessing jets in quasars and radio galaxies : models to fit high resolution data. , 262:478–496.

Gower, A. C., Gregory, P. C., Unruh, W. G., and Hutchings, J. B. (1982). Relativistic precessing jets in quasars and radio galaxies: models to fit high-resolution data. *The Astrophysical Journal*, 262:478–488.

Greisen, E. W. (2003). AIPS, the VLA, and the VLBA. In Heck, A., editor, *Information Handling in Astronomy - Historical Vistas*, volume 285 of *Astrophysics and Space Science Library*, page 109.

Hardcastle, M. J. and Croston, J. H. (2020). Radio galaxies and feedback from AGN jets. , 88:101539.

Hardee, P. E. (1987). Spatial Stability of Relativistic Jets: Application to 3C 345. , 318:78.

Hardee, P. E. and Clarke, D. A. (1992). Nonlinear Dynamics of a Three-dimensional Jet. , 400:L9.

Hargrave, P. J. and Ryle, M. (1974). Observations of cygnus a with the 5-km telescope. *Monthly Notices of the Royal Astronomical Society*, 166(2):305–319.

Hjellming, R. M. and Johnston, K. J. (1981). An analysis of the proper motions of SS 433 radio jets. , 246:L141–L145.

Hjellming, R. M. and Johnston, K. J. (1981). An analysis of the radio structure of ss 433. *Nature*, 290(5806):100–103.

Högbom, J. A. (1974). Aperture Synthesis with a Non-Regular Distribution of Interferometer Baselines. , 15:417.

Horton, M. A., Krause, M. G. H., and Hardcastle, M. J. (2020). 3D hydrodynamic simulations of large-scale precessing jets: radio morphology. , 499(4):5765–5781.

Horton, M. A., Krause, M. G. H., and Hardcastle, M. J. (2023). New mechanisms for forming multiple hotspots in radio jets. , 521(2):2593–2606.

Hota, A., Sirothia, S. K., Ohyama, Y., Konar, C., Kim, S., Rey, S.-C., Saikia, D. J., Croston, J. H., and Matsushita, S. (2011). Discovery of a spiral-host episodic radio galaxy. , 417(1):L36–L40.

Hubble, E. (1929). A Relation between Distance and Radial Velocity among Extra-Galactic Nebulae. *Proceedings of the National Academy of Science*, 15(3):168–173.

Hunstead, R. W., Murdoch, H. S., Condon, J. J., and Phillips, M. M. (1984). A QSO with precessing jets : 2300 - 189. , 207:55–71.

Häring, N. and Rix, H.-W. (2004). On the black hole mass–bulge mass relation. *The Astrophysical Journal Letters*, 604:L89–L92.

Högbom, J. A. and Carlsson, I. (1974). Observations of the structure and polarization of intense extragalactic sources at 1415 mhz. *Astronomy and Astrophysics*, 34:341–354.

Intema, H. T. (2014). SPAM: Source Peeling and Atmospheric Modeling. Astrophysics Source Code Library, record ascl:1408.006.

Intema, H. T., Jagannathan, P., Mooley, K. P., and Frail, D. A. (2017). The GMRT 150 MHz all-sky radio survey. First alternative data release TGSS ADR1. , 598:A78.

Intema, H. T., van der Tol, S., Cotton, W. D., Cohen, A. S., van Bemmel, I. M., and Röttgering, H. J. A. (2009). Ionospheric calibration of low frequency radio interferometric observations using the peeling scheme. I. Method description and first results. , 501(3):1185–1205.

Jansky, K. G. (1933). Radio Waves from Outside the Solar System. , 132(3323):66.

Jennison, R. C. and Das Gupta, M. K. (1953). Fine Structure of the Extra-terrestrial Radio Source Cygnus I. , 172(4387):996–997.

Kellermann, K. I. and Moran, J. M. (2001). The Development of High-Resolution Imaging in Radio Astronomy. , 39:457–509.

Koribalski, B. S., Duchesne, S. W., Lenc, E., Venturi, T., Botteon, A., Shabala, S. S., Vernstrom, T., Carretti, E., Norris, R. P., Anderson, C., Hopkins, A. M., Riseley, C. J., Gupta, N., and Velović, V. (2024). ASKAP reveals the radio tail structure of the Corkscrew Galaxy shaped by its passage through the Abell 3627 cluster. , 533(1):608–620.

Kormendy, J. and Gebhardt, K. (2001). Supermassive black holes in galactic nuclei. In Wheeler, J. C. and Martel, H., editors, *20th Texas Symposium on relativistic astrophysics*, volume 586 of *American Institute of Physics Conference Series*, pages 363–381. AIP.

Lacy, M., Baum, S. A., Chandler, C. J., Chatterjee, S., Clarke, T. E., Deustua, S., English, J., Farnes, J., Gaensler, B. M., Gugliucci, N., Hallinan, G., Kent, B. R., Kimball, A., Law, C. J., Lazio, T. J. W., Marvil, J., Mao, S. A., Medlin, D., Mooley, K., Murphy, E. J., Myers, S., Osten, R., Richards, G. T., Rosolowsky, E., Rudnick, L., Schinzel, F.,

Sivakoff, G. R., Sjouwerman, L. O., Taylor, R., White, R. L., Wrobel, J., Andernach, H., Beasley, A. J., Berger, E., Bhatnager, S., Birkinshaw, M., Bower, G. C., Brandt, W. N., Brown, S., Burke-Spolaor, S., Butler, B. J., Comerford, J., Demorest, P. B., Fu, H., Giacintucci, S., Golap, K., Güth, T., Hales, C. A., Hiriart, R., Hodge, J., Horesh, A., Ivezić, Ž., Jarvis, M. J., Kamble, A., Kassim, N., Liu, X., Loinard, L., Lyons, D. K., Masters, J., Mezcua, M., Moellenbrock, G. A., Mroczkowski, T., Nyland, K., O'Dea, C. P., O'Sullivan, S. P., Peters, W. M., Radford, K., Rao, U., Robnett, J., Salcido, J., Shen, Y., Sobotka, A., Witz, S., Vaccari, M., van Weeren, R. J., Vargas, A., Williams, P. K. G., and Yoon, I. (2020). The Karl G. Jansky Very Large Array Sky Survey (VLASS). Science Case and Survey Design. , 132(1009):035001.

LaMassa, S. M., Cales, S., Moran, E. C., Myers, A. D., Richards, G. T., Eracleous, M., Heckman, T. M., Gallo, L., and Urry, C. M. (2015). The Discovery of the First "Changing Look" Quasar: New Insights Into the Physics and Phenomenology of Active Galactic Nucleus. , 800(2):144.

Leahy, J. P. and Parma, P. (1992). Multiple outbursts in radio galaxies. In *Extragalactic Radio Sources. From Beams to Jets*, pages 307–308.

Leahy, J. P. and Williams, A. G. (1984). The bridges of classical double radio sources. *Monthly Notices of the Royal Astronomical Society*, 210(4):929–951.

Ledlow, M. J. and Owen, F. N. (1996). 20 cm vla survey of abell clusters of galaxies. vi. radio/optical luminosity functions. *The Astronomical Journal*, 112(1):9–+.

Lense, J. and Thirring, H. (1918). Lense Thirring Precession. *Phys. Z.*, 19:156–163.

Liska, M., Tchekhovskoy, A., Ingram, A., and van der Klis, M. (2018). Formation of precessing jets by tilted black hole discs in 3d general relativistic magnetohydrodynamic simulations. *Monthly Notices of the Royal Astronomical Society: Letters*, 474(1):L81–L85.

Lobanov, A. P. and Zensus, J. A. (2001). A Cosmic Double Helix in the Archetypical Quasar 3C273. *Science*, 294(5540):128–131.

Lopez, J. A., Meaburn, J., and Palmer, J. W. (1993). Kinematical Evidence for a Rotating, Episodic Jet in the Planetary Nebula Fleming 1. , 415:L135.

Lu, J.-F. (1990). Accretion disk-driven jet precession in active galactic nuclei. *Astronomy and Astrophysics*, 229:424–428.

Lu, J.-F. and Zhou, B.-Y. (2005). Observational evidence of accretion disk-caused jet precession in galactic nuclei. *The Astrophysical Journal*, 635(1):L17–L20.

Machalski, J., Jamrozy, M., and Saikia, D. J. (2009). A multifrequency study of giant radio sources – iii. dynamical age versus spectral age of the lobes. *Monthly Notices of the Royal Astronomical Society*, 395(2):812–828.

Machalski, J., Kozieł-Wierzbowska, D., and Goyal, A. (2021). An atlas of dynamical evolution models of 361 fanaroff–riley type ii radio sources. *The Astrophysical Journal Supplement Series*, 255(2):22.

MacLeod, C. L., Ross, N. P., Lawrence, A., Goad, M., Horne, K., Burgett, W., Chambers, K. C., Flewelling, H., Hodapp, K., Kaiser, N., Magnier, E., Wainscoat, R., and Waters, C. (2016). A systematic search for changing-look quasars in sdss. *Monthly Notices of the Royal Astronomical Society*, 457(1):389–404.

Merritt, D. and Ekers, R. D. (2002). Tracing black hole mergers through radio lobe morphology. *Science*, 297(5588):1310–1313.

Merritt, D. and Ferrarese, L. (2001). The m– relation for supermassive black holes. *The Astrophysical Journal*, 547:140–145.

Miley, G. (1980). The structure of extended extragalactic radio sources. *Annual Review of Astronomy and Astrophysics*, 18:165–218.

Miley, G. K. and Wade, C. M. (1971). Cygnus a: A study of the hot spots and the central region at 2.7 and 8.1 ghz. *Monthly Notices of the Royal Astronomical Society*, 153(4):473–486.

Miller, B. P. and Brandt, W. N. (2009). Chandra Observations of the Hybrid Morphology Radio Sources 3C 433 and 4C 65.15: FR IIs with Asymmetric Environments. , 695(1):755–764.

Misra, A., Jamrozy, M., and Weżgowiec, M. (2023). Multifrequency analysis of the radio emission from a post-merger galaxy CGCG 292-057. , 523(2):1648–1660.

Misra, A., Jamrozy, M., Weżgowiec, M., and Kozieł-Wierzbowska, D. (2025). Multiwavelength investigations of PKS 2300–18: S-shaped radio quasar with precessing jets and double-peaked broad emission-line spectrum. , 536(3):2025–2045.

Mohan, N. and Rafferty, D. (2015). PyBDSF: Python Blob Detection and Source Finder. Astrophysics Source Code Library, record ascl:1502.007.

Nakamura, M., Asada, K., Hada, K., Pu, H.-Y., Noble, S., Tseng, C., Toma, K., Kino, M., Nagai, H., Takahashi, K., Algaba, J.-C., Orienti, M., Akiyama, K., Doi, A., Giovannini, G., Giroletti, M., Honma, M., Koyama, S., Lico, R., Niinuma, K., and Tazaki, F. (2018). Parabolic Jets from the Spinning Black Hole in M87. , 868(2):146.

Nandi, S., Jamrozy, M., Roy, R., Larsson, J., Saikia, D. J., Baes, M., and Singh, M. (2017). Tale of J1328+2752: a misaligned double-double radio galaxy hosted by a binary black hole? , 467(1):L56–L60.

Nandi, S., Mohan, P., Gupta, A. C., and et al. (2021). Periodicities and jet precession in blazar jets: evidence for binary supermassive black holes. *The Astrophysical Journal*, 909(1):62.

Narayan, R., Igumenshchev, I. V., and Abramowicz, M. A. (2003). Magnetically arrested disk: An energetically efficient accretion flow. *Publications of the Astronomical Society of Japan*, 55(6):L69–L72.

Narayan, R., Mahadevan, R., and Quataert, E. (1998). Advection-dominated accretion around black holes. In Abramowicz, M. A., Björnsson, G., and Pringle, J. E., editors, *Theory of Black Hole Accretion Disks*, pages 148–182. Cambridge University Press.

Narayan, R., Sądowski, A., Penna, R. F., and Kulkarni, A. K. (2012). Grmhd simulations of magnetized advection dominated accretion on a non-spinning black hole: Role of outflows. *Monthly Notices of the Royal Astronomical Society*, 426(4):3241–3259.

Narayan, R. and Yi, I. (1995). Advection-dominated accretion: Underfed black holes and neutron stars. *The Astrophysical Journal*, 452:710–735.

Nemmen, R. S., Storchi-Bergmann, T., and Eracleous, M. (2014). Spectral models for low-luminosity active galactic nuclei in LINERs: the role of advection-dominated accretion and jets. , 438(4):2804–2827.

Netzer, H. (2015). Revisiting the Unified Model of Active Galactic Nuclei. , 53:365–408.

Nikonov, A. S., Kovalev, Y. Y., Kravchenko, E. V., Pashchenko, I. N., and Lobanov, A. P. (2023). Properties of the jet in M87 revealed by its helical structure imaged with the VLBA at 8 and 15 GHz. , 526(4):5949–5963.

Nolting, C., Ball, J., and Nguyen, T. M. (2023). Simulations of precessing jets and the formation of x-shaped radio galaxies. *arXiv preprint arXiv:2301.04343*.

Norris, R. P. et al. (2022a). Meerkat uncovers the physics of an odd radio circle. *Monthly Notices of the Royal Astronomical Society*, 513(1):1300–1310.

Norris, R. P., Marvil, J., Collier, J. D., Kapinska, A. D., O'Brien, A. N., Rudnick, L., Andernach, H., Asorey, J., Brown, M. J. I., Brüggen, M., et al. (2021a). The evolutionary map of the universe pilot survey. *Publications of the Astronomical Society of Australia*, 38:e046.

Norris, R. P., Marvil, J., Jarrett, T., Marais, A., Collier, J. D., Rudnick, L., Banfield, J. K., Filipovic, M. D., Franzen, T. M. O., et al. (2022b). Meerkat uncovers the physics of an odd radio circle. *Monthly Notices of the Royal Astronomical Society*, 513(1):1300–1310.

Norris, R. P., Rayner, T., Marvil, J., Hopkins, A., Hurley-Walker, N., Indermuehle, B., Collier, J. D., Galvin, T., Seymour, N., Filipovic, M. D., et al. (2021b). Discovery of a new extragalactic circular radio source with askap. *Monthly Notices of the Royal Astronomical Society: Letters*, 505(1):L11–L15.

O'Dea, C. P. and Baum, S. A. (2023). Wide-Angle-Tail (WAT) Radio Sources. *Galaxies*, 11(3):67.

O'Dea, C. P. and Owen, F. N. (1986). Vla observations of ngc 1265 at 4886 mhz. *The Astrophysical Journal*, 301:841–849.

O'Donoghue, A. A., Eilek, J. A., and Owen, F. N. (1993). Flow Dynamics and Bending of Wide-Angle Tailed Radio Sources. , 408:428.

Oei, M. S. S. L., Hardcastle, M. J., Timmerman, R., Gast, A. R. D. J. G. I. B., Botteon, A., Rodriguez, A. C., Stern, D., Calistro Rivera, G., van Weeren, R. J., Röttgering, H. J. A., Intema, H. T., de Gasperin, F., and Djorgovski, S. G. (2024). Black hole jets on the scale of the cosmic web. , 633(8030):537–541.

Offringa, A. R., McKinley, B., Hurley-Walker, et al. (2014). WSClean: an implementation of a fast, generic wide-field imager for radio astronomy. *MNRAS*, 444(1):606–619.

Offringa, A. R. and Smirnov, O. (2017). An optimized algorithm for multiscale wideband deconvolution of radio astronomical images. , 471(1):301–316.

Omar, A. (2022). On energetics and progenitors of odd radio circles: A causal connection with tidal disruption of stars? *Monthly Notices of the Royal Astronomical Society*, 516(1):L43–L47.

Pal, S. and Kumari, S. (2021). Winged Radio Sources from LOFAR Two-metre Sky Survey First Data Release (LoTSS DR1). *arXiv e-prints*, page arXiv:2104.00410.

Perucho, M., Lobanov, A. P., Martí, J. M., and Hardee, P. E. (2006). The role of Kelvin-Helmholtz instability in the internal structure of relativistic outflows. The case of the jet in 3C 273. , 456(2):493–504.

Perucho, M., Martí, J. M., Cela, J. M., Hanasz, M., de La Cruz, R., and Rubio, F. (2010). Stability of three-dimensional relativistic jets: implications for jet collimation. , 519:A41.

Perucho, M., Martí-Vidal, I., Lobanov, A. P., and Hardee, P. E. (2012). S5 0836+710: An FRII jet disrupted by the growth of a helical instability? , 545:A65.

Proctor, D. D. (2011). Morphological Annotations for Groups in the First Database. , 194(2):31.

Rawes, J., Birkinshaw, M., and Worrall, D. M. (2018). Extreme jet bending on kiloparsec scales: the 'doughnut' in ngc 6109. *Monthly Notices of the Royal Astronomical Society*, 480(3):3644–3654.

Reber, G. (1944). Cosmic Static. , 100:279.

Riley, J. M. (1972). The structure of some extragalactic radio sources. *Monthly Notices of the Royal Astronomical Society*, 157(4):349–361.

Ro, H., Yi, K., Cui, Y., Kino, M., Hada, K., Kawashima, T., Mizuno, Y., Sohn, B. W., and Tazaki, F. (2023). Transverse oscillations of the m87 jet revealed by kava observations. *Galaxies*, 11(1):33.

Rottmann, H. (2001). *The orientation and size of the 'Z' in X-shaped radio galaxies*. PhD thesis, University of Bonn.

Rubinur, K., Das, M., Kharb, P., and Honey, M. (2017). A candidate dual AGN in a double-peaked emission-line galaxy with precessing radio jets. , 465(4):4772–4782.

Ryle, M. and Smith, D. D. (1948). A new radio interferometer and its application to the observation of weak radio stars. *Nature*, 162(4125):462–463.

Sarazin, C. L., Begelman, M. C., and Hatchett, S. P. (1980). Disk-driven precession in SS 433. , 238:L129–L132.

Saripalli, L., Subrahmanyan, R., and Udaya Shankar, N. (2003). J0116–473: A new double-double radio galaxy. *The Astrophysical Journal*, 590(1):181–189.

Scheuer, P. A. G. (1974). Models of extragalactic radio sources with a continuous energy supply from a central object. *Monthly Notices of the Royal Astronomical Society*, 166(3):513–528.

Schoenmakers, A. P., de Bruyn, A. G., Röttgering, H. J. A., van der Laan, H., and Kaiser, C. R. (2000). A new sample of large double-double radio galaxies. *Monthly Notices of the Royal Astronomical Society*, 315(2):371–380.

Schwab, F. R. (1984). Relaxing the isoplanatism assumption in self-calibration; applications to low-frequency radio interferometry. , 89:1076–1081.

Sebastian, B., Caproni, A., Kharb, P., Nayana, A. J., Ali, A., Rubinur, K., O'Dea, C. P., Baum, S., and Nandi, S. (2024). A VLBA-uGMRT search for candidate binary black holes: study of six X-shaped radio galaxies with double-peaked emission lines. , 530(4):4902–4919.

Sethi, S., Kuźmicz, A., Jamrozy, M., and Slavcheva-Mihova, L. (2024). Discovery of a 100 kpc Narrow Curved Twin Jet in the S-shaped Giant Radio Galaxy J0644+1043. , 969(2):156.

Seyfert, C. K. (1943). Nuclear Emission in Spiral Nebulae. , 97:28.

Shakura, N. I. and Sunyaev, R. A. (1973). Black holes in binary systems. Observational appearance. , 24:337–355.

Shimwell, T. W., Hardcastle, M. J., Tasse, C., Best, P. N., Röttgering, H. J. A., Williams, W. L., Botteon, A., Drabent, A., Mechev, A., Shulevski, A., van Weeren, R. J., Bester, L., Brüggen, M., Brunetti, G., Callingham, J. R., Chyży, K. T., Conway, J. E., Dijkema, T. J., Duncan, K., de Gasperin, F., Hale, C. L., Haverkorn, M., Hugo, B., Jackson, N., Mevius, M., Miley, G. K., Morabito, L. K., Morganti, R., Offringa, A., Oonk, J. B. R., Rafferty, D., Sabater, J., Smith, D. J. B., Schwarz, D. J., Smirnov, O., O'Sullivan, S. P., Vedantham, H., White, G. J., Albert, J. G., Alegre, L., Asabere, B., Bacon, D. J., Bonafede, A., Bonnassieux, E., Brienza, M., Bilicki, M., Bonato, M., Calistro Rivera, G., Cassano, R., Cochrane, R., Croston, J. H., Cuciti, V., Dallacasa, D., Danezi, A., Dettmar, R. J., Di Gennaro, G., Edler, H. W., Enßlin, T. A., Emig, K. L., Franzen, T. M. O., García-Vergara, C., Grange, Y. G., Gürkan, G., Hajduk, M., Heald, G., Heesen, V., Hoang, D. N., Hoeft, M., Horellou, C., Iacobelli, M., Jamrozy, M., Jelić, V., Kondapally, R., Kukreti, P., Kunert-Bajraszewska, M., Magliocchetti, M., Mahatma, V., Małek, K., Mandal, S., Massaro, F., Meyer-Zhao, Z., Mingo, B., Mostert, R. I. J., Nair, D. G., Nakoneczny, S. J., Nikiel-Wroczyński, B., Orrú, E., Pajdosz-Śmierciak, U., Pasini, T., Prandoni, I., van Piggelen, H. E., Rajpurohit, K., Retana-Montenegro, E., Riseley, C. J., Rowlinson, A., Saxena, A., Schrijvers, C., Sweijen, F., Siewert, T. M., Timmerman, R., Vaccari, M., Vink, J., West, J. L., Wołowska, A., Zhang, X., and Zheng, J. (2022). The LOFAR Two-metre Sky Survey. V. Second data release. , 659:A1.

Shimwell, T. W., Tasse, C., Hardcastle, M. J., Mechev, A. P., Williams, W. L., Best, P. N., Röttgering, H. J. A., Callingham, J. R., Dijkema, T. J., de Gasperin, F., Hoang, D. N., Hugo, B., Mirmont, M., Oonk, J. B. R., Prandoni, I., Rafferty, D., Sabater, J., Smirnov, O., van Weeren, R. J., White, G. J., Atemkeng, M., Bester, L., Bonnassieux, E., Brüggen, M., Brunetti, G., Chyży, K. T., Cochrane, R., Conway, J. E., Croston, J. H., Danezi, A., Duncan, K., Haverkorn, M., Heald, G. H., Iacobelli, M., Intema, H. T., Jackson, N., Jamrozy, M., Jarvis, M. J., Lakhoo, R., Mevius, M., Miley, G. K., Morabito, L., Morganti, R., Nisbet, D., Orrú, E., Perkins, S., Pizzo, R. F., Schrijvers, C., Smith, D. J. B., Vermeulen, R., Wise, M. W., Alegre, L., Bacon, D. J., van Bemmel, I. M., Beswick, R. J., Bonafede, A., Botteon, A., Bourke, S., Brienza, M., Calistro Rivera, G., Cassano, R., Clarke, A. O., Conselice, C. J., Dettmar, R. J., Drabent, A., Dumba, C., Emig, K. L., Enßlin, T. A., Ferrari, C., Garrett, M. A., Génova-Santos, R. T., Goyal, A., Gürkan, G., Hale, C., Harwood, J. J., Heesen, V., Hoeft, M., Horellou, C., Jackson, C., Kokotanekov, G., Kondapally, R., Kunert-Bajraszewska, M., Mahatma, V., Mahony, E. K., Mandal, S., McKean, J. P., Merloni, A., Mingo, B., Miskolczi, A., Mooney, S., Nikiel-Wroczyński, B., O'Sullivan, S. P., Quinn, J., Reich, W., Roskowiński, C., Rowlinson, A., Savini, F., Saxena, A., Schwarz, D. J., Shulevski, A., Sridhar, S. S., Stacey, H. R., Urquhart, S., van der Wiel, M. H. D., Varenius, E., Webster, B., and Wilber, A. (2019). The LOFAR Two-metre Sky Survey. II. First data release. , 622:A1.

Slipher, V. M. (1917). Nebulae. *Proceedings of the American Philosophical Society*, 56:403–409.

Smolčić, V., Schinnerer, E., Finoguenov, A., Sakelliou, I., Carilli, C. L., Botzler, C. S., Brusa, M., Scoville, N., Ajiki, M., Capak, P., Guzzo, L., Hasinger, G., Impey, C., Jahnke, K., Kartaltepe, J. S., McCracken, H. J., Mobasher, B., Murayama, T., Sasaki, S. S., Shioya, Y., Taniguchi, Y., and Trump, J. R. (2007). A wide angle tail radio galaxy in the cosmos field: evidence for cluster formation. *The Astrophysical Journal Supplement Series*, 172(1):295–317.

Steffen, W. (1997). Signatures of helical jets. *Vistas in Astronomy*, 41(1):71–78.

Sądowski, A., Narayan, R., Penna, R., and Zhu, Y. (2013). Energy, momentum and mass outflows and feedback from thick accretion discs around rotating black holes. *Monthly Notices of the Royal Astronomical Society*, 436(4):3856–3874.

Ubertosi, F., Giroletti, M., Gitti, M., Biava, N., De Rubeis, E., Bonafede, A., Feretti, L., Bondi, M., Bruno, L., Liuzzo, E., Ignesti, A., and Brunetti, G. (2024). A JVLA,

LOFAR, e-Merlin, VLBA, and EVN study of RBS 797: can binary supermassive black holes explain the outburst history of the central radio galaxy? , 688:A86.

Urry, C. M. and Padovani, P. (1995). Unified schemes for radio-loud active galactic nuclei. *Publications of the Astronomical Society of the Pacific*, 107(715):803–845.

van Breugel, W., Balick, B., Heckman, T., Miley, G., and Helfand, D. (1983). The peculiar radio galaxy 3C 433. , 88:40–54.

van Haarlem, M. P., Wise, M. W., Gunst, A. W., Heald, G., McKean, J. P., Hessels, J. W. T., de Bruyn, A. G., Nijboer, R., Swinbank, J., Fallows, R., Brentjens, M., Nelles, A., Beck, R., Falcke, H., Fender, R., Hörandel, J., Koopmans, L. V. E., Mann, G., Miley, G., Röttgering, H., Stappers, B. W., Wijers, R. A. M. J., Zaroubi, S., van den Akker, M., Alexov, A., Anderson, J., Anderson, K., van Ardenne, A., Arts, M., Asgekar, A., Avruch, I. M., Batejat, F., Bähren, L., Bell, M. E., Bell, M. R., van Bemmel, I., Bennema, P., Bentum, M. J., Bernardi, G., Best, P., Bîrzan, L., Bonafede, A., Boonstra, A. J., Braun, R., Bregman, J., Breitling, F., van de Brink, R. H., Broderick, J., Broekema, P. C., Brouw, W. N., Brüggen, M., Butcher, H. R., van Cappellen, W., Ciardi, B., Coenen, T., Conway, J., Coolen, A., Corstanje, A., Damstra, S., Davies, O., Deller, A. T., Dettmar, R. J., van Diepen, G., Dijkstra, K., Donker, P., Doorduin, A., Dromer, J., Drost, M., van Duin, A., Eislöffel, J., van Enst, J., Ferrari, C., Frieswijk, W., Gankema, H., Garrett, M. A., de Gasperin, F., Gerbers, M., de Geus, E., Grießmeier, J. M., Grit, T., Gruppen, P., Hamaker, J. P., Hassall, T., Hoeft, M., Holties, H. A., Horneffer, A., van der Horst, A., van Houwelingen, A., Huijgen, A., Iacobelli, M., Intema, H., Jackson, N., Jelic, V., de Jong, A., Juette, E., Kant, D., Karastergiou, A., Koers, A., Kollen, H., Kondratiev, V. I., Kooistra, E., Koopman, Y., Koster, A., Kuniyoshi, M., Kramer, M., Kuper, G., Lambropoulos, P., Law, C., van Leeuwen, J., Lemaitre, J., Loose, M., Maat, P., Macario, G., Markoff, S., Masters, J., McFadden, R. A., McKay-Bukowski, D., Meijering, H., Meulman, H., Mevius, M., Middelberg, E., Millenaar, R., Miller-Jones, J. C. A., Mohan, R. N., Mol, J. D., Morawietz, J., Morganti, R., Mulcahy, D. D., Mulder, E., Munk, H., Nieuwenhuis, L., van Nieuwpoort, R., Noordam, J. E., Norden, M., Noutsos, A., Offringa, A. R., Olofsson, H., Omar, A., Orrú, E., Overeem, R., Paas, H., Pandey-Pommier, M., Pandey, V. N., Pizzo, R., Polatidis, A., Rafferty, D., Rawlings, S., Reich, W., de Reijer, J. P., Reitsma, J., Renting, G. A., Riemers, P., Rol, E., Romein, J. W., Roosjen, J., Ruiter, M., Scaife, A., van der Schaaf, K., Scheers, B., Schellart, P., Schoenmakers, A., Schoonderbeek, G., Serylak, M., Shulevski, A., Sluman, J., Smirnov, O., Sobey, C., Spreeuw, H., Steinmetz, M., Sterks, C. G. M., Stiepel, H. J., Stuurwold, K., Tagger, M., Tang, Y., Tasse, C., Thomas, I., Thoudam, S., Toribio, M. C., van der

Tol, B., Usov, O., van Veelen, M., van der Veen, A. J., ter Veen, S., Verbiest, J. P. W., Vermeulen, R., Vermaas, N., Vocks, C., Vogt, C., de Vos, M., van der Wal, E., van Weeren, R., Weggemans, H., Weltevrede, P., White, S., Wijnholds, S. J., Wilhelmsson, T., Wucknitz, O., Yatawatta, S., Zarka, P., Zensus, A., and van Zwieten, J. (2013). LOFAR: The LOw-Frequency ARray. , 556:A2.

Walker, S. A., Hlavacek-Larrondo, J., Gendron-Marsolais, M., Fabian, A. C., Intema, H., Sanders, J. S., Bamford, J. T., and van Weeren, R. (2017). Is there a giant kelvin-helmholtz instability in the sloshing cold front of the perseus cluster? *Monthly Notices of the Royal Astronomical Society*, 468(2):2506–2514.

Wellington, K. J., Banhatti, D. G., and Jaffe, W. J. (1973). Radio observations of ngc 1265 in the perseus cluster. *Astronomy and Astrophysics*, 29:323–328.

Worrall, D. M., Birkinshaw, M., Cameron, R. A., Lawrence, C. R., and Pearson, T. J. (1995). An x-ray study of the x-shaped radio galaxy 3c 403. *The Astrophysical Journal*, 449:93–102.